Development of a Gas-Particle Direct-Contact Trickle-Flow Heat-Exchanger for Application in Concentrating Solar Tower Systems

Entwicklung eines Gas-Partikel direktkontakt Riesel-Wärmeübertragers für die Anwendung in konzentrierenden Solarturmsystemen

Von der Fakultät für Maschinenwesen der Rheinisch-Westfälischen Technischen Hochschule Aachen zur Erlangung des akademischen Grades eines Doktors der Ingenieurwissenschaften genehmigte Dissertation

vorgelegt von

Markus Alois Reichart

Berichter: Univ.-Prof. Dr.-Ing. Robert Pitz-Paal
Univ.-Prof. Dr.-Ing. Thomas Wetzel

Tag der mündlichen Prüfung: 03.12.2025

With infinite love and gratitude

for

Mom and Dad

Acknowledgements

I would like to thank my first examiner, Univ.-Prof. Dr.-Ing. Robert Pitz-Paal[I], for supervising this work. In frequent and fruitful discussions, he provided highly valuable suggestions and guidance to my work. Univ.-Prof. Dr.-Ing. Bernhard Hoffschmidt[II] and Univ.-Prof. Dr. rer. nat. Christian Sattler[III] participated in our discussions whenever possible and contributed with high interest and meaningful comments, which was greatly appreciated. Furthermore, I would like to acknowledge Univ.-Prof. Dr.-Ing. Thomas Wetzel[IV] for his interest and support throughout this work and for acting as the second examiner for this dissertation.

Special recognition is due to my two tutors, Dr.-Ing. Martina Neises-von Puttkamer and Dipl.-Ing. (FH) Ralf Uhlig, for their committed support and guidance during my daily work. Their constructive ideas and advice were always very much appreciated and contributed highly to the successful outcome of this work.

I would also like to thank Dr.-Ing. Reiner Buck and Dipl.-Ing. (FH) Ralf Uhlig for entrusting me with this work in the first place and enabling my return to my scientific home, the DLR – Institute of Solar Research.

Expressions of gratitude are also extended to my former group leader, Dr.-Ing. Luka Lackovic. His interest and time spent in numerous technical discussions were invaluable, and his commitment in providing me with the freedom to conduct my research alongside my additional work as a research engineer at the Institute of Solar Research was unparalleled. I would also like to thank all my colleagues and former students for the outstanding teamwork, support, and working atmosphere.

For providing me with the encouragement when I needed it the most, I am especially grateful to Pollyanne Ferreira da Silva, Rose & Malte Kullak-Ublick, Johannes Steinebrei, Inmaculada Gallego Pérez & Sigfried Girardot Agulló, Lara Waltersmann, and Raoul Laribi. My deepest appreciation is reserved for my beloved family, on which I can always rely, for their trust and never-ending support.

Stuttgart, December 2025 Markus Alois Reichart

This work was compiled at the Institute of Solar Research of the German Aerospace Center in the context of the PREMA-project, funded from the European Union's Horizon 2020 Research and Innovation Programme under Grant Agreement No 820561.

[I] Head of DLR – Institute of Solar Research and Chair of Solar Technology at RWTH Aachen

[II] Head of DLR – Institute of Solar Research and Chair of Solar Components at RWTH Aachen

[III] Head of DLR – Institute of Future Fuels and professor for Solar Fuel Production at TU Dresden

[IV] Head of Institute of Thermal Process Engineering at Karlsruhe Institute of Technology

Abstract

Ceramic particles represent a viable alternative as heat transfer and storage medium in concentrating solar tower systems. The particles are heated in solar-receivers close to 1,000 °C. To transfer the stored heat in the particles the principles of a trickle flow reactor, was considered to be superior compared to state-of-the-art technologies, like fluidized bed- or cyclone-HX. The trickle-flow heat exchanger (TFHX) provides a relative high power density at a relative low pressure drop, meeting the requirement for the use in a CSP tower system. To date, no design recommendation is known to identify for a given particle type an optimized packing structure that emphasizes gas-particle interaction by comprising a high total particle surface and a uniform spatial particle distribution of the trickling particles within the packing void. This is why this work aimed to develop and investigated a gas-particle direct-contact trickle flow heat exchanger for the envisioned use in a particle based solar tower system, using bauxite particles of 1 mm diameter. Based on observations in literature, different packed columns were designed and investigated numerically. In the DEM simulations the dimensionless total particle surface, the particle hold-up, such as the spatial particle distribution were analyzed. It was found that, for the used particles, bar elements with a flat cross-sectional area increase the particle hold-up and provide an even spatial distribution of the trickling solids. In a developed test-setup at ambient temperature, the packing geometry was refined experimentally. During those experiments it was found, that packing structures, designed to allow the accumulation of static particles can increase the hold-up of the trickling particles. Those static particles can absorb the kinetic falling energy of the trickling solids, and thereby reduce the particle sink velocity and conversely increase the total particle surface, or hold-up. The refined packing geometry was used in hot experiments to assess the heat transfer capabilities. Particles at ambient temperature with varying flow rates were feed into the top of the column, while air at ambient pressure was induced at the bottom of the HX. Four air inlet temperatures up to 640 °C, such as five different media flow rates were defined, where the particle and air flow rates were chosen to achieve roughly equal heat capacity flow rates, since a high temperature change in both media flows was preferred. For the highest air inlet temperature, the power density of the investigated TFHX was determined over 1,000 $\mathrm{kW/m^3}$ for media flow rates above 2 $\mathrm{kg/(m^2 \cdot s)}$. The volumetric heat transfer coefficient ranges in the same flow conditions at approximately 15 $\mathrm{kW/m^3}$, with NTU numbers for the particle and air flow of approximately 5 and 8 respectively. In was shown and discussed, that the developed TFHX in this work is capable to increase the determined power densities, volumetric heat transfer coefficients, and NTU values by approximately 100 % compared to the available data in literature. It is assumed, that the increase in performance can be deduced by an increased surface of the trickling particles within the packed column, or conversely by a reduced sink velocity of the grains of approximately 0.1 m/s, compared to the determined velocities of roughly 0.2 m/s in the literature. This leads to the assumption that an optimized packing structure in a trickle flow reactor is capable to increase the surface that interacts with the gas flow and therefore can enhance the heat transfer capabilities substantially. Due to the analogy of heat- and mass-transfer, it is assumed that this finding can also be applied in chemical reactors.

Kurzfassung

Keramische Bauxitpartikel sind ein vielversprechendes, alternatives Wärmeträger- und Speichermedium in konzentrierenden Solarturmsystemen. Das sandähnliche Granulat wird in Solarturm-Receivern auf bis zu 1.000 °C erhitzt. Die gespeicherte Wärme kann in einem Riesel-Wärmeübertrager (*engl. trickle-flow heat exchanger*, TFHX) an ein Arbeitsgas wieder abgegeben werden. Im Vergleich zu state-of-the-art-Technologien wie Wirbelschicht- oder Zyklon-Wärmeübertragern, bietet der Riesel-Wärmeübertrager den Kompromiss einer relativ hohen Leistungsdichte bei vergleichsweise geringem Druckverlust, was ihn für den Einsatz in Solarturm-System interessant macht. In der Literatur sind bisher keine Auslegungsempfehlungen bekannt, welche für einen gegebenen Partikeltyp die geeignete Füllkörperkolonne identifizieren, mit dem Ziel einer hohen Gas-Partikel-Interaktion. Es wird erwartet dies durch eine hohe Gesamtpartikeloberfläche der rieselnden Partikel zu erreichen, welche gleichmäßig im Packungshohlraum verteilt sind. Deshalb wurde in der vorliegenden Arbeit ein Gas-Partikel-Direktkontakt-Rieselwärmetauscher für den angestrebten Einsatz in partikelbasierten Solarturmsystem entwickelt. Basierend auf Beobachtungen in der Literatur wurden verschiedene Packungsstrukturen designt und nummerisch untersucht. In den DEM-Simulationen wurde die dimensionslose Gesamtpartikeloberfläche bzw. der Partikel hold-up, sowie die räumliche Partikelverteilung für die Analyse der rieselnden Partikel in den unterschiedlichen Kolonnen gewählt. Es wurde festgestellt, dass für die verwendeten 1 mm Bauxitpartikel, Packungsstrukturen aus Stangenprofilen mit ebener Oberfläche einen hohen Partikel hold-up sowie eine gleichmäßige räumliche Verteilung des rieselnden Granulats bieten. In einem Testaufbau wurde die Packungsgeometrie unter Umgebungsbedingungen weiter verfeinert. Während der Kaltexperimente wurde festgestellt, dass eine Mindeststangenbreite es den Partikeln ermöglicht sich zu Granulatschichten ansammeln. Diese absorbieren die kinetische Fallenergie der rieselnden Partikel und verringern dadurch deren mittlere Sinkgeschwindigkeit, wodurch sich der hold-up erhöht. Die Packungsstruktur wurde in Heißtests weiter untersucht. Partikel bei Umgebungstemperatur wurden oben in die Kolonne eingeführt, während Luft bei atmosphärischem Druck von unten in den Wärmeübertrager einströmte. Die Lufteintrittstemperaturen wurden in vier Stufen auf bis zu 640 °C gesteigert. Es wurden für beide Medien fünf Massenströme festgelegt, um in etwa gleiche Wärmekapazitätsströme zu erreichten, für eine hohe Temperaturänderung in beiden Medienströmen. Es wurden Leistungsdichten von über 1.000 kW/m^3 ermittelt. Der volumetrische Wärmeübergangskoeffizient liegt bei ca. 15 kW/m^3, mit NTU-Zahlen für den Partikel- und Luftstrom von ca. 5 und 8. Die gemessenen Leistungsdichten, volumetrischen Wärmeübergangskoeffizienten und NTU-Werte konnten im Vergleich zur Literatur um etwa 100 % gesteigert werden. Dies lässt sich vermutlich durch die Erhöhung der verfügbaren Oberfläche der rieselnden Partikel innerhalb der Füllkörperkolonne erklären, beziehungsweise durch eine verringerte Sinkgeschwindigkeit des Granulats von ca. 0,2 m/s in der Literatur auf ca. 0,1 m/s. Dies legt die Vermutung nahe, dass eine optimierte Packungsstruktur in einem Rieselreaktor die Partikeloberfläche vergrößern und damit die Wärmeübertragereigenschaften steigern kann. Aufgrund der Analogie von Wärme- und Stoffübertragung wird angenommen, dass diese Erkenntnis auch auf chemische Reaktoren übertragbar ist.

Wissenschaftler fanden heraus…

… gingen kurz danach aber wieder rein.

Content

1 Introduction

1.1 Energy transition in the 21th century

Global warming, primarily driven by increasing carbon dioxide (CO_2) emissions, poses an existential threat to human life on our planet. The United Nations Framework Convention on Climate Change (UNFCCC) achieved a landmark agreement during its 21st Conference of the Parties (COP 21) by highlighting the pressing need to limit global warming to well below 2 °C, and preferably even below 1.5 °C, compared to pre-industrial levels. The Paris agreement, signed during the COP 21 in 2015, marked a historic turning point. For the first time, all 195[V] Parties to the UNFCCC committed to joint efforts to combat climate change and adapt to its effects. The primary objective is to mitigate global warming and its associated risks by collectively reducing greenhouse gas emissions. The aim is to limit the temperature increase below 2 °C and ideally within the range of 1.5 °C. [1]

Worldwide there is an increasing awareness and determination among nations, companies, and individuals to achieve transition towards a net-zero carbon future. The International Energy Agency (IEA) reported in 2022 global CO_2 emissions of 36.8 Gt CO_2 and categorized the emissions into four main sectors [2].

1. The power sector, which includes electricity and heat generation, is responsible for 43 % of global CO_2 emissions. Fossil fuel-fired power plants play a significant role in this sector.
2. The industry sector is responsible for 26 % of the CO_2 emissions, contributed by industries such as steel, cement, and chemicals.
3. The transport sector's emissions account for 22 % of global CO_2 emissions with 7.5 Gt. Despite the high percentage, the increasing sales of electric vehicles already reduce emissions by 13 Mt per year.
4. Additionally, the buildings sector contributes 9 % to global CO_2 emissions.

Within these sectors, the power sector for electricity and heat generation stands out due to its high dependence on fossil fuels. It provides immense potential for technical transformation and CO_2 savings to approach a net-zero carbon future. In addition to various technologies that can increase energy efficiency across all sectors, individual behavior regarding when and how energy is consumed can also have a positive impact on the overarching goal of reducing carbon dioxide emissions. Renewable energies will play a decisive role in meeting the world's energy needs in accordance with the climate agreement. These energy sources can be understood as energy sources that are inexhaustible in human time horizons. Quaschning [3] proposes to divide the energy sources into three groups. Solar energy, consisting of solar radiation originating from the sun of our solar system. This energy source drives numerous

---

[V] counting 194 countries and the European Union as one region regenerative, natural processes on our Earth, such as ocean waves, rainfall, wind and others, which can be harvested with the appropriate technical measures, see Fig. 1. Planetary energy is based on the gravitational attraction of celestial bodies. On our Earth, the Moon causes tides, which can be used energetically with corresponding technical methods. Furthermore, geothermal heat can also be used. Based on Quaschning [3], illustrates Fig. 1. the conversion of the mentioned energy into natural energy sources, which can be harvested by means of technical measures to obtain secondary energy, such as electricity, heat or fuel. Note, that the listed technical energy conversion systems are not considered as exhaustive, but rather mention some exemplarily technologies for the transition of renewable energy sources into secondary energy.

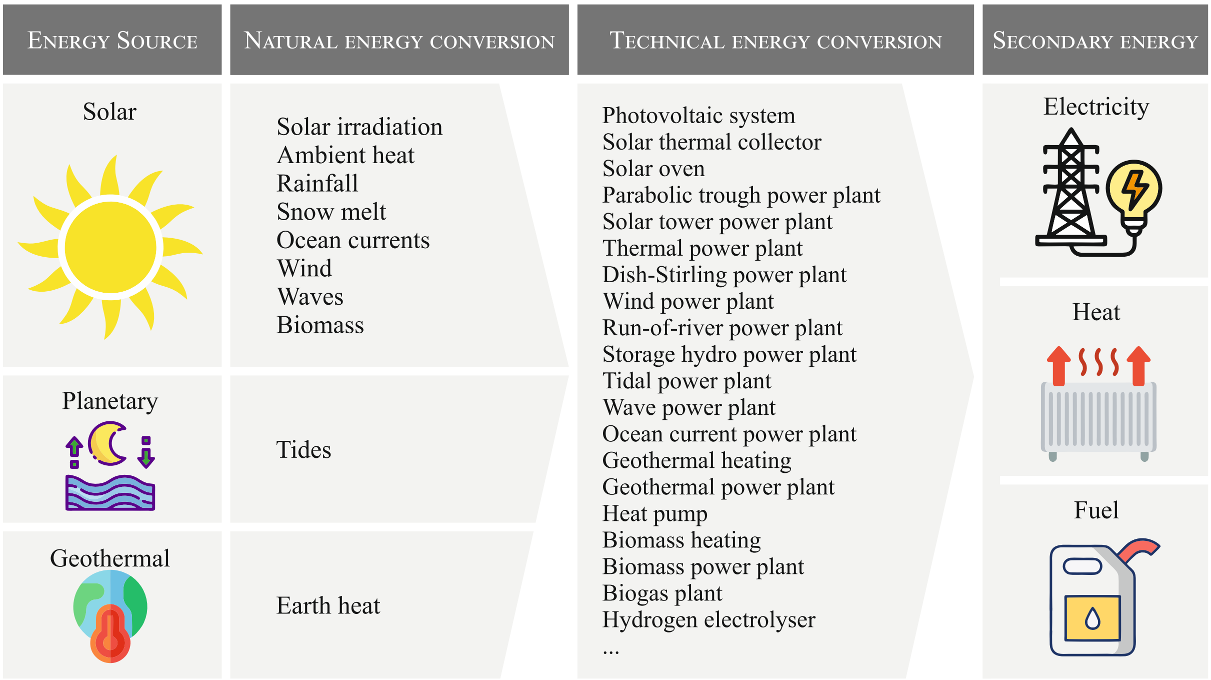

ENERGY SOURCE	NATURAL ENERGY CONVERSION	TECHNICAL ENERGY CONVERSION	SECONDARY ENERGY
Solar	Solar irradiation Ambient heat Rainfall Snow melt Ocean currents Wind Waves Biomass	Photovoltaic system Solar thermal collector Solar oven Parabolic trough power plant Solar tower power plant Thermal power plant Dish-Stirling power plant Wind power plant Run-of-river power plant Storage hydro power plant Tidal power plant Wave power plant Ocean current power plant Geothermal heating Geothermal power plant Heat pump Biomass heating Biomass power plant Biogas plant Hydrogen electrolyser ...	Electricity
Planetary	Tides		Heat
Geothermal	Earth heat		Fuel

Fig. 1 Sources and measures to use regenerative energy.

In an energy system based on fossil fuels, power plants typically operate and make adjustments to their output based on prevailing market demand, which in turn influences the amount of fuel consumed in the plants. The fossil fuels, which are typically stored on-site or in close proximity to the plant, serve as the energy storage of the plants, enabling them to respond to fluctuations in demand. A significant challenge in the transition from a fossil fuel-based energy system to a regenerative energy system is the development of new energy storage technologies that can align the fluctuations of natural energy resources with the demands of the energy market. Consequently, renewable technologies are frequently coupled with an energy storage system. A variety of energy storage technologies are currently available or under development, exhibiting varying degrees of maturity and market penetration. These include electro-mechanical energy storage (e.g. rotating flywheel or compressed air energy storage), electro-chemical energy storages (e.g. battery storage or hydrogen + fuel cell), thermal energy storage (TES); biomass storage systems and others. Generally, there is no one-size-fits-all solution of a renewable energy technology with suitable energy storage. Local conditions, such as climate, energy prices, the availability of personnel and infrastructure, and energy demand, assist experts in identifying sites that are individually suitable for the construction of regenerative energy systems. Nevertheless, the elevated specific storage costs associated with electrical storage systems present a challenge in the assessment of the financial viability of regenerative systems. In contrast, thermal energy storages offer the potential to store energy relatively inexpensively at high temperatures in large quantities for several days [4, 5]. Concentrating solar thermal power plants with integrated thermal storage represent a viable option to harvest the solar irradiation and store the heat in a thermal energy storage. The TES enables the utilization of stored energy for heat or power generation in accordance with prevailing market demand, independent of solar irradiation availability.

1.2 Objective of this work

The concentrating solar thermal (CST) technology's fundamental principle is its capability to focus and concentrate solar irradiation, such as in solar tower systems, up to 1,000 times, providing receiver temperatures at the top of the towers up to 1,000 °C. State-of-the-art (SotA) solar tower systems use air, thermal oil, or molten salt as heat transfer media [6]. While air shows a lack in direct storage capability, due to its poor ratio of specific heat capacity to density, oil and salt are limited in its process temperatures to approximately 400 ° and 600 °C respectively, which limits the storage power density potential that a concentration in a solar tower system could provide [7]. Research efforts are being undertaken to identify a heat transfer medium (HTF) capable of exploiting the high temperatures that solar tower systems can provide. Sand-like particles is investigated as alternative HTF and storage medium that could provide high process temperatures at the receiver. Particles made from materials such as bauxite or ceria are relatively inexpensive, widely available, do not freeze at ambient temperatures, and can be handled using SotA technology that has been used for centuries in the mining and cement industries. Although particle receivers have been successfully developed for technical-scale applications, demonstrating their capability to provide high particle temperatures at the receiver outlet, their most efficient use in matching the needs of a solar tower system power plant to provide process heat has yet to be investigated [8]. To utilize the stored thermal energy in the hot particles, various SotA heat exchanger technologies may be used to transfer the thermal energy from the particles to a working medium, such as air.

In contrast to photovoltaic systems, which convert sunlight directly into electricity using the photoelectric effect, solar thermal systems utilize solar irradiation and absorb thermal energy. The main advantage of solar thermal systems over PV systems is the ability to store excess energy in thermal energy storages, which are relatively easy and cost-effective compared to the battery technology. The field of battery technology is highly active, but storing large amounts of energy quickly and cost-effectively remains a technical and financial challenge. During times of regenerative overproduction, such as with PV or wind turbines, excess electricity can be stored in mechanical storage units, like flywheels, pumped-hydro stations, or compressed-air storage systems. However, these approaches have the disadvantage of converting the already existing electrical power, back and forth through the storage and discharge processes, thereby reducing the overall system efficiency. [6, 9]

This thesis focuses on developing a particle-air direct contact heat exchanger using the principles of a trickle flow reactor. The trickle flow heat exchanger (TFHX) is a promising technology that meets the specific requirements of a particle-based solar tower system. The TFHX's general design is developed through a preliminary numerical evaluation, followed by experimental studies to refine the packing design and investigate its heat transfer capabilities. The concept of the TFHX is evaluated and assessed for its heat transfer capabilities based on the experiments. The work discusses the first conceptual approaches to scale up the developed system and integrate it into a particle-based CST system, along with estimated cost figures.

2 State-of-the-art

2.1 Solar thermal systems

A solar thermal system is a technical system that receives solar radiation in a solar receiver and absorbs the energy in a heat transfer fluid, increasing its temperature and providing the potential to use the harvested energy. Solar thermal systems can be classified as either low temperature or high temperature systems. Low temperature systems typically consist of non-concentrating systems that provide process temperatures up to 100 °C, limited by HTFs mainly composed of water. However, there is no strict definition and it varies depending on individual cases. Flat-plate solar collectors are commonly used to harness solar radiation into the HTF and are an exemplary and widely used representative of a low-temperature solar thermal system. Solar thermal technology has matured to provide reliable heat for houses, neighborhoods, and industrial processes. Non-concentrating solar thermal technologies, such as solar updraft power plants and solar ponds, are also available, although they are less common. High-temperature solar thermal systems provide concentrated solar radiation to achieve process temperatures at higher levels. Depending on the field of application the receiver and HTF temperatures range from 300 °C for providing process heat in the food industry up to 1,000 °C for preheating processes in the mining and metal industry, or for powering thermodynamic cyclic processes. [9] Since this work focuses on the development of a TFHX for application in a solar tower system, further explanation of non-concentrating low temperature systems is omitted and referred to in the literature [9-14].

The type of solar thermal system used depends on the specific application and local conditions. Regardless of the temperature level and the type of system, solar thermal systems generally allow for harmonization of fluctuating solar radiation and time-shifted demand, since many HTFs allow for direct storage in relatively inexpensive, insulated TES that can be directly integrated into solar thermal systems. During periods of high power demand, the HTF can be retrieved from storage and used to provide thermal power, e.g. to drive a heating or drying process, or to provide heat for a cycle process for power generation. In addition, a current area of active research is the production of "solar fuel", which uses solar energy to produce hydrogen through chemical reactions. [6, 9]

2.1.1 Concentrating solar technology

Concentrating solar systems, focus the direct solar irradiation by means of optical systems. Thereby the energy density and the attainable temperatures at the focus point is increased compared to non-concentrating systems. The high concentration of irradiation is directed from the sun's rays onto a heat exchanger assembly placed into the focus point, the solar receiver (SR), which is capable of absorbing temperatures up to 1,000 °C in the HTF. Optical solar concentrators are characterized by their ability to concentrate the sunlight, which can be described by the geometric concentration factor, k, that is defined as the ratio of concentrator, like the solar field, and the absorber area [9].

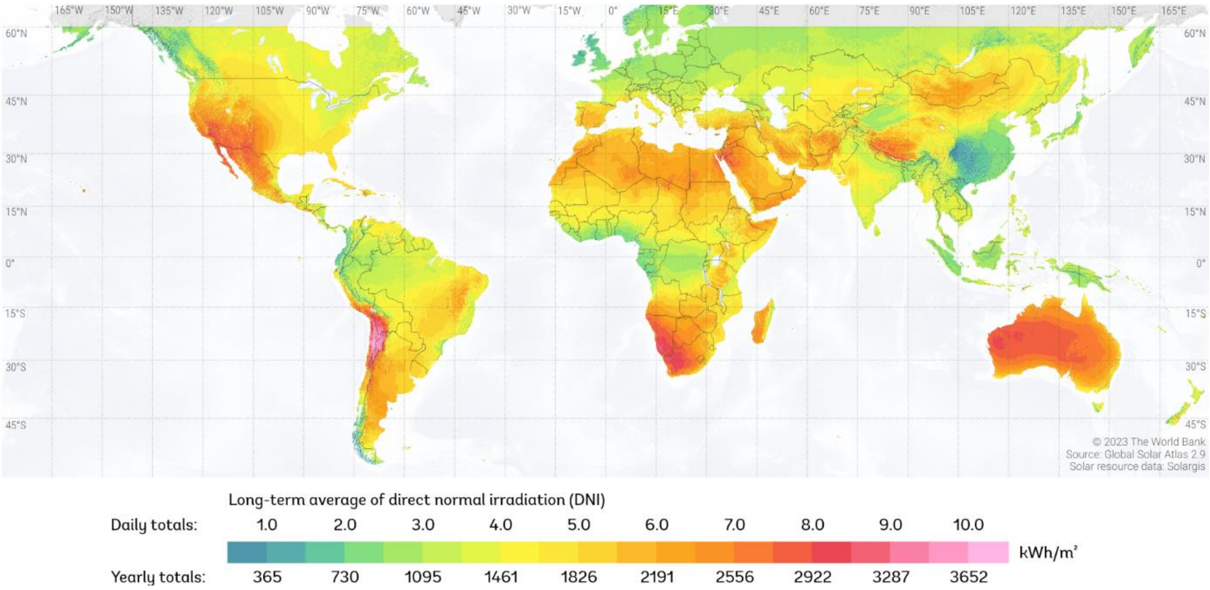

© 2023 The World Bank
Source: Global Solar Atlas 2.9
Solar resource data: Solargis

Fig. 2 Solar Resource Map - Direct Normal Irradiation, [15].

$$k = \frac{A_{\text{concentrator}}}{A_{\text{absorber}}} \tag{1}$$

Concentrating solar power (CSP) plants and concentrating solar thermal systems rely on a solar field (SF) consisting of mirrors that concentrate solar radiation up to a thousand times. CSP plants generate electricity, while CST systems provide process heat. The solar field in a CST or CSP plant utilizes only direct solar radiation reflected by focusing mirrors. The higher the solar irradiation, the higher are the attainable energy densities and process temperature at the solar receiver. This is why a solar thermal system should be installed in areas with high local direct normal irradiance (DNI), see Fig. 2. A techno-economic assessment must be performed for each site individually, since not only the local DNI needs to be considered, but also boundary conditions like CO_2 price, energy costs, and labor costs. Solar thermal plants are typically built in regions with a high direct normal irradiance like 2,600 $\text{kW}/(\text{m}^2\ \text{a})$, but plants also are installed in regions with a lower DNI of 1,900 $\text{kW}/(\text{m}^2\ \text{a})$ [6].

In practice, glass mirrors have gained broad acceptance as concentrating collectors due to their high reflectivity capabilities, affordability, and durability in outdoor conditions. To achieve the high degree of solar concentration in the SR aperture, sun-tracking of the mirrors is necessary throughout the day, requiring a certain level of maintenance. Concentrating solar systems can be differentiated based on the shape and assembly of the concentrating mirrors. Linear Fresnel and parabolic troughs are line-focusing systems that can concentrate solar irradiation on the receiver up to 100 times and require one-axis sun tracking. Parabolic dish concentrators and solar tower systems both utilize a point focusing principle to concentrate solar energy onto the receiver aperture, achieving concentration factors of several thousand. However, this high concentration requires a two-axis tracking system. [6] The different systems are described in the following sections.

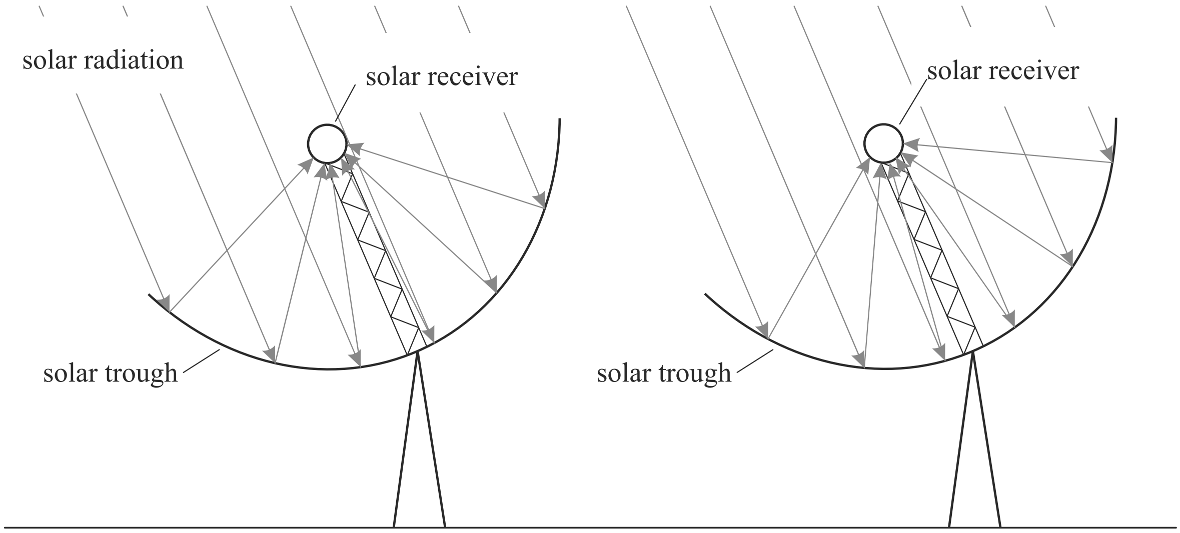

Fig. 3 Schematic setup of a solar trough collector with receiver tube.

2.1.1.1 Parabolic trough systems

Parabolic trough power plants are a mature technology that has been successfully implemented for several decades in various locations worldwide, including the USA, Spain, China, and South Africa. This system focuses solar radiation onto a focal line using mirrors with a parabolic profile that track the sun uniaxially. The solar receiver is installed in a fixed position along the focal line of the parabolic collector, and it is designed to rotate in conjunction with the collector assembly. The receiver tube consists of a metallic absorber tube, which is typically encased in an additional translucent glass tube. Vacuum separates the metal and glass tubes to minimize heat loss to the environment. [9, 12]

The solar-heated HTF can transfer thermal energy to a working medium, such as steam, which is generated in a boiler to provide process heat or to drive a cyclic process for power generation. During times of overproduction in the solar field, excess thermal energy can be temporarily stored in tanks. If oil is used as a heat transfer fluid in the parabolic trough system, the heat output is transferred to cheaper salt. The nitrate salt is pumped from the low-temperature storage, which has a temperature of approximately 290 °C, to the high temperature storage. In the oil-salt-heat exchanger, the salt is heated by the HTF. [9, 12] In addition to using thermal oil as HTF in the solar field, the direct use of pressurized water/steam is a viable option. In this case, the SF would replace the function of the boiler and generate pressurized steam directly in the SF [16-19]. A direct use of molten salt in the solar receiver and SF is possible, which omits the oil-salt HX and allows for the direct storage of thermal energy in the TES [20-22].

2.1.1.2 Fresnel systems

Similarly, to the parabolic trough, the Fresnel system also bundles solar radiation onto a focal line. However, in contrast to the parabolic trough, multiple narrow, parallel mirror strips are used to reflect the solar radiation onto a fixed receiver tube, which is located several meters above the solar field. For cost efficiency, these reflectors can be grouped into small clusters with one shared drive unit for one-axis solar tracking. Ideally, the reflectors should not be flat but have a slight curvature along the trailing axis to enhance the focal capabilities on the receiver. A secondary reflector is located above the receiver tube, reflecting scattered or misfocused radiation back to the SR, see Fig. 4. Manufacturing inaccuracies and wind load can cause mirror deformation, which is why a secondary reflector unit is often used to improve system efficiency. To further enhance system efficiency, a second glass tube can be added to the circumference of the metal absorber tube, reducing thermal losses to the environment. The absorber tube is a non-moving part in a Fresnel system, facilitating the use of water as a heat transfer fluid for direct evaporation at process parameters of 500 °C and 100 bars. An additional heat exchanger would be necessary for these systems to store the thermal energy from the SF into a TES that uses a storage medium such as molten salt. [12] Fig. 4 illustrates the structure of the Fresnel solar field and receiver.

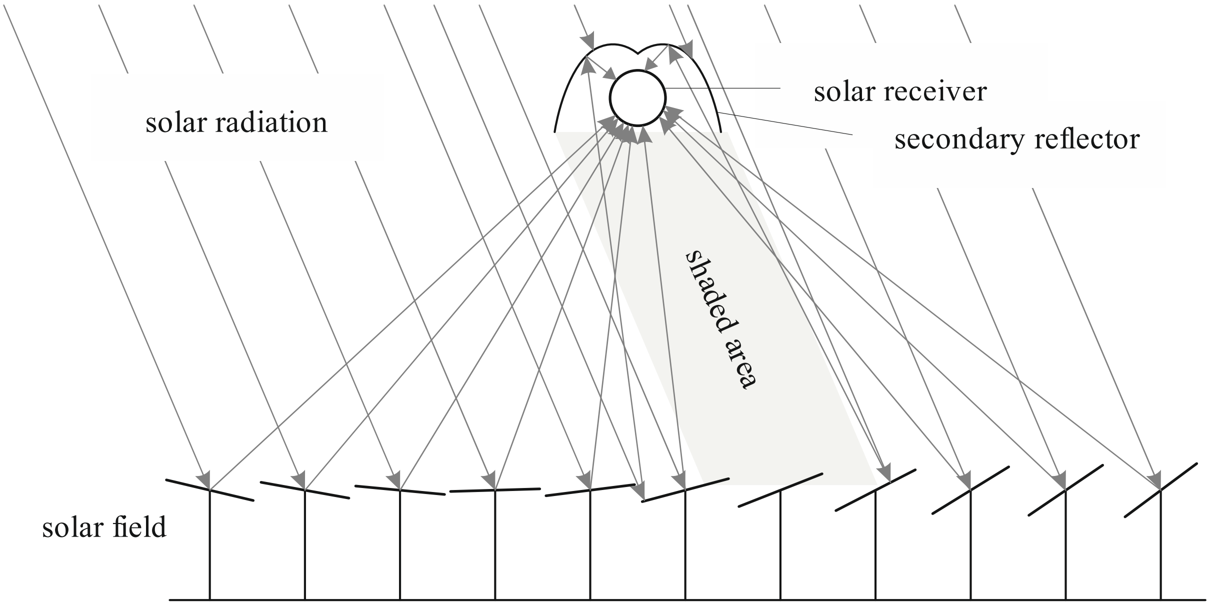

Fig. 4 Schematic setup of a Fresnel SF and SR assembly.

2.1.1.3 Dish-Stirling systems

Dish-Stirling systems are a type of point-focusing system that concentrate solar radiation onto a single spot using a rotationally symmetrical, parabolically curved concave mirror. This achieves concentration factors of up to 3000. Biaxial sun tracking of the reflector unit is necessary for spot-focusing solar thermal systems. The solar receiver, which contains the hot cylinder section of a Stirling machine, is located at the focal point. The Stirling cycle engine is well-suited for the Dish concept due to its ability to operate as a completely closed circuit with an external heat supply. This closed design enables the use of working gases with a high entropy exponent, such as helium or hydrogen, which increases the efficiency of the process compared to air. When the system is aligned with the sun, the irradiation drives the Stirling cycle process, providing mechanical power that can be used to operate a generator. The Stirling engine and generator combination form a compact unit, which is carried along with the paraboloid, see Fig. 5. A parabolic or Dish-Stirling system operates most efficiently as a single unit within the range of 1 to 50 kW_{el}, making it a viable option for decentralized power generation and a potential replacement for diesel generators to reduce dependency on fuel supply. [12]

Fig. 5 Example of a Dish-Stirling system, [23].

2.1.1.4 Solar Tower Systems

Similar to solar dish systems, concentrate solar towers systems the incident solar radiation to a focal point, achieving concentrating factors up to 1,000 and providing process temperatures over 1,000 °C. The solar field of a solar tower system is comprised of a multitude of individual mirrors, the heliostats, which are individually tracked in two axes. Collectively, they function as a circular Fresnel reflector, concentrating the solar irradiation at the central receiver situated at the top of the solar tower. The mirror surface of heliostats can extend up to 200 m^2, depending on individual design principles. These mirrors can be located in large solar fields, sometimes over one kilometer away from the solar tower, and can generate electrical capacities of around 10 MW. [6, 9, 12] The heliostats in the solar field can be arranged in a circular or one-sided array around the solar tower. The design of the solar field for a central receiver system depends on the desired power level, geographical location, and other design parameters and is described in according literature [24, 25]. Special SF design programs have been developed for the design processlike MIRVAL [26], SolTrace [27], DELSOL3 [28] from Sandia Labs and HFLCAL [29, 30] from the German Aerospace Center - Institute of Solar Research. As in parabolic trough systems, the HTF can be stored in high- and low-temperature storages to align the solar production with the power demand. The intended application fields dictate the requisite process temperatures. A range of heat transfer fluids, exhibiting varying degrees of maturity, are currently under investigation for use in different temperature ranges. These include liquid HTF such as molten salt, liquid metals, or water and steam; gaseous HTF such as air; and solid HTF such as ceramic particles.

2.1.2 Particles as HTF in central receiver systems

Central receiver systems can achieve radiation densities of up to 3,000 kW/m^2, resulting in receiver temperatures exceeding 1,000 °C [7]. In contrast, the use of thermal oil is common in parabolic trough systems, but its maximum temperature limit of approximately 400 °C [31] or, more recently, 450 °C [32] would not fully utilize the capabilities of a point focusing system.

Thermal oils are typically composed of a mixture of higher alkane compounds or artificially produced synthetic oils from chemically modified petroleum components. Both options are hazardous and easily flammable, and must be handled with care accordingly [9, 33]. Currently, liquid salt and air are the state-of-the-art heat transfer fluids for solar towers, both of which have a high level of maturity. Although air is free and can absorb high temperatures at the receiver, it lacks direct storage capabilities. On the other hand, solar salt can be stored relatively easily but is limited to around 550 °C [22]. As in the thermal oils sector, the liquid salt technique is also being investigated to further increase process temperatures [34-36]. Direct steam generation in central receiver systems is also being studied, which would require the installation of an additional heat exchanger if the thermal energy is to be stored, for example, in a steam-molten-salt-HX [37]. A recent advancement in the field of high-temperature HTF for central receiver systems is the utilization of liquid metals. This allows for high heat transfer coefficients and enables process temperatures to exceed 1,000 °C, depending on the specific mixture used [7, 33, 38]. Depending on the intended end use of the concentrating solar thermal plant, DNI, and other boundary conditions on site, the used HTF and the corresponding solar thermal plant design can differ, defining the individual plant components such as: receiver type and design, thermal energy storage system and design, HTF conveying system, and others. The various HTFs mentioned are not intended to be all-inclusive, but rather to provide a general overview. Each HTF can be further differentiated by its material composition, individual minimum and maximum operating temperatures, and operating pressure. The liquid HTFs - oil, salt, and metal - have good heat transfer and storage capacities. However, they come with a major pitfall: each material has a characteristic freezing temperature at which it solidifies. For state-of-the-art liquid HTFs those temperatures are above ambient temperature, what possess a constant threat to all HTF guiding and containing components in solar thermal systems. Therefore, technical efforts such as electrical heat tracing systems and thorough insulation are mandatory to prevent the HTF from freezing. [9, 12]

The limiting temperatures, freezing issues, and environmental and safety concerns associated with the aforementioned HTFs have motivated the search for alternative options. An alternative should be capable of handling higher process temperatures, leading to increased overall system efficiencies, and be easily integrated into a TES concept without any hazardous or polluting impact. HTFs based on ceramic particles allow process temperatures up to 1,000 °C, as the materials show a slight tendency to start a sinter process at 1,100 °C [39-41]. In contrast to SotA solar thermal systems, which typically pump fluids through tubular receivers, particles can be directly or indirectly heated by concentrated solar radiation [42]. Direct absorber receiver concepts are an attractive technology option, particularly because they eliminate the material limitation of a metallic receiver tube, which limits solar flux and maximum temperature at the absorber, by exposing the HTF directly to the concentrated radiation. The particles heated by solar energy can be stored in insulated silos or tanks and withdrawn for thermal power supply as needed. Therefore, in a corresponding particle heat exchanger, thermal energy must be transferred to a working fluid such as air, steam, or supercritical carbon dioxide (sCO_2). Compared to SotA storage systems using water, thermal oil or molten salt, the storage densities of a TES can be increased by using ceramic particles due to its high process temperatures. Furthermore, the use of affordable, sand-like particles as HTF and storage media could leverage mature technologies from the mining and process engineering industries. These technologies would need to be adapted to handle the high-temperature grain materials.

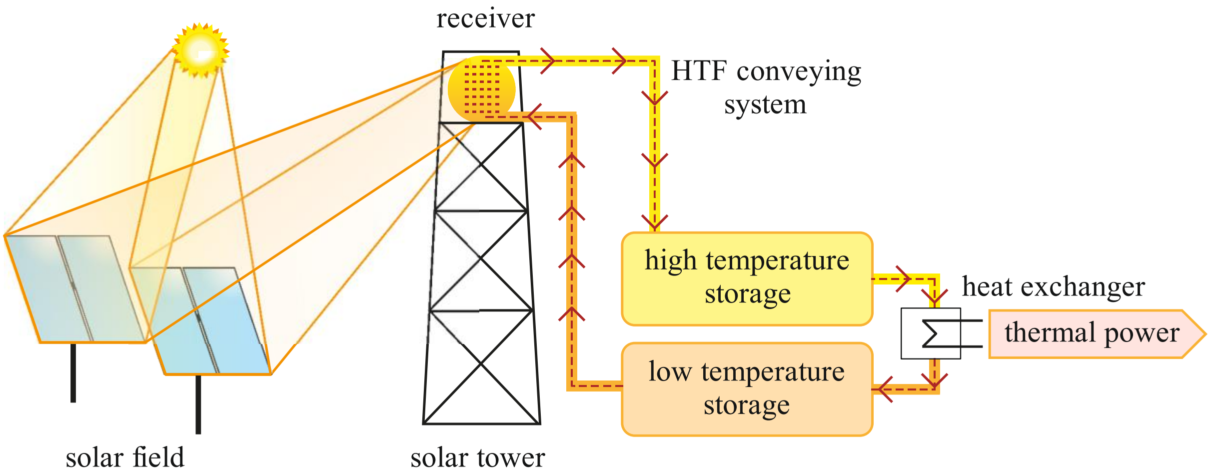

Fig. 6 Schematic design of a solar tower system, with thermal storage for the HTF.

Accordingly, a particle-based central receiver system would include the following components, see Fig. 6:

- Feed hopper: providing particles to the particle receiver
- Particle receiver: exposing the particles – directly or indirectly – the solar flux, heating the particles
- Hot storage: located below the particle receiver to store the harvested hot energy for later thermal power demand
- Particle heat exchanger: to provide thermal energy demand to a working fluid, like steam, air, sCO_2 or others
- Cold storage: collecting the cooled particles, leaving the particle heat exchanger, and storing the grains to be recirculated to the top of the solar tower
- Circulating system or particle lift, conveying the particles from the cold storage to the feeding hopper at the top of the solar tower

A variety of grains were investigated to be used in a particle based solar tower system. Commercially available proppants, used for hydraulic fracking, are ceramic particles with high abrasion resistance and good solar absorbance [42]. Natural sand, which is widely available at a low cost worldwide, is also being considered. However, it has inferior solar absorptance and is more likely to sinter at high temperatures [43]. Correspondingly, natural sand could be a viable option for indirect particle receivers where solar absorptance is not important. On the other hand, spherical particles composed of sintered bauxite have been found to be suitable for direct absorbing receivers due to their resistance to abrasion and sintering at high temperatures [44, 45] and high solar absorptance, remining durable and constant at high temperatures up to 700 °C [44]. Exposing a particle HTF directly to solar irradiation has advantages in open receiver concepts, but potential particle loss at the receiver must be considered individually based on the receiver type, particle size, local weather conditions, and other factors [46]. In Tab. 1 some exemplarily particle materials are listed.

Tab. 1 Some exemplarily materials of solid particles, [46].

Material	Composition	ρ in kg/m^3	c_p in J/(kg · K)	Pro	Con
Silica sand	SiO_2	2,610	1,000	materially stable, abundant, low cost	low solar absorptivity and conductivity
Alumina oxide	Al_2O_3	3,960	1,200	materially stable	high cost
Coal ash	$SiO_2 + Al_2O_3 +$ minerals	2,100	720 (at ambient temperature)	materially stable, abundant, no/low cost	identification of suitable ash
Calcined Flint Clay	SiO_2, Al_2O_3, TiO_2, Fe_2O_3	2,600	1,050	mined, abundant, used as filler in FB boiler	low absorptivity
Ceramic proppants	75 % Al_2O_3 11 % SiO_2 9 % Fe_2O_3 3 % TiO_2 2 % others	3,300	1,200 (at 700 °C)	high solar absorptivity, stable	synthesized, higher cost

Mehos, Turchi [46] suggest that in the development of particles for use in central receiver systems, it is important to improve particle durability and identify grains with low abrasion to the materials. Additionally, they recommend identifying low-cost particles significantly below 1 $/kg and enhancing solar absorptance while reducing thermal emittance.

Various designs of particle receivers have been developed and investigated, including the free-falling receiver [47, 48] with recirculation [49, 50], centrifugal receiver [8, 51-57], obstructed flow receiver [58-62], fluidized- and flowing-bed tubular receivers [63-67], and others [68, 69]. Fig. 7 provides an overview of high-temperature particle receivers for concentrating receiver systems, which are described in more detail in Tab. 2.

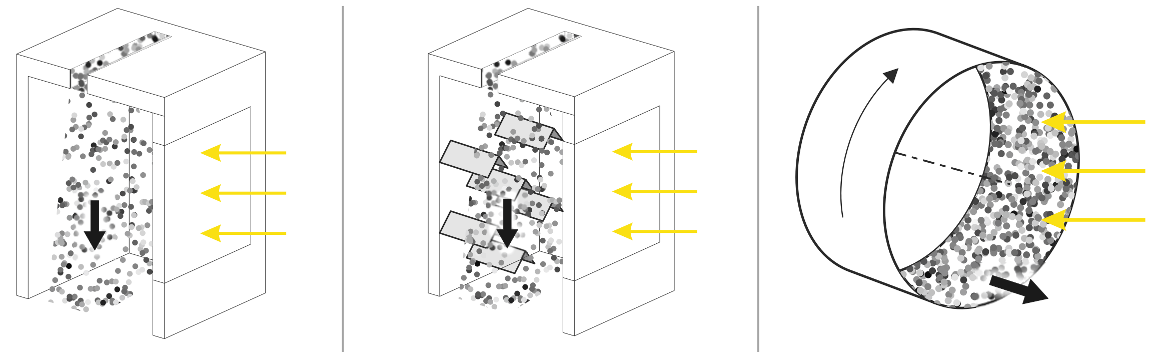

a) free-fall

b) obstructed flow

c) centrifugal

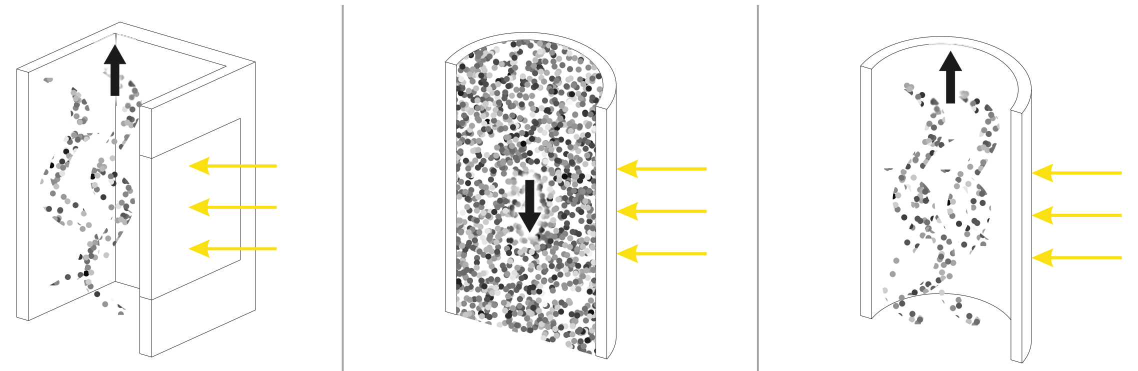

d) fluidized bed

e) gravity-driven in enclosure

f) fluidized flow tube

Fig. 7 Types of particle receivers.

Depending on the desired temperature increase and plant design, different receiver types face varying design tasks that must be considered. To achieve a specific outlet temperature in a free-falling receiver, recirculating the particles might be necessary [50]. On the other hand, a centrifugal receiver can modulate the residence time of the particles by adjusting the rotary speed, enabling a constant particle outlet temperature even under varying solar flux conditions [55].

Simulations estimate that thermal receiver efficiency can reach up to 90 % for large-scale systems in the 100 MW_{el} range. Technical scale prototypes of centrifugal and falling-particle receivers have already achieved up to 80 % efficiency. To further increase thermal efficiency, it is necessary to mitigate thermal radiative, convective, and solar reflective losses. [46]

All particle receivers share a common need for a feed hopper located in the solar tower above the receiver. This hopper provides the capability to adjust the particle mass flow to react to short-term system fluctuations. The feed hopper serves the purpose of distributing grains at the entrance of the receiver and providing sufficient storage volume in case of malfunctioning of the particle lift system. This guarantees the particle mass flow required to maintain the solar receiver in operation and prevents overheating of the absorber until the defocus of the heliostats from the receiver aperture is completed. [46]

Tab. 2 Overview of various particle receiver types, [42].

Receiver type		Temperature and efficiency	Advantages	Research challenge	References
Direct particle receivers	Free-falling	> 700 °C ~ 50 – 70 %	Capable of achieving high temperatures, direct irradiance of particles reduces flux limitations (on tubular receivers), particles can be stored at high temperatures, particles can be cheaper than molten salt	Radiative and convective heat losses, concentration ratios, particle attrition, solar absorptance, thermal emittance, particle residence time, particle/fluid heat exchangers	[41, 48, 50, 61, 70-77]
	Obstructed flow	> 700 °C ~ 60 – 80 %	Capable of achieving high temperatures, obstructions slow particle flow and increase residence time, flow is more stable than free-fall, less particle loss	Hot spots and continuous flow over obstructions may cause deterioration or failure if mass flow and cooling is not maintained; additional cost of fabricating obstructions	[60-62, 78, 79]
	Centrifugal	> 900 °C ~ 75 %	High particle temperatures, control of residence time to manipulate particle outlet temperature via receiver rotational speed	Maintaining a constant and sufficient mass flow rate of particles at larger scales, parasitic energy requirements, and reliability associated with a large rotating receiver system	[53, 54, 56, 57]
	Fluidized bed	> 1,000 °C ~ 20 – 40 %	Excellent heat transfer to fluidized particles with increased residence time	Parasitic energy requirements to fluidize particles, maintaining sufficient mass flow for desired power requirements	[80-85]
Indirect particle receivers	Gravity-driven flow in enclosures	no data	High particle temperatures theoretically achievable; no particle loss due to containment	Additional heat transfer resistance from irradiated walls to particles; hot spots on enclosures may cause deterioration or failure if mass flow and cooling is not maintained; maintaining sufficient mass flow at large scales	[64, 68, 85]
	Fluidized flow in tubes	750 °C no efficiency reported	Enhanced heat transfer from walls to particles due to fluidization; no particle loss due to containment	Parasitic energy requirements to fluidize particles; maintaining sufficient mass flow at large scales; hot spots on enclosures may cause deterioration or failure if mass flow and cooling is not maintained	[66, 67, 86]

In order to continuously generate hot particles in a central receiver system, the feed hopper must be constantly refilled with particles from the cold storage silo. Therefore, a particle conveyance system is required that is capable of lifting the particles to the top of the solar tower and into the feeding bin. Different particle lifts may be feasible depending on the specific task, such as bucket elevators, vertical screw-feeders like the Olds elevator used in the Sandia on-sun prototype system [87], and mine or skid hoist systems [46]. The feasibility of each option depends on factors such as the temperature of the transported particles, receiver design, particle mass flow, and lifting height. The Olds elevator, which is used in the Sandia system, has low lifting efficiencies in the range of 5 % due to interstitial grain friction and the conveying system components [46]. It is expected that skid-hoist systems, which are more suitable for large-scale applications, can provide lift efficiencies of up to 80 % [88]. Typical applications of available large-scale transport systems operate in the range of approximately 300 °C to 550 °C. It is expected that these systems can be adapted for central receiver systems without major hurdles [46].

After leaving the receiver, the heated particles are guided to an insulated high-temperature storage. Ma, Davenport [89] provide a design analysis, applying standard guidance for particle temperatures up to 900 °C. However, the insulation methods and materials still need to be refined, and the thermal cycle durability of the available insulation materials and mechanical structure needs to be tested [46].

Many components required to run a particle-based central receiver system are readily available in the industry and have a high level of maturity. Bulk handling processes is applied in the mining, process, chemical, food, and cement industries for over a hundred years and have been continuously refined. In contrast, particle receivers had to be extensively developed from scratch in the last decade. For the application in a CST or CSP, existing technologies must be empowered to withstand new technical challenges, such as system temperatures exceeding 700 °C and the need for durability during thermal cycling. Additionally, new working fluids like sCO_2 [90, 91], impose additional material demands to withstand not only the temperature load but also the corresponding mechanical stress caused by high gas pressures. Additionally, when exploring new temperature ranges in particle handling technology, it is important to evaluate existing systems for attrition and erosion.

This section outlined the implementation of particles as HTF in a central receiver system and described the different system components and design options. One essential component was omitted, the particle heat exchanger, capable to transfer the thermal energy from the particles to a working medium like air. The present work aspires to develop a corresponding system, suitable to the specific needs of a solar tower system.

2.2 Particle-gas heat exchanger for particle based solar tower systems

2.2.1 Requirements

Depending on the specific use-case, the types of gas-particle heat-exchanger in a concentrated solar tower system may vary, therefore a reference application will be defined in reference to the successful on sun testing of the 2.5 MW_{th} centrifugal receiver at the Juelich Solar Tower in Germany [51]. In the experiments, 1 mm bauxite particles were used, which left the receiver with an average outlet temperature of 965 °C [51]. To provide continuous high-temperature process heat for industrial applications, such as preheating or drying processes in the metal or mining industry, air at ambient conditions is a viable heat transfer fluid due to its unlimited availability and low technical hurdles in handling. This makes it a suitable gas to transfer thermal energy to particles and to further deploy the solar heat for industrial processes (SHIP). Therefore, a gas-particle heat exchanger technology shall be identified and empowered for the use in central solar power systems capable to work with the particles and the temperature range of the reference application and the further technical criteria:

- High power density:
  In contrast to the illustration in Fig. 6, the hot and cold storage units in a particle-based solar tower system should ideally be integrated into the solar tower itself. This allows for dual usage of the tower structure as both a storage container and a means of reducing transport distances for the HTF, thereby reducing thermal losses. Ideally, the hot particle storage is located below the particle receiver in the solar tower, with the particle-air heat exchanger beneath the hot storage. This system enables the hot particles to be gravity-fed from the hot silo into the HX, where they transfer the thermal energy to air. The cooled particles exit the HX and fill the cold storage. Afterwards, a lift system recirculates the particles to the top of the receiver, into the feeding hopper, and back to the receiver. Regarding the defined use case, the objective is to cool particles with temperatures exceeding 900 °C using air, while minimizing thermal losses. To achieve this, it is necessary to keep the outer surface of the corresponding heat exchanger as small as possible, requiring a high power density of the unit.
- Close temperature approach:
  For effective heat transfer, both media flows should have a close temperature approach at the inlets and outlets of the HX device. Therefore, a countercurrent heat exchanger assembly is preferred over a parallel flow arrangement.
- Low pressure drop:
  To keep operational costs low, it is preferred to maintain a low pressure drop for the gas flow.

2.2.2 Evaluation of available gas-particle heat exchanger technologies

Heating or cooling grain material is a common task in industrial and agricultural processes, which has led to the development of corresponding systems for these fields. Indirect heat transfer can typically be achieved in a shell-and-tube heat exchanger by using a moving particle bed in the shell that surrounds the tubes of the heat exchanger. This method can be used with coolants such as water for steam generation [92, 93] or sCO_2 [87]. A widely applied method for cooling or heating particles is through a shell-and-plate heat exchanger. This method involves vertical layers of plates that form chambers containing flowing particles and a cooling fluid, such as water/steam or gas [90, 94]. Separation of both fluids is preferred in some applications to avoid mixing or contamination. Also, if pressurized gas is used as fluid, an indirect HX with tubes, containing the pressurized gas, can be realized more easily and with thinner wall thicknesses than if the whole HX or the shell would be pressurized. In both cases of indirect particle to fluid heat transfer, the overall heat transfer thermal resistance must be overcome. This resistance is composed of the fluid-wall heat transfer, the thermal wall conductivity of the plate or tube material, and the wall-particle heat transfer. Accordingly, heat transfer capabilities of an indirect gas-particle heat exchanger can be considered as inferior, compared to a direct-contact HX [46]. It is widely recognized that indirect heat exchangers have significantly lower heat transfer capabilities compared to fluidized bed heat exchangers, where both media are in direct contact and the vast surface area of all particles can directly participate in heat transfer without a limiting intermediate material. Additionally, the limit temperature of such an indirect HT system can be dominated by the material properties of the separating material used in the HX. Hence, the current work aspires to identify and develop a gas-particle direct contact heat exchanger, capable to exploit the particle surface of all particles in the HX for the gas-particle heat transfer, and to overcome the limiting nature of a separating material regarding heat transfer and limiting working temperature.

Fig. 8 illustrates the most common basic types of gas-particle direct contact heat exchangers. The specific application and design criteria determine the types, which are further outlined in corresponding literature for process engineering or heat transfer [95-100]. The different types of heat exchangers, shown in Fig. 8, facilitate interaction between the gas and particle phases. These technologies are not only used in heat transfer problems but are also widely employed in reactor and combustion technologies. A relatively straightforward concept of gas-particle interaction can be achieved through a moving particle bed with countercurrent or cross-flowing gas flow, see Fig. 8 a) and Fig. 8 b). Both options provide the highest particle surface per volume of the device, resulting in a relatively low porosity of $\epsilon \sim 0.4$ [101].

$$\epsilon = \frac{\overbrace{V_{\mathrm{bulk}} - \sum V_{\mathrm{p}}}^{V_{\mathrm{void}}}}{V_{\mathrm{bulk}}} = 1 - \frac{\rho_{\mathrm{bulk}}}{\rho_{\mathrm{p}}} \quad (2)$$

This leads to a relatively high pressure drop that must be overcome if an amplified gas flow is desired. The countercurrent layout must also overcome the challenge of uneven gas flow distribution caused by a decrease in porosity $\epsilon \to 0$ [101] near the boundary of a particles containing shell. This leads to a mal distribution of the gas flow and significantly affects the heat transfer of the device [102]. This effect can for instance be overcome in changing the vertical gas flow to a horizontal gas flow by replacing the front and back walls of the moving particle bed containing vessel with porous elements, see Fig. 8 b). The HX design causes a relatively high pressure drop and a diagonal temperature and gas distribution due to its cross-flow design. At higher gas flow rates, the moving particle bed is pushed against the porous wall on the exiting air side, causing it to stop [103-105]. A gas cross-flow variation can be designed for a moving particle bed, whether it is vertical, inclined, or even horizontal [100].

If the gas velocity exceeds the particle terminal velocity the drag forces of the gas increase to the point where the particles are conveyed with the high gas velocity, see Fig. 8 c). This state of pneumatic particle conveying is also known as fast fluidization and typically occurs for small particles at high air superficial velocities typically larger than 20 times the particle terminal velocity $\left(u_{\mathrm{a},0} > 20\, u_{\mathrm{t}}\right)$ [100]. Although the effects of pneumatic particle conveying have been widely published, there have been relatively few studies on gas-particle heat transfer in pneumatic conveying systems [106]. However, depending on parameters such as air velocity, particle loading, particle material, and particles size, it can be assumed that the conveyed grains and the air may equalize within seconds to the same temperature, based on the high reaction kinetics due to the prevailing turbulence in the pneumatic conveying system [100, 107]. To apply these phenomena to gas-particle heat transfer, the conveyed particles must be separated in a separation cyclone. In the cement industry, multi-staged cyclones are used to preheat the raw material before it enters the rotating kiln [108]. This allows for a countercurrent like heat exchanger behavior and results in higher temperature changes in the media flow rates, see Fig. 8 d). The falling particle cloud provides a simple design setup for a gas-particle direct-contact application, see Fig. 8 e). The concept is based on a vertical channel where particles fall freely, while a countercurrent gas flow reacts with the grains. To prevent particle entrainment, the gas velocity must be kept below the terminal velocity. It is assumed, that this method should only be applicable to small particles that cannot reach high terminal velocities, in order to avoid high levels of particle attrition and abrasion of the HX containment. As the particles fall in a free vertical duct, there is a risk of uneven particle distribution or particle segregation, which can result in poor utilization of the available HX volume for heat transfer.

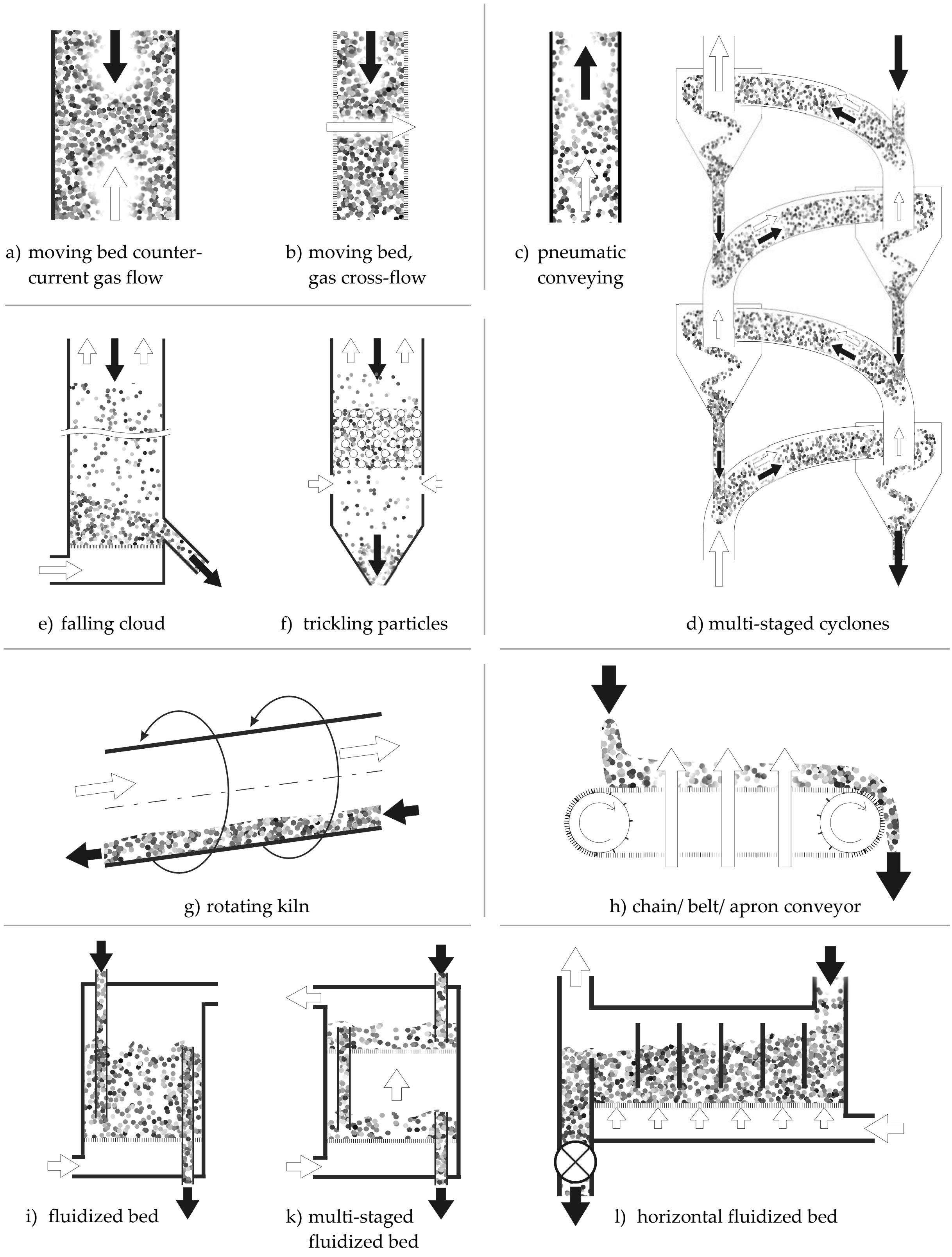

a) moving bed counter-current gas flow

b) moving bed, gas cross-flow

c) pneumatic conveying

d) multi-staged cyclones

e) falling cloud

f) trickling particles

g) rotating kiln

h) chain/ belt/ apron conveyor

i) fluidized bed

k) multi-staged fluidized bed

l) horizontal fluidized bed

Fig. 8 Types of gas-particle direct-contact heat exchanger.

Additionally, the concept is expected to be sensitive to heat losses to the surroundings due to the relatively high falling height required to overcome the aforementioned disadvantages and achieve a high temperature change in the heat exchanger media. To improve radial mixing of the falling particles, fixed obstacles or a packing structure can be placed in the vertical duct, see Fig. 8 f). This packing structure reduces the average falling velocity of particles, u_{p}, which in turn reduces the required falling height for a desired temperature change and thereby reduces thermal losses to the environment. The rotary kiln, see Fig. 8 g), is widely used in the process industry, like the cement production. The rotating kiln is a suitable method for gas-solid heat transfer and is commonly used for grain materials that tend to sinter or agglomerate [100]. In the process industry, to provide heat treatment or dry grain, materials are transported horizontally by means of a chain, belt or apron conveyor in combination with a vertical air flow passing through the vertical conveyor assembly, see Fig. 8 h). Also, various designs of fluidized bed (FB) reactors or heat exchangers are available. The most basic form of a fluidized bed consists of a perforated horizontal plate through which only gas can flow; particles cannot penetrate. When air velocities are below the pneumatic conveying of particles and above the gas flow rates used in moving particle beds, the grains can achieve a state of fluidization. The gas velocity is high enough to fluidize the bed, but not enough to entrain the particles. Geldart and Abrahamsen [109], proposed a method to classify the behavior of grains with vertical air flow into four distinct groups based on observations of various particle types during fluidization at varying air velocities and is widely accepted and applied [100].

- Group C: Cohesive, or very fine powders like flour, face powder or starch. The interparticle forces are dominate over the gas drag forces, making normal fluidization rather difficult.
- Group A: Aeratable, or materials with a small particle size and/or a relative low particle density of $\lesssim 1.4\ \mathrm{g/cm^3}$ like fluid cracking catalyst (FCC) is typical for this grain type. The particles can be easily fluidized at relatively low gas velocities, forming small bubbles at higher velocities.
- Group B: Sand-like particles with $40\ \mu\mathrm{m} < d_{\mathrm{p}} < 500\ \mu\mathrm{m}$ of size and densities in the range of $1.4\ \mathrm{g/cm^3} < \rho_{\mathrm{p}} < 4\ \mathrm{g/cm^3}$, fluidize well pronounced bubbling action that grow large.
- Group D: Spoutable, large and/or dense particles like drying peas or grains, gasified coals, roasting coffee beans or some roasting metals can be categorized in this group. Fluidizing high beds of these particles can be challenging due to their tendency to fluidize sporadically in the form of large exploding bubbles or pronounced channeling. Uneven gas distribution can also cause spouting. As a result, it is recommended to process these particles in shallow beds or in spouting mode.

One option to gradually drain the particles from the FB is a downcomer pipe, while constantly feeding new particles into the unit, see Fig. 8 i). The shell of an appropriately designed FB reactor or heat exchanger unit must be able to withstand the resulting overpressure in the device. The established overpressure should at least equal the gravitational weight of the particle mass in the vessel to achieve a fluidizing state. Accordingly, for large fluidized bed reactors or heat exchangers with a high particle mass, the required blower power can be significant. This must be considered in the design of the pressurized vessel, as well as in the expected operational and investment costs of a FB system. [100] Similar to a parallel flow heat exchanger, the outlet temperatures of both media flow rates in a one-stage FB reactor can be assumed to converge, provided there is sufficient residence time for the particles in the FB. Fluidized beds can also be staged multiple times vertically to assimilate a countercurrent media flow characteristic, see Fig. 8 k), similar to a multi-stage cyclone heat exchanger, see Fig. 8 d). Vertical fluidized beds can be designed with a horizontal perforated plate fluidizing one particle bed, while vertical baffle plates serve to section the fluidized bulk mass. The baffle plates stand out of the fluidized bed, but provide a clearance gap to the perforated plate. As the particles change their behavior during fluidization, they resemble the flowing characteristics of a liquid. This causes the FB to act like communicating pipes, allowing the particles to flow from the section of the fluidized bed with the highest bed height to the next section with a lower bed height until they exit the unit, see Fig. 8 l).

Evaluation criteria were derived based on the requirements outlined in section 2.2.1 to evaluate the technologies depicted in Fig. 8. A pairwise comparison was conducted to weigh the assessment criteria and perform a utility analysis. This evaluated the different gas-particle heat transfer technologies according to the defined requirements. A group of experienced scientists in the bulk handling area and heat transfer performed the pairwise comparisons, such as the utility analysis. They applied the following assessment criteria.

- Applicability for temperatures up to 1,000 °C
- Media flowrates controllable/ part load capability
- Countercurrent flow characteristic
- High temperature change at compact volume

The presented selection criteria apply to the defined requirements and the use of 1 mm bauxite particles, according to the reference scenario. Other authors with different boundary conditions and design criteria may define different evaluation criteria for their engineering tasks [90, 93].

After conducting a utility analysis on the eleven technologies presented in Fig. 8, the top four options were identified as follows:

- Multi-staged cyclones
- Multi-staged fluidized bed
- Falling cloud
- Trickling particles

To identify the heat exchanger technology that provides high volumetric power density at a relatively low volumetric pressure drop, a quantitative assessment of the four technology options was necessary. Information about reference systems is limited to protect intellectual property and knowledge advantages from competitors. Furthermore, comparing different pre-heater types directly is challenging due to variations in reference systems operational conditions, design specifications, and the lack of generalized comparison parameters. [108, 110]

Tab. 3 Characteristics of available reference systems of eligible heat exchanger technologies.

Technology	$\dot{Q}_{\mathrm{HX}}$ in kW	$p_{\mathrm{a,in}}$ in bar	Δp_{a} in Pa	ΔT in K	$\bar{T}_{\mathrm{a}}$ in °C	References
Multi-staged fluidized bed (concept)	100 000	10	37 340	820	560	[111]
Falling cloud (simulation)	600	4	24	650	555	[112]
Multi-staged cyclones (concept)	31 690	1	4000	530	585	[108]
Trickling particles (lab-scale)	7	1	120	280	260	[113]

Tab. 3 shows for each of the four heat exchanger technologies an exemplarily system and its operating conditions and illustrates the mentioned problem in comparing different systems, varying in power level, $\dot{Q}_{\mathrm{HX}}$, air pressure, p_{a}, pressure drop, Δp_{a}, temperature change, ΔT, and air mean temperature, $\overline{T}_{\mathrm{a}}$. Due to the limited availability of data, some of the examples in Tab. 3 only are available at the concept or simulation stage. For a quantitative comparison of the technologies listed in Tab. 3, the systems would have to be normalized to the same power level, pressure level, and temperature level. This could be achieved by applying the Buckingham π-theorem method. This method allows a system to be described in a dimensionless way. Accordingly, the systems in Tab. 3 would first be described non-dimensionally and then transferred analytically to the same level of power, pressure and temperature. However, due to the limited availability of data, it was not possible to apply this approach in a meaningful way. In order to conduct a comprehensive analysis and comparison of the four different technologies, it would be necessary to have a statistical relevant number for exemplary examples of each system.

Another method to select among the confined heat exchanger technologies is to qualitatively categorize the devices according to the before defined volumetric power density and volumetric pressure drop requirements. A fluidized bed HX, which requires the gas flow to be at least fast enough to lift the weight of the total particle mass to achieve particle fluidization at the expense of a corresponding pressure drop [100], is considered to provide the highest power density at the cost of the highest pressure drop. On the other hand, the size of the multi-stage HX cyclone, typically used in the mining and cement industries with heights up to 50 m or more [108], would not provide the required compactness for placement in a solar tower. The Falling cloud HX and the trickle flow HX are both expected to provide a reduced heat transfer capability compared to the FB HX at a significantly lower pressure drop, while the disadvantages of the falling cloud reactor in terms of uneven particle distribution and large fall heights are expected to be significantly improved due to radial particle distribution when a fixed packing structure is placed in the HX shell, at the cost of an expected moderate increase in pressure drop. Among the available options, the TFHX is considered the most viable middle ground in providing a relatively high power density at still moderate pressure drop capable of meeting the before design criteria. A fixed packing structure is considered applicable, since there is no risk of particle clogging, since the 1 mm bauxite particles, used in this work, show no tendency to agglomerate at temperatures up to 1,100 °C, as mentioned in section, 2.1.2.

2.2.3 The gas-particle trickle flow reactor and its applicability as heat exchanger

As outlined, the gas-particle trickle flow direct contact heat exchanger is considered a promising technology option for gas-particle direct contact heat transfer. Other names are also used in the literature, such as the raining packed bed exchanger (RPBE), countercurrent gas-solid-solid trickle flow reactor (SSTFR) or a gas-solid trickle flow (GSTF) system.

The trickle-flow reactor operates by having the trickling particles collide with the fixed packing structure in the column, which reduces the average particle sink velocity and increases the particle residence time in the column [114]. The concept of particle trickling in a packed column was first mentioned in a DSM patent in 1948 [115] and applied in a heat exchange process by Saint-Gobain [116]. A trickle flow reactor can be used to separate gas mixtures at high temperatures, e.g. for flue gas cleaning or solvent recovery [117]. In addition, a gas-solid packed bed column used for equilibrium reactions is known to provide high reaction rates by absorbing and extracting one of the reaction products from the reaction zone at the trickling solid sorbent [117]. Typically, the gas-particle-trickling reactor is used in the food or process industries for drying or chemical processes. For example, trickling particles are used as sorbents to extract the product gas from chemical reactions, such as Freon 12 [118], methanol or ammonia in synthesis processes [119-121], CO_2 captured in steam reforming- or post-combustion processes [122, 123], and for the desulfurization of flue gas [124]. In addition, trickle flow reactors are being investigated using trickling particles as a catalyst in the catalytic oxidation of sulfide to produce sulfur [125, 126]. The solids used should not have an excessive tendency to agglomerate, as this can cause the void volume within the packing structure to clog and prevent the unit from operating properly.

The literature highlights the advantages of a trickle flow reactor with its compact and simple design, low pressure drop, potential for a high degree of gas-particle interaction, and the inherent countercurrent characteristic with low axial mixing of both media along their flow path, resulting in high capacities for mass and heat transfer reactions. [113, 118, 127-131]. By increasing the air velocity, the heat transfer capacity can be further increased at the expense of an increased pressure drop [127, 129]. However, the pressure drop is still relatively low because up to 50 % of the particle weight is carried by the fixed packing structure [131, 132]. For dilute particle flow, the Ergun equation [133] can be applied to determine the pressure drop as a composition of the fractional pressure drop caused by the fixed packing structure and the trickling particles [128, 129]. Diluted particle flow often can be assumed in packed column below the flooding point, providing particle concentrations in the packing void space or particle hold-up, β, in the range of 10^{-3} [114, 126, 134].

$$\beta = \frac{\sum V_\mathrm{p}}{V_\mathrm{void}} \tag{3}$$

For dilute particle flow single particle behavior can be assumed, also the influence of particle shielding and agglomeration is reduced [114]. The underlying assumption of this work is, that a high particle volume fraction or particle hold-up, β, in the packed column resulting in a low particle sink velocity, are preferred. β correlates proportionally with the volume specific particle surface area within the packed column, a_p, which participates in the gas-particle interaction. The corresponding correlation will be derived in section 3.3. Accordingly, to use a trickle flow reactor in heat exchanger operation, it is desirable to increase the particle surface area, a_p, to increase the gas-particle heat transfer rate and consequently increase the volumetric power density as defined by the criteria before. Large, Naud [135] confirm that within stable flow regimes a high particle hold-up has a positive effect on the performance of a TFHX. Furthermore, a uniform particle distribution of trickling grains within the packing structure is preferred to avoid particle segregation and further optimize the gas-particle interaction. Therefore, understanding the hydrodynamic behavior and its characteristics is considered essential for the development of a gas-particle trickle flow heat exchanger.

Based on the various applications of trickle flow reactors, the hydrodynamic behavior of gravity-driven particle flow within the packing structure, with and without countercurrent air flow, has been studied, see e.g. [114, 124, 128-131]. The literature focuses on the analysis and/or prediction of particle hold-up, particle distribution, and pressure loss in the gas phase for various particle and packing types. By aggregating the available literature in the form of a meta-analysis, correlations were proposed, sometimes using dimensionless numbers, to predict the pressure loss or the particle hold-up in the packed column with a prediction accuracy of 20 %

to 40 % [136-138]. Other authors describe kinetic and hydrodynamic models for their specific pairing of particle and packing type. It has been found that the hydrodynamic behavior of a gas-solid system in a reactor with fixed elements shows analogies to gas-liquid systems with respect to particle hold-up, pressure loss, "loading" and "flooding" [114, 123, 130, 131, 139]. The loading point can be determined by measuring the hold-up of trickling particles and is reached when, for a constant solid flow rate, the hold-up increases with the gas flow rate [114]. In analogy to gas-liquid packed reactors, the loading point correlates with the particle flow rate and the corresponding gas velocity and decreases with increasing solid flow rates [117, 131]. Verver and van Swaaij [114], Roes and Van Swaaij [131], Large, Naud [135] found, that the particle velocity in the range of low gas velocities can be considered as constant, since the effect of the exerted drag force of a low gas flow rate cannot be measured thoroughly, but for sufficiently small particles, even small gas velocities show an effect on the particle sinking velocity. For increased gas velocities different states of the immersed particles in the packing void volume is described as "loading point" and "flooding point". Below the loading point, sometimes referred to as the pre-loading zone, the retention of trickling particles is proportional to the solid flow rate and rather independent of the gas flow rate [128, 139]. Depending on the particles studied, the packing structure used and the experimental conditions, it is not always possible to unambiguously identify the before-mentioned loading or flooding points [135]. Also, the particle flow behavior of trickling solids is strongly influenced by the grain size and the packing structure [135]. For gas velocities above the loading point, the slip velocity or the relative velocity between gas and particles evolves towards a constant value while approaching a more fluidized state, called the flooding point, which is recognizable by a steep increase in pressure drop and particle hold-up. By increasing the solid flow rates, flooding is more likely to occur at lower gas velocities [128, 131]. By gradually increasing the gas flow rate and passing the flooding point, the particle hold-up also begins to increase until the unstable fluid region is reached [131, 135, 139]. When the flooding point is reached in a trickle flow reactor, the particle motion no longer shows any orientation in the direction of gravity. In this state, particle mixing in the axial direction prevails and the ability to operate as a TFHX with countercurrent behavior is no longer provided, which is why operation in conditions without particles in a fluidized-like state is mandatory. For idealized countercurrent behavior, both media flow rates should exhibit plug flow behavior [131]. For gas flow rates below the flooding point, axial mixing of the solids can be assumed to be low and nearly independent of the gas flow rate [132, 140].

The radial distribution of particles in a counterflow packed column was first studied by Roes and Van Swaaij [141]. They mention that if the distribution of the particle mass flow within the cross-sectional area deviates significantly from the mean value, the local capacitance ratio may deviate significantly from the preferred value, which can sensitively disturb the equilibrium reaction between the interacting phases and thus negatively influence the column capacity. Under the operating conditions investigated, the radial distribution of the particles seemed to be influenced only by the particle mass flow, but not by the gas mass flow; exactly the opposite has been observed in gas-liquid systems [141]. It can be assumed that a radially uneven particle distribution has a negative effect on the performance of a TFHX, which is why several authors in the literature have devoted their research to the detailed investigation of the radial distribution of trickling particles within a packed column with and without countercurrent gas flow. To measure the radial distribution of particles, concentric, centrally arranged circular rings are placed under the packing, which is placed on a porous plate, so that the air required for the gas flow can be passed through and the particles in the concentric rings can be picked up to derive the radial distribution from the solid filling height [141]. Alternatively, honeycombs placed under the packing structure can provide an even more detailed resolution in measuring the radial particle distribution, where the particle filling height in each honeycomb and its deviation from the mean filling height would allow estimation of deviations from the average particle mass flow distribution in the cross-sectional area [123].

Large, Naud [135] and Saatdjian and Large [129] qualitatively observed the radial particle distribution in their experiments. They observed a uniform particle distribution in the packing at low gas velocities. However, as the gas velocity increased, dead zones free of sand began to form. As the flooding point was approached, no pronounced flooding or blocking was observed, which is likely to occur in packed columns with smaller diameters, but a rather unstable flow behavior was observed, which subsequently led to a complete radial segregation of gas and particles, resulting in the formation of visible thick particle strands, see Fig. 10. It has also been observed at high gas velocities that particles begin to segregate in the packing and flow along the wall, while the gas flows in the center of the packing [130, 142]. Kiel, Prins [143] suggest that the development of view trickling particle strands is likely to occur since it reduces the frictional or drag force experienced by the particles. Fig. 9 and Fig. 10 illustrate the effect of radial particle segregation in packed columns, forming visible thick particle strands that cause the column efficiency to decrease.

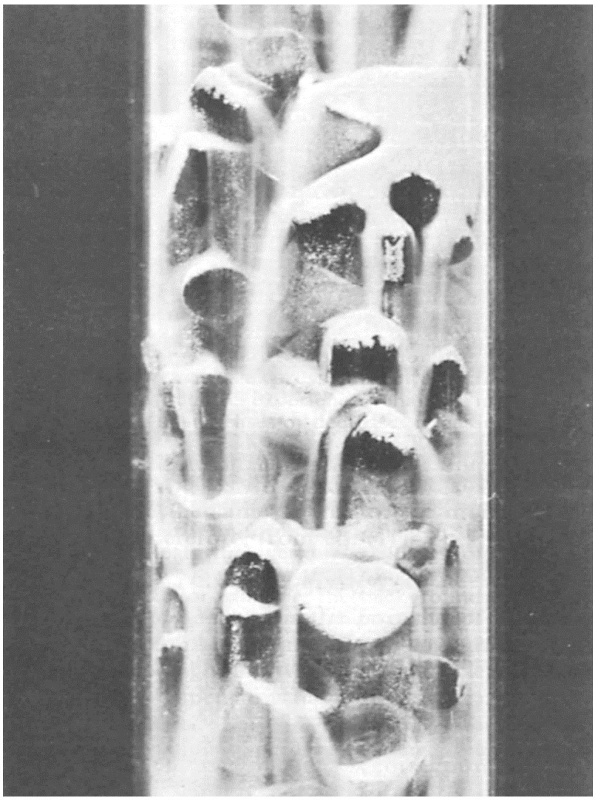

Fig. 9 Silica-alumina powder with an average particle diameter of 90 μm trickle over a dumped packing, consisting of 5 x 5 mm catalyst pellets and 7 x 7 x 1 mm glass Raschig rings, [128].

Fig. 10 Sand particles with an average particle diameter of 200 μm trickle over a dumped packing, consisting of metallic pall rings 15 x 15 mm, [135].

The ideal operating state, particle hydrodynamics and efficiency of a packed column depend mainly on the particles used, the type of packing and the way in which the gas and the particles are brought into contact with each other [127, 130]. As the gas velocity is increased from zero, the efficiency of the heat exchanger reaches a maximum. As the gas velocity is further increased, the efficiency decreases again and a transition from a uniform particle distribution to a radially segregated, inefficient particle flow is observed. [130] The occurrence of an operating maximum has also been observed by Saatdjian and Large [142].

Large, Guignon [130] state that in their investigated column of Pall rings it can be observed that the particles start to form strands after a certain height, which limits the performance in their experimental setup of a single packed column to a height of about 50 cm and cannot be increased further by increasing the packing height. Saatdjian and Large [142] observed the same behavior for their experimental configuration and mention that after a packing height of 40 cm, no increase in heat transfer was observed by further increasing the column, packed with Pall rings. As a solution to this limitation of the packing height, Large, Guignon [130] subdivided the packed bed horizontally and placed static mixers between the subdivided column and obtained a better performance of the reactor, probably due to a better redistribution of the particles. The same improvement was observed by Obradović and Levec [123], who noticed that the particles in their experiments had a tendency to tend outwards, they divided their packing structure into equidistant sections of 10 cm each by interposing ring-shaped screens to redirect the particles towards the center. By maintaining the overall packing height, multistaging has a positive effect on the performance of a packed column at the cost of a slightly increased pressure drop [130].

Similar to the subdivision of the packing structure along its height and the installation of elements to redistribute the particles, different methods for the initial distribution of the particles in the column was investigated. Static particle distributors, rotating particle distributors, and a shallow fluidized bed with multiple downcomer were studied and confirmed an improvement in column performance [130]. Roes and Van Swaaij [131] installed an additional packing structure of Pall rings above the packing column of the reactor. Verver and van Swaaij [114], Kiel [144] mention that uniformly arranged packing structures consisting of rods or tubes with a round or rectangular cross-sectional area, when properly designed, provide a better particle distribution in the packing void than unstructured arrangements, eliminating the need for an initial distribution devices or redistribution elements within the column for the trickling solids. Furthermore, Verver and van Swaaij [114] observed that in contrast to unstructured packed columns, regular structured packings had no negative effect on the radial distribution of the particles. Even at high gas velocities below the flooding point, an adequate radial particle distribution was observed. They also mention that the accumulation of non-moving static particles, which do not contribute to gas-particle interaction, is less likely to occur in structured packing arrangements. Kiel, Prins [143] confirm this finding and mention that radial particle segregation can be neglected due to the regular arrangement of the packing elements. A regular arranged packing structure and its inherent equal placing of obstructing elements provide a more efficient exploitation of space within the column than randomly packed elements [129]. In addition, Verver and van Swaaij [114], Kiel [144] mention that the pressure drop in a regular packing was observed to be lower than in unstructured packed columns, which is why the focus of this work is on the development of a TFHX with a regular packing structure.

2.2.4 Deduction of research question

As outlined before, comprehensive work is available in literature, investigating trickle-flow reactors. In terms of a meta-analysis, efforts were undertaken to generalize the particle hydrodynamics in such reactors, with uncertainties in the range of 20 % to 40 %. A generalized analysis of such systems would require consideration of all the dominant variables. However, the number of important parameters affecting the particle hydrodynamics in a trickle-flow system ranges from the operating conditions, such as the particle and gas flow rates and their temperatures, to geometrical parameters, such as the type of packing and how its elements are arranged, the mean particle diameter and its size distribution, the column diameter and the initial particle distribution [129]. Westerterp and Kuczynski [128] state that despite extensive investigations and data availability in the literature, no conclusive and general behavior of the hydrodynamics of a gas-solid trickle flow can be derived. Based on the information provided in the literature, it is understood that despite the efforts of a generalized concept to describe gas-particle flow in a packed column bed, the prediction accuracy shows a relatively high degree of uncertainty. Emphasizing the aforementioned literature findings, that the numerous variables, governing the particle flow in a packed column, make it challenging to identify a generalized approach to describe the particle flow. In contrast to the efforts to provide a general description in the reviewed literature, it was found that no methodical approach or selection method was conducted to identify a packing structure that would provide the highest gas-particle interaction for a given particle type. This work therefore focusses on the design process for a TFHX for a given particle type, with the objective of achieving an optimized gas-particle interaction. Based on the aforementioned findings in literature, an optimized gas-particle interaction in a trickle flow reactor is understood to be achieved when the packing structure is capable of providing, within the media flow conditions of interest, an even spatial particle distribution within the void structure and a high particle hold-up.

Despite the extensive hydrodynamic investigations in the literature, using predefined structured or unstructured packing geometries, no methodical process for selecting a favorable packing geometry is known. Solely Verver and van Swaaij [114] mention their motivation to rotate the squared bar elements by 45° parallel to the horizontal bar axis to avoid particle accumulation. The literature also agrees that packing structures in packed columns, e.g. using regularly arranged round [143] or rhomboidal [114] bar elements, are generally found to provide superior gas-particle interaction capabilities than unstructured packed beds, as investigated by [121, 128-131, 135, 142, 143, 145].

In the literature, great emphasis has been placed on the study of reaction kinetics and gas-particle hydrodynamics, while only limited information is available on the heat transfer capabilities of a TFHX. It is often stated that the gas-particle reactor, with its high capabilities for mass transfer, is expected also to provide high heat transfer capabilities due to the analogy of heat and mass transfer [113, 117, 124, 126]. Previous work using regular packing structures has investigated and confirmed the high heat transfer capabilities up to temperatures of 400 °C [113, 146].

Inspired by the aforementioned work and findings, the concept of a gas-particle direct contact trickle-flow heat exchanger shall be further developed and tested for an intended application in a particle-based solar tower system, based on the before-mentioned reference system. This leads to the research question of this thesis:

- How can a gas-particle direct contact trickle-flow heat exchanger be designed for a given particle type?

Accordingly, the main tasks and sub-research questions can be derived as follows:

- How can an optimized packing geometry be designed for a given particle type to provide a high particle hold-up and even particle distribution?
- What is the heat transfer capability of a trickle-flow heat exchanger with an optimized packing structure?

To address the mentioned research questions in chapter 3 the analytical methods are outlined to describe and assess the spatial distribution of particles, such as to calculate the particle hold-up. In the same chapter a numerical pre-selection process is applied, using DEM, to identify a packing type, that can be refined in chapter 4. In that chapter, the measurement setup is described for the cold- and the hot-tests, such as the measurement method to measure the parameters of interest. The first part of chapter 4 is dedicated to describe the cold-experiments to refine the packing structure. The second section of chapter 4 investigates the thermal performance of the TFHX, comparing the measurements with the available data in literature. Chapter 5 brings the work to a conclusion by presenting a preliminary design for an industrial scale-up and a simplified cost estimation.

3 Numerical evaluation of regular packed columns with regular structure for trickling particles

---

The results of this chapter have already been published by the author of this thesis:

Reichart, M, Neises-von Puttkamer, M, Buck, R, & Pitz-Paal, R. "Numerical Assessment of Packing Structures for Gas-Particle Trickle Flow Heat Exchanger for Application in CSP Plants." *Proceedings of the ASME 2021 15th International Conference on Energy Sustainability.* Virtual, Online. June 16–18, 2021. V001T02A006. ASME. https://doi.org/10.1115/ES2021-62746

For optimized gas-particle heat transfer the evaluation criteria for different geometry settings were previously derived:

- The packed column obstructs the solids flow, resulting in a high particle retention, respectively particle hold-up. Thereby the grain residence time increases, leading to a decrease in the mean particle sink velocity in the gravitational direction, u_p. Likewise, the volumetric particle surface area, a_p, which can potentially interact with the gas is enhanced.
- To achieve a high level of gas-particle interaction, a uniform distribution of particles across the cross-sectional area of the TFHX is desirable.

For a given particle type it is conceived advantageous to identify the matching packing structure, capable to provide high particle hold-ups. Solely Verver [126] mentions the motivation to incline the rectangular bars by 45 ° along the bar-axis to prevent the accumulation of solids [126]. Furthermore, there is currently no known methodical approach in the literature for arranging bar shapes in a regular pattern that provides both high particle hold-up and even particle distribution for a given particle type. This will be investigated during the numerical pre-selection process in this chapter, in order to identify a general bar shape that is capable of providing a high particle hold-up and an evenly distribution of the trickling particles. Therefore, the Discrete Element Method (DEM) without gas presence will be used, to compare for each geometrical structure the in section 2.2.4 defined assessment criteria - particle hold-up and particle distribution.

The following section describes the fundamentals of evaluating the particle distribution and determining the particle hold-up. It also explains the notation system and general composition of the packing structures used in the DEM simulation, including the particles used in the reference application [51].

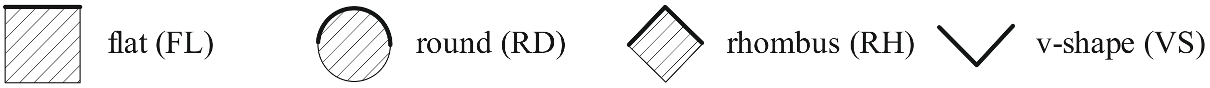

Fig. 11 Four basic geometries, providing different obstructive surfaces (bolt) for trickling particles.

3.1 Packing geometry

As previously mentioned, literature indicates that regularly arranged bar structures in a packed column are preferred over irregular packing structures such as dumped Pall or Raschig rings. However, accessible work does not go into detail in describing the motivation for the chosen geometries and dimensions of the regular packing structures. For the following numerical assessment, the in Fig. 11 shown four basic bar elements are chosen, providing different surface types for the trickling particles: flat (FL) surface, round (RD) surface, diamond or rhombus (RH) shaped surface, and v-shaped (VS) surface.

In the numerical pre-selection process, the bar elements are arranged in accordance with Verver and van Swaaij [114], Kiel, Prins [124], Verver [126]. The packing structure will be assembled using vertical stacked packing layers (PL) consisting of a specific number of horizontally equally spaced bar elements, n_{bar}. In their work, the authors rotate each packing layer by 90° parallel to the axis of gravity. However, they do not provide a clear explanation for this choice. After two PL, the number of bars is reduced by one for the subsequent two layers. Those packing layers, are horizontally rearranged with the vertical axis of symmetry and staggered respectively to the colinear PL above and below. After four layers the packing structure repeats, forming one packing unit (PU). Fig. 12 (right) shows an example of a correspondingly arranged packing structure that consists of four rhombus shaped bar elements per packing layer.

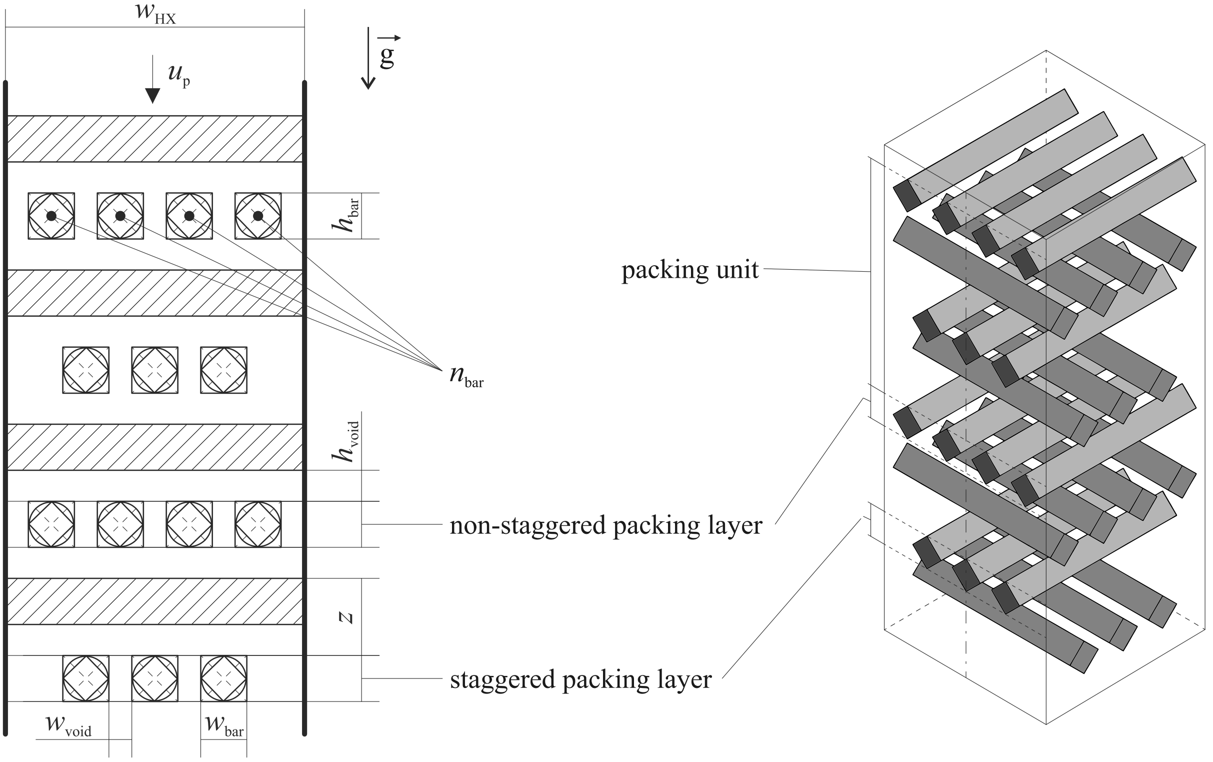

Fig. 12 Generic packing dimensioning (left) and example of packing unit using RH bars (right).

Tab. 4 Horizontal void distance in mm, for varying bar number and width; selected geometries, marked bold.

	number of bars per packing layer, n_{bar}					
w_{bar} in mm	1	2	3	4	5	6
4	46	21	**12.7**	**8.5**	**6**	4.3
6	44	19	**10.7**	**6.5**	4	2.3
8	42	**17**	**8.7**	4.5	2	0.3
10	40	**15**	**6.7**	2.5	0	
12	38	**13**	**4.7**	0.5		

$w_{\text{void}} > 20$	$20 > w_{\text{void}} > 10$	$10 > w_{\text{void}} > 0$	$w_{\text{void}} < 0$

To uniquely identify the different packing geometries, a concatenation of the following parameters is used to label the geometries according to the used bar width w_{bar} in mm, the bar height h_{bar} in mm, the number of horizontal bar elements in a non-staggered PL n_{bar}, and the particle falling height z in mm. Fig. 12 (left) assigns the geometry parameters to an exemplarily packing assembly. The according abbreviation of the in Fig. 11 shown bar types, is added as a prefix to the packing labeling. Fig. 12 (right) illustrates an exemplary packing geometry with rhombus shaped bar elements that can be named accordingly as "RH w06 h06 n4 z12".

When designing packing geometries, the void spaces between the bar elements have to be considered. These spaces should not be too narrow, as this can cause trickling particles to clog and flood the column with particles. As a general rule, it is recommended to design the void distances with at least 10-times the particle diameter [99]. In the reference application [51], which uses 1 mm bauxite particles, the minimum void distance accordingly is estimated to 10 mm.

In the simulations the same channel width, $w_{\text{HX}} = 50$ mm, as in the experimental test setup was used. To reduce the number of geometry options, the bar width and height were set to be equal: $w_{\text{bar}} = h_{\text{bar}}$, as well as the void height and width: $w_{\text{void}} = h_{\text{void}}$. Hence, by varying in a non-staggered PL the bar number, n_{bar}, and the bar width, w_{bar}, the resulting horizontal void distance, w_{void}, can be determined according to (4).

$$w_{\text{void}} = \frac{w_{\text{HX}}}{n_{\text{bar}}} - w_{\text{bar}} \qquad (4)$$

Tab. 4 shows w_{void} for varying geometrical parameters of n_{bar} and w_{bar}. The vertical distance between two layers is set equal to the horizontal distance of the maximum bar number of each group with the same bar width in Tab. 4. For example, h_{void} of the geometry settings w08 n3 and w08 n2 equals 8.7 mm for both settings, whereas $h_{\text{void}} = 6$ mm is set for w04 n3, w04 n4 and w04 n5. Geometries in the range of the estimated bridging distance, are selected and marked bold to be investigated further during the numerical pre-selection process.

The effective packing porosity, ϵ_{eff} (6), is the void area within a packing layer, A_{void}, normalized to the free cross-sectional area of the heat exchanger channel without packing structure, A_{HX}. Whereas A_{void} (5) can be determined by subtracting the projected packing surface of a bar layer, A_{pac}, from the cross-sectional area of the HX channel, A_{HX} (7).

$$A_{\text{void}} = A_{\text{HX}} - A_{\text{pac}} = w_{\text{HX}}^2 - w_{HX}\, w_{\text{bar}}\, n_{\text{bar}} \tag{5}$$

$$\epsilon_{\text{eff}} = \frac{A_{\text{void}}}{A_{\text{HX}}} = \frac{A_{\text{HX}} - A_{\text{pac}}}{w_{\text{HX}}^2} = 1 - \frac{w_{\text{bar}}\, n_{\text{bar}}}{w_{\text{HX}}} \tag{6}$$

with

$$A_{\text{HX}} = w_{\text{HX}}^2 \tag{7}$$

Similarly, the packing void fraction or packing porosity, ϵ_0 (9), is defined as the total void volume within the packing structure, V_{void} (8), normalized with the volume of the heat exchanger, V_{HX} (10).

$$V_{\text{void}} = V_{\text{HX}} - V_{\text{pac}} = w_{\text{HX}}^2\, h_{\text{HX}} - V_{\text{pac}} \tag{8}$$

$$\epsilon_0 = \frac{V_{\text{void}}}{V_{\text{HX}}} \tag{9}$$

with

$$V_{\text{HX}} = w_{\text{HX}}^2\, h_{\text{HX}} \tag{10}$$

According to Westerterp and Kuczynski [128], the occupied volume of the particles within the void volume needs to be considered to determine A_{void} and V_{void} and thus estimate the true gas velocity within A_{void}. However, as the volumetric fraction of moving particles within the void structure of the column is anticipated to be within the range of 1 %, this effect is presumed to be inconsequential within the context of this work.

3.2 Mixing quality of grain systems

For optimized gas-particle interaction, it is desirable to evenly distribute particles within the packing void. The spatial distribution of the trickling particles will be evaluated by applying the method for determining the mixing quality of two components A and B. Component A represents the volume fraction of the trickling particles, while component B represents both the packing void fraction and the volume of the packing structure. The mixing quality is determined by the mean square deviation of the empirical variance, u_n^2, of n samples X_i for a known total mixture composition P of the components A and B [101].

$$u_n^2 = \frac{1}{n} \sum_{i=1}^{n} (X_i - P)^2 \tag{11}$$

$$P = \sum_{i=1}^{n} X_i = \frac{\sum_{i=1}^{n} V_{\text{A},i}}{\sum_{i=1}^{n} V_{\text{sa},i}} = \sum_{i=1}^{n} \frac{V_{\text{A},i}}{V_{\text{sa},i}} \tag{12}$$

The determined mixing quality or particle density distribution, u_n^2, is compared to the limited nature of mixtures. When the components of the mixture are completely separated, it is referred to a segregated mixture, σ_0^2. An ideal uniform mixture, σ_{id}^2, can be considered as a particle system where all components are perfectly equally spaced and distributed. However, in practical applications, the best achievable mixing quality can be described by the stochastic uniform mixing, σ_{z}^2, as the theoretical case for σ_{id}^2 cannot be achieved through mechanical mixing processes, see Fig. 13.

$$\sigma_0^2 = P\,(1-P) \tag{13}$$

$$\sigma_{\mathrm{id}}^2 \equiv 0 \tag{14}$$

$$\sigma_{\mathrm{z}}^2 = \sigma_0^2\,\frac{V_{\mathrm{A}}}{V_{\mathrm{sa}}} \tag{15}$$

For an, linear interpretation of the particle mixing quality in a specific packing structure, and to compare it to its extrema, the relative linear, particle distribution, u_{rel}, was defined, where 0 represents the best and 1 the worst mixing quality [147].

$$u_{\mathrm{rel}} = \frac{\sqrt{u_n^2} - \sqrt{\sigma_{\mathrm{z}}^2}}{\sqrt{\sigma_0^2} - \sqrt{\sigma_{\mathrm{z}}^2}} \tag{16}$$

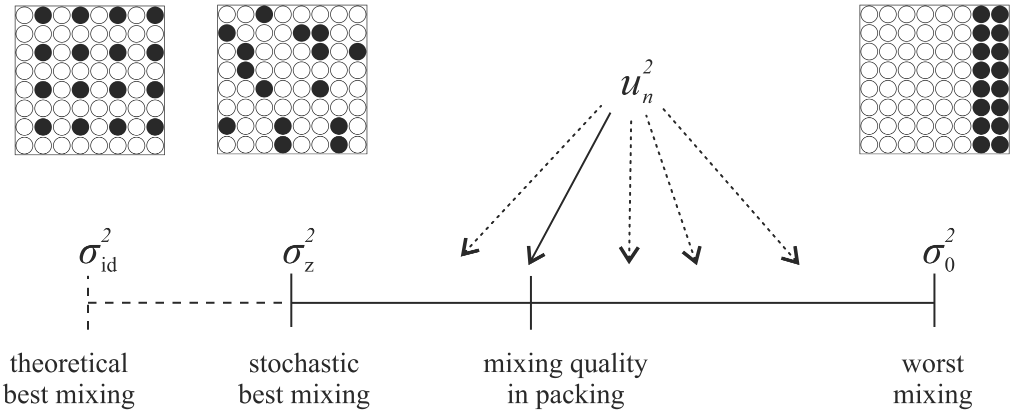

Fig. 13 Assessment procedure to determine the quality of mixtures, [147].

3.3 Particle hold-up in a packed column

A high particle volume fraction or particle hold-up, β, is preferred since it correlates proportionally with the specific particle surface, a_{p}, describing the surface of all particles within the packing void, $A_{\mathrm{p,pac}}$, normalized to the column or HX volume, V_{HX}, see (18). To enhance the gas-particle heat transfer rate and consequently increase the volumetric power density in a trickle flow reactor used in heat exchanger operation, it is desirable to increase a_{p}. The specific particle surface is calculated based on the volume specific surface of a sphere, $a_{V_{\mathrm{s}}}$ (17), which is derived from the Sauter diameter, d_{S}, [101].

$$a_{V_{\mathrm{s}}} = \frac{6}{d_{\mathrm{S}}} = \frac{A_{\mathrm{p,pac}}}{V_{\mathrm{p,pac}}} \tag{17}$$

The specific particle surface area for all particles in the TFHX can be calculated by multiplying a_{V_s} with the particle hold-up (19) and the packing porosity (9).

$$a_{\mathrm{p}} = a_{V_{\mathrm{s}}}\,\beta\,\epsilon_0 = \frac{6}{d_{\mathrm{p}}}\,\beta\,\epsilon_0 = \frac{A_{\mathrm{p,pac}}}{V_{\mathrm{p,pac}}}\frac{V_{\mathrm{p,pac}}}{V_{\mathrm{void}}}\frac{V_{\mathrm{void}}}{V_{\mathrm{HX}}} = \frac{A_{\mathrm{p,pac}}}{V_{\mathrm{HX}}} = \frac{6\,\dot{m}_{\mathrm{p}}^{\#}}{\rho_{\mathrm{p}}\,d_{\mathrm{p}}}\,\frac{1}{\bar{u}_{\mathrm{p}}} \qquad (18)$$

Where, the particle hold-up is defined as the fractional volume of all particles within the packed column, $V_{\mathrm{p,pac}} = n_{\mathrm{p,pac}}\,V_{\mathrm{p}}$, normalized by the packing void volume, V_{void}, [113].

$$\beta = \frac{V_{\mathrm{p,pac}}}{V_{\mathrm{void}}} = \frac{m_{\mathrm{p,pac}}/\rho_{\mathrm{p}}}{V_{\mathrm{HX}}\,\epsilon_0} = \frac{\dot{m}_{\mathrm{p}}^{\#}}{\epsilon_0\,\rho_{\mathrm{p}}}\,\frac{1}{\bar{u}_{\mathrm{p}}} \qquad (19)$$

If the average particle sink velocity, $\bar{u}_{\mathrm{p}}$, is known, according to (18) β can be determined with the packing porosity, the particle density, and mass flow rate of the particles, $\dot{m}_{\mathrm{p}}^{\#}$, normalized to A_{HX}. The general approach to calculate β is defined by (19), however the particle hold-up can be broadly divided between static particles, β_{stat}, resting on the packing structure, and dynamic particles freely trickling within the void space of the packed column, β_{dyn}, see Fig. 14. The sum of the dynamic and static particles, represents the total number of all particles within the packed column, (20). Similarly, α_{p} also can be determined separately for the static and dynamic particle fractions.

$$\beta_{\mathrm{tot}} = \beta_{\mathrm{dyn}} + \beta_{\mathrm{stat}} \qquad (20)$$

A more detailed differentiation of the different particle states of motion is described by Westerterp and Kuczynski [128] but it is not preserved as necessary for the scope of this work. It is assumed that the fraction of particles that is predominantly involved in the gas-particle heat transfer is provided by the trickling particles, represented by the dynamic hold-up, β_{dyn}, [97]. Therefore, unless stated otherwise, references to the particle hold-up will refer to the dynamic particle hold-up.

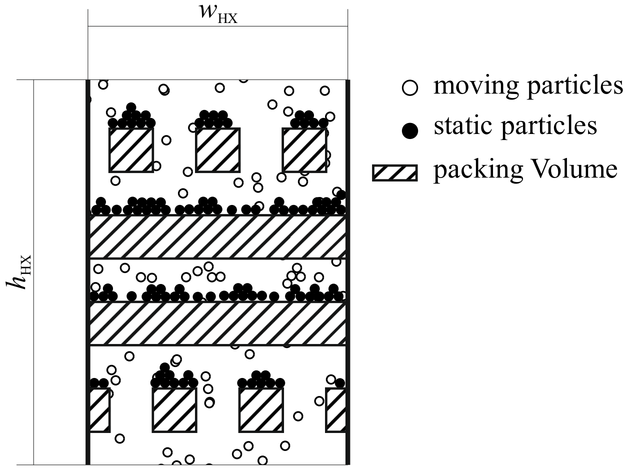

Fig. 14 Moving and static particles within a regular packing with FL bar shape.

In the literature on particle hydrodynamics within packing structures, the packing geometry remains unchanged, resulting in V_{void} as a constant referable value for normalization, see (19). In this work, the void structure and correspondingly ε_0 can vary substantially with changing packing geometries, why in this work the extended particle hold-up, β^*, is defined with respect to the heat exchanger volume, V_{HX}:

$$\beta^* = \frac{V_{\mathrm{p,pac}}}{V_{\mathrm{HX}}} = \beta\,\epsilon_0 = \frac{m_{\mathrm{p,pac}}/\rho_{\mathrm{p}}}{V_{\mathrm{HX}}} \qquad (21)$$

With alternating packing structures V_{HX} remains constant, allowing for comparison of different geometries, by using β^*.

3.4 Used particles

The selection of particles in this work was based on a successful large-scale technical demonstration of a solar direct absorbing particle centrifugal receiver. The particles were heated to an average outlet temperature of 965 °C [51]. Saint-Gobain Proppants 16/30 sintered bauxite was used in the experiment [8]. Tab. 5 lists the properties of the grains, which have a diameter of approximately 1 mm.

Tab. 5 Properties Saint-Gobain Proppants 16/30 sintered bauxite, [148].

particle size distribution	cumulative wt. %
< 0.595 mm	12
< 0.841 mm	84
< 1.190 mm	4
mean particle diameter	d_{p} = 0.98 mm
sphericity	ψ_{p} = 0.9 -
bulk density	ρ_{p} = 2.04 g/cm^3

With the provided cumulative weight distribution of the particle size fractions the main particle- or sieve diameter, d_{p}, can be calculated, see (22). For spherical or near spherical particles the volume diameter is equal to the sieve diameter. A sieve analysis allows the calculation of d_{p} by using the retained particle mass at each sieve screen, $m_{\mathrm{p},i}$, with the corresponding sieve class mean value, $\bar{d}_{\mathrm{p},i}$, [134]. The results of the corresponding sieve analysis are illustrated in Fig. 62 in section A.2.1.1.

$$d_{\mathrm{p}} = \frac{1}{\sum(m_{\mathrm{p},i}/\bar{d}_{\mathrm{p},i})} \qquad (22)$$

Using (22), the particle diameter can be determined to be 0.98 mm. To ensure accuracy in the experimental analysis, the uncertainty of the particle diameter, $u_{d_{\mathrm{p}}}$, is estimated along with other additional uncertainties in section A.1. As the particles have a high sphericity of $\psi_{\mathrm{p}} = 0.9$, they are assumed to be perfect spheres for the purpose of calculating particle volume or surface area in this work.

3.5 Assessment procedure

Tab. 4 highlights eleven geometrical dimensions, while Fig. 11 depicts four different bar shapes. This results in a total of 44 packing geometries that were investigated. To simplify the numerical assessment procedure, no gas presence within the column void is assumed. Thereby, omitting the generation, the meshing, and calculation of the gas-particle interaction in a gas simulation domain. In the following experimental chapter 4, the effect of air flow will be considered. However, based on experiments conducted later in this work and available data in literature [114], it seems feasible to neglect the impact of air at this early stage of investigation. This is because the determined average particle sink velocities within the column did not exceed 0.6 m/s, and therefore are one order of magnitude lower than the particle sink velocities ranging from 7.9 m/s to 11.3 m/s, for gas temperatures in the envisioned operating range of 20 °C to 900 °C, respectively, see Tab. 23. The terminal velocity, u_{t}, can be determined by calculating the drag coefficient of single spheres using for example the approach provided by Kaskas [101], see section A.5 and Tab. 23. Similarly, for non-moving gas or low air flow, the effect of air on particle trajectories for the used grains can be disregarded since the exerted gas drag force, F_{D} (214), is estimated to be two orders of magnitude lower than the gravitational force of the particles, F_{g} (212). Roes and Van Swaaij [131] confirmed experimentally that for low gas flow rates, the particle hold-up remains nearly constant. Only for higher air flow rates above the loading point the measured hold-ups started to increase.

The solids flowing through the empty space, obstructed by objects, were simulated using DEM with the open source DEM software LIGGHTS-PUBLIC. The DEM is a simulation approach based on the Lagrangian method. It tracks and calculates the motion and interaction between all grains while also considering limiting geometries in the simulation domain. The DEM is commonly used to simulate disperse particle flow systems. While the DEM represents a discrete simulation approach by calculating the Lagrangian equations of the particles in the simulation domain, also the continuous Eulerian methods have also been widely applied to investigate particle flow of disperse grain systems [60]. Cundall and Strack [149] first applied a discrete numerical model to a granular system by embedding the Newtonian conservation of momentum equations. The model includes force-displacement equations for particle-particle and particle-wall collisions, with a slight overlap during the collisions [60]. The DEM method has been extensively studied and has been explained by various authors, including Sandlin [60], Grobbel [150], and others [151-157], why a detailed description of the method is omitted in this work.

The simulations were conducted using two different materials in the simulation domain:

- Aluminum oxide particles
- Steel packing structure and shell

To conduct DEM simulations, it is crucial to determine the material properties, including particle density, coefficient of restitution (COR), coefficient of friction (COF), and Young's modulus, E, of all interacting materials and others [154]. Grobbel [150] conducted extensive calibration efforts on various particle types to match DEM and experimental results under ambient conditions. He also calibrated the DEM simulation parameters for the Saint Gobain 16/30 sintered bauxite particles, that were applied in this work, see Tab. 6. The particle size distribution, of the used particles, see Tab. 5 or Fig. 62, was not considered, this allowed for a more efficient contact detection between objects, resulting in faster simulation times. Therefore, in line with Grobbel [150], mono-sized spheres, with the same representative diameter, $\bar{d}_{\mathrm{S}}$, were used.

The simulation time is usually set between 10 % [158] and 30 % [159] of the Rayleigh timestep, $\Delta t_{\mathrm{Rayleigh}}$, [60, 150]. This time is deduced by the propagation of Rayleigh waves along the surface of a solid body [160].

$$\Delta t_{\mathrm{Rayleigh}} = \frac{\pi \left(\frac{d_{\mathrm{p}}}{2}\right)_{\mathrm{min}}}{b} \sqrt{\frac{\rho_{\mathrm{p}}}{G_{\mathrm{p}}}} \tag{23}$$

Assuming isotropic material, the shear modulus can be expressed using the Young's modulus and the Poisson's ratio, ν.

$$G = \frac{1}{2\,(1+\nu)}\,E \tag{24}$$

The variable b in (23) represents one of the roots of (25).

$$(2-b^2)^4 = 16\,(1-b^2)\left[1 - b^2 \frac{1-\nu}{2\,(1-\nu)}\right] \tag{25}$$

The relevant root in (25) is approximated by [160] with:

$$b = 0.8766 + 0.163\,\nu \tag{26}$$

Therefore, (23) can be simplified and rewritten:

$$\Delta t_{\mathrm{Rayleigh}} = \frac{\pi \left(\frac{d_{\mathrm{p}}}{2}\right)_{\mathrm{min}}}{0.8766 + 0.163\,\nu} \sqrt{\frac{2\,\rho_{\mathrm{p}}\,(1+\nu)}{E_{\mathrm{p}}}} \tag{27}$$

If the high values of the Young's modulus of steel and aluminum oxide are applied in (27), the simulation timestep required would be relatively small, resulting in long simulation times. To increase the simulation speed, it is common to reduce the Young's modulus of the materials by several orders of magnitude [60, 150, 154]. Yan, Wilkinson [161] investigated the behavior of particle flow released from a flat-bottomed hopper and allowed the grains to accumulate into a pile on a flat surface below. They found that reducing the Young's modulus of the particles by a factor of 10,000 did not affect the discharge rate, the particle speed, or the angle of repose. Despite the significant reduction of E, the behavior of the particles was observed to remain unchanged. Therefore, the Young's modulus of the materials used in the simulation was set to the minimum possible value in LIGGHTS-PUBLIC, which is 5 MPa. This value and procedure is consistent with other authors conducting similar investigations [60, 150]. Using (27), the Rayleigh time can be estimated to 7^{-5} s. Therefore, the simulation timestep was set to 1^{-5} s, which falls within the recommended range of 10 % to 30 % of $\Delta t_{\mathrm{Rayleigh}}$.

Tab. 6 Used parameters for DEM simulation at ambient conditions, [150].

particle properties	Sauter diameter	d_S	=	1.201	mm
	Young's modulus	E_p	=	5	MPa
	particle density	ρ_p	=	3,560	$\mathrm{kg/m^3}$
	Poisson's ratio	ν_p	=	0.3	–
steel properties	Young's modulus	E_w	=	5	MPa
	Poisson's ratio	ν_w	=	0.3	–
COR	particle-particle contact	ϵ_pp	=	0.46	–
	particle-wall contact	ϵ_pw	=	0.43	–
sliding COF	particle-particle contact	$\mu_\mathrm{S,pp}$	=	0.53	–
	particle-wall contact	$\mu_\mathrm{S,pw}$	=	0.31	–
rolling COF	particle-particle contact	$\mu_\mathrm{R,pp}$	=	0.16	–
	particle-wall contact	$\mu_\mathrm{R,pw}$	=	0.38	–

For the simulative identification of a bar-element shape, the parameters shown in Tab. 6 were used. Within the scope of a pre-selection of a geometry type. The influence of temperature was neglected during the pre-selection of the geometry type, as the calibration parameters are only available at ambient conditions. Also, the same boundary conditions were applied alongside the same calibration parameters used by Grobbel [150]:

- Sauter diameter, d_S, is used for the representative diameter in DEM simulation
- Particles are assumed to be perfect spheres
- Contact Force Model: tangential history model
- Rolling Friction Model: modified elastic-plastic spring dashpot (EPSD2)

Grobbel [150] mentions that during the simulative calibration of the friction coefficients, it was not possible to match fully the particle-wall rolling friction coefficient, $\mu_\mathrm{R,pw}$, with the experimental results. This must be considered while interpreting the simulation results, that means a direct interpretation like particle sink velocity or hold-up has to be done carefully. Instead, a relative comparison of particle hydrodynamics between different packing structures seems feasible.

The simulation domain's geometrical setup consists of two vertically stacked packing units (PU), as defined in section 3.1. The grain was induced in the simulation through a seeding plane, which evenly distributed the particles in the first PU where the grain flow can develop. The analysis of particles was then performed in the second PU, as shown in Fig. 15. This packing unit was divided into approximately 1,000 equally sized discrete cells (DC). For each analyzed time step, all particles within the second PU are assigned to their corresponding discrete cells based on the current position of the grains. By applying (12) and (11), the particle concentration, X_i, and the mixing quality, u_n^2, can be determined for each discrete cell in the 2nd PU, where $V_{\mathrm{sa},i}$ is set equal to $V_{\mathrm{DC},i}$.

Fig. 15 (right) shows a packed column with a regular arrangement of bar shapes that provide flat surfaces for non-trickling or non-moving particles to accumulate in static zones, representing the static particle hold-up, β_stat, (20). The volume fraction of the particles in motion, trickling over the packed elements, is accounted for the dynamic particle hold-up, β_{dyn}, (20). In the evaluation process, it is necessary to identify a minimum velocity, u_{min}, for each geometry. This velocity separates the dynamic particles from the non-moving static particles, allowing for the calculation of the corresponding mass fractions and hold-ups. The method to identify u_{min} will be outlined in the following section.

The simulation begins with an empty domain that only includes the geometry, without any particles. The grains are then introduced through the seeding plane at the top of the column using a predetermined particle mass flow rate, see Fig. 15. The analysis is conducted after reaching steady-state conditions. Therefore, the seeding mass flow in the model must be equal to the particle flow rate leaving the simulation domain, resulting in a converging total particle hold-up with increasing simulation time step, β_{tot}, (20). As previously stated, a diluted particle flow can be expected within the column, resulting in a scattered distribution of particles at each time step. To assess the simulation results with statistical significance, a sensitivity analysis showed that for the presented setup, after reaching steady-state conditions, the calculated hold-ups of 50 time steps must be averaged to account for the fluctuating positions and distribution of the trickling particles.

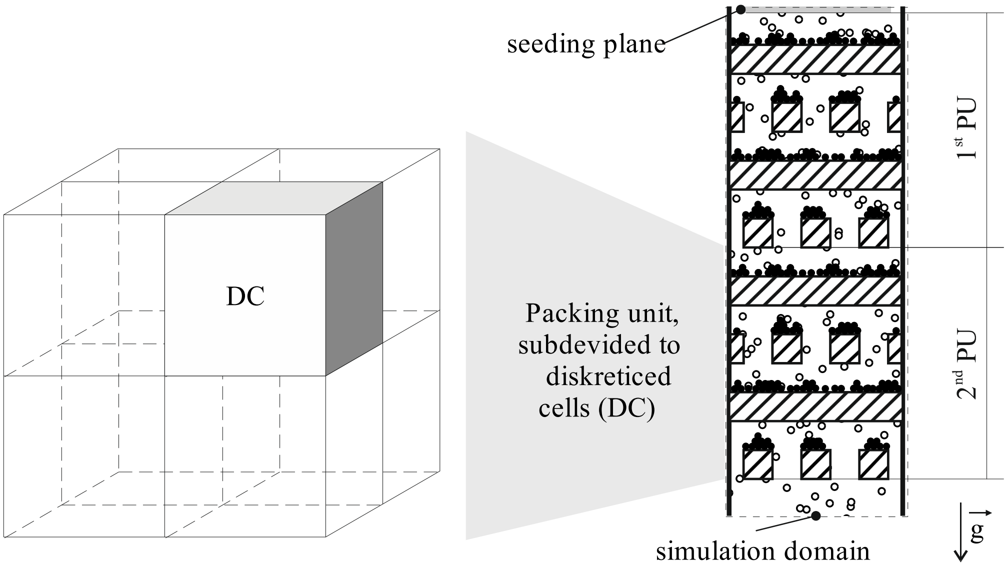

Fig. 15 Geometrical setup of DEM simulation domain (right), and schematically discretized packing unit.

3.6 Results and discussion

DEM simulations were performed for the 44 packing geometries mentioned before. The estimated maximum particle mass flow rate assumes equal heat capacity flows for the solid and gas phases, $\dot{W}_{\mathrm{r}} \approx 1$. For the upper boundary condition of gas flow, represented by $u_{\mathrm{t}} = 7.9\ \mathrm{m/s}$ and assuming a low particle velocity, the relative velocity of the particles can be assumed to be equal to the air velocity $u_{\mathrm{a}} \approx u_{\mathrm{t}}$. This allows for an estimation of the maximum particle mass flow at ambient conditions of $\dot{m}_{\mathrm{p}}^{\#} = 2\ \mathrm{kg/(s \cdot m^2)}$. After reaching steady-state conditions in each packing geometry the particle hold-up and the mixing quality were determined. Fig. 16 displays an exemplary result for a "RH w06 h6 n4 z6.5" packing. The histogram shows the frequency of occurrences of the velocity distribution for the particles in the evaluated second PU. Because the rhomboid bar element does not allow for particle accumulation, $\beta_{\mathrm{stat}} = 0$, the dynamic particle mass fractions are equal to the total components $\beta_{\mathrm{stat}} = \beta_{\mathrm{tot}}$, see (20). Therefore, there is no need to differentiate between static and dynamic mass fractions in this case.

The averaged particle sink velocity, $\bar{u}_{\mathrm{p}}$, is determined to be 0.32 m/s, confirming the assumption that u_{p} can be assumed to be small compared to u_{t}. This is consistent with the experimental results of Verver and van Swaaij [114] for low and zero gas flow, as the range of u_{p} and β_{dyn} is of the same magnitude. The particle distribution of the trickling particles in the RH w06 h6 n4 z6.5 packing can be considered to be relatively uniform since the values of u_{n}^2 and ${\sigma_{\mathrm{z}}}^2$ are relatively close to each other, compared to ${\sigma_0}^2$. This results in a low relative linear particle distribution of the dynamic particle fraction, $u_{\mathrm{rel,dyn}} =$ 3.2 %. Since no static particles can accumulate in the RH packing, the dynamic values apply for this case also for the total values, $u_{\mathrm{rel,dyn}} = u_{\mathrm{rel,tot}}$, see (20).

Fig. 17 shows the evaluation results of the packing: SQ w06 h6 n4 z6.5. The y-axis is shown in logarithmic scale because the SQ-shaped bar geometries allow the particles to accumulate in the packed column. In a sensitivity analysis, a division of the velocity spectrum into 50 equally spaced intervals was found to be convenient for distinguishing between static and dynamic particles for the evaluation of different geometries within this work. The threshold for distinguishing between static and dynamic particles is set to the upper limit of the lowest velocity interval for all geometries, which is in the shown example $u_{\mathrm{min}} =$ 0.02 m/s. Using this value, the particle hold-up can be determined by applying (19) separately for the dynamic, static, and total volume fractions, using the corresponding particle mass, $m_{\mathrm{p,pac}}$. In this example, more than 80 % of β_{tot} is assigned to β_{stat}. Compared to the previous example in Fig. 16, which used RH bar elements, the mean particle sink velocity is reduced by over fifty percent to $\bar{u}_{\mathrm{p}} =$ 0.14 m/s. For this example, the relative linear particle distribution of the moving particles is determined to be $u_{\mathrm{rel,dyn}} =$ 1.5 %. When comparing the dynamic particle hold-ups of a RH shaped bar geometry to a SQ geometry, while keeping the other geometrical dimensions and particle mass flow constant, see Fig. 12 (left), an increase of approximately 100 % in β_{dyn} was observed.

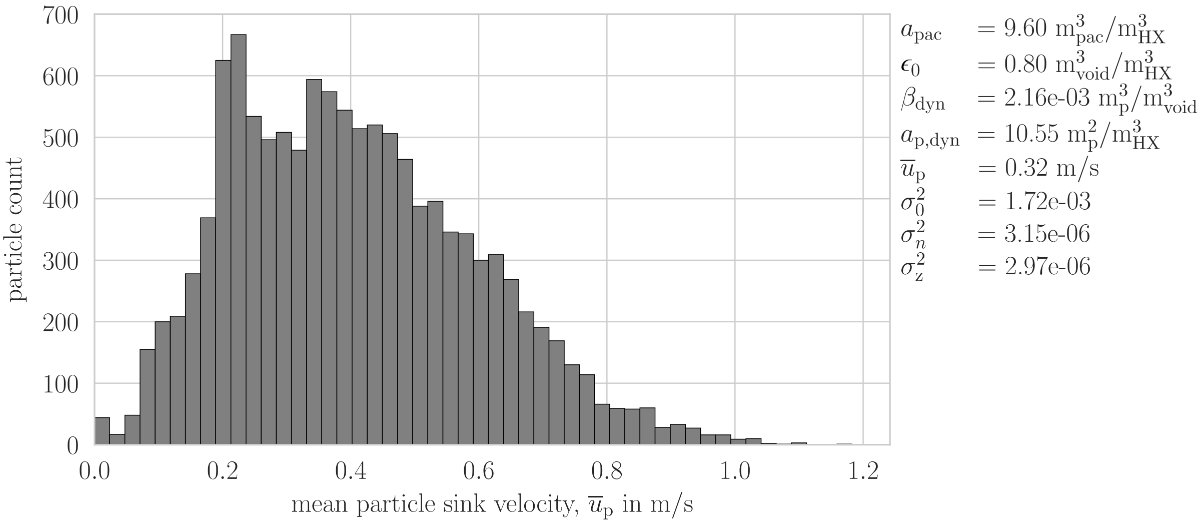

Fig. 16 Velocity distribution of all particles in the packing: “RH w06 h6 n4 z6.5”; particle flow 2 kg/(s · m^2).

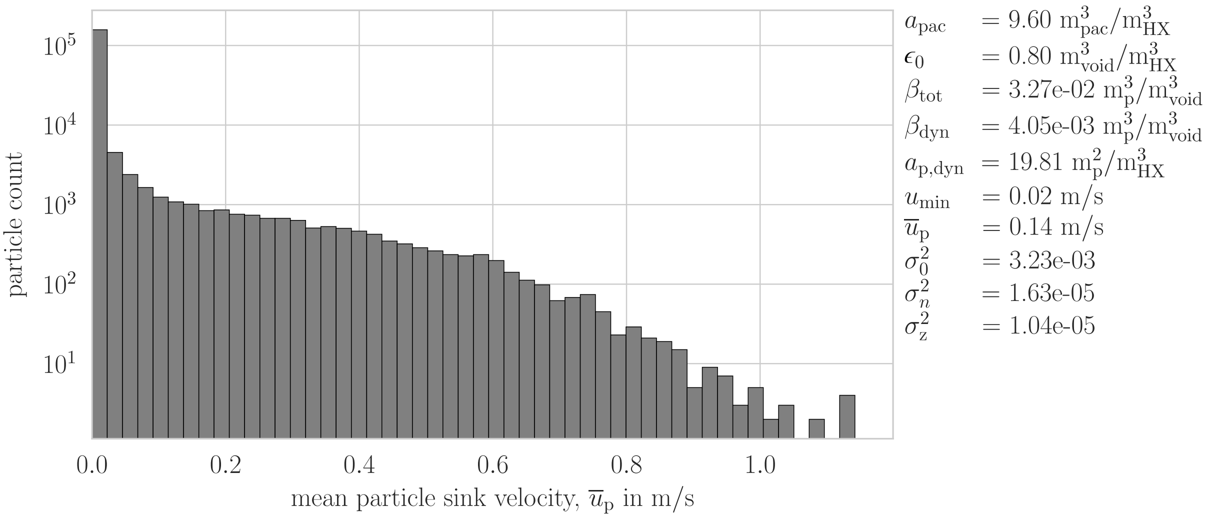

Fig. 17 Velocity distribution of all particles in the packing unit, “SQ w06 h6 n4 z6.5”; particle flow 2 kg/(s · m²).

These two examples already illustrate the significant influence of the bar shape when optimizing a packed column for high dynamic particle hold-up. This observation is further supported by Fig. 18, which plots the extended particle hold-up, β^*_{dyn}, against the relative linear particle distribution, $u_{\mathrm{rel,dyn}}$. To make an overall direct comparison of different packing geometries, the average particle sinking velocity [147] or likewise the extended particle hold-up, β^*_{dyn} (21), can be used as a reference value to compare the corresponding dynamic particle fractions for all 44 simulated packings. The latter is used to preliminary identify and select a preferred bar shape for a packed column with a regular geometry.

Fig. 18 shows the calculated dynamic particle hold-up as a function of linear particle distribution for all 44 different packing geometries. Each dot type represents a different bar cross-sectional area, as defined in Fig. 11, varying in dimensions such as bar width, bar height, and number of bars per packing layer as shown in Tab. 4. To improve clarity, the labeling of different geometries is omitted in Fig. 18. In a separate study, no clear tendency of a certain geometry parameter could be identified as dominant with respect to the evolution of $\overline{u}_{\mathrm{p}}$, and vice versa for β^*_{dyn} according to (18), [147]. Additionally, Tab. 7 summarizes the maximum, minimum, and median values of β^*_{dyn} and $u_{\mathrm{rel,dyn}}$ for each group of bar shape.

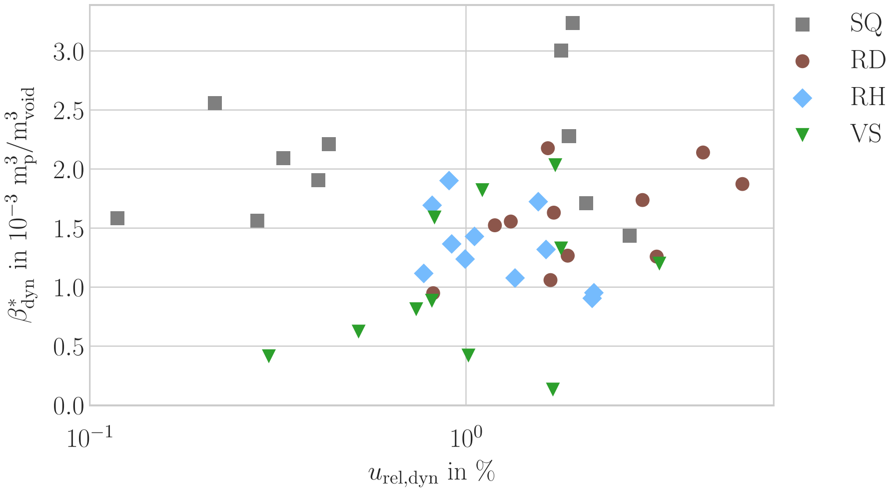

Fig. 18 Extended dynamic particle hold-up vs. linear particle distribution in varying packing geometries.

Tab. 7 Minimum and maximum values of particle hold-up and particle distribution with corresponding median of all simulated geometries for each bar shape.

bar shape	$\beta^*_{\mathrm{dyn,min}}$ in %	$\beta^*_{\mathrm{dyn,max}}$ in %	$\tilde{\beta}^*_{\mathrm{dyn}}$ in %	$u_{\mathrm{rel,dyn,min}}$ in %	$u_{\mathrm{rel,dyn,min}}$ in %	$\tilde{u}_{\mathrm{rel,dyn}}$ in %
SQ	0.14	0.32	0.21	0.12	2.72	0.43
RD	0.09	0.22	0.16	0.82	5.43	1.71
RH	0.09	0.19	0.13	0.77	2.19	1.05
VS	0.01	0.20	0.08	0.30	3.27	1.06

Fig. 18 and Tab. 7 demonstrate that the particle distribution in all simulations varies between 0.1 % and 5.4 %, indicating a relatively uniform spatial distribution of all trickling particles. Tab. 7 also shows that the SQ-shaped profiles provide the highest total particle retention, with β^*_{dyn} values ranging from 0.14 % to 0.32 %. The corresponding median value, $\tilde{\beta}^*_{\mathrm{dyn}}$ for SQ bar elements also presents the highest value among the four bar shapes. To reduce the dominance of value outliers, the median value is chosen over the arithmetic mean. Both the RD and RH shaped bar elements show particle retention in the same range but below the SQ bars. Whereas the VS bar geometry provides the lowest particle retention, see Tab. 7. The simulation results can be compared relatively among the packing structures, but the quantitative interpretation should be approached with caution. This is due to the particle-wall rolling friction coefficient not being fitted satisfactorily to the calibration experiments, as previously mentioned. Therefore, a conclusive decision cannot be made yet regarding the final dimensioning of the geometry setting. In summary, the simulation results indicate that structures composed of SQ bar elements are the most promising to compose a packing geometry for the TFHX, based on the initially defined selection criteria. The following chapter will conduct the experimental investigations to identify the most suitable packing geometry and dimensions, considering the influence of the air flow, followed by the experimental performance evaluation of the developed device.

4 Experimental development and investigation of a trickle flow heat exchanger

In the preceding chapter, a general basic bar shape of a trickle flow reactor was identified through the application of DEM simulations. The analysis demonstrated that a regular packing geometry, comprising vertical bars with a squared cross-sectional area, can offer promising characteristics when an equal particle distribution and high particle hold-up of the trickling particles is desired. Nevertheless, further development was needed in order to identify a suitable sizing of the packing geometry that aligns with the flow behavior of the used 1 mm bauxite particles. Consequently, an experimental test setup was designed to conduct cold experiments for the purpose of identifying a preferred packing geometry, and subsequently, to perform hot tests with the objective of assessing the thermal heat transfer capabilities of the developed unit.

4.1 Experimental qualification of packing structures

The results of this section have already been published by the author of this thesis:

Reichart, M, Hirt, A, Technau, J, Raab, A, Lackovic, L, Uhlig, R, Neises-von Puttkamer, R, & Pitz-Paal, R. " Experimental Development of Packing Structures in a Gas-Particle Trickle Flow Heat Exchanger for Application in Concentrating Solar Tower Systems." Advanced Powder Technology; ISSN: 0921-8831, Elsevier; London; ISSN 0921-8831; published on 27. May 2024; https://doi.org/10.1016/j.apt.2024.104481

A test rig was constructed for the purpose of developing a packing structure to be used in a trickle flow heat exchanger. This setup allowed for the conduction of cold test campaigns, during which the grain flow behavior of a specific particle type within different packing geometries was examined. The aim of this approach was to identify a packing geometry that would be most effective in providing a high particle volume fraction of the trickling particles in the packed column and also provide an even particle distribution in the void space.

This section outlines the experimental development of a packing structure. It begins with a description of the measurement setup and the cold testing procedure, followed by an analysis of the particle flow behavior at varying media flow rates in different packing structures. This analysis is intended to identify a preferred packing geometry, which will be analyzed in the hot tests, as described in section 4.2.

4.1.1 Experimental setup and measurement procedure

Fig. 19 depicts the test rig, which has been designed to install a variety of packing structures. The instrumentation has been installed with the purpose of measuring the inlet and outlet temperatures of both media, the particle and air mass flow rates that can be altered, the pressure drop, and the particle hold-up. For the hot experiments, insulation was installed, although this is not depicted in the sketch.

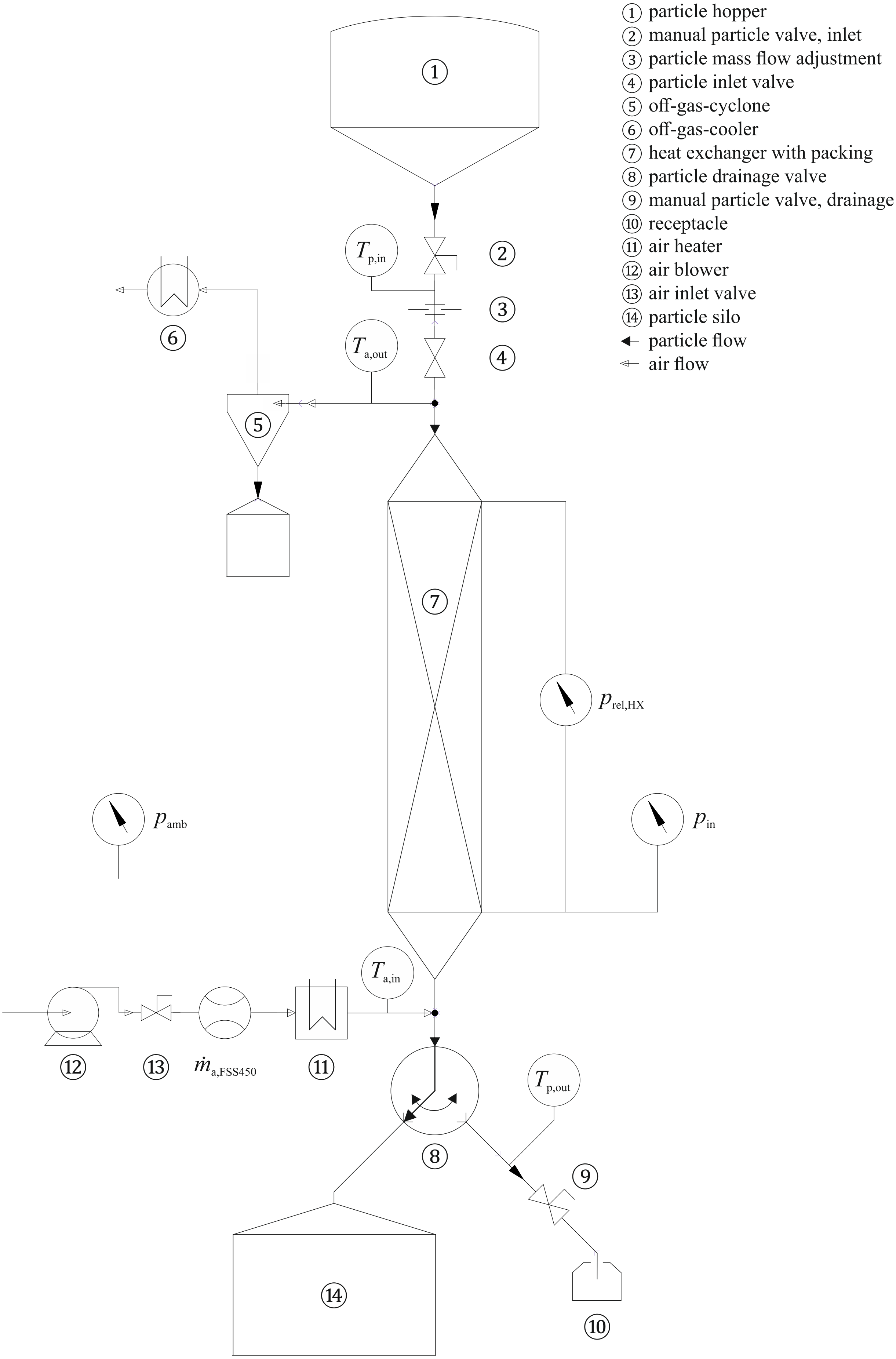

Fig. 19 Experimental set-up for the cold testing of packing structures.

The particle mass flow is adjusted by swappable orifice plates ③, causing the particles above to dam and form a moving particle bed fed by the particle-filled hopper ①. The orifice plates are changed when the test rig is not in operation, therefore the manual particle valve of the inlet ② is closed and the orifice plate can be changed. Through the orifice, the particles fall down by gravity, pass through the electro-pneumatically actuated particle inlet valve ④ and enter the heat exchanger with the mounted packing ⑦. The particles trickle through the HX channel and are by default, guided into the particle silo ⑭ by means of a drainage valve ⑧. By operating the drainage valve ⑧, particles can be separated into the drainage tube during operating. A blower ⑫ feeds ambient air into the setup, which is continuously measured before entering the heat exchanger. Special care has been taken in assembling the test bench components of the "air inlet area," ensuring that they are airtight with respect to the heat exchanger and the components below (⑥, ⑦, ⑧, ⑩). The air leakage was quantified in a separate pretest during the commissioning of the system by pressurizing the air inlet area and recording the pressure reduction of the pressurized system over time. The air leakage did not exceed 5 % of the air flow rate and was embedded in the gas flow measurement as a function of overpressure in the test setup with its corresponding uncertainty, see section A.3.6.2. The airtightness of the air inlet area causes the air to flow upwards through the packing structure ⑦ while interacting with the trickling particles. The exhaust gas leaves the system between the HX and the particle inlet valve ④, where potentially entrained particles are separated in an exhaust gas cyclone ⑤. Due to the relatively narrow heat exchanger width of only 50 mm, no additional engineering measures were taken to evenly distribute the incoming particles or the gas flow. Qualitative observations and preliminary DEM and CFD simulations confirmed a uniform distribution of both media flow rates after entering the TFHX, which is why the installation of devices to evenly distribute the incoming media flow, as mentioned in the literature in section 2.2.3, was omitted.

State-of-the-art butterfly valves were used for the valves ② and ④ in the inlet section. A manufacturer was found to supply valves that would operate at temperatures up to 1,000°C. However, no suitable drainage valve supplier could be found. Therefore, a drainage valve was designed that would be able to drain the potentially hot particles at higher temperature levels, according to section 2.2.1. Fig. 20 shows a CAD sectional view of the drainage valve. The particle silo, the TFHX, and the manual particle valve are not shown. Particles exiting the packed column enter the top of the drainage valve. From the side, the pre-conditioned air enters likewise the upper section of the drainage valve. The slope in the air inlet tube is designed to prevent the air inlet tube from gradually filling with ejected particles. The air stream enters the drainage vale and exits directly in countercurrent direction of the particle flow upwards to the TFHX. The particle flow falls into the centerpiece of the drainage valve, a pivoting funnel, that can swing 11 ° to either side from the neutral center position. When the funnel swings to the right, the particle stream is guided into the drainage tube. When the funnel swings to the left, the particles fall into the particle silo ⑭. The installed TC and the trace heating elements are needed for the determination of the particle outlet temperature and will be described in the sections 4.2.1.2 and A.3.7.

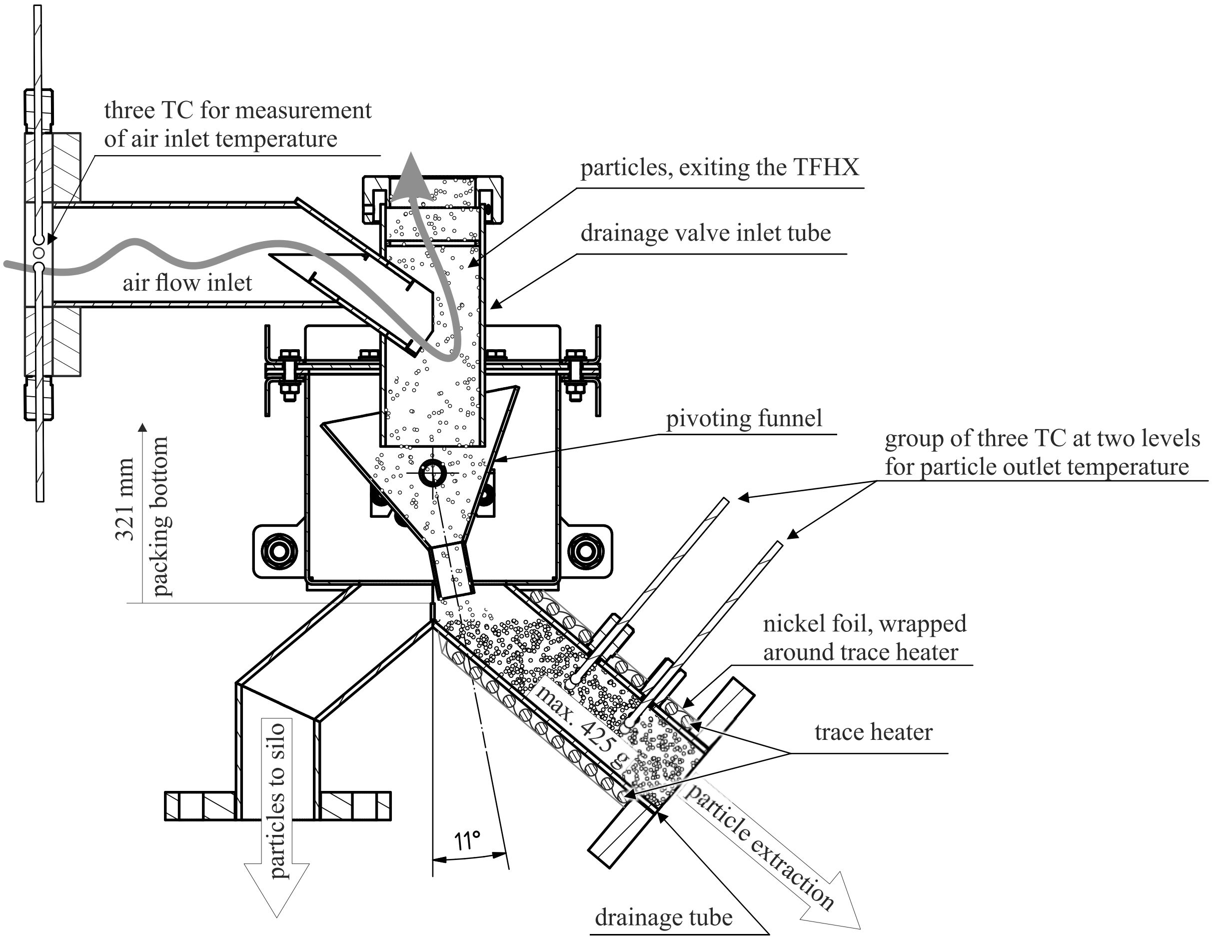

Fig. 20 Section view of particle drainage valve, see Fig. 19 ⑧.

Fig. 21 (left) shows the open drainage valve, without the tap, containing the piping for the incoming air and particles. Both pictures in Fig. 21 were taken from the back view of the system, which is why the pivoted funnel to the left is pointing toward the outlet into the particle silo. Fig. 21 (right) shows the drainage tube as the test stand is being assembled. Also, it can be seen the axe-flange assembly, which includes air seals located on the outside of the unit's insulation to provide air tightness to the pivoting drive shaft. In Fig. 20 and Fig. 21 (right), on the drainage tube, it can be seen the weld-in fittings for the installation of six thermocouples (TC) for the non-continuous measurement of the particle outlet temperature at two filling levels within the discharged particle mass. This will be relevant during the hot test in section 4.2. The electro-pneumatic actuation unit, which swivels the pivoting hopper in the valve, is not shown. The actuation unit will be explained in detail, e.g. in the determination of the uncertainty equations for the particle mass flow or the dynamic particle hold-up in the appendix, see A.3.

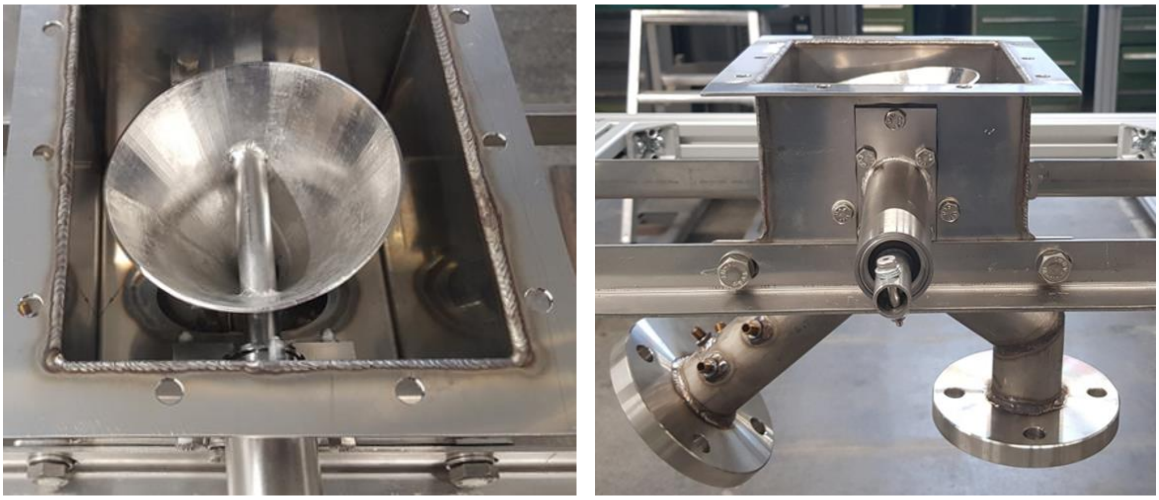

Fig. 21 Top view of the drainage valve (left) back view of the drainage valve (right).

Fig. 22 shows the main components of the cold experiments test setup with an exemplary packing structure assembled. During the cold experiments, transparent walls were installed to observe the particle flow behavior.

Fig. 22 Test setup structure for the cold testing procedure, showing the vertical HX channel with an assembled packing, the drainage valve on the bottom and the off-gas cyclone in the back.

4.1.1.1 Flexible installation of packing geometries in the test setup

A uniform particle density distribution is desired while the particles trickle downwards through the packing structure of the HX. As described in chapter 3 and demonstrated in previous work [147], horizontal packing layers with a number of equally spaced bar elements, n_{bar}, will be used to assemble the packing structure. The packing layers are stacked with staggered and non-staggered layers. In chapter 3, and in previous work [147] each packing layer was rotated alternately 90 °, to conduct the numerical assessment in accordance to packing arrangements in the available literature. The arrangement of the bar elements in this experimental chapter is chosen slightly different, see Fig. 23, by stacking one staggered and one non-staggered packing layer directly on top of each other and collinear aligned. This arrangement of two packing layers is repeated vertically by alternately rotating the group of layers 90° parallel to the axis of gravity. Like in the structure in chapter 3, after four packing layers, the sequence of layer repeats, and forms one packing unit (PU).

This arrangement was used for the experimental investigation, since it was observed qualitatively that the grains form particle curtains when falling from a non-staggered packing layer to a collinear aligned staggered packing layer. This mimics multiple times a zig-zag contactor, forcing the countercurrent flowing gas to pass the particle curtains, resulting in a high gas-particle interaction and hence high capabilities for heat and mass transfer [162, 163]. A further advantage of the used packing arrangement is that the probability of the trickling particles increases to hit a bar element in the packing layer below. This causes a decrease of the mean particle sink velocity in the packing structure, $\bar{u}_{\mathrm{p}}$, and conversely increases the dynamic particle hold-up, since β is proportional to $\bar{u}_{\mathrm{p}}^{-1}$, see (18).

The same labeling system as described in section 3.1 is applied to name the geometries uniquely. However, the pre-fix of the bar type will be omitted in this chapter, since only one bar type with a square or rectangular cross-sectional area will be investigated. Fig. 23 shows the labeling for an exemplary “w04 h04 n4 z10” packing geometry with rectangular bar elements.

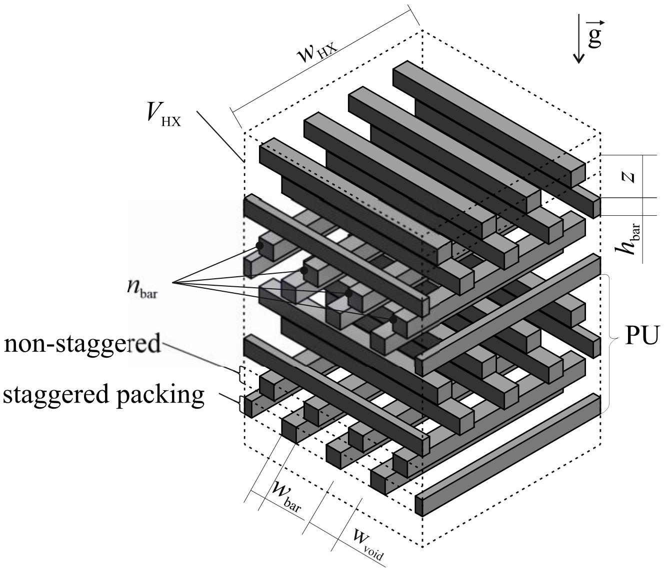

Fig. 23 Exemplarily packing arrangement, with geometrical parameters.

When designing different packing geometries, it has to be considered that the resulting void spacing between the horizontal bar elements in a packing layer, w_{void}, should not be chosen too small, to prevent the moving particles from clogging and flooding the HX with particles. As a rule of thumb, it is advised to design openings with at least 10-times the particle diameter to prevent particles from clogging [99]. During the experiments, it was observed, that for the setup in this work, a void spacing of 6 times the particle diameter also still provided reliable particle flow.

During the numerical pre-selection of packing structures, idealized packing geometries were designed and investigated such as depictured in Fig. 12. For the experimental tests, an assembly procedure was developed, allowing to install and assess different packing geometries. Fig. 24 and Fig. 25 shows an example of how an idealized arrangement of rectangular bar elements can be assembled in the experimental setup. Sheet metals (SM) with the thickness t_{sm} are laser cut to the desired width and number of bar elements per packing layer. The effective bar height, h_{bar}, for a certain packing geometry is the result of the number of staged sheet metal elements per packing layer, n_{sm}.

$$h_{\mathrm{bar}} = n_{\mathrm{sm}}\, t_{\mathrm{sm}} \qquad (28)$$

In the exemplary geometry, shown in Fig. 24 (middle and right), each packing layer consists of two packing SMs to provide a certain bar height. In order to hold the packing SMs at defined heights, empty frame SM of the same thickness, $t_{\mathrm{sm}} = 2$ mm, and the inner size of the cross-sectional area of the HX channel, $A_{\mathrm{HX}} = w_{\mathrm{HX}}^2$, with $w_{\mathrm{HX}} = 50$ mm were used. The packing SMs can be mounted flexibly in the developed holding arrangement tray support (TS), consisting of two plates with a number of 176 fins, n_{ts}, opposing each other with a vertical spacing of $h_{\mathrm{ts}} = 5$ mm. In total the HX-channel of the experimental setup provides a usable heat exchanger height of $h_{\mathrm{HX}} = h_{\mathrm{ts}}\,(n_{\mathrm{ts}} - 1) = 875$ mm.

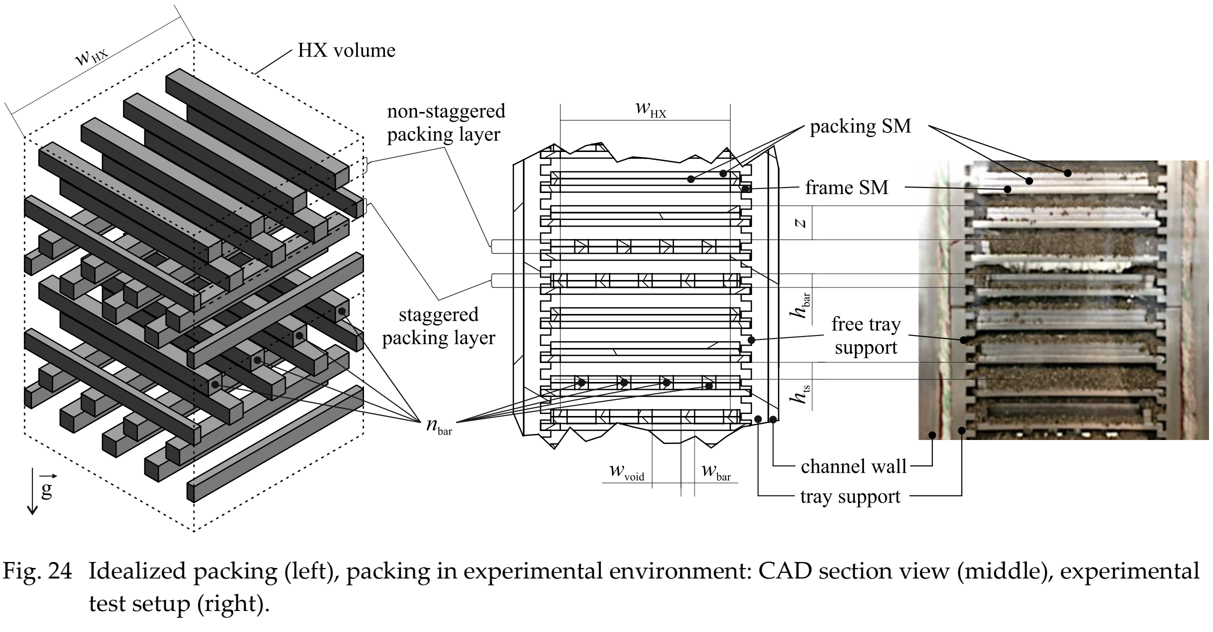

Fig. 24 Idealized packing (left), packing in experimental environment: CAD section view (middle), experimental test setup (right).

Fig. 25 Heat exchanger channel while assembling the “w10 h02 n3 z10” packing structure.

The particle falling height from one packing layer to the next layer below, z, can be selected in discrete steps due to the finned structure of the TS, where $n_{\mathrm{ts,f}}$ is the number of free TSs between two packing layers.

$$z = h_{\mathrm{ts}} \left(1 + n_{\mathrm{ts,f}}\right) \tag{29}$$

The same definitions as in section 3.1 apply to describe the geometrical parameters of the packing structure. Hence by inserting (28) and (29) the definitions of the void surface (5), the void volume (8) such as the effective packing porosity (6) and the packing porosity (9) can be updated and rewritten accordingly to the parameters of the test setup.

$$A_{\mathrm{void}} = w_{\mathrm{HX}}^2 - w_{\mathrm{HX}}\, w_{\mathrm{bar}}\, n_{\mathrm{bar}} \tag{30}$$

$$\epsilon_{\mathrm{eff}} = 1 - \frac{w_{\mathrm{bar}}\, n_{\mathrm{bar}}}{w_{\mathrm{HX}}} \tag{31}$$

$$V_{\mathrm{void}} = w_{\mathrm{HX}}^2\, h_{\mathrm{HX}} - \frac{w_{\mathrm{HX}}\, h_{\mathrm{bar}}\, n_{\mathrm{ts}}\, n_{\mathrm{bar}}\, w_{\mathrm{bar}}}{1 + n_{\mathrm{tf,f}}} \tag{32}$$

$$\epsilon_0 = 1 - \frac{n_{\mathrm{sm}}\, t_{\mathrm{sm}}\, n_{\mathrm{ts}}\, w_{\mathrm{bar}}\, n_{\mathrm{bar}}}{w_{\mathrm{HX}}\, h_{\mathrm{HX}} \left(1 + n_{\mathrm{ts,f}}\right)} \tag{33}$$

Fig. 26 View in the "w14 h02 n2 z10"-packing structure with static particles during cold testing.

Fig. 26 shows an exemplarily view of a w14 h02 n2 z10 during the cold testing procedure. The tray supports, the frame SM with the packing SM placed on top of it, such as the accumulation of static particles in the column.

4.1.1.2 Spatial particle density distribution

In section 3.2 the theory is outlined to measure the spatial particle density distribution. During the numerical simulation, in chapter 3, this method could be directly applied in the analysis. Unlike in the DEM, in the experimental analysis, a time discrete information of all particles within the packing structure is not available, why a simple, optical 2D measurement technique for the assessment of the spatial density distribution of dilute particle flow in a trickle flow reactor was developed, see A.4. This likewise, allowed the application of the definition of u_{rel} to evaluate the mixing quality of the particle flow within different geometries. To measure the spatial particle density distribution in different packing structures, additional measurements were conducted during the cold test campaign. Free observation areas without packing layers within the column had to be created to observe the particle flow. Therefore, transparent walls on the front and back side were installed. The particle flow in the observation area was filmed and analyzed for different packing geometries and varying media flow rates using a setup of a consumer digital camera with a 100 mm macro lens. Section A.4 in the appendix describes the corresponding measurement procedure.

4.1.1.3 Particle mass flow

Particle flow is measured discontinuously by discharging a mass flow of particles into the drainage tube for a defined period of time. This process can be performed with or without airflow in the system. In particular, when air flow is applied to the test bench, and in order to obtain accurate particle mass flow measurements, the extracted particle mass flow must be drained in the drain tube while the manual drain valve, see Fig. 19 ⑨ is closed to prevent erroneous air flow at ⑨ and to avoid shifting the equilibrium mass flow conditions within the test setup, which will influence the resulting particle mass flow, as explained below in this subsection.

When discharging particles in the closed drainage tube, special care must be taken to avoid flooding the drainage tube, which would cause some of the discharged particulate mass to flow into the particle silo. Thereby, not the complete drained mas of the solid flow would be recorded by measuring the extracted particle mass in the drainage tube, and an erroneous particle mass flow would be determined. Depending on the orifice plate used and the current air flow conditions, the drainage time for each particle mass flow measurement was iteratively adjusted so that the drainage tube was sufficiently but not excessively filled with particles. Ideally, the drained particle mass for the setup used in this work should be in the range of 350 g to 410 g for the solids flow measurement, since the maximum particle mass in the drain tube determined was 425 g, see Fig. 20. For each determination of the current particle mass flow, a repeated measurement of the drained particle mass was made five to eight times. For the determination of the particle mass flow, the measurement uncertainty was corrected according to the t-distribution, see A.3.2 and Tab. 18. Unless otherwise noted, all uncertainties of measurements made and presented in this work are reported with a confidence level of p = 95.0 % and were processed accordingly during the data analysis.

At the beginning of the present work, it was initially suggested that in order to change the particle mass flow rate, only the appropriate orifice plate, see Fig. 27, needs to be placed in the test rig at Fig. 19 ③ in order to provide a reproducible particle mass flow rate according to the previously determined and calibrated particle mass flow rate for all plates with different orifice diameters. However, it was found that especially the orifice plates with smaller diameters, close to the diameter where particle blockage is more likely to occur, show a high sensitivity to the applied air mass flow to the resulting solid flow rate passing through the orifice. It has been measured that this effect is further influenced when hot air is introduced into the test rig.

Fig. 28 shows the resulting particle mass flow for different orifice plates, with orifice diameters, ranging from 5.0 mm to 6.7 mm. Different airflow rates were applied at ambient conditions and at 450 °C air inlet temperature while the resulting particle mass flow was measured. Fig. 28 (top right) illustrates how, for air at ambient conditions, the measured particle flux decreases with increasing air flow. This effect is more pronounced for smaller diameter orifices. For some airflow rates, the particle flow even stops, such as for the 5.0 mm orifice at $\dot{m}_a = 17$ kg/h. No normalized airflow rates are used in Fig. 28 because it is assumed that this is a very small scale effect that could be neglected for larger orifice diameters. Performing the same experiment at an air inlet temperature of 450 °C shows a further reduction in the measured particle mass flow at higher air flow rates. Only particle mass flows up to $\dot{m}_a = 17$ kg/h could be measured reproducibly, for higher values of $\dot{m}_a$ the particle flow stopped for the diameters shown. Fig. 28 (left) shows a direct comparison of four orifice diameters and the measured particle flow for varying air flow rates and the two different air inlet temperatures.

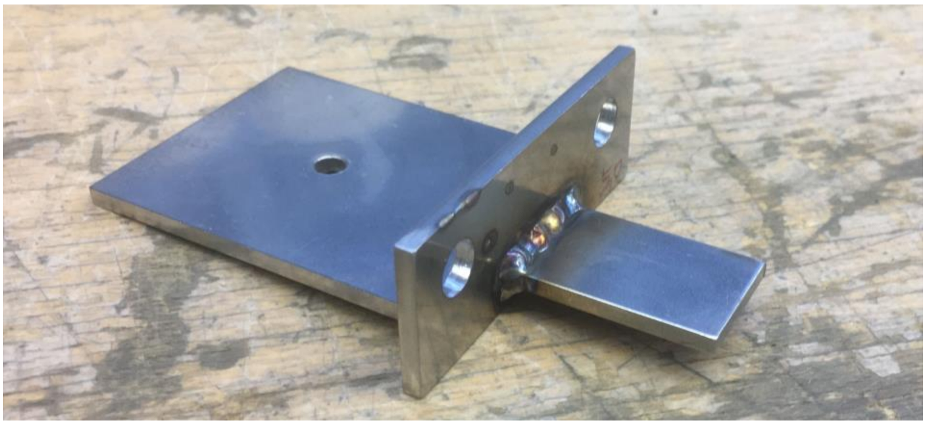

Fig. 27 Orifice plate with exemplarily diameter of 5.0 mm, to adjust particle mass flow rates.

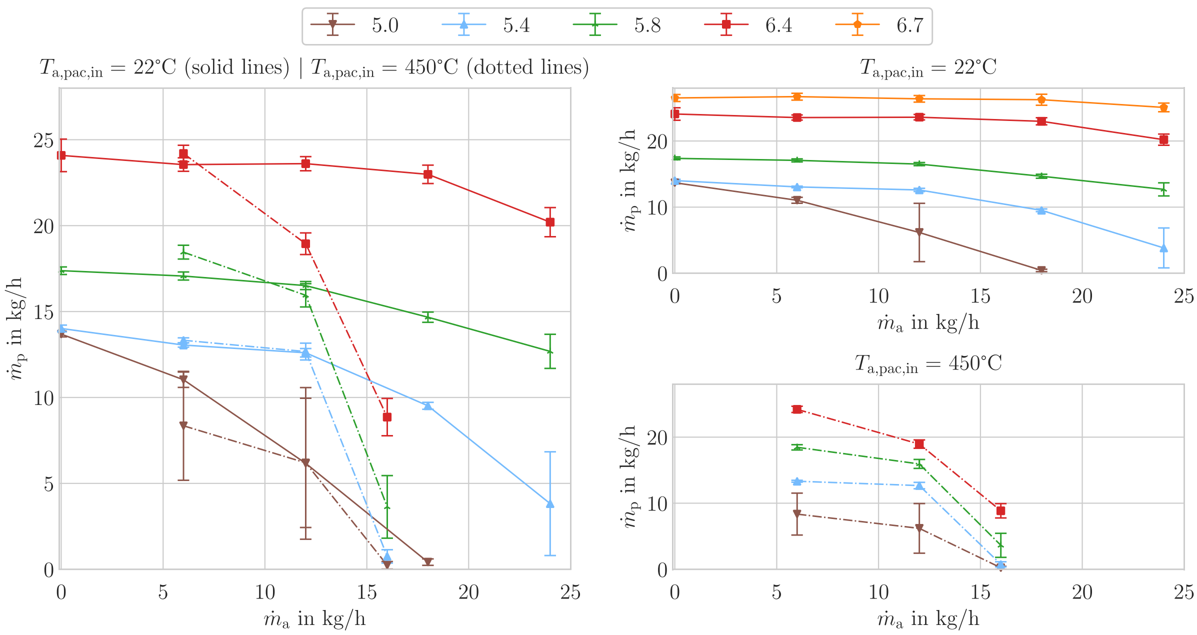

Fig. 28 Measured particle mass flows for different orifice diameters at varying air flow for two different air inlet temperatures.

This observed effect is not yet fully understood and is not the focus of this work. However, it is mentioned to demonstrate that in order to obtain a given particle mass flow at a given airflow rate and air inlet temperature, the orifices would have to be installed and tested experimentally, iteratively, and individually until a desired flow condition is obtained.

4.1.1.4 Particle hold-up

The measurement of the particle hold-up in packing structures can be performed using optical approaches with tracer particle detection [125, 164]. By using tracer particles, the average time for the particles to pass through the packed column can be determined, and conversely, the averaged particle sink velocity, $\bar{u}_{\mathrm{p}}$, can be determined and used in (19) to calculate the dynamic particle hold-up. An alternative, mechanical approach is to take a " snapshot" of the particle cloud currently trickling within the void fraction of the column [60, 114, 123, 128, 131, 135]. The latter is used in this work because it is expected that resting particles on the chosen rectangular packing structures would mix with the tracer particles and thus falsify the measurement procedure.

Once steady state conditions were reached within the packing structure, the measurement of the dynamic particle hold-up was performed, by simultaneously closing the particle inlet valve and opening the particle drainage valve, see Fig. 19 ④ and ⑧. This will stop the flow of particles into the packed column at ④, and a snapshot of the trickling particles will be taken and directed at ⑧ into the drainage tube, which is hermetically sealed by the manual drainage valve, see Fig. 19 ⑨. By opening the same valve ⑨, the collected particles can be drained from the system.

While the before mentioned literature, using the same mechanical measurement method, mentions to stop the air flow during the hold-up measurement, it was found to be advantageous, if the gas flow is not stopped. In the setup of this work, it was observed that for gas flow rates of $\dot{m}_{\mathrm{a}}^{\#} > 1\,\mathrm{kg/(s \cdot m^2)}$, the static particles resting on the bar elements begin to be blown off the bar elements. This resulted in a in a desaturation of the static particle piles within the packed column. If the gas flow would have been stopped during the hold-up measurement, the trickling particles would not be completely drained, as some particles would partially rain down and remain on the desaturated packing structure. Therefore, it was decided to keep the air flow on. This measurement method should be explicitly considered for packing structures that allow the accumulation of static particles.

It is assumed that the drained solids during the mechanical hold-up measurement represent the total amount of particles contributing to the dynamic particle hold-up. It can be expressed by the volume of drained particles, $V_{\mathrm{p,pac}}$, normalized to an appropriate reference volume. In the literature, the particle hold-up is typically normalized to the packing void volume, V_{void}, see (19). However, as described in section 3.3 the extended particle hold-up, β^*, is used in this work to evaluate and compare different packing structures.

For each measurement of the particle hold-up, the corresponding uncertainty is determined. According to (19), the uncertainty of the particle hold-up, u_β, was derived for u_{β^*} (21). Further details on the derived measurement uncertainty of the particle hold-up can be found in the appendix in section A.3.7. There also the measures are described to analytically compensate for the erroneously additional drained particles. The particle "snap shoot" of the hold-up measurement additionally captures a fraction of the particle mass outside the packed column that is currently within the vertical distances above and below the packed columns and the actuating valves. Verver and van Swaaij [114] estimate that at least 80 % of the drained particle mass is represented by the trickling particle cloud within the column, why thy assume that the rest of the additionally drained solid mass, that resided within the before mentioned vertical distances, can be neglected. However, in this work, efforts were undertaken to analytically address and compensate for the effects of the additional particle mass within the falling heights above and below the TFHX, which is why the distances in Fig. 19 from ④ to ⑦ and from ⑦ to ⑦ considered with their effects on the additionally drained particle mass, see section A.3.8.1. Also, the closing times of the actuating valves and their influence on the drained particle mass, such as the uncertainties of the packing geometry, were considered and outlined in the same section.

4.1.2 Testing of different packing structures for a trickle flow reactor

The test rig described in section 4.1.1 was designed with great emphasis on being able to assemble a wide variety of different packing structures. In order to identify a packing geometry for the given particle type, that is most capable of providing a high dynamic particle hold-up at a good spatial particle density distribution in the column void volume, three types of experiments were performed, see Tab. 8. The numerical study in chapter 3 provides the initial starting point for the first experiments, where packing geometries based on the numerically investigated geometries were installed in the test rig. Like in chapter 3, for a first pre-selection these tests were performed only with particle flow but without gas flow. Based on this experiment, a set of packing geometry was identified and refined, that formed the base for the second test campaign, where alongside to the particle flow, also air flow was included into the experiments, to identify the maximum operation conditions of the packing structures, such as "flooding". The series of measurements was concluded with a qualitative evaluation of the spatial particle distribution using the optical measurement method described in the sections 4.1.1.2 and A.4.

Tab. 8 Overview of conducted cold experiments for the qualification of packing structures.

Experiment	Identification of…	Varied	Constant
Comparison of different packing geometries without gas flow	packing with highest hold up	packing structures	particle flow no air flow
Comparison of different packing geometries with gas flow	packing with highest hold up	packing structures air flow	particle flow
Comparison of particle density distribution in packing structures	packing, providing most even particle distribution	packing structures air flow	particle flow range

4.1.2.1 Comparison of different packing geometries without gas flow

For the following comparison of different packing geometries, a particle mass flow rate of $\dot{m}_\mathrm{p}^{\#} = 2\ \mathrm{kg/(s \cdot m^2)}$ was used. This flow rate was derived for the case of the air superficial velocity in the empty HX duct matching the particle sink velocity at the envisioned operation temperatures of approximately 900 °C: $\dot{m}_\mathrm{a}^{\#} \approx 4\ \mathrm{kg/(s \cdot m^2)}$. Applying this criterion within the void spaces of the packing layers by assuming $\epsilon_\mathrm{eff} \approx 0.5$, the limiting air flow reduces accordingly to $2\ \mathrm{kg/(s \cdot m^2)}$. Like mentioned in section 3.6, equal heat capacity flowrates of the air and the solid flow are preferred, $\dot{W}_\mathrm{r} \approx 1$, why simplified equal media flow rates can be assumed.

The measurement campaign was initiated with resembling structures to the geometries investigated in chapter 3 by measuring the particle hold-up's for different design configurations of width, height, number of bars and falling height, shown in Fig. 29. Using the particle hold-up normalized to V_void, the figure shows a relatively high value of β for "w12 h12 n3 z15", which can be explained by the relatively low void volume compared to the other evaluated structures. This underlines the in section 3.3 mentioned approach to compare different packing structures on the same basis, such as V_HX, and to use β^* instead of β.

Furthermore, "w12 h12 n3 z15" shows a notable high uncertainty in the measured hold up. This can be explained by the way the packing structure is installed in the test rig. By assembling the mentioned geometry along the height of the heat exchanger channel, a relatively high number of sheet metal plates, n_sm, is needed to generate the desired bar height of 12 mm along h_HX. For the determination of the uncertainty of the packing void fraction, the large number of plates and their individual manufacturing, such as assembly, uncertainties accumulate according to (32). The sensitivity analysis for u_β, see (170), applied to the "w12 h12 n3 z15" packing, shows a dominant relative variance for the fraction of the packing geometry of 82 % see (34). This further confirms the approach of using the extended particle hold-up to compare the hold-up behavior between different packing geometries.

$$\left[\left(\frac{\partial \beta}{\partial \epsilon_0}\right)\frac{u_{\epsilon_0}}{u_\beta}\right]^2 = 82\ \% \tag{34}$$

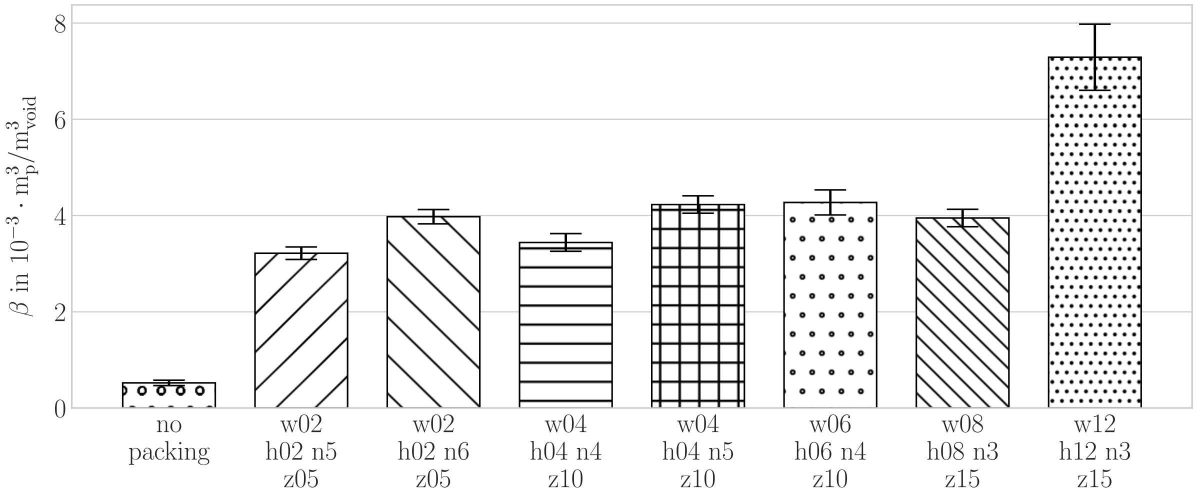

Fig. 29 Initial measurement of particle hold-up; particle flow 2 kg/(s · m²).

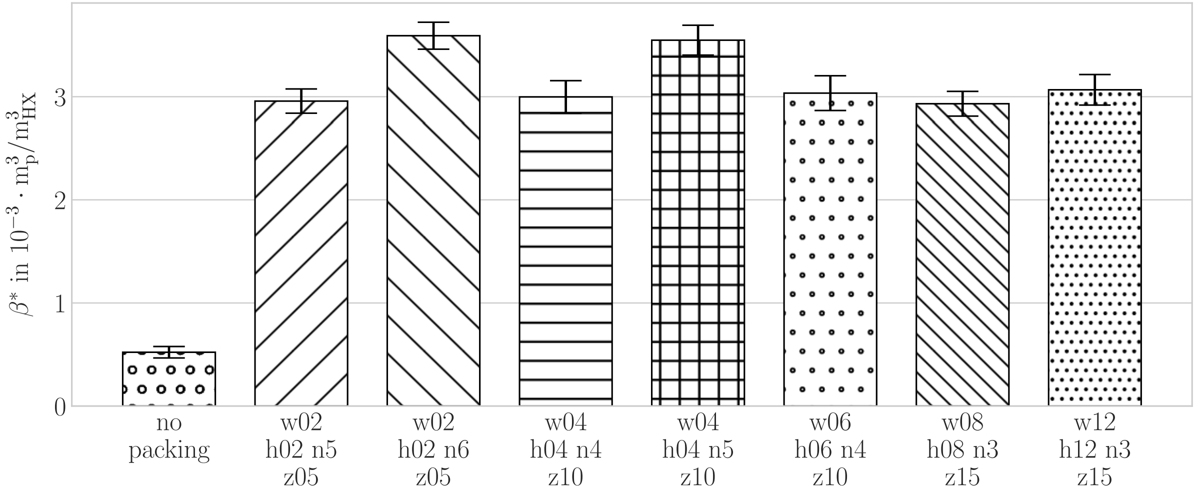

Fig. 30 Initial measurement of extended particle hold-up; particle flow 2 kg/(s · m²).

Fig. 30 shows the same initial geometry set as in Fig. 29 with the extended particle hold-up applied. All structures provide an extended hold-up in the range from $3 \cdot 10^{-3}$ to $3.5 \cdot 10^{-3}$ This relatively narrow band of β^* however spreads over a relative wide range of geometric changes, such as bar-width, -number, -height and also the vertical falling distance, z.

To further increase the particle hold-up, additional packing structures were investigated by assembling geometries with the smallest possible vertical spacing, z, and bar height, h_bar. Fig. 31 shows the measured hold-up for packing geometries with the smallest possible vertical spacing that can be installed in the designed test rig. By reducing the number of sheet metals per packing layer to $n_\mathrm{ts} = 1$, the vertical distance can be further reduced to z = 5 mm for a large number of investigated packings. In addition, for some of these structures, the hold-up was measured for an increased falling height of z = 10 mm, while the “w10 h02 n03”, “w12 h02 n03” and “w14 h02 n2” packings could only be measured with a greater vertical distance, since at z = 5 mm particle blocking occurred immediately, causing the entire column to flood with particles.

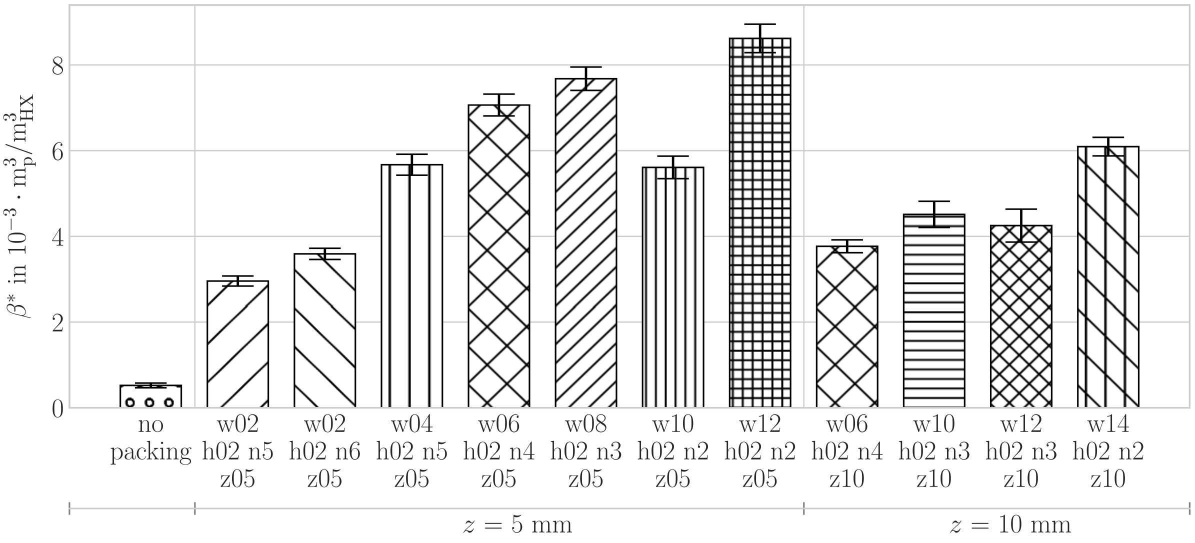

Fig. 31 Extended particle hold-up, with lowest bar height h02; particle flow 2 kg/(s · m²).

Fig. 31 illustrates that packing structures with a relatively high number of bar elements per packing layer ($n \geq 5$) for the investigated setup do not lead to a higher particle hold-up than those with a lower number ($n < 4$). Very narrow structures represented by “w02 h02 n5 z05” or “w02 h02 n6 z05” provide a relatively low particle hold-up. The hold-up increases as the bar width increases, while the number of bars is gradually reduced to keep the void distance large enough to prevent particles from blocking. Also, the assumption in a previous work, that a resting particle pile up on the packing structure reduces the mean particle sink velocity [147], can be strengthened. During the experiments, it was observed that a resting particle pile on the packing surface composed of more than one particle layers has the potential to absorb and dissipate the kinetic energy of the trickling grains, causing a further reduction of the particle sink velocity, and conversely, increasing the dynamic particle hold-up. Accordingly developed particle piles were observed for bar widths of $w_{\text{bar}} \geq 6$ mm.

4.1.2.2 Comparison of different packing geometries with gas flow

Based on the results shown in Fig. 31, additional countercurrent gas flow tests were conducted with packing geometries ranging in bar widths from 6 mm to 14 mm and a correspondingly adapted number of bars. Fig. 32 depictures the measured hold-ups for varying gas flow rates within the different packing geometries.

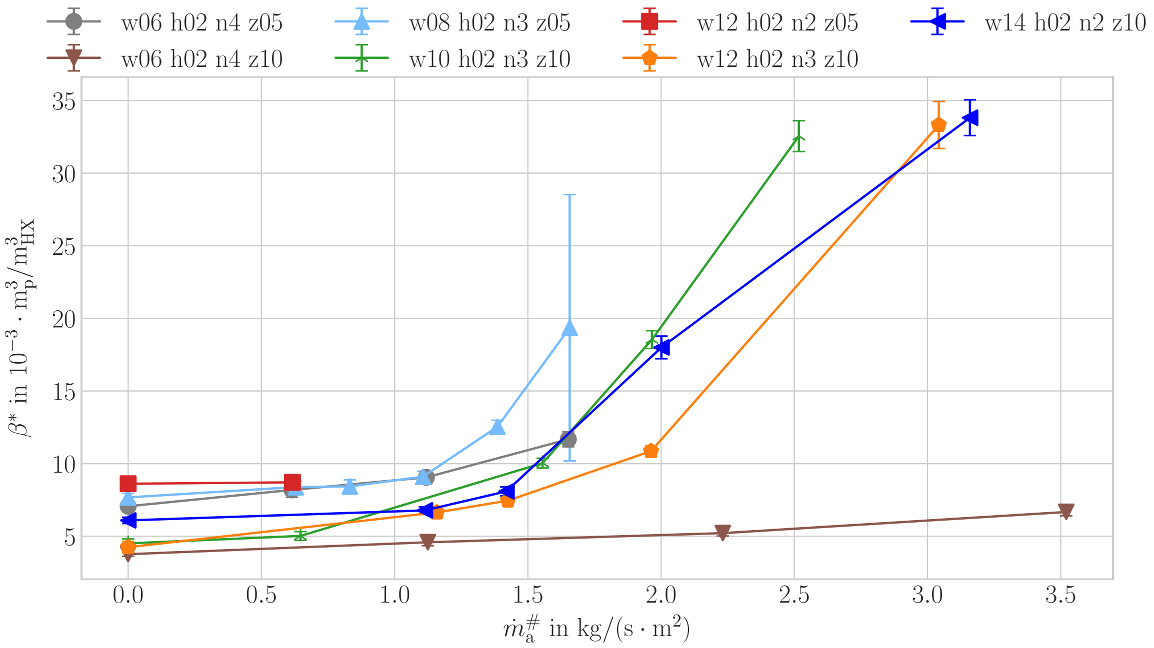

Fig. 32 Extended particle hold-up vs. gas flow for varying geometries; particle flow 2 kg/(s · m^2).

With increasing gas flow rates, the measured hold-ups increase until flooding occurs. The transition of the particle flow regime, where flooding of particles within the packing void occurs, can be observed in a steep increase of β^* with $\dot{m}_\mathrm{a}{}^\#$ accompanied by a high relative uncertainty of the measured data points. The w08-packing shows a relative uncertainty of $u_{\beta^*} = 19.7\,\%$ for the highest measured value of β^* indicating the particle hydrodynamics being close to flooding, while typically u_{β^*} rarely exceeds 3.5 % for measurements sufficiently far from the flooding point. The heat capacities of the particles and the air provide a ratio above the average temperature range of interest of $c_{p,\mathrm{a}}/c_{p,\mathrm{p}} \approx 1.2$. Simplified, the ratio can be assumed as equal. Or a preferred operating condition of the TFHX with equal heat capacity flow rates, stable operation is preferred hence for equal media flow rates: $\dot{m}_\mathrm{a}^\# \approx \dot{m}_\mathrm{p}^\# = 2\,\mathrm{kg/(s \cdot m^2)}$. The packing structures with vertical falling distances of $z = 5$ mm cannot be operated up to this airflow without the occurrence of flooding. This was observed for the packings “w12 h02 n2 z05”, “w08 h02 n3 z05”, and “w06 h02 n4 z05”, where no measurement for β^* could be performed for gas flow rates above 0.6 kg/(s · m^2) and 1.6 kg/(s · m^2), respectively. By increasing z to 10 mm, the measured hold-ups are reduced. This was already illustrated in Fig. 31, as the particles can accelerate to higher falling velocities due to the increased vertical distance between the packing layers. The geometries “w10 h02 n3 z10”, “w12 h02 n3 z10”, and “w14 h02 n2 z10” exhibit stable flow conditions for the preferred air flow rate and beyond, from those the w10-packing provides the highest particle hold-up. The w12-packing shows similar hold-up performance up to 2 kg/(s · m^2) air flow, while the w14-type provides the lowest retention of trickling particles in the HX.

4.1.2.3 Comparison of particle density distribution in packing structures

The three last mentioned geometries provide all good particle retention. To further identify the most suitable packing structure, the mixing quality of the packing “w10 h02 n3 z10” and the packing “w14 h02 n2 z10” was directly compared. Therefore, in separate experiments, see A.4, observation areas in the packing structures were created and videos of the particle flow with different air and mass flow rates were recorded to determine the relative linear particle distribution, u_rel, described in section 3.2.

Tab. 9 Resulting particle mass flow rates in $\mathrm{kg/(s \cdot m^2)}$ for different orifice diameter and air flow rates.

	orifice diameter in mm		
air flow in $\mathrm{kg/(s \cdot m^2)}$	5.0	5.6	6.4
0	1.5	1.9	2.7
9	0. 6	1.4	2.3

Fig. 33 shows the corresponding values of $\bar{u}_{\mathrm{rel}}$ for each packing at varying flow conditions. Air mass flow rates ranging from $0\ \mathrm{kg/(s \cdot m^2)}$ to $9\ \mathrm{kg/(s \cdot m^2)}$ were investigated. In addition, three orifice plates with different diameters were installed to obtain different exemplarily particle mass flow rates for the measurements. As outlined in section 4.1.1.3, it was observed that for one orifice plate the resulting particle mass flows are not constant, but decrease with increasing air mass flow rates, see Tab. 9. Accordingly, only ranges of particle mass flows can be provided for the results in Fig. 33.

The origins of this observation are not yet fully understood and will be investigated in more detail in future work. What can be observed is that a narrower orifice, with a diameter closer to a critical diameter where particle blocking is more likely to occur, shows a greater sensitivity to an increased air flow of the resulting particle mass flow.

Fig. 33 shows that a packing structure with an increased bar width of 14 mm results in a measurable deterioration of particle mixing quality. The effect of increased particle shaded areas was measured. For both packing structures an enhancement of particle mixing with increasing air flow was observed for air flow rates beyond $4\ \mathrm{kg/(s \cdot m^2)}$. By surpassing flow rates of $8\ \mathrm{kg/(s \cdot m^2)}$ and thus entering the range of the particle terminal velocity at ambient temperature, the hydrodynamics of the particles start to change from a trickling state to a fluidized state, resulting in mixing qualities close to ideal stochastic uniform mixing. Since the blower used in the presented setup was not able to provide higher air flow rates than $9\ \mathrm{kg/(s \cdot m^2)}$, no data for air mass flow rates higher than this is available.

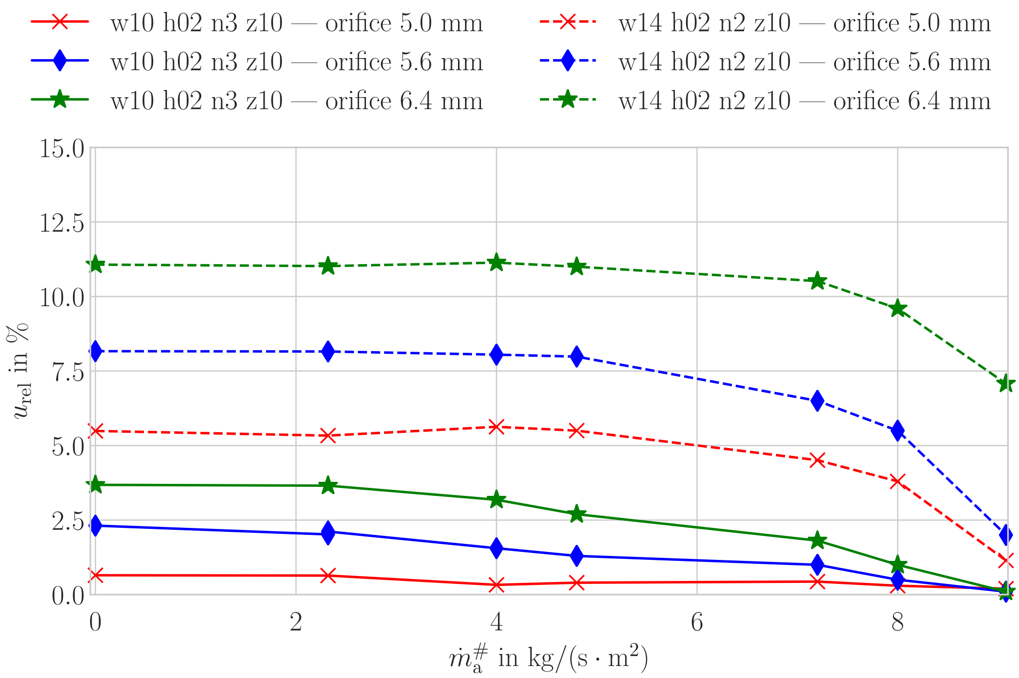

Fig. 33 Relative, linear particle distribution in two packing geometries, for varying air and particle mass flow.

By assessing the particle hold-up and the particle distribution in all conducted experiments, the „w10 h02 n3 z10" packing structure was identified to be the most suitable geometry for the chosen setup. It provides the desired requirements of the particle hydrodynamic for the used particles within a TFHX and will be used in further hot test to evaluate the heat transfer performance of the system.

4.1.3 Conclusive discussion of the identification of a packing geometry

Experimental cold tests were conducted with the objective of identifying a packing geometry that would provide high particle hold-up at stable flow regimes for a trickle flow heat exchanger. A further selection criterion was uniform particle distribution within the void space. The results in chapter 3 showed that it is advantageous to use packing structures consisting of regular arrangements of rectangular bar elements. Subsequently, the test setup described before was developed to investigate different packing geometries under varying media flow conditions. The extended particle hold-up, β^*, was used to compare the different columns. It was shown that the particle hold-up decreases as the vertical falling height between two successive packing layers increases. In addition, it was observed that a small bar width and a high number of bars do not result in a higher dynamic particle hold-up. For the particles in question, bar widths of 6 mm and above were found to be beneficial in providing sufficient width to accumulate a pile of static particles capable of absorbing the kinetic fall energy of the trickling particles, thereby reducing the mean particle settling velocity and conversely increasing the dynamic particle hold-up. However, the bar width should not be chosen too wide to avoid the influence of particle shadowing, which would result in a reduced quality of the spatial particle distribution. A packing structure with $w_{\mathrm{bar}} = 10$ mm, $h_{\mathrm{bar}} = 2$ mm, $n_{\mathrm{bar}} = 3$ and $z_{\mathrm{bar}} = 10$ mm was found to be most suitable for the described experimental conditions. This geometry provides stable operating conditions and the highest dynamic particle retention within the desired media flow rates with a relatively uniform spatial particle density distribution. In addition, the pressure drop can be considered as relatively low and a correlation of the pressure coefficient has been derived experimentally for the identified packing structure, see section 4.2.2.6.

4.2 Experimental investigation of a trickle flow heat exchanger

The following section outlines the hot testing of the previously identified „w10 h02 n3 z10" packing structure. The influence of varying air and particle flow rates, including different media inlet temperatures, was used to determine the heat transfer performance of the developed TFHX.

4.2.1 Experimental setup

The hot tests were performed in a modified version of the test setup presented in section 4.1.1. At the beginning of the design of the test rig, great emphasis was placed on the design, construction and selection of materials that would be able to withstand not only the cold tests, but also the later planned operation at higher temperatures, according to the requirements defined in section 2.2.1. Therefore, only a few additional modifications to the setup were required to perform the hot tests.

4.2.1.1 Upgrading the test bench for hot testing

To upgrade the test bench described in section 4.1.1, 100 mm thick insulation and additional monitoring TCs were installed, such as replacing the previously used transparent channel walls with metal plates. Fig. 34 shows an image of the test rig modified for the hot test campaign. In the center is the insulated packed column containing the "w10 h02 n3 z10" packing. Below, the drainage valve is located and from the left the air inlet section enters the system. The multiple TCs exiting laterally from the insulated column are partially temperature measurement points to monitor the temperature at different levels within the heat exchanger, but also within the insulation, see Fig. 74. The TCs installed within the column are not designed to measure the grain or gas flow temperature. A TC within the HX would measure a mixed temperature of both media. TC shielding elements or baffles would have to be placed within the column to separate the media flow at the temperature measurement point and determine only the particle or air temperature. However, it was decided not to do this as the additional elements would significantly disturb the packing composition in the 5x5 cm channel width and therefore negatively affect the particle flow. Therefore, it was decided to measure the media temperatures only at the inlet and outlet, where the two media are completely separated. The TC elements placed in the insulation are assigned to opposing groups of three TCs that measure the temperature under, between and on the surface of the insulation at four different levels along the height, see Fig. 74.

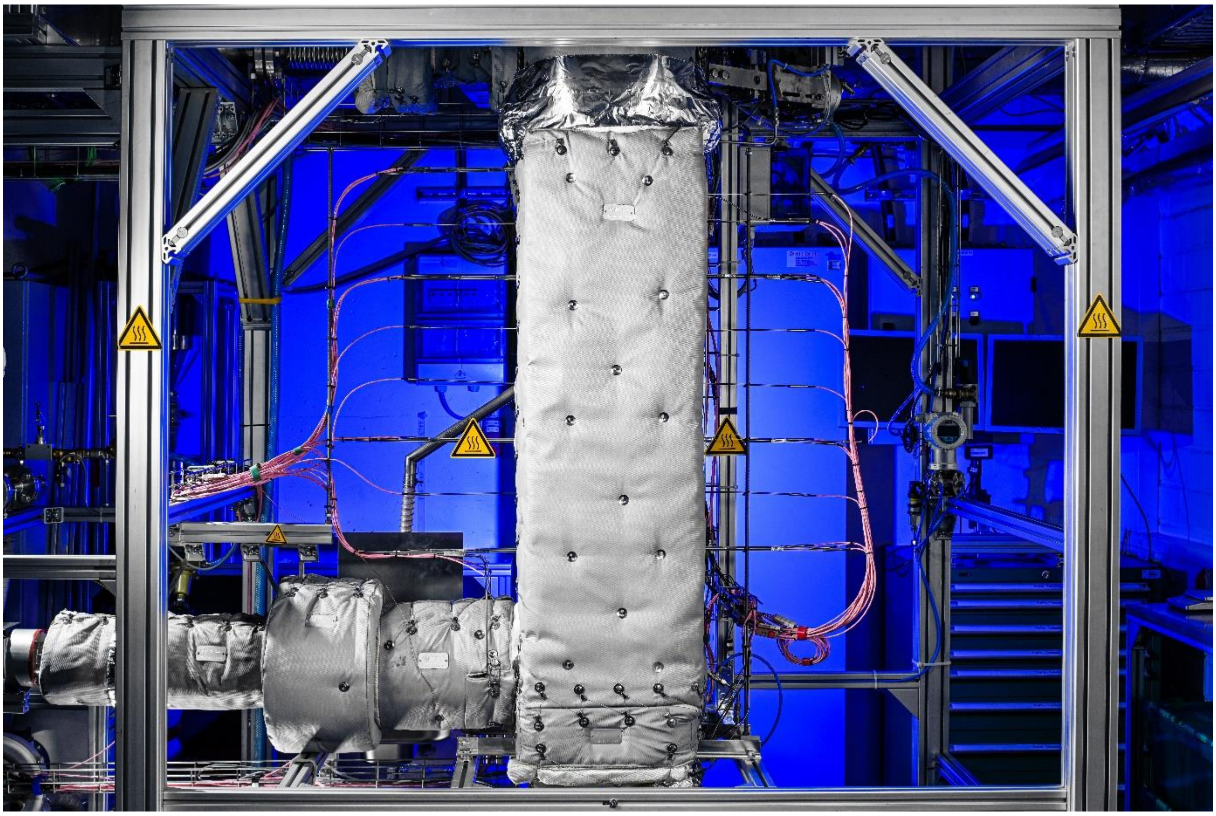

Fig. 34 Trickle flow heat exchanger test setup, modified for the hot test campaign.

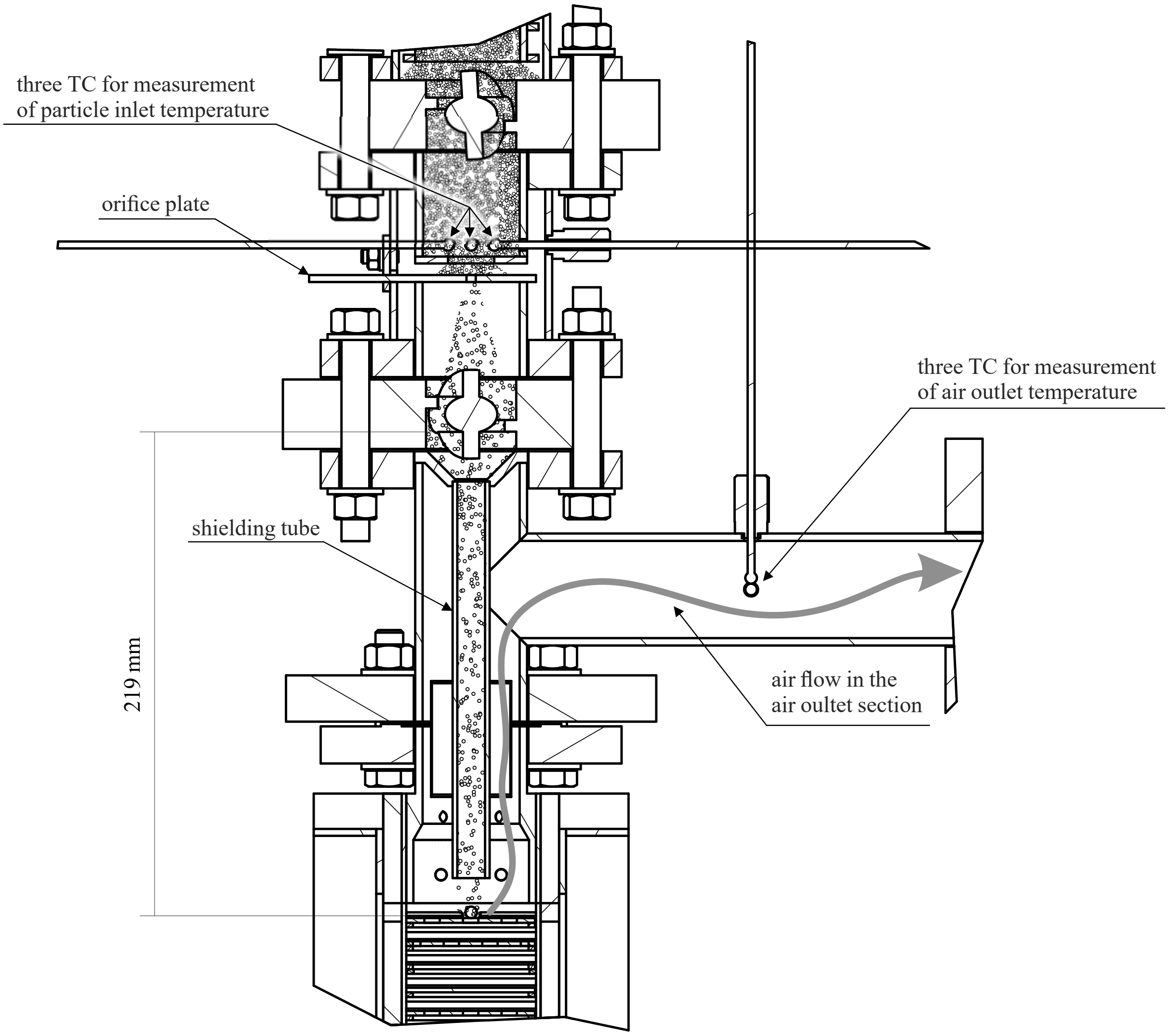

Fig. 35 CAD cross view from the particle inlet and air outlet section.

4.2.1.2 Temperature measurement

All installed temperature sensors were continuously measured and recorded during all test procedures. Fig. 19 shows the positions of the temperature measurements for the entering and exiting medias. The particle temperatures are measured in the particle bulk. For the particle inlet temperature, three TCs are placed at the last possible position where the solid feed is available as a bulk. This is just above the orifice plate, see Fig. 19 ② that dams the grain flow to a moving bulk. Fig. 35 shows a cross-view of the particle inlet and air outlet section, illustrated as CAD model. Three TCs for measuring the particle inlet temperature are placed in the moving particle bed slightly above the orifice plate where the particle begins to fall freely toward the packed bed. The particles pass through the particle inlet valve, see Fig. 19 ④, and are guided by the shielding tube to the top of the TFHX. The shielding tube is designed in the inlet section to prevent direct contact with the exiting air stream. As a result, gas-particle interaction between the air leaving the packed bed and the particles falling from the orifice plate toward the column is expected to be low. By installing the shielding tube, the resulting temperature change from the measuring TC for the particle inlet temperature to the top of the packed column was assumed to be negligible. Furthermore, the shielding tube has the additional purpose of preventing the incoming particles from being partially blown out vertically by the outgoing air stream towards the separation or off-gas-cyclone, see Fig. 19 ⑤. There, any entrained small particles or dust are separated from the air stream. The gas temperature of the exiting air was measured with three redundant TCs in the exhaust tube leading to the exhaust cyclone, see Fig. 35.

Fig. 20 shows the similar temperature measurement approach at the bottom of the TFHX test setup. The air inlet temperature is measured by three redundant TCs in the air inlet section before the air contacts the particle in the drainage valve. Particles exiting the packed column enter the inlet tube at the top of the drainage valve, where the airflow also enters laterally and contacts the free-falling particles for a short distance of approximately 7 cm. The falling particles pass through the inlet tube of the drainage valve and are directed by the funnel by default into the particle silo. For measurements of particle mass flow, see 4.1.1.3, the particle hold-up, see 4.1.1.4, or the particle outlet temperature, the funnel swivels toward the drainage tube to separate the particles from the system.

The concept of an overflow funnel is used in the literature to measure particle outlet temperature [165]. A funnel is placed in a falling particle curtain where the particle flow exiting the funnel at the bottom is lower than the collected solid flow at the top of the funnel, causing the device to overflow with particles and creating a moving particle bed within the funnel. Within this moving particle bed, TC can be placed to measure the bulk temperature and therefore the particle temperature can be inferred. Another indirect method to measure the particle outlet temperature of a TFHX is mentioned by Large, Guignon [130]. They mention that separate temperature measurement of the gas and particle phases is quite difficult due to flow instabilities in dilute two-phase flows. Therefore, they place a fluidized bed below the packed column. The entering gas flow, as well as the exiting particle flow of the fluidized bed can be determined in its flow rate and temperature, such as the mixing temperature of the FB. Thus, by balancing the fluidized bed and applying the energy balance, the particle temperature of the grain flow exiting the TFHX and entering the FB can be determined by the known variables. Both approaches offer the possibility to continuously measure the particle exit temperature. However, both approaches were not applied in the test setup because a properly designed overflow funnel for the selected particle type would not fit into the cross-sectional area of the test bench, and the installation of a FB below the test setup could not be integrated due to the limited ceiling height available in the workshop. Furthermore, since only steady-state conditions were of interest in this work, continuous measurement of particle outlet temperatures is not necessary to characterize an HX. Therefore, a non-continuous method was developed to determine the particle outlet temperature. Therefore, as for the measurement of the particle mass flow in section 4.1.1.3 , the discharge tube is flushed with particles and the TCs shown in Fig. 20 are immersed in the discharged mass to measure the particle outlet temperature. Two groups of three redundant TCs were installed at two levels within the drain tube to detect if potentially not enough particle mass is being drained. This can be detected immediately by observing the average temperature of the two TC groups in the outlet tube for temperature differences of more than 5 K.

As mentioned before, the interaction time between the particles exiting the column and the air entering the drainage inlet tube and flowing upward to the bottom of the column is relatively short. In addition, the further falling distance of the particles through the pivoting funnel shields and isolates the particles, as does the shielding tube in the inlet section, from further temperature exchange. Why simplified it is assumed, that the temperature change of the particles leaving the packing to the drainage tube is neglectable. In order to prevent temperature losses of the extracted particle bed through the wall of the drainage tube, its insulation and to the surrounding environment, which would falsify the measured particle temperature, a trace heating element was attached to the outside of the discharge tube to compensate for thermal losses of the particle outlet temperature measurement, Fig. 20 and Fig. 36. The trace heater is wrapped around the outside of the drainage tube. In addition, nickel foil covers the heater to reflect heat radiation to the inside of the tube, increasing heating efficiency and improving uniform temperature distribution of the electrical heater. The temperature of the heater is set and controlled in a separate power unit by an additional trace heater control TC located directly on the heater under the nickel foil, see Fig. 36. The additional impact of the trace heater on the measured particle temperature can be neglected as described in the following measurement procedure.

The determination of the particle outlet temperature was combined with the measurement of the particle mass flow, see section 4.1.1.3. For both measurements, the drainage tube must be flooded with a particle mass with approximately 400 g of particles. While the drainage time and the drained particle mass are used to determine the particle mass flow, the TCs are used to determine the particle outlet temperature. This method had to be applied iteratively by adjusting the trace heater to the estimated particle outlet temperature. If the drained particle mass was hotter than the estimated heating temperature of the trace heater, an initial temperature peak of the TCs in the drainage tube could be observed, see Fig. 37 a). Conversely, if the set point of the trace heater was assumed to high, the TC in the drainage tube showed an initial temperature drop when the drainage tube was flooding with particles, see Fig. 37 b). The heating element was adjusted to the correct heating extend, when the thermocouples within the drainage tube didn’t detect a change of temperature during the process of flooding of the drainage tube with hot particles, see Fig. 37 c). This indicates that only the heat losses to the environment were compensated by the electrical heating, but no additional thermal energy was added to the drained particles.

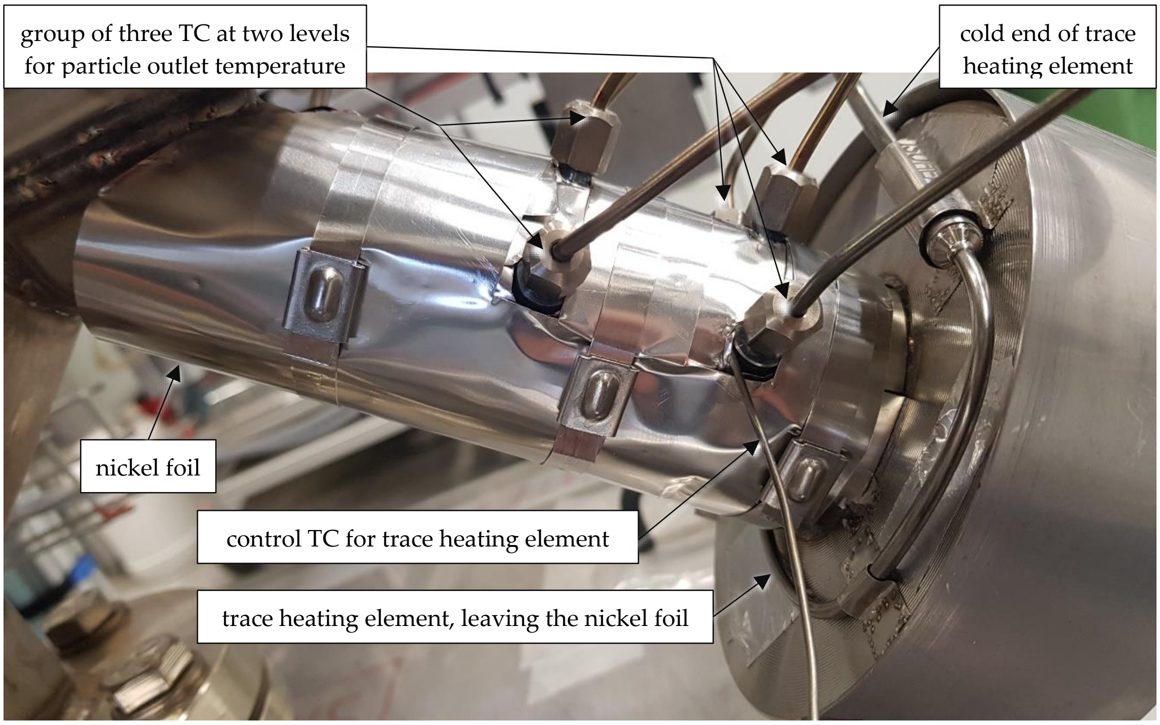

Fig. 36 Drainage tube, without insulation, with the nickel foil assembled, covering the trace heating element.

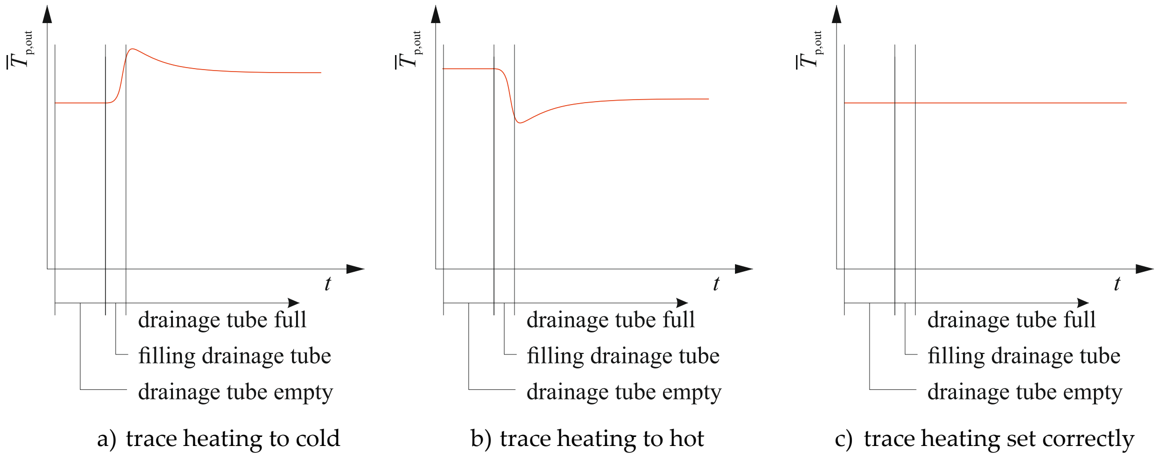

Fig. 37 Temperature development of TC, when draining particles in the drainage tube, depending on different status of trace heating conditions.

Each inlet and outlet temperature measurement was made by a group of redundant TCs as described. The corresponding mean value and the deviation of the measurement uncertainty of the temperature measurement are described in the appendix in section A.3.7. Furthermore, it was outlined before that the temperature determination of the particles entering and leaving the packed column and the potential falsification of thermal losses due to the described particle free fall sections, see Fig. 20 and Fig. 35 , were assumed to be negligible by technical measures. Also, the gas has to flow a certain distance between the packed column and the corresponding measurement positions in the air inlet and outlet sections, it was expected that these thermal losses cannot be neglected, since along the mentioned distances it must be assumed that the air has a high interaction with the walls, causing thermal losses to the surroundings and thus falsifying the determination of the air inlet and outlet temperatures at the packing. Therefore, the influence on the temperature change of the air flow were estimated and derived for the air inlet and outlet sections, respectively. The corresponding uncertainties were also developed and implemented in the overall thermal analysis of the TFHX, see appendix section A.3.9.4.

4.2.1.3 Measurement procedure

At the time of this work the deployment of different grain flow rates with adjustable particle temperatures over a longer period of time of several hours, to attain steady-state conditions in the HX, was not possible. Therefore, a cold particle feed with different flow rates was provided by means of interchangeable orifices, see Fig. 19 ③, Fig. 27, and section 4.1.1.3, in combination with an air flow that was heated up to more than 600 °C. By adjusting the speed of the air blower, see Fig. 19 ⑫, the gas mass flow was manipulated and simultaneously measured in the range of 5 kg/h to 45 kg/h using an ABB SwirlMaster 450 flowmeter. The determination of the air flow, its measurement uncertainty and the possible compensation of the air leakage mass flow rate as a function of the overpressure in the system are described in the appendix in section A.3.6.

As defined in section 2.2.1, and mentioned in the sections 3.6 and 4.1.2, equal heat capacity flow rates are preferred, to attain a high temperature change in both media. Following this requirement, the maximum particle mass flow can be analytically estimated to be approximately $\dot{m}_{\text{p}}^{\#} = 2\ \text{kg}/(\text{s} \cdot \text{m}^2)$, based on the single particle terminal velocity, u_{t}, of the particles at the envisioned operational temperature range over 900 °C. The minimum particle mass flow of $\dot{m}_{\text{p}}^{\#} = 1.3\ \text{kg}/(\text{s} \cdot \text{m}^2)$ was determined iteratively and uniquely for the presented test setup, where reproducible particle mass flow measurements could still be obtained and measured for a small orifice plate at high gas flow rates. Three additional particle mass flows were defined between the two extremes. Thus, five particle mass flow rates were investigated in the experiment. Five gas flow rates were also defined, slightly below the range of particle flow rates. Applying the operating criteria of preferably equal heat capacity ratios, the air mass flow rates were determined accordingly, considering that the average heat capacity of air is slightly higher than those of particles ($c_{p,\mathrm{a}}/c_{p,\mathrm{p}} \approx 1.2$). The air inlet temperatures were selected, based on the capacities of the air heater, see Fig. 19 ⑪. The used HERZ L62 air heater, with a power input of 4.4 kW, is capable of providing an air temperature of 700 °C at the design point of $300\,\mathrm{l/min} = 2\,\mathrm{kg/(s \cdot m^2)}$. In the test setup, no bypass system was installed that would have allowed the air heater to operate constantly at set point conditions, and the desired air mass flow for the experiments would have been branched off as desired. In the existing experimental setup, the entire air mass flow was measured and then passed through the air heater and into the packed column. Therefore, the maximum air inlet temperature for the experiments was chosen to be 640 °C in order to provide hot air flows below $1\,\mathrm{kg/(s \cdot m^2)}$ and not to risk damaging the air heater.

Tab. 10 Experimental conditions for hot testing of the TFHX.

$T_{\mathrm{a,pac,in}}$ in °C	$\dot{m}_{\mathrm{p}}^{\#}$ in $\mathrm{kg/(s \cdot m^2)}$	$\dot{m}_{\mathrm{a}}^{\#}$ in $\mathrm{kg/(s \cdot m^2)}$
170	1.3	0.9
325	1.6	1.1
480	1.9	1.4
640	2.2	1.7
	2.4	1.9

The experimental conditions are listed in Tab. 10. At each temperature level for $T_{\mathrm{a,pac,in}}$, each particle mass flow was tested with all the predefined airflow rates, resulting in 5 x 5 test conditions. Thus, a total of 4 x 25 test conditions was run and measured for the hot experiments.

As the experiments were run and all 100 defined test conditions were approached, the time required to reach steady state was considered individually. Preliminary FEM simulations were performed to determine the time required to reach steady-state conditions in the test rig. The simulations examined the change in heat flux density from the inside of the duct through the HX duct and insulation to the surrounding environment. A wall temperature of 700 °C was applied to the inside of the HX channel and the heat flux evolution was observed as the 100 mm high temperature insulation was heated from ambient temperature. It was observed that after 1 h the simulated flux density approached the final converging value in a range of 100 %. After 8 h and 16 h, the flux densities approached the final converging value within a range of 10 % and 1 %, respectively. The results obtained are valid when the test bench is heated from ambient conditions. When performing the experiments, at the beginning of a test day, the HX channel was preconditioned for 4-6 hours by using the air heater without particle flow to preheat the test bench to an intermediate temperature. During a test day, after changing a boundary condition of the experiment, e.g., changing the air flow rate, the temperature profile in the test bench was already considered to be relatively evolved from the steady-state condition of the previous experiment. This is why after pre-conditioning or after changing the boundary conditions during the experiments, no transient time of several hours had to be waited to reach steady-state conditions and to start the data measurement. After changing the boundary conditions, the temperature measurements within the HX packing, $T_{\mathrm{ci},i}$, but also in the insulation, see Fig. 74, were observed. When the gradients of the mentioned temperatures reached 10 K/h or below, it was considered as stationary and the designated measurement of particle mass flow, particle hold-up and particle temperature was started. In practical terms, between two measurements a waiting period of 1 h to 2 h must be waited. All other temperature and pressure measurements were logged constantly.

4.2.2 Characterization of trickle flow heat exchanger with optimized packing geometry

In the following section, the experimental results of the test conditions defined in Tab. 10 are presented and discussed. The measurement results are plotted for different media flow rates. Furthermore, according to Tab. 10 , the results are shown separately for four different air inlet temperatures at the packing inlet, $T_{\mathrm{a,pac,in}}$, and are referred to as "temperature level". The determination of $T_{\mathrm{a,pac,in}}$ and its uncertainty is described in A.3.9.4. During the experiments, the air mass flow was set to the flow rates given in Tab. 10, and the specified particle mass flow was approximated by changing and adjusting the orifice plates. As mentioned in section 4.1.1.3, in the system setup described, the determined particle mass flow is the result of the combination of the orifice plate used, the air inlet temperature, and the gas mass flow. Therefore, the particle mass flows given in Tab. 10 could only be approximated, whereas the air mass flows could be set reproducible for all measurements in the test campaign. Under these circumstances, it was advantageous to group the results for each air mass flow and plot the particle solid flow rate on the x-axis. If there was a trend in the results, a dashed line was added to the result plots for each air mass flow group by applying an exponential curve fit.

First, the logarithmic mean temperature difference (LMTD), ΔT_{m}, and the measured specific particle surface area, a_{p}, are displayed and will be referred to in the interpretation of the heat transfer coefficient after the discussion of the transferred power and the discussion of the power densities. The analysis of the NTU values will complete the experimental evaluation of the developed TFHX. The analysis of the heat transfer coefficient, the transferred thermal heat and the NTU values were embedded in a comparison with the available data in the literature.

4.2.2.1 Logarithmic Mean Temperature Difference

Typically, in heat transfer problems, the temperature difference between the two media changes constantly along the length of the HX. To determine the average heat transfer coefficient between two media flows, a constant average temperature difference, ΔT_{m}, is required and the specific heat flux, $\dot{q}$, must be known.

$$\dot{q} = k \, \Delta T_{\mathrm{m}} \qquad (35)$$

The LMTD can be considered as a representative value of a fictive, constant temperature difference along the heat exchanger to determine the heat transfer coefficient between the particles and the air. Therefore, the inlet and outlet temperatures of both media streams must be known and are calculated as follows:

$$\Delta T_\mathrm{m} = \frac{\left(T_\mathrm{a,in} - T_\mathrm{p,out}\right) - \left(T_\mathrm{a,out} - T_\mathrm{p,in}\right)}{\ln\left(\frac{T_\mathrm{a,in} - T_\mathrm{p,out}}{T_\mathrm{a,out} - T_\mathrm{p,in}}\right)} \qquad (36)$$

The corresponding uncertainty can be determined as follows:

$$u_{\Delta T_\mathrm{m}} = \sqrt{\left(\frac{\partial \Delta T_\mathrm{m}}{\partial T_\mathrm{a,in}} u_{T_\mathrm{a,in}}\right)^2 + \left(\frac{\partial \Delta T_\mathrm{m}}{\partial T_\mathrm{a,out}} u_{T_\mathrm{a,out}}\right)^2 + \left(\frac{\partial \Delta T_\mathrm{m}}{\partial T_\mathrm{p,in}} u_{T_\mathrm{p,in}}\right)^2 + \left(\frac{\partial \Delta T_\mathrm{m}}{\partial T_\mathrm{p,out}} u_{T_\mathrm{p,out}}\right)^2} \qquad (37)$$

The partial derivatives by the variables of (36) provide the corresponding sensitivity coefficients, to be inserted in (37).

$$\frac{\partial \Delta T_\mathrm{m}}{\partial T_\mathrm{p,in}} = \ln\left(\frac{T_\mathrm{a,in} - T_\mathrm{p,out}}{T_\mathrm{a,out} - T_\mathrm{p,in}}\right)^{-1} - \frac{\left(T_\mathrm{a,in} - T_\mathrm{p,out}\right) - \left(T_\mathrm{a,out} - T_\mathrm{p,in}\right)}{\left(T_\mathrm{a,out} - T_\mathrm{p,in}\right)\,\ln\left(\frac{T_\mathrm{a,in} - T_\mathrm{p,out}}{T_\mathrm{a,out} - T_\mathrm{p,in}}\right)^2} \text{ in } - \qquad (38)$$

$$\frac{\partial \Delta T_\mathrm{m}}{\partial T_\mathrm{p,out}} = -\ln\left(\frac{T_\mathrm{a,in} - T_\mathrm{p,out}}{T_\mathrm{a,out} - T_\mathrm{p,in}}\right)^{-1} + \frac{\left(T_\mathrm{a,in} - T_\mathrm{p,out}\right) - \left(T_\mathrm{a,out} - T_\mathrm{p,in}\right)}{\left(T_\mathrm{a,in} - T_\mathrm{p,out}\right)\,\ln\left(\frac{T_\mathrm{a,in} - T_\mathrm{p,out}}{T_\mathrm{a,out} - T_\mathrm{p,in}}\right)^2} \text{ in } - \qquad (39)$$

$$\frac{\partial \Delta T_\mathrm{m}}{\partial T_\mathrm{a,in}} = \ln\left(\frac{T_\mathrm{a,in} - T_\mathrm{p,out}}{T_\mathrm{a,out} - T_\mathrm{p,in}}\right)^{-1} - \frac{\left(T_\mathrm{a,in} - T_\mathrm{p,out}\right) - \left(T_\mathrm{a,out} - T_\mathrm{p,in}\right)}{\left(T_\mathrm{a,in} - T_\mathrm{p,out}\right)\,\ln\left(\frac{T_\mathrm{a,in} - T_\mathrm{p,out}}{T_\mathrm{a,out} - T_\mathrm{p,in}}\right)^2} \text{ in } - \qquad (40)$$

$$\frac{\partial \Delta T_\mathrm{m}}{\partial T_\mathrm{a,out}} = -\ln\left(\frac{T_\mathrm{a,in} - T_\mathrm{p,out}}{T_\mathrm{a,out} - T_\mathrm{p,in}}\right)^{-1} + \frac{\left(T_\mathrm{a,in} - T_\mathrm{p,out}\right) - \left(T_\mathrm{a,out} - T_\mathrm{p,in}\right)}{\left(T_\mathrm{a,out} - T_\mathrm{p,in}\right)\,\ln\left(\frac{T_\mathrm{a,in} - T_\mathrm{p,out}}{T_\mathrm{a,out} - T_\mathrm{p,in}}\right)^2} \text{ in } - \qquad (41)$$

Fig. 38 shows the determined values of ΔT_m for the hot experiments performed. It can be observed that for the measurements made, the LMTDs are in the same range for each temperature stage, independent of the media flow rates, and increase proportionally with $T_\mathrm{a,pac,in}$, see Tab. 11.

Tab. 11 LMTD and uncertainty for each temperature level with varying media flow rates.

$T_\mathrm{a,pac,in}$ in °C	ΔT_m in K	$U_{\Delta T_\mathrm{m}}$ in K
639	78.1	6.1
479	54.4	9.0
325	31.0	6.6
170	19.2	1.3

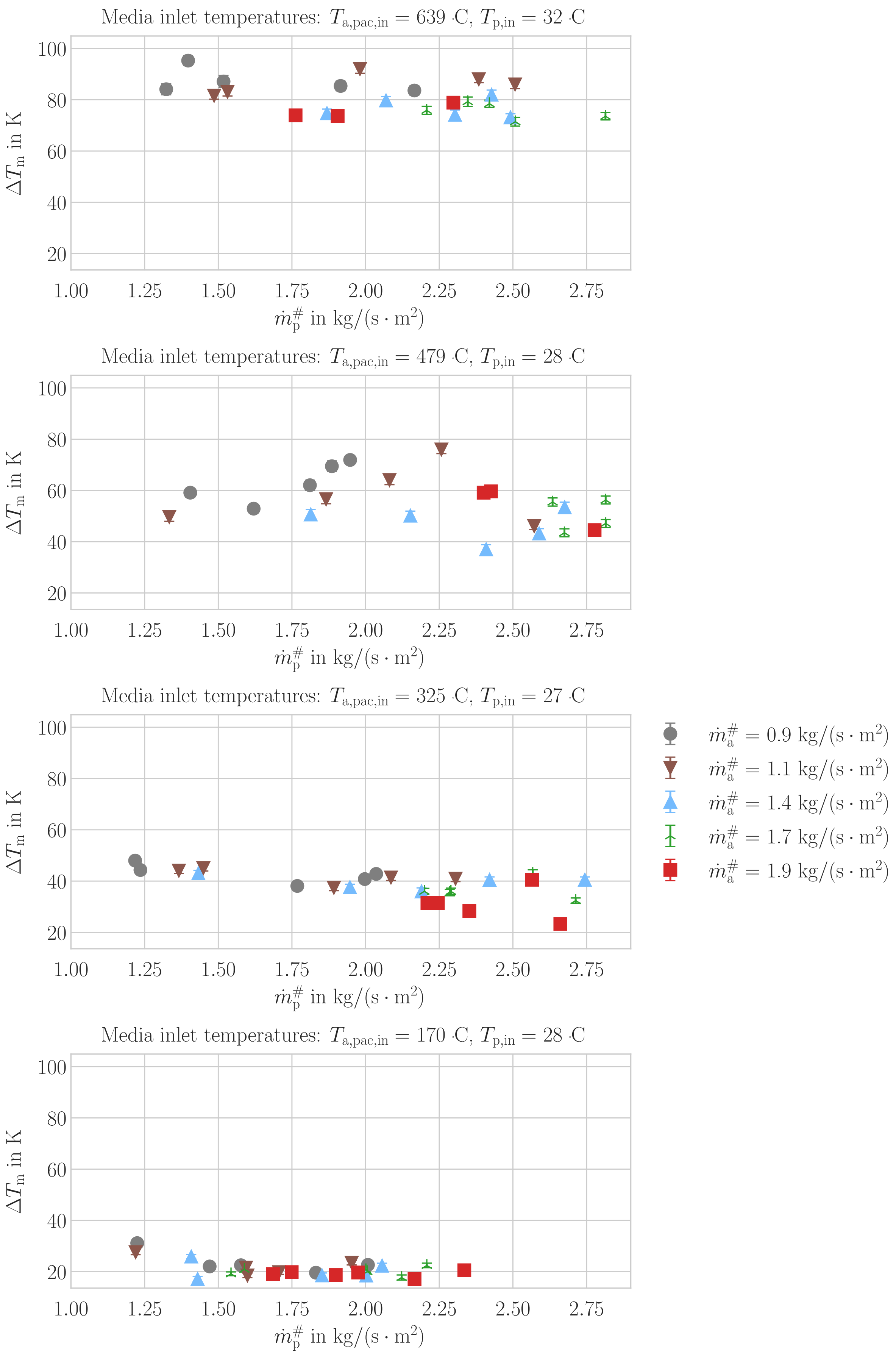

Fig. 38 LMTD at four temperature levels with varying media flow rates.

4.2.2.2 Particle surface

The theory for determining the volume specific surface area of particles within a packed column, a_{p}, was derived in section 3.3. There, it was outlined that α_{p} is directly proportional to the particle hold-up and can be determined by multiplying β by the constant values of the idealized particle volume specific surface area, $a_{V_{\mathrm{s}}}$, and the packing porosity, ϵ_0, see (18). This proportionality leads to a similar behavior of α_{p} and β, hence the explicit analysis of the particle hold-up is omitted in this section. Furthermore, α_{p} is the available heat transfer area represented by the trickling particles and is one of the driving factors to characterize the heat transfer capabilities of the TFHX, which is the scope of this investigation.

Based on (18), the uncertainty for the volume specific particle surface area can be derived for the analysis of the experiments.

$$u_{a_{\mathrm{p}}} = \sqrt{\left(\frac{\partial a_{\mathrm{p}}}{\partial d_{\mathrm{p}}} u_{d_{\mathrm{p}}}\right)^2 + \left(\frac{\partial a_{\mathrm{p}}}{\partial \beta} u_{\beta}\right)^2 + \left(\frac{\partial a_{\mathrm{p}}}{\partial \epsilon_0} u_{\epsilon_0}\right)^2} \quad (42)$$

While the corresponding partial derivatives represent the sensitivity coefficients to be inserted in (42).

$$\frac{\partial a_{\mathrm{p}}}{\partial d_{\mathrm{p}}} = -\frac{6}{d_{\mathrm{p}}^2}\,\beta\,\epsilon_0 \text{ in} \frac{1}{\mathrm{m}^2} = \frac{1}{\mathrm{m}} \cdot \frac{\mathrm{m}^2}{\mathrm{m}^3} \quad (43)$$

$$\frac{\partial a_{\mathrm{p}}}{\partial \beta} = \frac{6}{d_{\mathrm{p}}}\,\epsilon_0 \text{ in} \frac{1}{\mathrm{m}} = \frac{\mathrm{m}^2}{\mathrm{m}^3} \quad (44)$$

$$\frac{\partial a_{\mathrm{p}}}{\partial \epsilon_0} = \frac{6}{d_{\mathrm{p}}}\,\beta \text{ in} \frac{1}{\mathrm{m}} = \frac{\mathrm{m}^2}{\mathrm{m}^3} \quad (45)$$

A direct comparison of the experimentally determined specific particle surface area with the reference work is omitted. Verver and Van Swaaij [113] provide their data for a_{p} for their 0.37 mm particles based on a single particle hydrodynamic model with a specific particle flow in the range of $\dot{m}_{\mathrm{p}}^{\#} = 0.7\ \mathrm{kg/(s \cdot m^2)}$ and give values for a_{p} in the range of 10 $\mathrm{m^2/m^3}$ to 40 $\mathrm{m^2/m^3}$. For higher flow rates, the particles would enter the flooding range and unstable flow conditions would result in the inoperability of the TFHX. Fig. 39 illustrates that the heat exchanger developed in this work provides particle surface areas in the range of 20 $\mathrm{m^2/m^3}$ to 150 $\mathrm{m^2/m^3}$ at stable flow conditions for all experimental data points. a_{p} increases with temperature level and shows directly proportional behavior with air flow rate and particle flow rate. The particle surfaces of the trickling particles shown in Fig. 39 are in the same order of magnitude as the wettable surface of the "w10 h02 n3 z10" packing structure with 143 $\mathrm{m^2/m^3}$. This makes it interesting to operate the TFHX in temperature ranges where radiative heat transfer is expected to become noticeable.

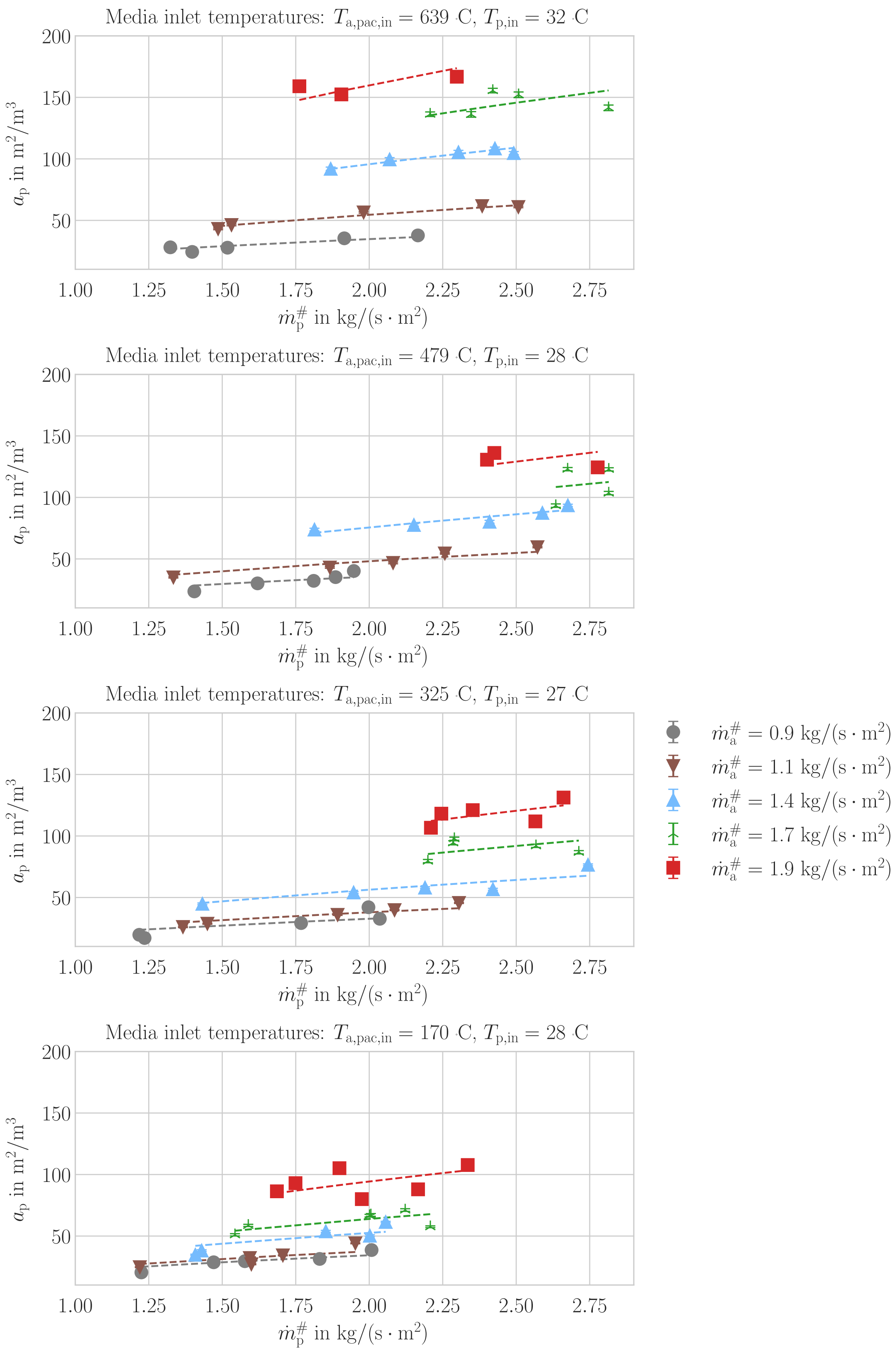

Fig. 39 Specific particle surface at four temperature levels with varying media flow rates.

4.2.2.3 Transferred heat and power density

The thermodynamic balance for each particle or airflow can generally be calculated as follows:

$$\dot{Q} = \dot{m} \int_{\mathrm{in}}^{\mathrm{out}} c_p \,\mathrm{dT} = \dot{m}\,(c_{p,\mathrm{out}}\,\mathrm{T_{out}} - c_{p,\mathrm{in}}\,\mathrm{T_{in}}) \tag{46}$$

A constant thermal heat capacity was assumed for both media, since only the inlet and outlet temperatures were measured in the experimental setup, see section 4:

$$\bar{c}_p = \frac{1}{\mathrm{T_{out}} - \mathrm{T_{in}}} \int_{\mathrm{in}}^{\mathrm{out}} c_p \,\mathrm{dT} \approx \frac{1}{2}\big(c_p(\mathrm{T_{out}}) + c_p(\mathrm{T_{in}})\big) \tag{47}$$

$$\dot{Q} = \dot{m}\,\bar{c}_p\,(\mathrm{T_{out}} - \mathrm{T_{in}}) \tag{48}$$

The determination of $\dot{m}$, T, and c_p is outlined in the sections 4.1.1.3, A.3, and A.2.1.3. The determination of the different uncertainties is also outlined in the corresponding sections. The uncertainty of the transferred thermal power, $u_{\dot{Q}}$, is determined as follows:

$$u_{\dot{Q}} = \sqrt{\left(\frac{\partial \dot{Q}}{\partial \dot{m}} u_{\dot{m}}\right)^2 + \left(\frac{\partial \dot{Q}}{\partial \bar{c}_p} u_{\bar{c}_\mathrm{p}}\right)^2 + \left(\frac{\partial \dot{Q}}{\partial T_{\mathrm{out}}} u_{\mathrm{T_{out}}}\right)^2 + \left(\frac{\partial \dot{Q}}{\partial T_{\mathrm{in}}} u_{T_{\mathrm{in}}}\right)^2} \tag{49}$$

While the partial derivatives represent the sensitivity coefficients of each variable and are derived below and inserted in (49) and multiplied with the corresponding uncertainties.

$$\frac{\partial \dot{Q}}{\partial \dot{m}} = \bar{c}_p\,(T_{\mathrm{out}} - T_{\mathrm{in}})\ \mathrm{in}\,\frac{\mathrm{J}}{\mathrm{g}} \tag{50}$$

$$\frac{\partial \dot{Q}}{\partial \bar{c}_p} = \dot{m}\,(T_{\mathrm{out}} - T_{\mathrm{in}})\ \mathrm{in}\,\frac{\mathrm{g}}{\mathrm{s}}\mathrm{K} \tag{51}$$

$$\frac{\partial \dot{Q}}{\partial T_{\mathrm{out}}} = \dot{m}\,\bar{c}_p\ \mathrm{in}\,\frac{\mathrm{W}}{\mathrm{K}} \tag{52}$$

$$\frac{\partial \dot{Q}}{\partial T_{\mathrm{in}}} = -\dot{m}\,\bar{c}_p\ \mathrm{in}\,\frac{\mathrm{W}}{\mathrm{K}} \tag{53}$$

In accordance with Verver and Van Swaaij [113], it is assumed that the dominant fraction of the heat losses to the environment can be attributed to the air flow when performing measurements with hot air entering the test bench. As in section 4, it was assumed that the interaction with the wall of the TFHX channel with air can be considered as dominant compared to the thermal losses in the particle flow. Following this assumption, it can be said in a simplified way that the measurable reduction of the thermal power in the air flow according to (48) represents the raw heat transferred from the air flow, which provides the thermal power for the heat transfer between particles and air, but also to the surroundings. Consequently, it is assumed that the thermal losses occurring in the TFHX are accounted only to the air flow, and the power transferred to the particle flow represents exclusively the heat transferred from the air to the particles.

$$-\dot{Q}_{\mathrm{a,raw}} = -\left(\dot{Q}_{\mathrm{a}} + \dot{Q}_{\mathrm{loss}}\right) = \dot{Q}_{\mathrm{p}} + \dot{Q}_{\mathrm{loss}} = \dot{Q} + \dot{Q}_{\mathrm{loss}} \tag{54}$$

The transferred power, normalized to the volume of the heat exchanger, V_{HX}, is used to illustrate the results of the TFHX:

$$\dot{Q}_{\mathrm{vol}} = \frac{\dot{Q}}{V_{\mathrm{HX}}} \tag{55}$$

With the corresponding uncertainty:

$$u_{\dot{Q}_{\mathrm{vol}}} = \sqrt{\left(\frac{\partial \dot{Q}_{\mathrm{vol}}}{\partial \dot{Q}} u_{\dot{Q}}\right)^2 + \left(\frac{\partial \dot{Q}_{\mathrm{vol}}}{\partial V_{\mathrm{HX}}} u_{V_{\mathrm{HX}}}\right)^2} = \sqrt{\left(\frac{1}{V_{\mathrm{HX}}}\, u_{\dot{Q}}\right)^2 + \left(-\frac{\dot{Q}}{V_{\mathrm{HX}}^2}\, u_{V_{\mathrm{HX}}}\right)^2} \tag{56}$$

Fig. 40 shows, based on (55), the normalized transferred thermal heat, $\dot{Q}_{\mathrm{vol}}$. The maximum transferable power is in the range of 1,250 $\mathrm{kW/m^3}$, see Fig. 40. As expected, the transferred power relates directly proportional with the media flow rates and the temperature level.

As illustrated in Fig. 58 in A.1.1, the raw heat flow in the air stream, $\dot{Q}_{\mathrm{a,raw,vol}}$, exhibits comparable behavior to $\dot{Q}_{\mathrm{vol}}$. However, the values are augmented by the thermal losses to the surroundings, according to (54). Fig. 41 presents a synthesis of the findings from Fig. 40 and Fig. 58, illustrating the trend lines of the heat flow rates conveyed by the air stream (solid line) and the heat flow, that is absorbed by the particle flow (dashed line) across varying media flow ranges and temperature levels. For purposes of clarity, only the trend lines of both graphs are depicted in the analysis. Additionally, the absolute values of $\dot{Q}_{\mathrm{a,raw,vol}}$ are plotted in the graph, given that they are typically defined to be negative.

The discrepancies between the solid and the dashed lines illustrate according to (54) the trend of the heat losses for the varying operational conditions. The extent of heat loss varies between 5 % to 15 % in accordance with the specific mass flow rates and temperature levels. As the temperature level decreases, the magnitude of heat loss also decreases, and vice versa. Additionally, an increase of air flow rates is accompanied by an increase in thermal losses, $\dot{Q}_{\mathrm{loss,vol}}$, as evidenced by the widening of the distance between the dotted and dashed lines. The higher air velocities within the HX channel result in an increased heat transfer rate between the air and the inner wall, which in turn enhances the transfer of heat transfer to the insulation and subsequently to the surrounding environment. However, this cannot be observed for the temperature level of 479 °C air inlet temperature, where $\dot{Q}_{\mathrm{loss,vol}}$ appears to be relatively low for $\dot{m}_{\mathrm{a}}^{\#} = 1.9\ \mathrm{kg/(s \cdot m^2)}$. This behavior must be interpreted as an erroneous result, and is caused by the measurement uncertainty and the relatively low number of five measurement points available to generate a behavioral trend line. As expected, the highest heat losses of as much as 25 % were found for the highest mass flow rates at the highest temperature level, see Fig. 40, where 3 $\mathrm{kW_{th}}$ respectively 1,500 $\mathrm{kW_{th}/m^3}$ heat was transferred into the particles. At this high temperature level, the unfavorable ratio of the heat exchanger volume to its surface area is noticeable. Therefore, to test the developed concept at higher temperature levels, an upscaled version of the TFHX should be considered to reduce the dominance of thermal losses at higher operating temperatures.

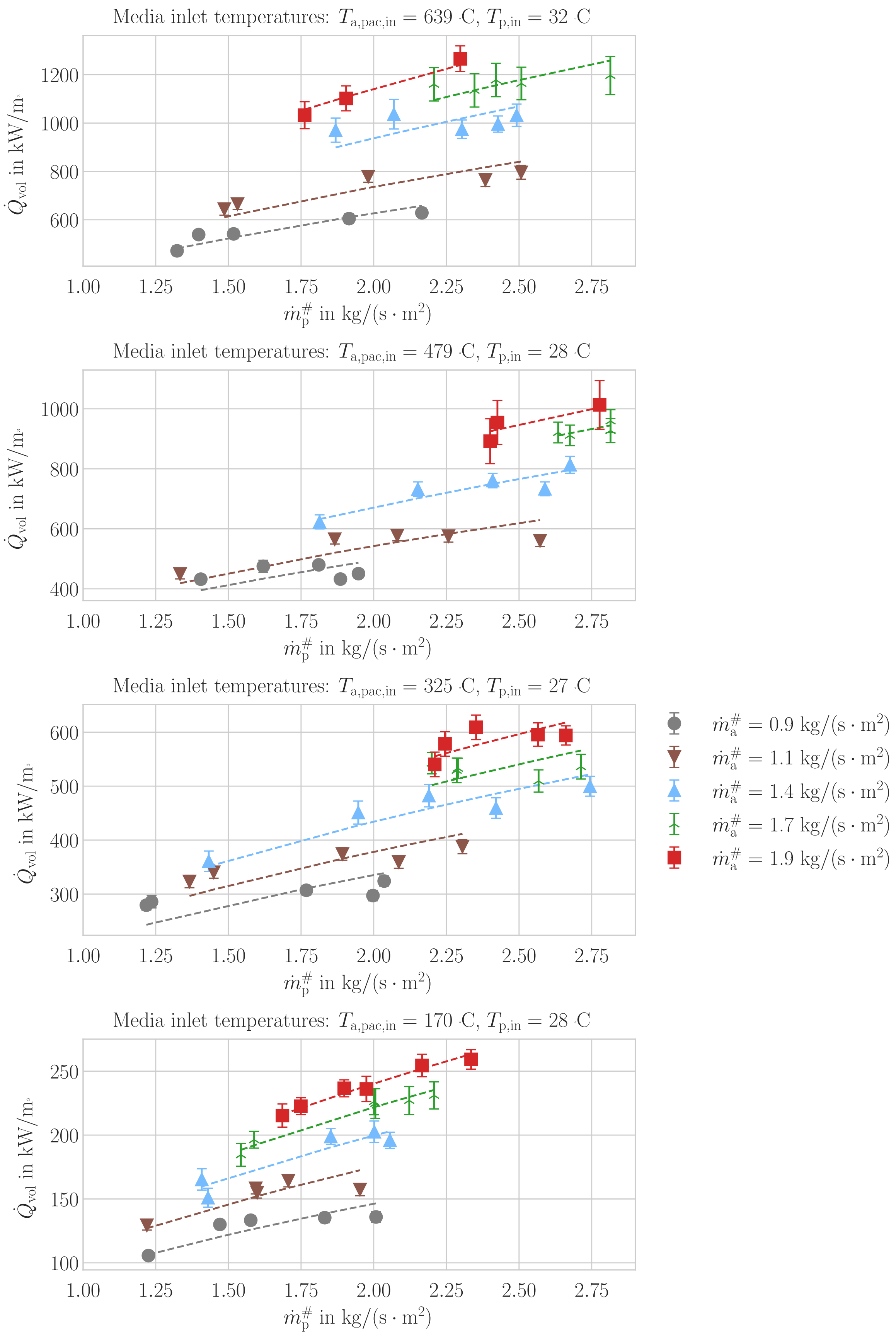

Fig. 40 Normalized transferred heat at four temperature levels with varying media flow rates.

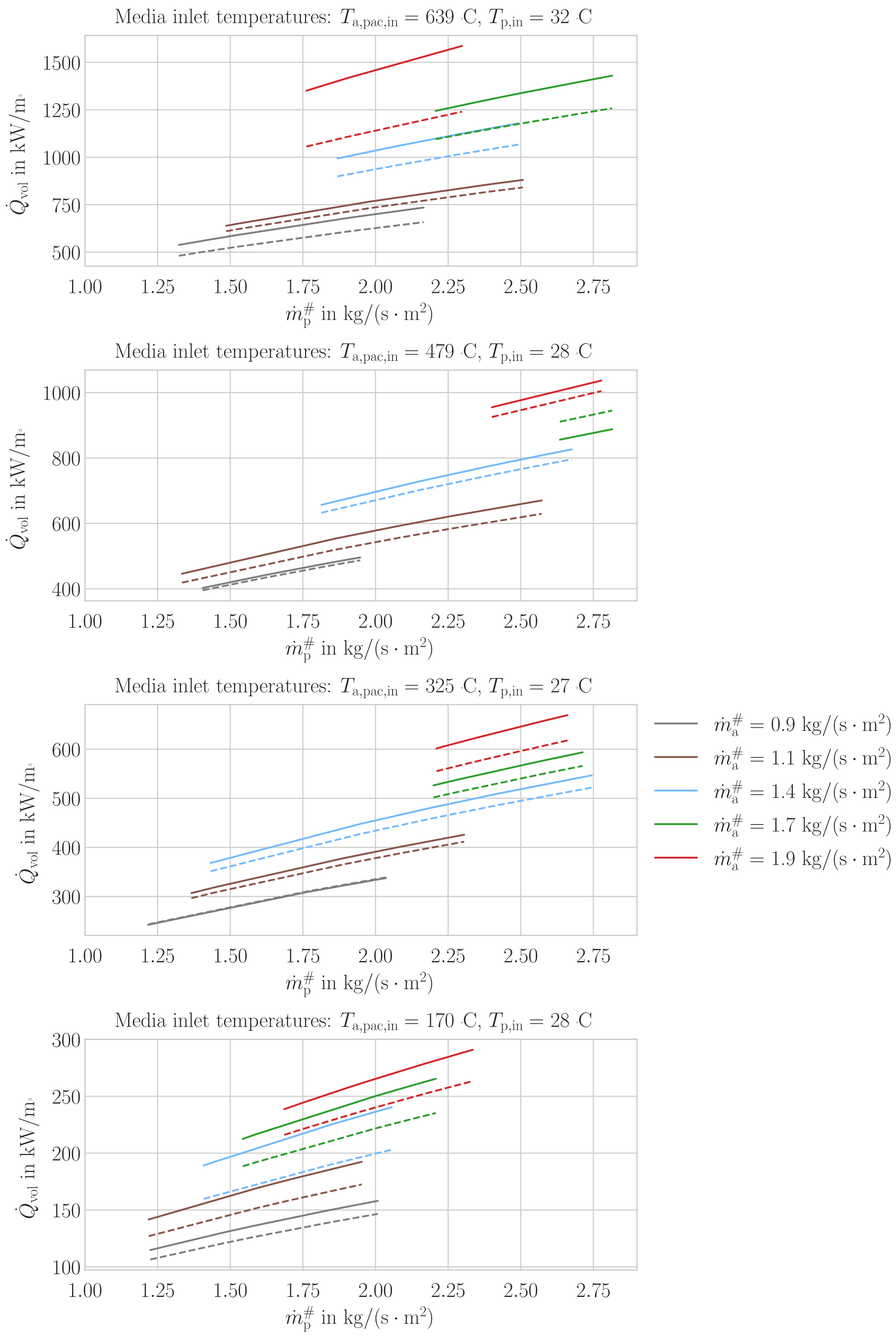

Fig. 41 Trendlines of the normalized transferred raw heat from the air (solid) and absorbed heat to the particles (dashed), at four temperature levels with varying media flow rates.

In order to frame the results shown in Fig. 40, available literature data was used to compare the power density of other trickle flow heat exchangers. Verver and Van Swaaij [113] and Nagata, Ohara [146] provide data in their work that allow the power densities to be calculated for varying particle and air flow rates. The packing structure of Nagata, Ohara [146] is similar to the structure illustrated in Fig. 50 Packing B. Only the packing layers rotated by 90° parallel to the axis of gravity are omitted, which is why the packed column investigated by Nagata, Ohara [146] use only parallel angled metal strips. Both works use 0.37 mm particles with a similar density of 2650 $\mathrm{kg/m^3}$. Nagata, Ohara [146] mention the use of silica, while Verver and Van Swaaij [113] do not describe the material particles in detail and solely name the particles e.g. "Sand 425", so it's assumed that they also used a material consisting mainly of silica. The same particle density in both works supports this assumption.

For a comparison of the power densities in Fig. 40, the temperature level $T_{\mathrm{a,pac,in}} = 325\ \mathrm{°C}$ is chosen, since it most closely approximates the temperature ranges used in the available work, see Fig. 42. The results presented could suggest that the experiments carried out in this work are a continuation of the available data. However, it has to be considered that the particle diameter used in the reference works is 0.37 mm [113, 146], and correspondingly the air flow to reach the corresponding terminal velocity, u_{t}, is lower than for the 1 mm particles used in this work, see Tab. 23 in the appendix in section A.5. The calculated values for u_{t} refer to an air velocity in the free cross-sectional area of the HX channel, without the packed column. However, the blocking of the packing structure must be considered, which reduces the effective cross-sectional area for the airflow. For the identified geometry, the effective packing porosity is approximately 0.5 and can be considered by multiplying $u_{\mathrm{a,0}}$ by ϵ_{eff}. Furthermore, assuming equal heat capacity flow rates to obtain a high temperature change in both media in the TFHX, with an estimated heat capacity ratio of $c_{p,\mathrm{a}}/c_{p,\mathrm{p}} \approx 1.2$, the corresponding ideal, maximum particle flow can be estimated. Accordingly, in Tab. 12 the calculated particle flow rates describe an estimated, theoretical optimal operating condition for the corresponding airflow for each reference work. It shows that the works of Verver and Van Swaaij [113] and Nagata, Ohara [146] approach their dedicated theoretical maximum air flow rates at 1.03 $\mathrm{kg_{a,250\,°C}/(s \cdot m^2)}$ and 0.89 $\mathrm{kg_{a,350\,°C}/(s \cdot m^2)}$, respectively. With their corresponding maximum particle flow rates at 1.44 and 1.20 $\mathrm{kg_p/(s \cdot m^2)}$. As mentioned before, these limits are based on the theory of terminal velocity for a single particle. In practice, the effect of particles falling in a submerged cloud must be considered. Due to particle agglomeration, u_{t} can be expected to be higher for dense particle flows. This effect has been investigated, for example, Kim, Siegel [166] or Gobereit [47], who studied the evolution of the fall velocity for particle clouds with different particle diameters, see Fig. 71 (right). This effect of a higher particle falling velocity than the theoretical maxima at u_{t} is more pronounced for smaller particles, which is why Nagata, Ohara [146] and Verver and Van Swaaij [113] were able to perform experiments in airflow ranges slightly exceeding the theoretical limits for the terminal conditions of a single particle, see Tab. 12. The terminal conditions in Tab. 12 are calculated based on the single particle terminal velocity theory, see section A.5 in the appendix. The terminal conditions for the particles used in this work with the corresponding particle densities can be found in Tab. 23 to Tab. 27.

Tab. 12 Terminal conditions in packing structure in available work for individual air temperatures.

air flow in $\mathrm{kg_a/(s \cdot m^2)}$		terminal conditions in $\mathrm{kg_a/(s \cdot m^2)}$		particle flow in $\mathrm{kg_p/(s \cdot m^2)}$ for $\dot{W}_\mathrm{r} \approx 1$
		free cross-sectional area	blocking of packing $\epsilon_\mathrm{eff} \approx 50\ \%$	
$\dot{m}^{\#}_{\mathrm{a,Ver86,250\ °C}}$	0.6	2.05	1.03	0.72
	0.7			0.84
	1.0			1.20
	1.2			1.44
$\dot{m}^{\#}_{\mathrm{a,Nag98,350\ °C}}$	1.0	1.78	0.89	1.20
$\dot{m}^{\#}_{\mathrm{a,Rei24,325\ °C}}$	0.9	5.76	2.88	1.08
	1.1			1.32
	1.4			1.68
	1.7			2.04
	1.9			2.28

Fig. 42 shows that the power densities of the reference literature are in the range of 250 $\mathrm{kW/m^3}$ up to 350 $\mathrm{kW/m^3}$ and can be considered as the maximum operating capabilities of the devices, since at higher air flow rates it can be expected that the particles start to flood. The experiments performed in this work allow higher air velocities due to the larger particle diameter and higher particle density, resulting in potentially higher particle flow rates, see Tab. 12. It can be seen that the developed TFHX module provides power densities in the range of 500 $\mathrm{kW/m^3}$ to 600 $\mathrm{kW/m^3}$. Comparing the results with the available work in the literature, the power density was increased by approximately 100 %.

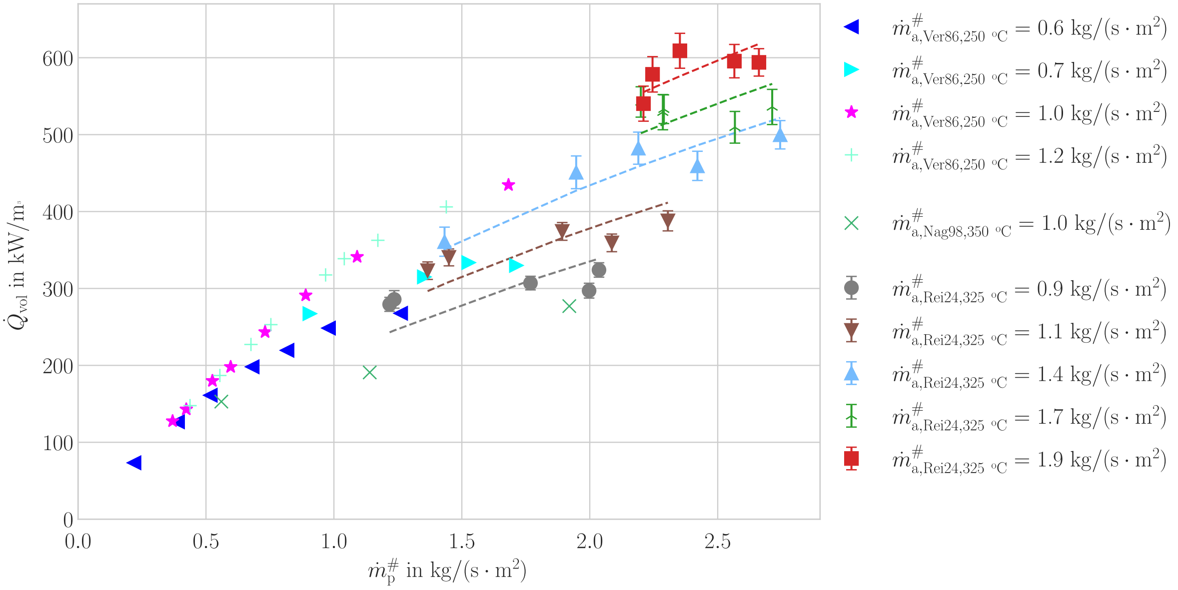

Fig. 42 Thermal power densities in a TFHX. Results of this work, compared to literature at approximately equal temperature levels, with varying air and particle flow rates.

The author tries to frame this result on the basis of the available knowledge. The comparison of the results in this work with the two reference works [113, 146] is made due to the limited availability of more suitable experimental work capable of comparison. It should be noted that by reducing the particle diameter from 1 mm to e.g. 0.37 mm, u_{t}, e.g. under ambient conditions, decreases from 7.9 m/s to 3.6 m/s, see Tab. 23. Correspondingly, the maximum air and particle flow rate is reduced, see Tab. 24. However, due to the smaller particle diameter, the volume specific particle surface area within the packed column is expected to increase, which would reduce the column height required to achieve a desired temperature change of the flowing media. This leads to the assumption that the achievable power densities in a TFHX could be independent of the particle diameter. Consequently, to achieve the same absolute heat transfer in a TFHX with a reduced particle diameter, the height of the packed column could be reduced, but the cross-sectional area of the TFHX would have to be increased. However, this would pose a technical challenge for measures to uniformly feed the packing structure with the incoming grain flow over the entire cross-sectional area. The assumption that the power densities of a TFHX can be considered independent of the particle diameter used is only expected to be valid if an optimized packing structure, based on the selection criteria in this work, is used for the different particle types. This leads to the assumption that the noticeable increase of the power densities in the developed TFHX compared to the reference work might be mainly driven in the optimized packing structure and the accumulated particles in the packed column, causing to dissipate the kinetic fall energy of the trickling grains and conversely causing to increase the volumetric particle surface, see (17) and (18). The finding of this work, that sufficiently wide bar elements can be beneficial to increase the dynamic particle hold-up in a trickle flow reactor, needs to be investigated if this is applicable to a range of grain diameters. It should be noted that the particle flow behavior changes significantly with the diameter and condition of the powders, and the results presented here may not be applicable to e.g. powdery materials, where adhesive forces, such as van der Waals forces, or an increased moisture content could already have a significant impact on the flow behavior of the particle stream [96].

The maximum air flow with an air inlet temperature of $T_{\mathrm{a,in}} = 325$ °C and correspondingly the particle flow could have been even higher than the predefined conditions in Tab. 10. At a temperature level of 325 °C and assuming the same heat capacity flow rates for operation, a theoretical air flow in the range of 2.88 $\mathrm{kg_{a,325\,°C}/(s \cdot m^2)}$ would be expected, resulting in power densities exceeding 600 $\mathrm{kW/m^3}$. However, in order to ensure cross-comparability between all temperature stages, it was decided to select the air and particle flow rates accordingly to achieve stable flow conditions within the TFHX up to the envisaged maximum media temperatures in the range of 900 °C, see section 2.2.1. Considering also ϵ_{eff}, the theoretical maximum air flow would be limited to 1.7 $\mathrm{kg_{a,900\,°C}/(s \cdot m^2)}$, so for the experiments in this work a maximum air flow rate slightly above the estimated limit of 1.9 $\mathrm{kg_a/(s \cdot m^2)}$ was chosen.

4.2.2.4 Heat transfer coefficient

To further characterize the developed TFHX, along with the transferred thermal heat, the heat transfer coefficients, k, are also determined and compared with the values available in the literature. k can be determined based on (35). Therefore, the transferred heat, $\dot{Q}$, the media inlet and outlet temperatures for determining the LMTD, and the heat transfer area, represented by the total surface of the trickling particles, $A_{\mathrm{p,pac}}$, in the TFHX, were determined experimentally.

$$k = \frac{\dot{q}}{\Delta T_{\mathrm{m}}} = \frac{1}{\Delta T_{\mathrm{m}}} \frac{\dot{Q}}{A_{\mathrm{p,pac}}} \qquad (57)$$

Accordingly, the uncertainty of k can be determined as follows:

$$u_k = \sqrt{\left(\frac{\partial k}{\partial \dot{Q}} u_{\dot{Q}}\right)^2 + \left(\frac{\partial k}{\partial \Delta T_{\mathrm{m}}} u_{T_{\mathrm{m}}}\right)^2 + \left(\frac{\partial k}{\partial A_{\mathrm{p,pac}}} u_{A_{\mathrm{p,pac}}}\right)^2} \qquad (58)$$

With the corresponding sensitivity coefficients:

$$\frac{\partial k}{\partial \dot{Q}} = \frac{1}{\Delta T_{\mathrm{m}}\, A_{\mathrm{p,pac}}} \ \mathrm{in} \frac{1}{\mathrm{K\, m^2}} \qquad (59)$$

$$\frac{\partial k}{\partial \Delta T_{\mathrm{m}}} = -\frac{\dot{Q}}{\Delta T_{\mathrm{m}}^2\, A_{\mathrm{p,pac}}} \ \mathrm{in} \frac{1}{\mathrm{K^2\, m^2}} \qquad (60)$$

$$\frac{\partial k}{\partial a_{\mathrm{p}}} = -\frac{\dot{Q}}{\Delta T_{\mathrm{m}}\, A_{\mathrm{p,pac}}^2} \ \mathrm{in} \frac{1}{\mathrm{K\, m^4}} \qquad (61)$$

As described in sections 4.2.2.3 and A.1.2, it is assumed, in a simplified way, that the thermal losses to the environment are attributed exclusively to the air flow, see (54). Fig. 43 shows the experimental results of the averaged heat transfer coefficient for varying air inlet temperatures and media flow rates. It shows that the experimentally determined heat transfer coefficients are in the range of 100 $\mathrm{W/(m^2 \cdot K)}$ to 300 $\mathrm{W/(m^2 \cdot K)}$ for all four temperature levels. Albrecht and Ho [167] determined in their simulative work the overall heat transfer coefficient to 110 $\mathrm{W/(m^2 \cdot K)}$. They simulated in their work the heat transfer in a shell and tube HX for a moving particle bed to sCO2 using 0.75 mm particles, with similar material properties as the bauxite particles used in this work.

Fig. 43 counterintuitively shows that an indirect proportional correlation between k and $\dot{m}_{\mathrm{a}}^{\#}$ can be observed for all temperature levels. In a standard heat transfer problem, a typical method to increase the heat transfer from fluid to wall, for example in a pipe, is to increase the

Nusselt number. This can be achieved by increasing the Reynolds number, Re, which is proportional to the fluid velocity. The local fluid velocities can be increased by increasing the flow rate or by installing a structure that reduces the boundary thickness at the contact area and conversely increases the turbulence. However, Fig. 43 shows that in the experiments, increasing the air flow rate causes the heat transfer coefficients to decrease. This behavior can be explained by the definition of k, see (57). In typical engineering heat transfer problems, the surface area involved in heat transfer remains constant. However, in a TFHX the surface $A_{\mathrm{p,pac}}$ changes with the air mass flow, see Fig. 39 in section 4.2.2.2. There it was described that the particle surface area correlates proportionally with the countercurrent airflow. A similar behavior is described for the transferred heat, $\dot{Q}$, see Fig. 40 in section 4.2.2.3. For the determination of k, see (57), the LMTD, ΔT_{m}, can be assumed constant for each temperature level within the range of the conducted experiments, see Fig. 38 and Tab. 11 in section 4.2.2.1.

Assuming a constant LMTD for each temperature level within the range of experiments conducted, k is directly proportional to the ratio of heat transferred to the heat transfer surface area of the trickling particles, $\dot{Q}/A_{\mathrm{p,pac}}$, see (57). Fig. 44 shows the evolution of this ratio for varying media flow rates for each of the four temperature levels. It can be observed that the ratios in Fig. 44 show similar behavior to k in Fig. 43. The plotted ratios decrease as the air flow rate increases. By increasing the air mass flow rate, the particle surface area, $A_{\mathrm{p,pac}}$, increases more dominantly than the heat transferred in the TFHX, $\dot{Q}$. This explains the decrease of k according to (57), while the LMTD can be assumed to be constant for each temperature level. The observations can be interpreted that despite a higher availability of particle surface, the transferable heat doses do not increase at the same rate as $A_{\mathrm{p,pac}}$. This leads to the assumption that the increased particle surface area may not be used as efficiently due to potential particle agglomeration, why effectively not the whole particle surface may be usable for heat transfer. However, this assumption would need to be tested and confirmed in additional experiments and investigations beyond the scope of the present work.

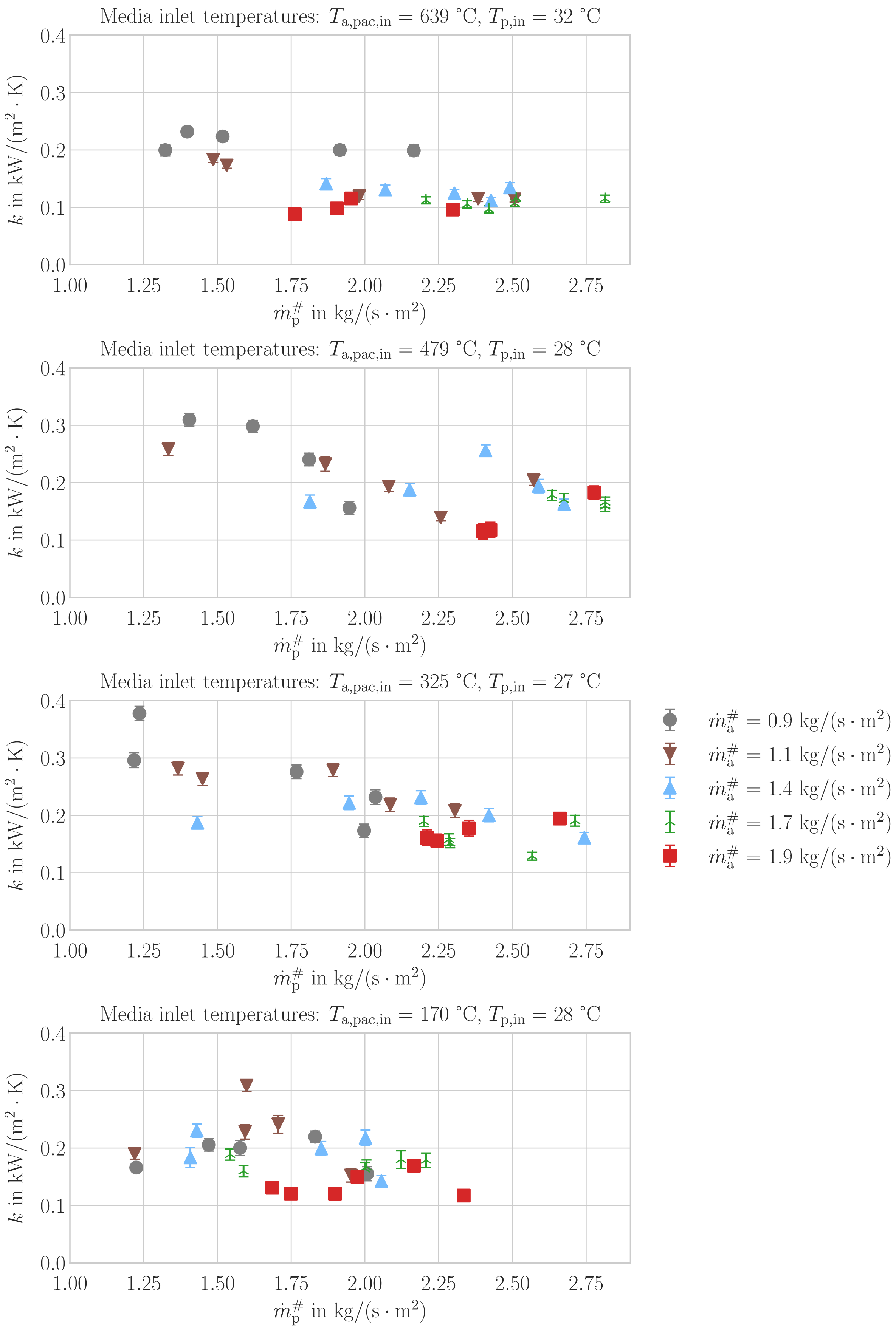

Fig. 43 Experimental heat transfer coefficient at four temperature levels with varying media flow rates.

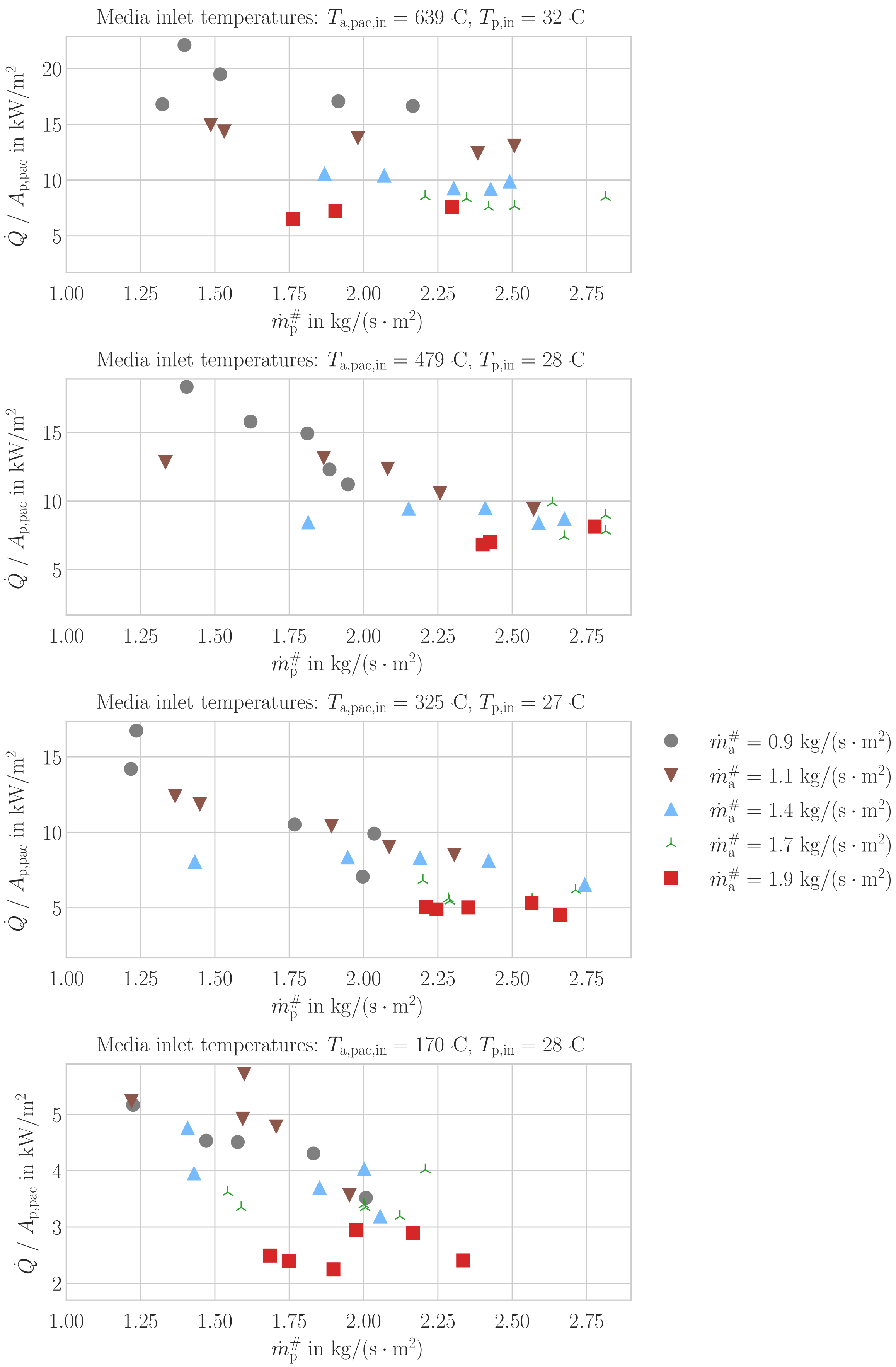
Media inlet temperatures: $T_{\mathrm{a,pac,in}} = 639$ C, $T_{\mathrm{p,in}} = 32$ C

Media inlet temperatures: $T_{\mathrm{a,pac,in}} = 479$ C, $T_{\mathrm{p,in}} = 28$ C

Media inlet temperatures: $T_{\mathrm{a,pac,in}} = 325$ C, $T_{\mathrm{p,in}} = 27$ C

Media inlet temperatures: $T_{\mathrm{a,pac,in}} = 170$ C, $T_{\mathrm{p,in}} = 28$ C

Fig. 44 Ratio of transferred heat to particle surface at four temperature levels with varying media flow rates.

Based on the observations before, a reference system independent of $A_{\mathrm{p,pac}}$ was chosen to classify the heat transfer. Therefore, and in analogy to the extended particle surface area, β^*, the heat transfer is calculated and referenced not to the particle surface area in the packing, but to the heat exchanger volume. The volumetric heat transfer coefficient, k_{vol}, normalizes the heat transfer coefficient to one cubic meter of the trickle flow reactor by multiplying k by the specific particle surface area, see (62). Alternatively, the transferred heat can be divided by the LMTD and the heat exchanger volume, see (62).

$$k_{\mathrm{vol}} = k\, a_{\mathrm{p}} = \frac{\dot{Q}}{\Delta T_{\mathrm{m}}\, V_{\mathrm{HX}}} \qquad (62)$$

The uncertainty of k_{V} can be determined as follows:

$$u_{k_{\mathrm{vol}}} = \sqrt{\left(\frac{\partial k_{\mathrm{vol}}}{\partial k} u_k\right)^2 + \left(\frac{\partial k_{\mathrm{vol}}}{\partial a_{\mathrm{p}}} u_{a_{\mathrm{p}}}\right)^2} = \sqrt{\left(a_{\mathrm{p}}\, u_k\right)^2 + \left(k\, u_{a_{\mathrm{p}}}\right)^2} \qquad (63)$$

Fig. 45 shows k_{vol} where the volumetric heat transfer rate behaves as expected. The volumetric heat transfer varies in the range of 5 $\mathrm{kW/m^3}$ to 20 $\mathrm{kW/m^3}$ and increases with increasing media flow rates. There is a slight tendency for the volumetric heat transfer rate to decrease with increasing temperature level. This can be explained since the averaged particle Reynolds numbers for the measurements show a slight tendency to decrease with increasing temperature level, see Fig. 61. This is outlined in the appendix in section A.1.3.

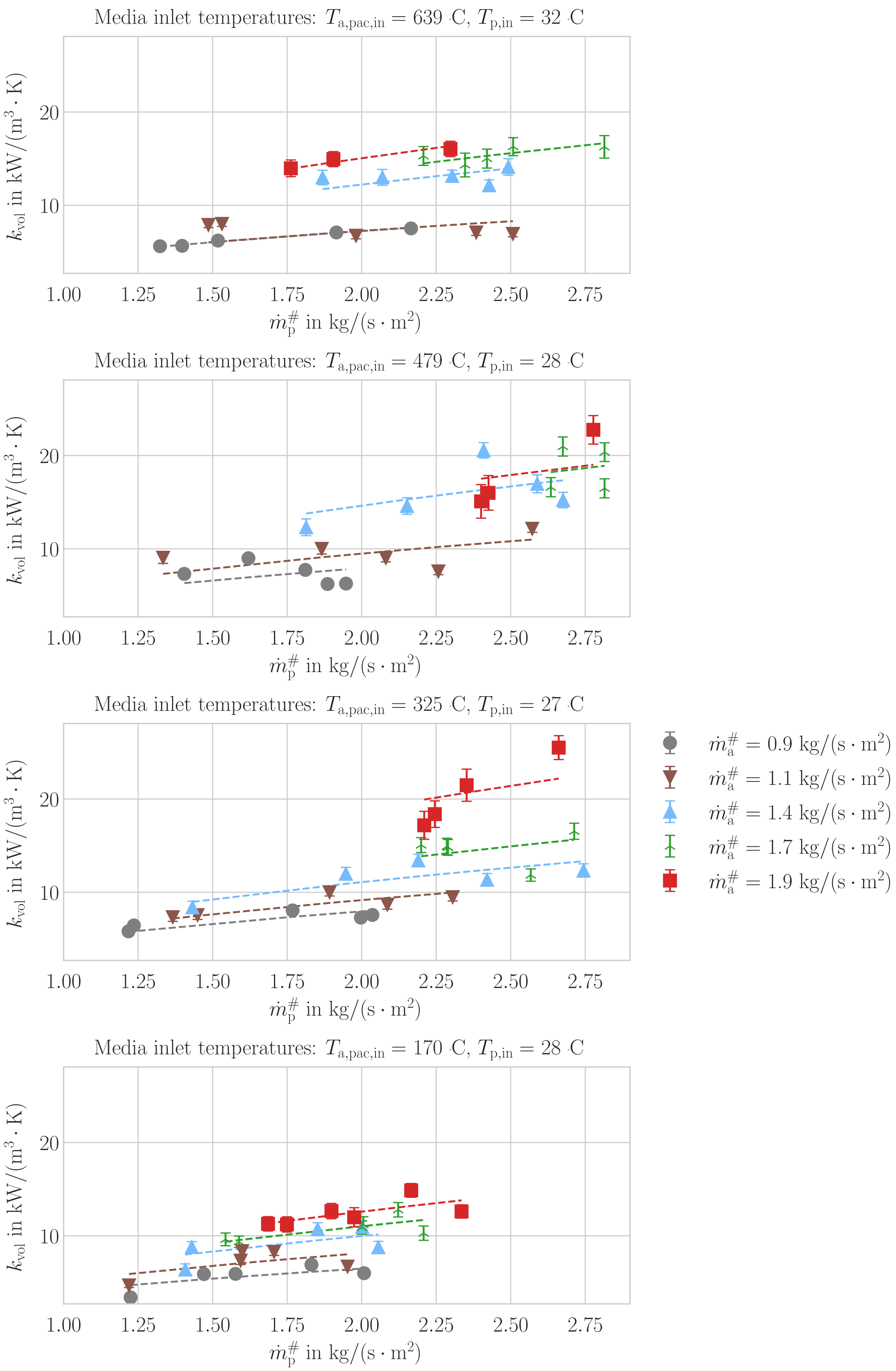

Fig. 45 Volumetric heat transfer coefficient at four temperature levels with varying media flow rates.

To compare the experimental results with the available data, as in section 4.2.2.4, the closest temperature range of $T_{\mathrm{a,pac,in}} = 325\,°\mathrm{C}$ was chosen to frame the experiments to the available data in literature, see Fig. 46. As in Fig. 42, it could be erroneously assumed that the experimental results could be a continuation of the work provided by the two available reference works of Verver and Van Swaaij [113] and Nagata, Ohara [146]. However, the same has to be considered as outlined in section 4.2.2.4. The theoretical operating limits of the particles have to be considered, see Tab. 12. Accordingly, the volumetric heat transfer coefficients provided by Verver and Van Swaaij [113] range up to $8\,\mathrm{kW/m^3}$. A direct comparison of the same air flow rates, e.g. $0.9\,\mathrm{kg_{a,Rei24,325\,°C}/(s \cdot m^2)}$ and $1.0\,\mathrm{kg_{a,Ver86,250\,°C}/(s \cdot m^2)}$, shows that the heat transfer capacities are almost equal. With increasing air flow rates, the values of k_{vol} increase. Nagata, Ohara [146] also provide their experimental results directly as volumetric heat transfer in $\mathrm{kW/m^3}$, normed to V_{HX} of their investigated TFHX. However, the values seem rather high compared to the values for the same particle diameter given by Verver and Van Swaaij [113]. Furthermore, the power densities given by Nagata, Ohara [146] in Fig. 42 are rather in the same range as those of Verver and Van Swaaij [113], or even slightly lower. This is why the rather high values for the volumetric heat transfer mentioned in the work of Nagata, Ohara [146] cannot be further traced and interpreted with the data provided. Verver and Van Swaaij [113] provide experimental data at $T_{\mathrm{a,in}} = 400\,°\mathrm{C}$ of only one, rather low air flow rate $0.7\,\mathrm{kg_a/(s \cdot m^2)}$. Like in Fig. 45 k_{vol} seems not to change significantly with a change of temperature from 250 °C to 400 °C, see Fig. 46.

It can be assumed that higher airflow experiments with the small 0.37 mm particles would not have been possible because of flooding or other unstable flow conditions. The theoretical air flow rate is $0.8\,\mathrm{kg_{400\,°C}/(s \cdot m^2_{\epsilon_{eff}=0.5})}$, see Tab. 27. As in section 4.2.2.4, the comparison with the reference literature must be made with care. Fig. 46 shows that the developed TFHX is able to provide heat transfer coefficients up to $20\,\mathrm{kW/m^3}$. The used 1 mm particles allow a theoretically stable operation up to $2.88\,\mathrm{kg_p/(s \cdot m^2)}$. However, as outlined in section 4.2.2.4, it can be assumed that the apparent superiority in volumetric heat transfer capability is not necessarily based on the fact of the larger particle diameter and the resulting potentially higher media flow rates, but could rather be the result of a particle-focused optimization of the packing structure carried out in chapter 3 and section 4.1.

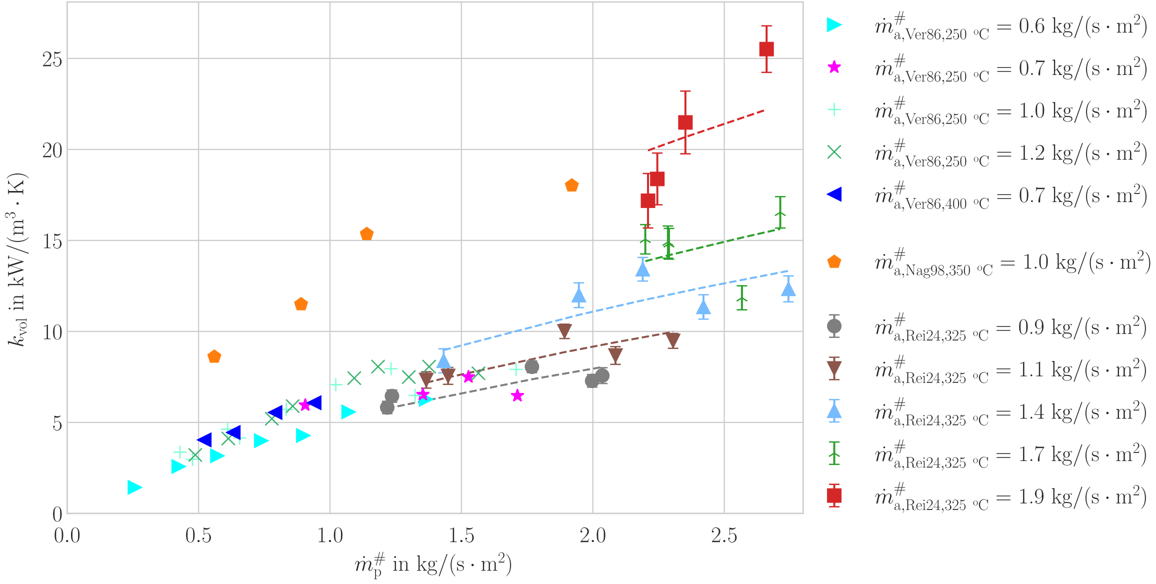

Fig. 46 Volumetric heat transfer rate in a TFHX. Results of this work, compared to literature at approximately equal temperature levels, with varying air and particle flow rates.

4.2.2.5 Number of transfer units

The Number of Transfer Units (NTU) values are a standardized method of nominalizing heat transfer to a dimensionless number that represents a dimensionless heat transfer surface for the heat exchanger and can be determined separately for each media flow in the HX. The higher the NTU, the higher the available surface for the heat transfer.

$$NTU = \frac{k\,A_{\mathrm{p,pac}}}{\dot{W}} \tag{64}$$

Whereas the uncertainty can be determined as follows:

$$u_{NTU} = \sqrt{\left(\frac{\partial NTU}{\partial k} u_k\right)^2 + \left(\frac{\partial NTU}{\partial A_{\mathrm{p,pac}}} u_{A_{\mathrm{p,pac}}}\right)^2 + \left(\frac{\partial NTU}{\partial \dot{W}} u_{\dot{W}}\right)^2} \tag{65}$$

with the corresponding partial derivatives.

$$\frac{\partial NTU}{\partial k} = \frac{A_{\mathrm{p,pac}}}{\dot{W}} \ \mathrm{in} \frac{\mathrm{m}^2\, s\, K}{\mathrm{J}} \tag{66}$$

$$\frac{\partial NTU}{\partial A_{\mathrm{p,pac}}} = \frac{k}{\dot{W}} \ \mathrm{in} \frac{1}{\mathrm{m}^2} \tag{67}$$

$$\frac{\partial NTU}{\partial \dot{W}} = -\frac{k\,A_{\mathrm{p,pac}}}{\dot{W}^2} \ \mathrm{in} \frac{\mathrm{K\,s}}{\mathrm{J}} \tag{68}$$

The heat capacity flow rate, $\dot{W}$, can be calculated for each media in the heat exchanger.

$$\dot{W} = \dot{m}\, c_p \ \mathrm{in} \frac{\mathrm{J}}{\mathrm{g\,K}} \tag{69}$$

with the corresponding uncertainty:

$$u_{\dot{W}} = \sqrt{\left(\frac{\partial \dot{W}}{\partial \dot{m}} u_{\dot{m}}\right)^2 + \left(\frac{\partial \dot{W}}{\partial c_p} u_{c_p}\right)^2} = \sqrt{\left(c_p\, u_{\dot{m}}\right)^2 + \left(\dot{m}\, u_{c_p}\right)^2} \tag{70}$$

Fig. 47 and Fig. 48 show the NTU values of the particle stream and the air stream. It can be seen in both graphs that the NTU values increase with increasing temperature level and increasing air flow rate. It would be expected that as the particle flow rate increases, the NTU values would also increase. A slight tendency in this direction can be interpreted for the two lowest temperature levels shown in Fig. 48. However, at particle flow rates of 2.0 $\mathrm{kg_p/(s \cdot m^2)}$ and above, one could assume that the determined NTU values might show some tendency to decrease, which would reinforce the assumption made in 4.2.2.4 that at a certain particle loading in the TFHX, the usability of the total particle surface area of all trickling particles $A_{\mathrm{p,pac}}$ might decrease due to particle agglomeration, causing the heat transfer coefficient, but also the corresponding NTU values, to decrease. However, in order to verify this assumption, future work should include additional experiments in a wider range of media flow ranges.

In designing the experimental setup for the present work, great emphasis was placed on characterizing the TFHX for media flow conditions in the range of approximately equal heat capacity flow rates in order to identify the operating conditions in the sweet spot. The emphasis in the design of the experimental campaign was to operate the test rig under these conditions rather than to vary the mass flow rates over a very wide range. Furthermore, in order to operate such a test bench over a wide range of particle and air mass flow rates, the experimental setup would have to be designed with other design emphases, since e.g. the lowest air mass flow rate, especially at high temperatures, is very limited to the minimum mass flow of the air heater, which is used to prevent damage to the air heater. As mentioned in 4.2.1.3, this could have been overcome by using a bypass system. Also, the minimum particle mass flow is limited by the particle diameter used, see section 4.1.1.3. The maximum particle flow was limited by the available ceiling height in the workshop and the corresponding maximum particle mass, in order to provide sufficient operating time to reach steady state conditions in the TFHX for a given mass flow. Depending on the temperature level, it took up to 4 to 5 hours to reach steady-state conditions. In order to measure and identify the full operating range of the TFHX, the test bench would have to be adapted or, even better, a scaled-up version of the heat exchanger would have to be installed in a full-scale test facility, such as the Julich Solar Tower.

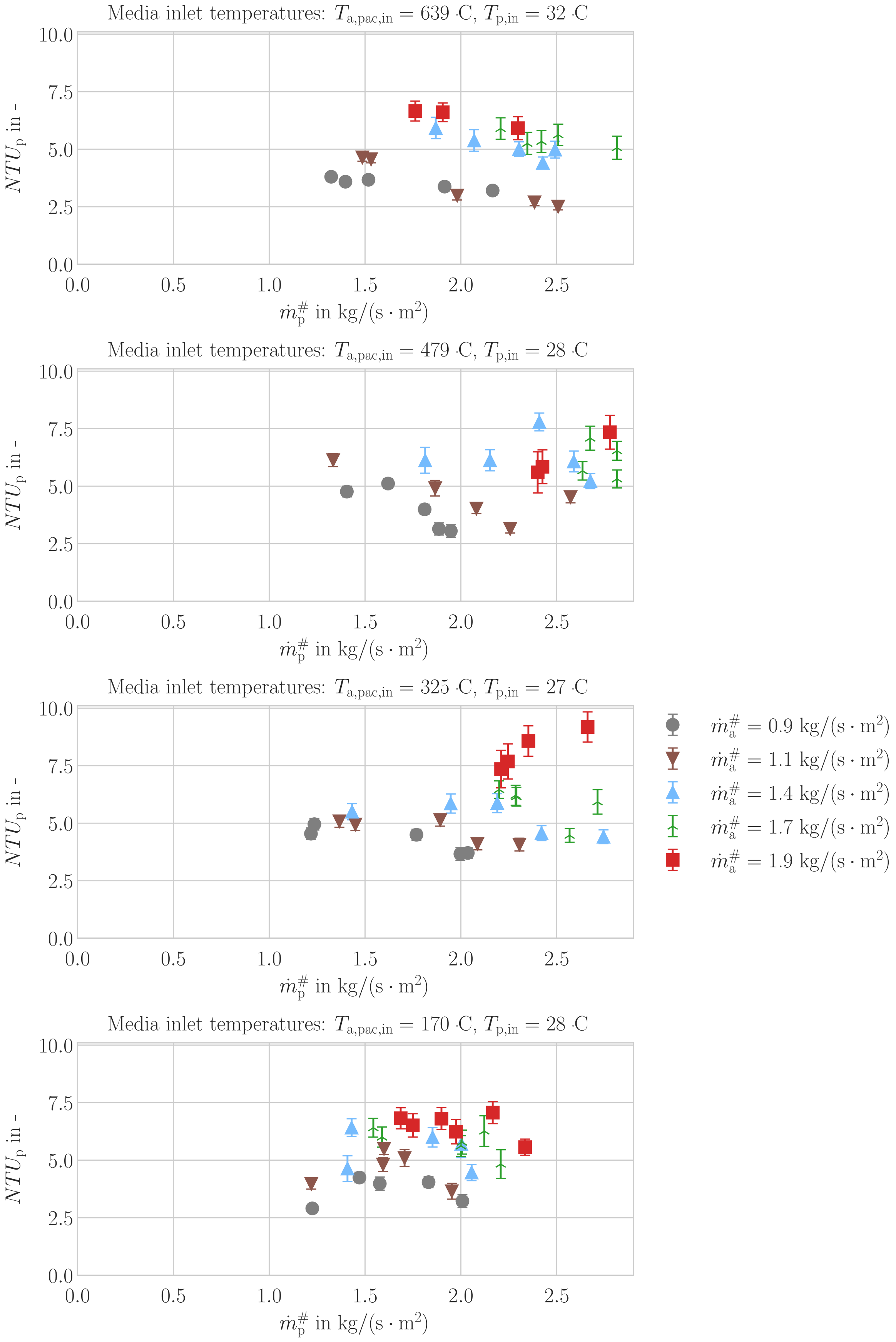

Fig. 47 *NTU* values of the particle flow at four temperature levels with varying media flow rates.

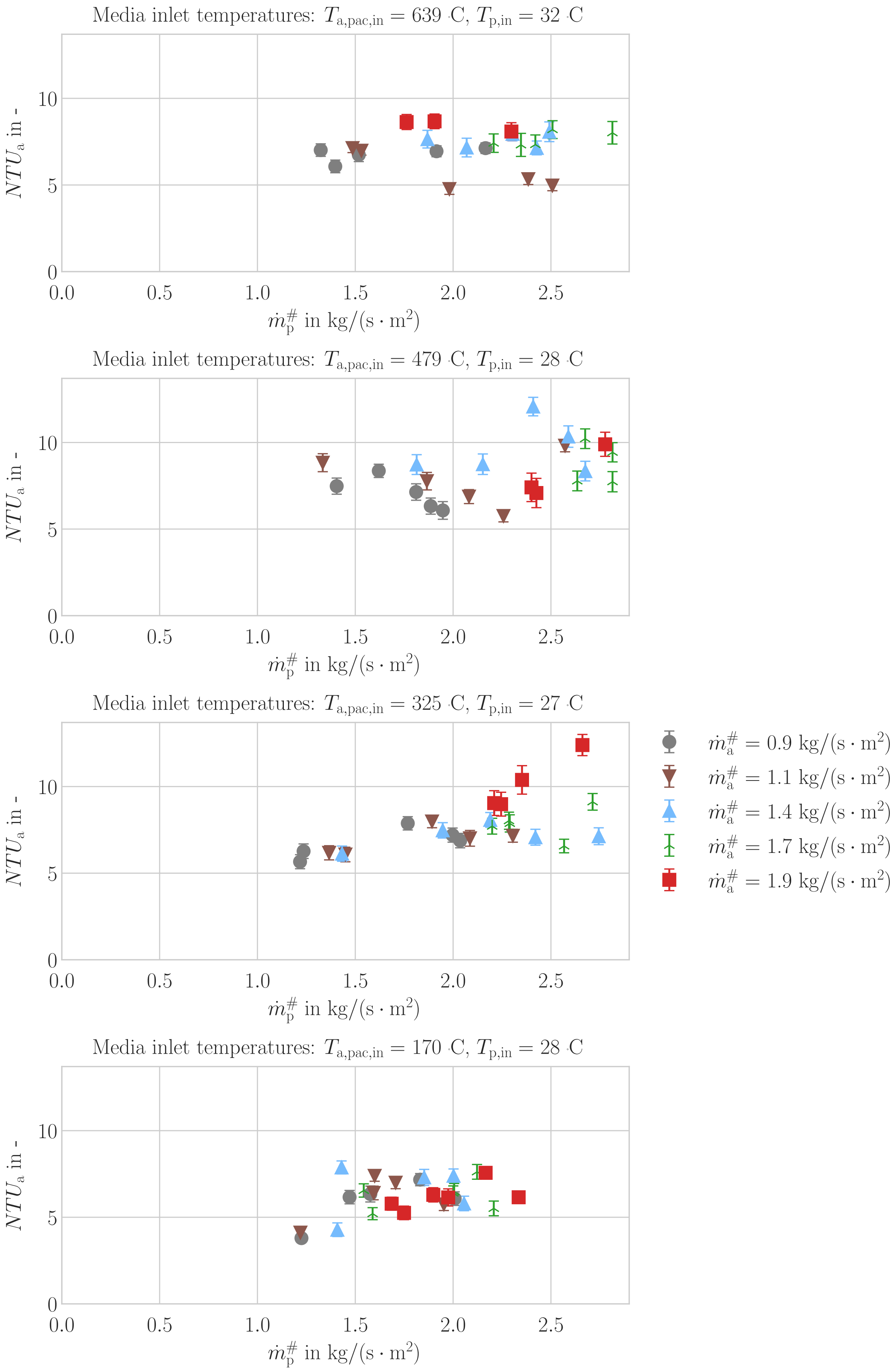

Fig. 48 *NTU* values of the air flow at four temperature levels with varying media flow rates.

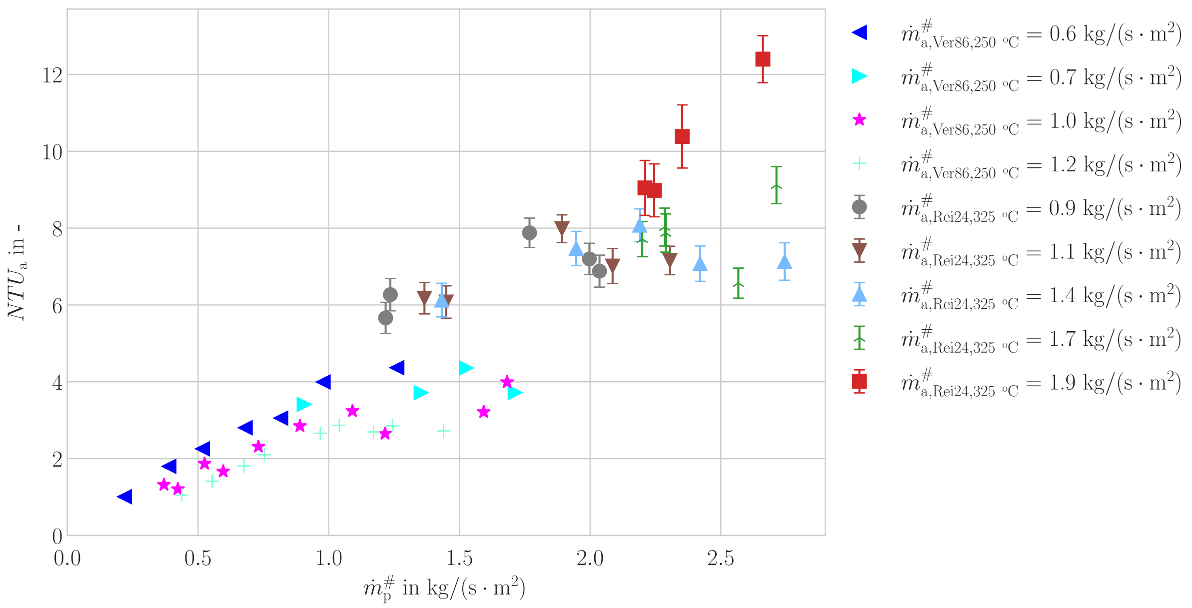

Fig. 49 *NTU* values of the air flow in a TFHX. Results of this work, compared to literature at approximately equal temperature levels, with varying air and particle flow rates.

In order to frame the obtained experimental results in the section with the available data, as in the previous sections, the closest temperature range of $T_{\mathrm{a,pac,in}} = 325$ °C is chosen to compare the experiments with the available data in the literature, see Fig. 49. Similar to Fig. 42 and Fig. 46, it could be assumed that the experimental results are a continuation of the work of Verver and Van Swaaij [113]. However, as described in sections 4.2.2.3 and 4.2.2.4, the theoretical operating limits of the individually selected particles must be taken into account, see Tab. 12. Accordingly, the NTU_a values provided by Verver and Van Swaaij [113] are close to 5. Considering the maximum operating condition of 0.37 mm particles with equal heat capacity flow rates, the theoretical maximum particle mass flow is around 1.5 $\mathrm{kg_{p=0.37\,mm}/(s \cdot m^2)}$, see Fig. 49. The 1 mm particles allow stable operation conditions up to 2.88 $\mathrm{kg_{p=1\,mm}/(s \cdot m^2)}$, see Tab. 12, which provides NTU values for air up to 10 and higher. A direct comparison of similar air flow rates e.g. 0.9 $\mathrm{kg_{a,Reic24,325\,°C}/(s \cdot m^2)}$ and 1.0 $\mathrm{kg_{a,Ver86,250\,°C}/(s \cdot m^2)}$, shows that the experimental NTU_a values range up to 8 and 4, respectively. This represents the overall observation that the NTU values of the developed TFHX can be increased by approximately 100 % compared to the available data in the literature.

4.2.2.6 Pressure drop in packed column

Complimentary to the thermal analysis of the TFHX, also the pressure drop was monitored and recorded throughout the course of the cold and hot test campaigns. To quantify and describe the pressure drop, or relative pressure, of the gas flow along the height of the packed column, $p_{\mathrm{rel,HX}}$, an ABB 266MST relative pressure sensor was integrated into the experimental apparatus, as illustrated in Fig. 19 and detailed in A.3.1. Since throughout this study, the pressure is consistently referenced to air, thus the additional subscript "a" is omitted for brevity.

The determined pressure drop within the packed column can be understood as superposition of the pressure drop, caused by the packing structure and by the trickling particles [113].

$$p_{\mathrm{rel,HX}} = p_{\mathrm{rel,pac}} + p_{\mathrm{rel,p}} \tag{71}$$

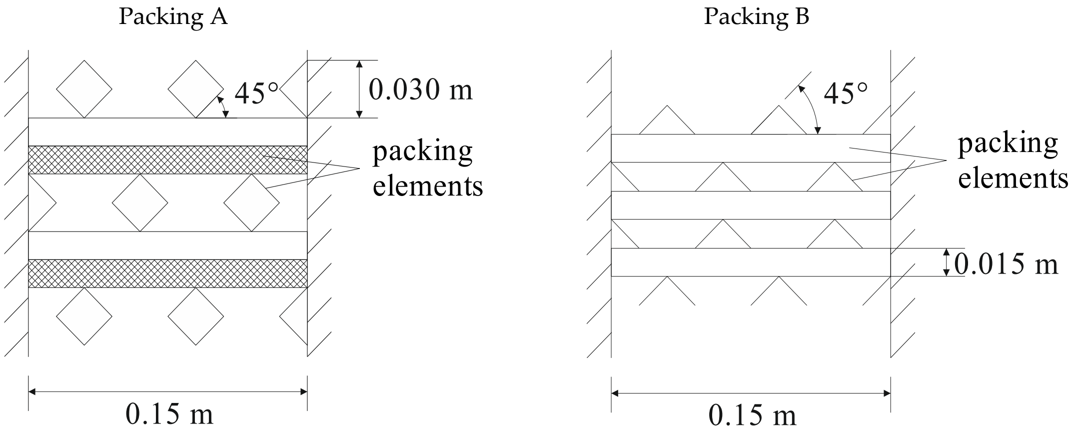

Fig. 50 Different investigated packing structures by Verver and Van Swaaij [113].

In the field of trickling reactors, it is typical to normalize the pressure drop with the height of the packed column, h_{HX}. p'_{rel} indicates a normalization along the packing height inside the reactor or heat exchanger. By normalizing, a comparability with other works can be achieved.

$$p'_{\mathrm{rel}} = \frac{p_{\mathrm{rel}}}{h_{\mathrm{HX}}} \tag{72}$$

The corresponding uncertainty can be determined with:

$$u_{p'_{\mathrm{rel}}} = \sqrt{\left(\frac{\partial p'_{\mathrm{rel}}}{\partial p_{\mathrm{rel}}} u_{p_{\mathrm{rel}}}\right)^2 + \left(\frac{\partial p'_{\mathrm{rel}}}{\partial h_{\mathrm{HX}}} u_{h_{\mathrm{HX}}}\right)^2} = \sqrt{\left(\frac{1}{h_{\mathrm{HX}}} u_{p_{\mathrm{rel}}}\right)^2 + \left(\frac{p_{\mathrm{rel}}}{h_{\mathrm{HX}}^2} u_{h_{\mathrm{HX}}}\right)^2} \tag{73}$$

Verver and Van Swaaij [113] determined in their work the pressure drop of the packed column with and without particle flow. They investigated two distinct packing types, designated as "packing A" and "packing B" as illustrated in Fig. 50. Exanimating the pressure drop with absence of particles, the two authors found that $p'_{\mathrm{rel,pac}}$ in packing A was lower than in packing B. Also, they found, that the heat transfer capacity in packing A is lower than packing B. The reduced pressure drop observed for packing A can be attributed to a more favorable aerodynamic configuration, with the airflow passing in an upward direction starting from the bottom [113]. The higher heat transfer capacity of packing B can be explained by the reduction in the falling distance from 30 mm to 15 mm. This results in an increased residence time of the particles within the packing structure, thereby enhancing the particle hold-up and surface area contributing to the heat transfer, as observed in [113]. This is in accordance with the findings of this work, as detailed in section 4.1.2.1. Given that the primary objective of this study is to optimize the heat transfer capacity in a trickle flow heat exchanger, only packing B will be utilized as a reference.

In the absence of particles, the pressure drop only of the packed column, $p'_{\mathrm{rel,pac}}$, was measured for different air temperatures and flow rates. Fig. 51 illustrates the pressure drop in the absence of particle flow for varying air flow rates of the "w10 h02 n3 z10" packing, in comparison to the packing B as described by Verver and Van Swaaij [113]. The identified packing structure exhibits a lower pressure drop than that observed in the reference work. This can be attributed to the unfavorable aerodynamic geometry of the B packing, which is composed of stacked angular metal strips, resulting in a relatively high pressure drop in the direction of the air flow. Additionally, the "w10 h02 n3 z10" does not offer the optimal aerodynamic configuration and could be further geometrically refined to reduce the pressure drop. One potential approach is the incorporation of triangular-shaped bar elements oriented with the apex of the triangle downwards. This would provide a more favorable aerodynamic shape while maintaining the flat surface, allowing static particles to accumulate and absorb the kinetic energy of the trickling particles.

The pretests, conducted to determine the pressure drop of the packing structure without particle flow for varying air flow rates, enabled the calculation of the coefficient of pressure loss of the packing structure, ζ_{pac}. Consequently, the pressure values are not normalized. The conditions for air density and velocity are averaged from the packing inlet and outlet.

$$\zeta_{\mathrm{pac}} = 2\,\frac{p_{\mathrm{rel,HX}}}{\rho_{\mathrm{a}}\,u_{\mathrm{a,0}}^2} \approx 2\,\frac{p_{\mathrm{rel,HX}}}{\bar{\rho}_{\mathrm{a}}\,\bar{u}_{\mathrm{a,0}}^2} \tag{74}$$

With the corresponding uncertainty:

$$\begin{aligned} u_{\zeta_{\mathrm{pac}}} &= \sqrt{\left(\frac{\partial \zeta_{\mathrm{pac}}}{\partial p_{\mathrm{rel,HX}}} u_{p_{\mathrm{rel,HX}}}\right)^2 + \left(\frac{\partial \zeta_{\mathrm{pac}}}{\partial \rho_{\mathrm{a}}} u_{\rho_{\mathrm{a}}}\right)^2 + \left(\frac{\partial \zeta_{\mathrm{pac}}}{\partial u_{\mathrm{a,0}}} u_{u_{\mathrm{a,0}}}\right)^2} \\ &= \sqrt{\left(\frac{2}{\rho_{\mathrm{a}}\,u_{\mathrm{a,0}}^2} u_{p_{\mathrm{rel,HX}}}\right)^2 + \left(-2\,\frac{p_{\mathrm{rel,HX}}}{\rho_{\mathrm{a}}^2\,u_{\mathrm{a,0}}^2} u_{\rho_{\mathrm{a}}}\right)^2 + \left(-4\,\frac{p_{\mathrm{rel,HX}}}{\rho_{\mathrm{a}}\,u_{\mathrm{a,0}}^3} u_{u_{\mathrm{a,0}}}\right)^2} \end{aligned} \tag{75}$$

The air velocity is referenced to the superficial velocity, $u_{\mathrm{a,0}}$, which would occur in the empty heat exchanger channel in the absence of the packing structure.

$$u_{\mathrm{a,0}} = \frac{\dot{m}_{\mathrm{a}}}{\rho_{\mathrm{a}}\,A_{\mathrm{HX}}} = \frac{\dot{m}_{\mathrm{a}}^{\#}}{\rho_{\mathrm{a}}} \tag{76}$$

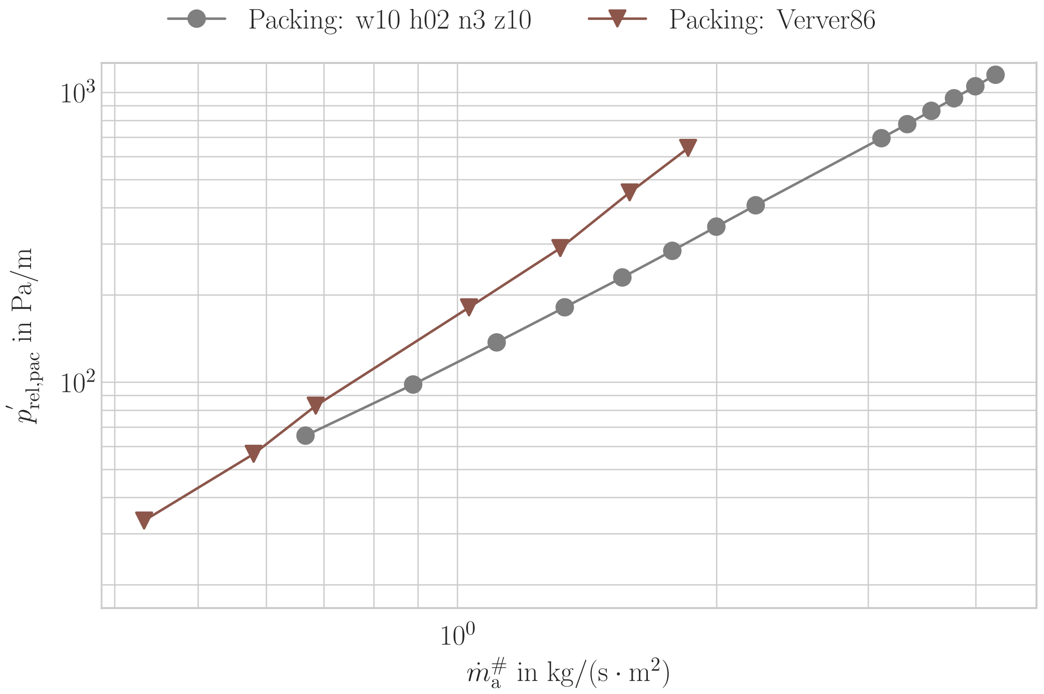

Fig. 51 Pressure drop of packing structure, in comparison to literature at ambient temperatures.

With the corresponding uncertainty:

$$u_{u_{\mathrm{a,0}}} = \sqrt{\left(\frac{\partial u_{\mathrm{a,0}}}{\partial \dot{m}_{\mathrm{a}}^{\#}} u_{\dot{m}_{\mathrm{a}}^{\#}}\right)^2 + \left(\frac{\partial u_{\mathrm{a,0}}}{\partial \rho_{\mathrm{a}}} u_{\rho_{\mathrm{a}}}\right)^2} = \sqrt{\left(\frac{1}{\rho_{\mathrm{a}}} u_{\dot{m}_{\mathrm{a}}^{\#}}\right)^2 + \left(-\frac{\dot{m}_{\mathrm{a}}^{\#}}{\rho_{\mathrm{a}}^2} u_{\rho_{\mathrm{a}}}\right)^2} \tag{77}$$

In calculating the Reynolds number within the heat exchanger, the same mean values for air density and air velocity were employed. Additionally, the characteristic diameter was determined using the hydraulic diameter of the heat exchanger channel.

$$Re_{\mathrm{HX}} = \frac{\rho_{\mathrm{a}}\, u_{\mathrm{a,0}}\, d_{\mathrm{h}}}{\eta_{\mathrm{a}}} = \frac{u_{\mathrm{a,0}} \left(4 \frac{w_{\mathrm{HX}}^2}{4\, w_{\mathrm{HX}}}\right)}{\nu_{\mathrm{a}}} = \frac{u_{\mathrm{a,0}}\, w_{\mathrm{HX}}}{\nu_{\mathrm{a}}} \tag{78}$$

With the corresponding uncertainty:

$$\begin{aligned} u_{Re_{\mathrm{HX}}} &= \sqrt{\left(\frac{\partial Re_{\mathrm{HX}}}{\partial u_{\mathrm{a,0}}} u_{u_{\mathrm{a,0}}}\right)^2 + \left(\frac{\partial Re_{\mathrm{HX}}}{\partial w_{\mathrm{HX}}} u_{w_{\mathrm{HX}}}\right)^2 + \left(\frac{\partial Re_{\mathrm{HX}}}{\partial \nu_{\mathrm{a}}} u_{\nu_{\mathrm{a}}}\right)^2} \\ &= \sqrt{\left(\frac{w_{\mathrm{HX}}}{\nu_{\mathrm{a}}} u_{u_{\mathrm{a,0}}}\right)^2 + \left(\frac{u_{\mathrm{a,0}}}{\nu_{\mathrm{a}}} u_{w_{\mathrm{HX}}}\right)^2 + \left(-\frac{u_{\mathrm{a,0}}\, w_{\mathrm{HX}}}{\nu_{\mathrm{a}}^2} u_{\nu_{\mathrm{a}}}\right)^2} \end{aligned} \tag{79}$$

In a similar manner, the correlation between the coefficient of pressure and the Reynolds number in the packing structure can be expressed as follows:

$$\zeta_{\mathrm{pac}} = 2 \frac{p_{\mathrm{rel,HX}}}{\bar{\rho}_{\mathrm{a}} \left(\frac{Re_{\mathrm{HX}}\, \bar{\nu}_{\mathrm{a}}}{w_{\mathrm{HX}}}\right)^2} \tag{80}$$

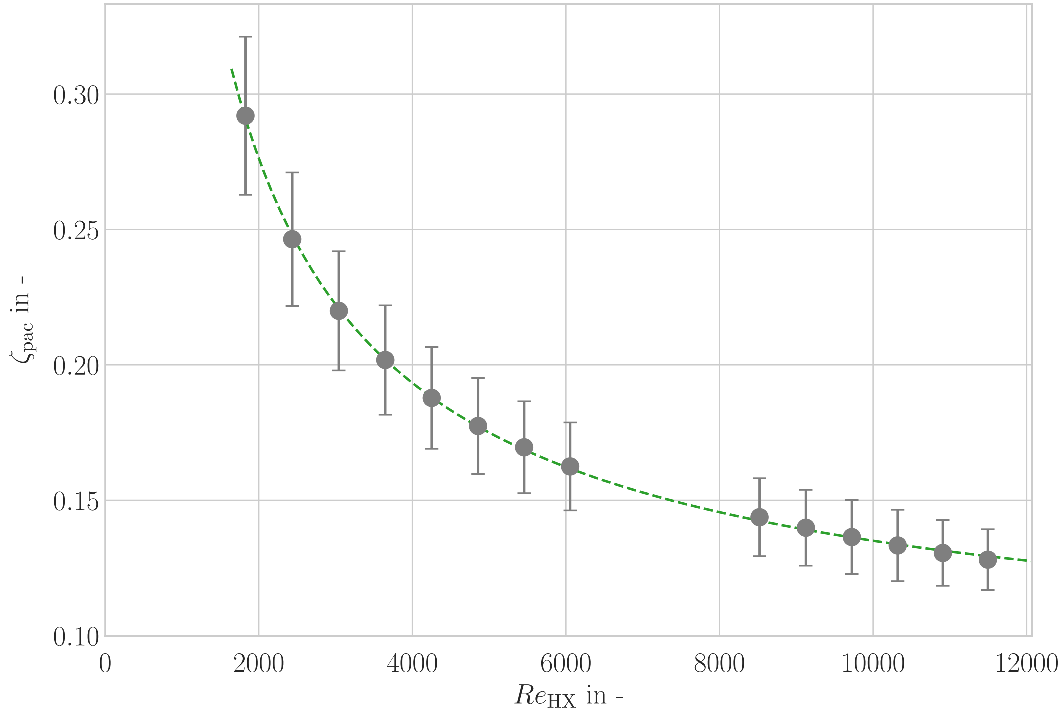

Fig. 52 Coefficient of pressure for w10 h02 n3 z10 packing structure for varying Reynolds numbers.

Fig. 52 illustrates the coefficient of pressure as a function of the Reynolds number in the heat exchanger, $\zeta_{\mathrm{pac}}(Re_{\mathrm{HX}})$, by employing (80) for the determined relative pressure in the packed column under varying air flow conditions. An exponential fit was performed for the aforementioned measurement points, resulting in the following correlation of $\zeta_{\mathrm{pac}}(Re_{\mathrm{HX}})$, with the uncertainty not exceeding 10 %.

$$\zeta_{\mathrm{pac}} = 83.4849 \frac{1}{Re_{\mathrm{HX}}^{0.7968}} + 0.0808$$

$$\text{for } 1800 \leq Re_{HX} \leq 11500\,; R^2 = 0.9997 \qquad (81)$$

The normalized pressure drop is determined for different air inlet temperatures in the conducted experiments. Fig. 53 illustrates that with increasing particle flow rate, the pressure drop increases across all temperature stages. However, the rise in pressure drop is less pronounced than the corresponding rise in air flow. Additionally, a slight increase in pressure drop is evident with elevated air inlet temperatures.

The normalized pressure drop, which is solely attributable to the particle flow, $p'_{\mathrm{rel,p}}$, can be determined by subtracting the packing-caused pressure drop by applying (71) and (80). This is depicted in Fig. 54 and shows the same behavior of the pressure drop as observed in Fig. 53. For very low air flow rates, the pressure drop can be within the range of uncertainty and may be considered negligible.

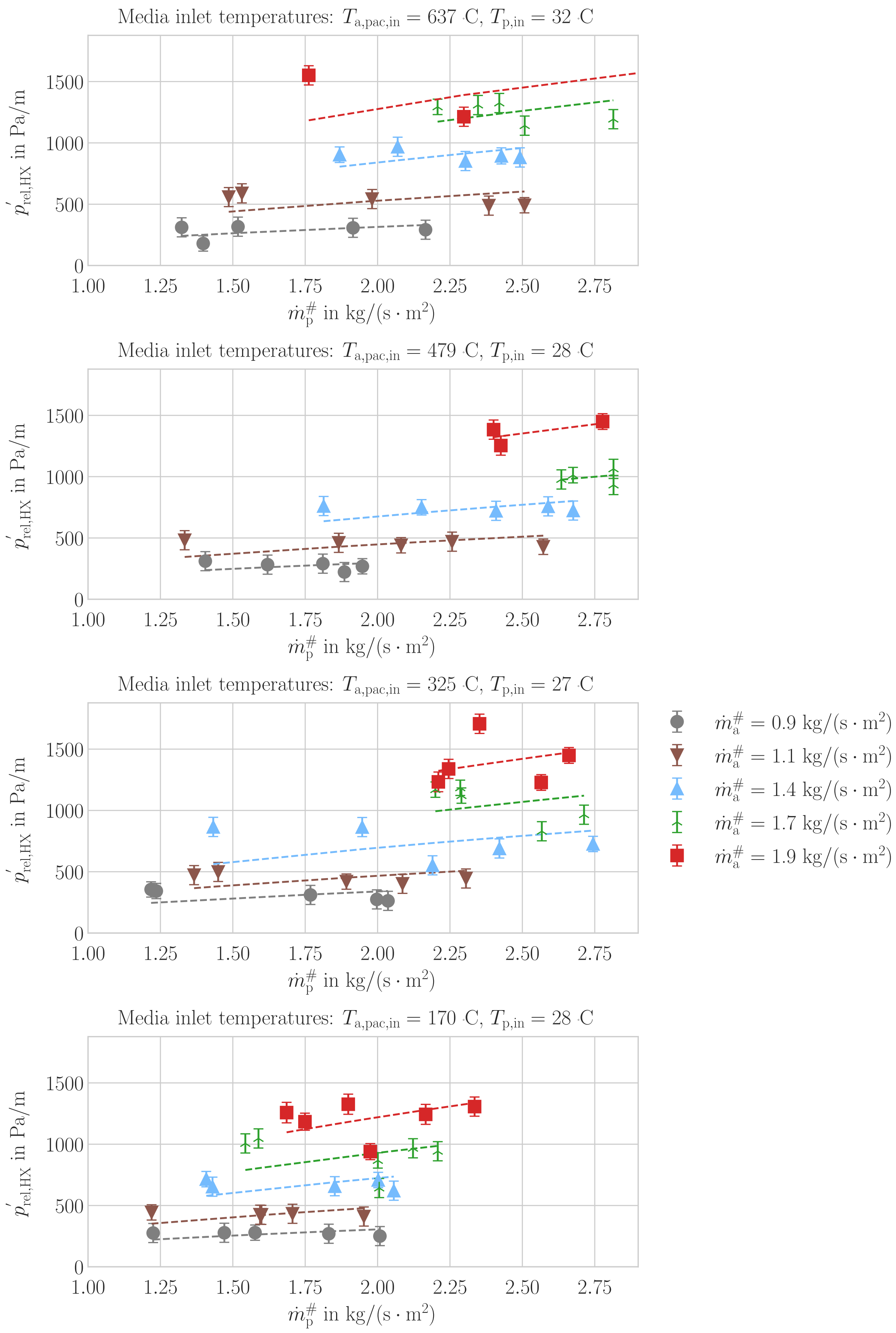

Fig. 53 Normalized HX pressure drop at four temperature levels with varying media flow rates.

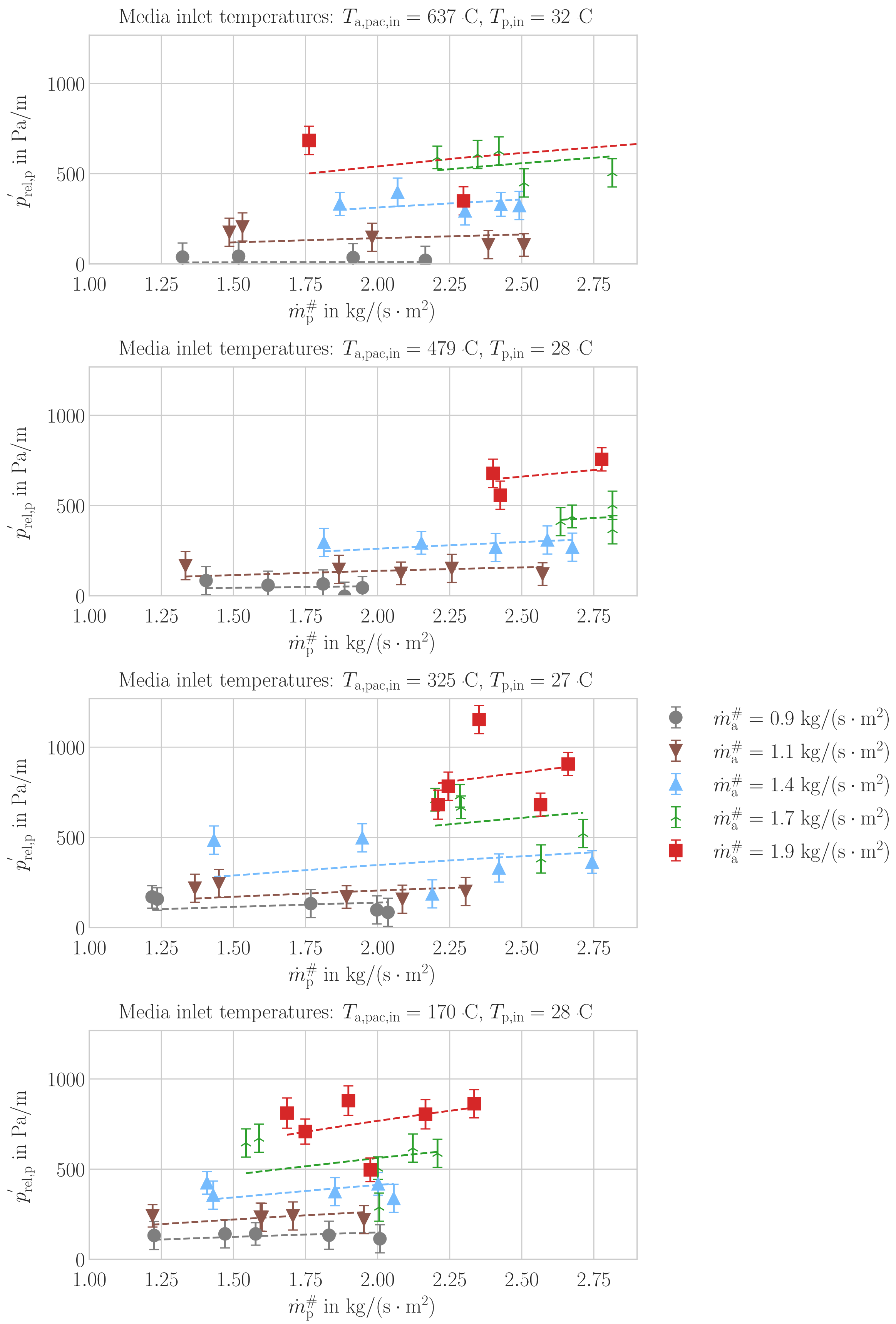

Media inlet temperatures: $T_{\mathrm{a,pac,in}} = 637$ C, $T_{\mathrm{p,in}} = 32$ C

Media inlet temperatures: $T_{\mathrm{a,pac,in}} = 479$ C, $T_{\mathrm{p,in}} = 28$ C

Media inlet temperatures: $T_{\mathrm{a,pac,in}} = 325$ C, $T_{\mathrm{p,in}} = 27$ C

Media inlet temperatures: $T_{\mathrm{a,pac,in}} = 170$ C, $T_{\mathrm{p,in}} = 28$ C

Fig. 54 Normalized particle pressure drop at four temperature levels with varying media flow rates.

4.2.3 Conclusive discussion of the tested TFHX with an optimized packing structure

The previous section 4.2.2 outlined the results of the experimental characterization of the heat transfer capabilities for the packing structure optimized in section 4.2.1 Due to the unavailability of suitable peripherals to adjust not only the flow rate but also the inlet temperature of the particle flow, the experiments were performed with particle flows entering the TFHX at ambient temperature, while the air flow was adjusted in its flow rate and inlet temperature. It is considered equally comparable to the heat transfer capabilities if the particle feed is cold while the air flow enters the HX hot, or vice versa. Only when approaching the boundary conditions of flooding within the TFHX at higher air flow rates, the unit shows a tendency to become more likely to clog with particles if the air inlet is hotter than the particle inlet. In this case, the hotter part of the HX is at the bottom of the unit. Since the theoretical airflow rates to reach end conditions are lower in hotter areas than in areas with cooler air, see Tab. 24, it is more likely that the TFHX will clog from the bottom up when local terminal conditions are reached. In an operation with hot particles, fed from above, and cooler gas, fed from below, the region where flooding is more likely to occur first is transferred to the upper part of the TFHX, why a constipation of the unit is less likely, since potentially an incipient particle flooding process would rather blow out the particles with the hot air flow towards the exhaust cyclone. Both operating conditions in which flooding would occur in the TFHX are undesirable, but it is assumed that a tendency to flood in the upper part of the TFHX would provide an operating mode more robust to constipation of the packed column than in the lower part. Since the present work did not aim to perform heat transfer experiments in the range of particle flooding, the presented results are considered independent of the flow direction of hot and cold media.

Regarding the thermal performance of the investigated trickle-flow heat exchanger, it was found that the volumetric heat transfer coefficient k_{vol}, which describes the transferable heat per volume of the unit, V_{HX}, should be used to describe the heat transfer capabilities. The reference works [113, 146] also provide k_{vol} directly in kW/m^3. The volumetric heat transfer coefficient, the transferable heat capabilities, such as the number of transfer units of the developed TFHX show up to double in capabilities, regarding the two available reference systems. However, as already discussed in the previous sections, it must be assumed that the increase in heat transfer capabilities is rather the result of the optimized packing structure for the particles used, which provides a higher residence time of the particles, compared to the reference work. It is assumed that also for the smaller particles in the reference work [113, 146], using 0.37 mm, higher power densities could be achieved if the packing structure had been optimized accordingly. As mentioned in section 4.2.2.3, it is assumed that higher power densities could be achieved with the smaller particles, but the falling height of a corresponding design would be lower and the cross-sectional area would have to be designed larger, which entails the technical challenge of evenly distributing the particle feed flow over a wider area of the packed column at high temperatures. Nevertheless, it has been demonstrated that a well-designed packing geometry can significantly increase the heat transfer capability. Following the analogy of heat transfer to mass transfer, benefits in the area of mass transfer can also be expected for the applications of the trickle flow reactor discussed in section 2.2.3.

5 Conceptual design of a TFHX

In the present work the development and investigation of a trickle-flow heat exchanger was described, with emphasis for the application in a particle based solar tower system. The envisioned application field is the use of the TFHX to transfer the thermal heat in the hot particles with temperatures up to 1,000 °C to a working gas, like air. In the present work, a test bench was developed to investigate the heat transfer capabilities for air inlet temperatures up to 640 °C. The current knowledge in literature of similar investigation to date was limited to solely 400 °C. Hence, the findings of the present work enhanced the current state of knowledge for the heat transfer performance of trickle flow reactors, used for air-particle direct-contact operation. While this work does not claim to provide a comprehensive constructive solution for a correspondingly large-scale application, in the following two sections, primary upscaling ideas and cost estimations were made to provide a guidance and basis for further development.

5.1 Scaling and part load operation

As mentioned in 4.2.2.3, the thermal losses of the experiments for high temperatures and flow rates range in its extrema up to 25 %, based on the transferred thermal heat into the particles. The high thermal losses are based on the unfavorable ratio of the rather narrow and high heat exchanger channel of $V_{\mathrm{HX}} = 0.875\ \mathrm{m} \times (0.05\ \mathrm{m})^2 = 2.2 \cdot 10^{-3}\ \mathrm{m}^3$. Also, it was mentioned, to conduct further experimental testing in an upscaled version of the developed TFHX, to reduce the impact of thermal losses to increase further the thermal performance.

Large, Guignon [127] mention in their work, that one reason that inhibited the further development of TFHX systems, is the lack of information regarding the particle flow behavior and instabilities in a scaled-up version. As described in section 2.2.3, particle segregation and correspondingly poor reactor efficiency can occur, when the particles are not feed into the packing evenly. This is relevant, since the scaling of a TFHX only could be done by increasing the cross-sectional area of the unit, since the height, h_{HX}, solely is a design criterion that determines the achievable temperature change in the media flow. A HX height in the current work of $h_{\mathrm{HX}} = 0.875\ \mathrm{m}$ was capable to provide a temperature change in the particle flow up to more than 400 K. If higher temperature changes in a correspondingly designed TFHX are desired, the height must be adapted accordingly. Solely Saatdjian and Large [142], using 25 mm Pall-rings, provide a minimum design criterion for unstructured packed columns. They state that for scale-up and efficient operation of the reactor, at least a column to packing ratio of greater than 8 is required. It is not known if this design criteria can be applied for regular packed elements.

As outlined before, it is considered as a mayor technical challenge to evenly distribute the grain flow in a wide spread cross-sectional area in a upscaled version of a TFHX. Previous work mentioned and investigated technical measures, as outlined in section 2.2.3, however it is considered as not applicable, if a scaled-up concept would be used in operation with particle feeding temperatures at the envisioned temperature range of up to 1,000 °C. This is why it is considered as preferable to operate the TFHX as a scaled-up version, that is constituted by a two-dimensional array of multiple, discrete TFHX-segments.

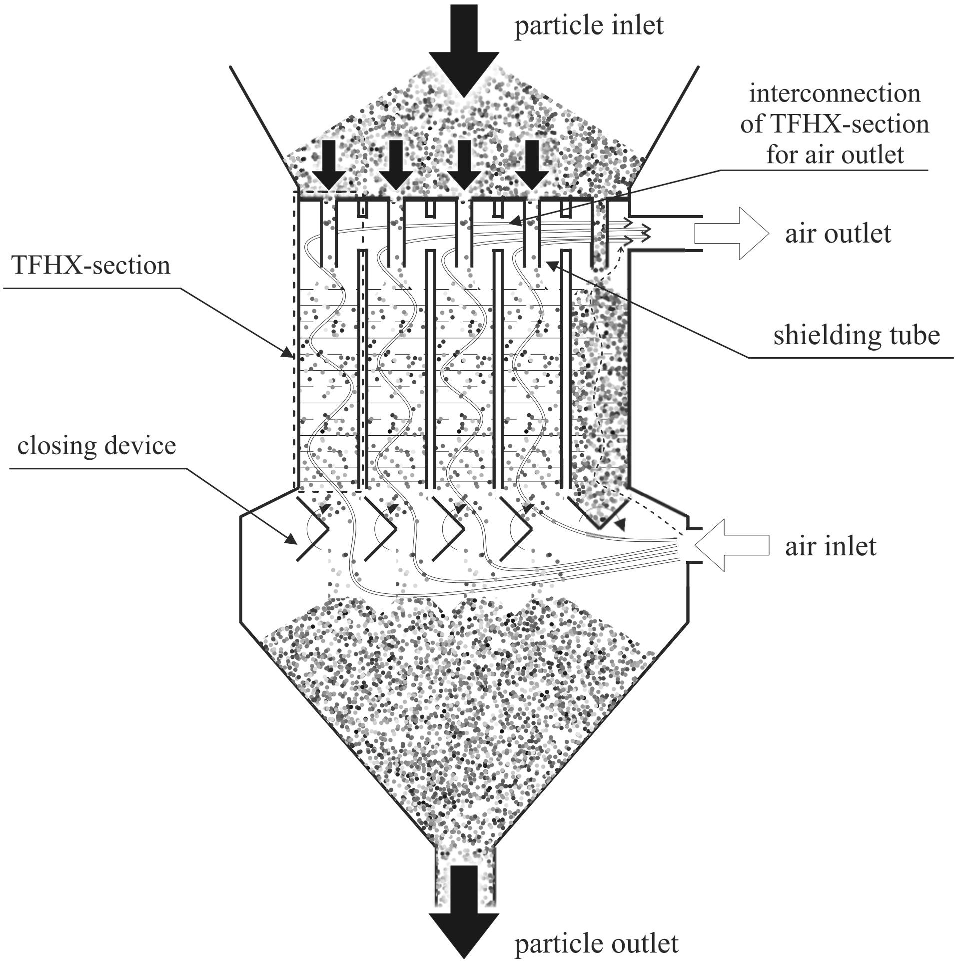

Fig. 55 Conceptual design of a scaled TFHX, capable for discrete part load operation.

A comparable segmented scaling approach also was proposed by Maarup [108] to attain a certain power level, by proposing an one-dimensional alignment of multiple HX units, operating each in its optimized working conditions. Correspondingly, each TFHX-segment would be equipped on the top with a fixed orifice plate, that allows to operate each discrete TFHX-segment in its optimal working condition. For the investigated unit in this work, the corresponding mass flow rate would be in the range of 2.5 $\mathrm{kg/(s \cdot m^2)}$, providing power densities over 1,000 $\mathrm{kW/m^3}$ for air inlet temperatures at the packing of 640 °C, see Fig. 40. Within those working conditions, the temperature change of the particle flow is capable to reach over 400 K for $h_{\mathrm{HX}} = 0.875$ m. For higher temperature changes, the packing height of just under a meter would have to be increased accordingly. According to Fig. 53, the pressure drop can be estimated for the measured temperature ranges to approximately 1,500 Pa in the design point. Presuming that the determined pressure drops in a cross-sectional area of 50x50 mm can be applied also to cross sectional areas of other sizes, but the same number of magnitudes. To scale the HX system to a desired power level, a two-dimensional arrangement of TFHX-segments could be installed to one HX.

Fig. 55 shows a conceptual design to scale a trickle flow heat exchanger, by means of a horizontal arrangement of TFHX-segments. Like in the test bench in this work, see Fig. 35 in section 4, below each orifice plate a shielding tube is installed. In this upper area, the segments are interconnected to unify the air outlet of each segment to the air outlet of the TFHX. As mentioned before, it is intentionally preferred to operate each TFHX-segment permanently at its design conditions, why a fixed orifice plate for each segment is suggested. For part load operation single segments or a group of segments can be shoot down by flooding the channels with particles, causing them to block. Thereby the transferable power of the TFHX is reduced and the airflow predominantly passes through the unblocked segments, still in operation. The air flow in the segments flooded with particles adjusts according to an equal distribution of pressure drop in all TFHX-segments, blocked and unblocked. Since the coefficient of pressure loss is much higher in the flooded segments, accordingly the air flow within those elements is reduced drastically. Fig. 55 depicts an array of five horizontal arranged TFHX-segments, showing the one segment on the right flooded with particles, by means of a closing device. The closing devices for example can be realized via rotating elements, that are set below each segment. In the shown design example v-shaped bars are used to flood the TFHX-segments with particles, by rotating the v-shape in a position, causing the particles to accumulate. To discharge the flooded particles out of the channels, the rotating elements are rotated further in a position where the particles can flow out unimpaired. For clarity, only a one-dimensional arrangement of TFHX-elements is shown in Fig. 35, however for scaling a two-dimensional scaling is recommended. Using rotating elements, to shut down TFHX-segments, not only one but several segments would be flooded according to the number of aligned segments along the rotating element, in a two-dimensionally scaled HX version. Alternatively, to rotating elements, also a sliding gate valve below the TFHX-segments could be installed as closing device, to partially flood the channels in the HX. Subdividing one slide gate to multiple stipes, would provide a multiple slide valve, providing potentially a more refined modulation of the HX power. However, based on the experience of the author it is recommended to use preferably rotating elements rather that translational elements in particle application. Especially in areas of increased temperatures the use of translational mechanical elements to manipulate particle flow provide a high risk of blocking and reduced durability.

5.2 Cost estimations and design example

Fig. 56 shows a conceptual design example for a TFHX segment. The segment was elaborated in collaboration with the EUGEN ARNOLD GmbH, specialized in high temperature insulation solutions and advanced sheet metal processing. The concept of the TFHX segment is composed of an inner rectangular channel with laser cut clippings, to place the bar elements in place. To avoid welding of the multiple bar elements in the inner channel and to guarantee air tightness along the segment height, the inner channel is assembled in an outer segment shell, see Fig. 56. The segment shell provides like the inner channel the same rectangular flange to bolt together the inner and outer segment parts and for installation in an HX array. On the bottom of each shell an expansion joints compensate the thermal expansion of each segment, while holding each element in position.

Tab. 13 shows the cost estimations for the in Fig. 56 depicted TFHX segment for varying cross sectional areas of the inner channel width. The cost estimation was elaborated in 2022, inflation, change of material cost and labor cost has to be considered accordingly to today's standards. In Tab. 13 it is shown that for a 50 x 50 channel size the material and loan cost have equal shares at the total cost. With increasing cross-sectional area, the total costs per segment reduces, but also the share of loan cost reduces drastically. It must be considered, that with an increasing cross-sectional area per TFHX segment, the hydrodynamic behavior of the trickling particles within the packing structure must be investigated and evaluated regarding the spatial particle density distribution. It is considered, that as function of packing geometry, particle type and size, envisioned operational parameters the segment cross-sectional area might provide limitations in scaling and by further increasing the channel width particle segregation could occur, leading to poor gas-particle interaction.

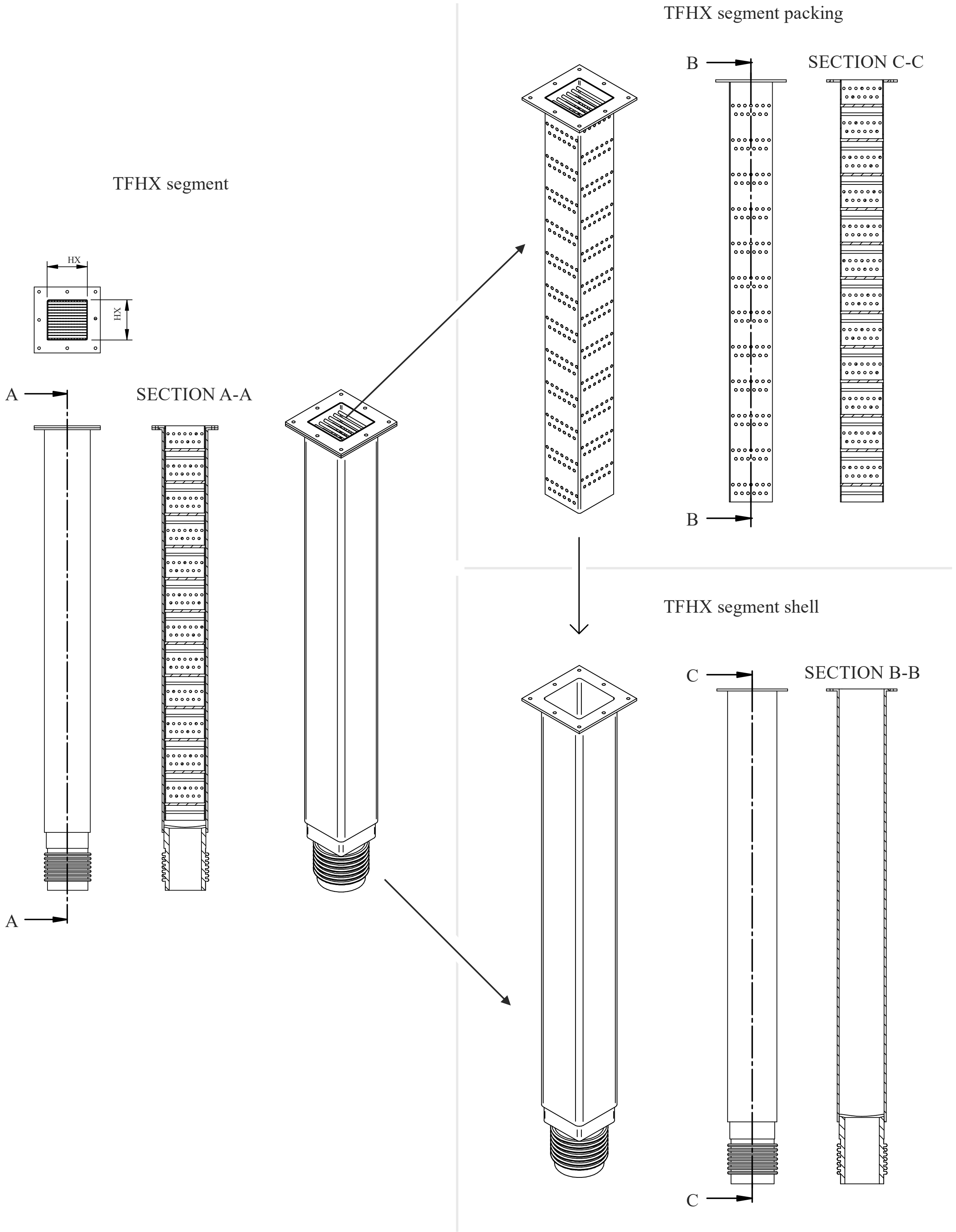

Fig. 56 Design example of a TFHX segment.

Tab. 13 Cost estimation of a TFHX segment for varying cross-sectional areas.

TFHX segment type	50 x 50	100 x 100	200 x 200	300 x 300
width w_{HX}	50 mm	100 mm	200 mm	300 mm
inner channel area	25 cm^2	100 cm^2	400 cm^2	900 cm^2
height	1000 mm	1000 mm	1000 mm	1000 mm
steel material cost	1284 €	3699 €	11928 €	25149 €
	51 €/m^2	37 €/m^2	30 €/m^2	28 €/m^2
loan cost	1147 €	2294 €	4588 €	7341 €
	46 €/m^2	23 €/m^2	11 €/m^2	8 €/m^2
total cost	2431 €	5993 €	16516 €	32490 €
	97 €/m^2	60 €/m^2	41 €/m^2	36 €/m^2

In the presented work a paced column with a (50 x 50) mm cross-sectional area was investigated, due to limited ceiling height and limited large-scale equipment availability to handle and circulate particle masses for higher flow rates. Already a packing with a (100 x 100) mm cross-sectional area world have required in absolute terms a four times higher mass flow, with a correspondingly higher particle mass in the test setup. While for the scope of this work w_{HX} was chosen to 50 mm, for a scaled version of a TFHX, consisting of multiple segments, it is considered to increase the channel width to 100 mm, when using 1 mm bauxite particles. This would require additional investigation to clarify if at this channel width the particles still show good particle distribution in space, or if already particle segregation occur.

A cost estimation of a trickle-flow heat exchanger, composed of two-dimensional array of 5 by 5 was performed. The used TFHX segments were set to a channel width of 100 mm and 1 m packing height. As mentioned before, a segment height of 0.875 m and the same operational condition as provided in this work, is capable to provide a temperature change of over 400 K for equal media heat capacity flow rates. Hence, for a segment height of 1 m, a temperature change of 450 K is estimated. For the total HX, a height of 2.8 m is assumed, considering the auxiliary areas above and below the segments to distribute the particles by means of a particle bed, see Fig. 55, the orifice plates, the shielding tubes in the air outlet section, the closing devices and the particle bed below, collecting the particles exiting the segments. An outer surface of the HX of approximately 10 m^2 is assumed, that is insulated with 100 mm high-temperature insulation. The thermal losses were estimated analytically, resulting in a maximum value of 3 % of the design point. With assumed insulation costs of 300 €/m^2, the total cost of the insulation is approximately 150 k€. It has to be mentioned, that in the estimations, not the closing devices, nor the designated particle inlet area of each TFHX segment, nor the holding structure and shell of the device was include, allowing to service and to open the HX. Tis is estimated with additional 100 k€. According to Fig. 40, power densities of more than 1,000 kW/m^3 in the investigated operational conditions were determined. Assuming the same power density for each TFHX segment, the total transferable thermal heat of the exemplarily scaling example would range to 250 kW at particle flow rates of $2.5\ \mathrm{kg/(m^2 \cdot s)} \approx 0.6\ \mathrm{kg/s}$, at a cost of 250 k€. Not considered in the cost estimations is the durability of the HX system and costs for maintenance. The durability of the packing structure to abrasion is not fully clear, however Westerterp and Kuczynski [145] observed after six months of operation of a packing, consisting of 7 x 7 x 1 mm Raschig rings, low wear of the particles and packing, and assume it due to the soft trickle-flow provided by the packed column.

However, due to the limited long-time experience of particle systems cost estimations must be regarded with a high degree of uncertainty. Also, with increasing engineering and operation experience it can be expected that components in particle systems will be improve its performance, durability and also cost estimations can be predicted more precisely. Mehos, Turchi [46] perform a techno-economic analysis for a particle based CSP system, citing the work of Ho [42] and Stoddard, Galluzzo [168]. They estimate the total costs of a CSP receiver system and estimated the capital costs 30 % less than a comparable molten-salt system, while also mentioning the high uncertainties in the estimated cost figures. For further details, it is referred to the work of Mehos, Turchi [46] since this work does not claim to provide a fully worked out techno-economic analysis for a particle based CSP system.

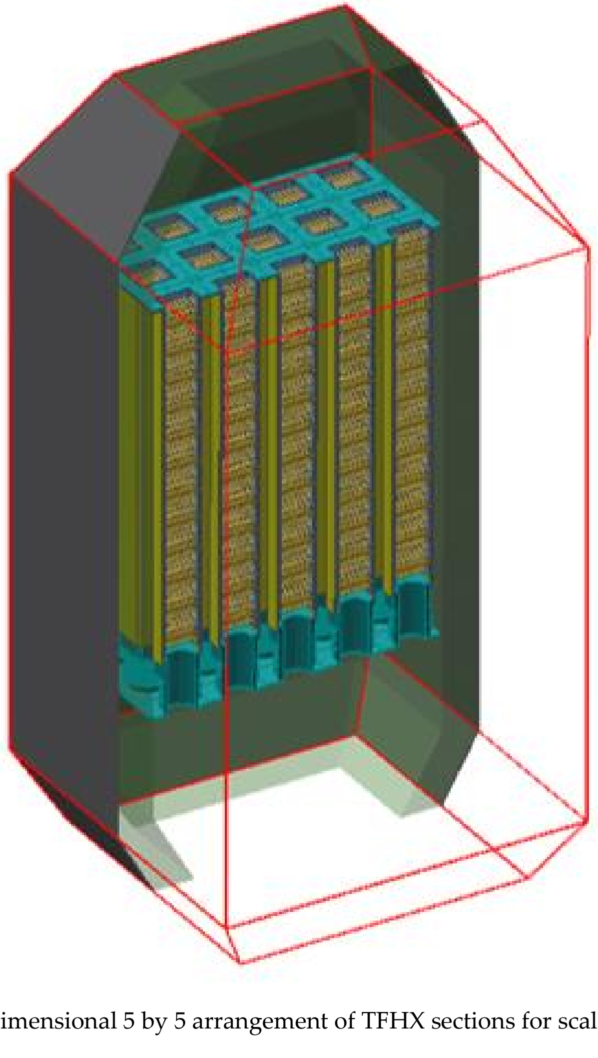

Fig. 57 Exemplarily two-dimensional 5 by 5 arrangement of TFHX sections for scale up.

6 Conclusion and outlook

6.1 Conclusion

In the present work, a gas-particle direct-contact trickle flow heat exchanger was developed and investigated. The motivation was the development of a heat exchanger, to be used in a particle based solar tower system, where ceramic bauxite particles of 1 mm diameter can be heated close to 1,000 °C. To transfer the stored heat in the particles, the TFHX, based on the principles of a trickle flow reactor, was considered to be superior compared to state-of-the-art technologies, like fluidized bed- or cyclone-HX. A more detailed classification of the technology, compared to other technologies, was not possible, due to limited availability of other technologies, see 2.2.2 and Tab. 3, and also the specific and wide range of applications different technologies are used. It was conceived that the TFHX could provide the best middle way of compactness, providing high power densities, and relative low pressure drop, meeting the requirement for the use in a CSP tower system, see section 2.2.

In literature available work in the field of chemical trickle flow reactors, repeatedly mention expected high heat transfer capacities, due to the analogy of mass transfer and heat transfer. However, few literature is available investigating experimentally the heat transfer capabilities up to 250 °C and 400 °C. Across, all available work in the field of trickle flow reactors or heat exchangers, view motivation was found in the selection of the used packing structure in the reactor. Literature indicates, that regular packing structures provide a better spatial particle distribution, enhancing the gas-solid interaction and consequently the heat transfer. Therefore, within the scope of this work, the focus was set on the investigation of regular packing structures. Additionally, assessment criteria for the selection of a packing structure were defined and applied. In chapter 3, those criteria were applied during a numerical pre-selection to identify a basic bar geometry. It was found that, packed columns, composed of horizontal arranged bar geometries with rectangular cross-sectional area, provide the highest potential to increase the particle volume-fraction or particle hold-up of the trickling particles. The total surface of the trickling particles within the reactor provide the surface for the gas-particle interaction respectively heat transfer, why a high particle hold-up along with an even spatial distribution of the grains was defined as assessment criteria.

The theoretical findings were applied during cold experiments, described in section 4.1, where a variety of packing geometries, composed with flat bar elements, were tested. The developed test bench was capable to assemble a variety of different packing geometries. Furthermore, the setup was developed to also conduct hot experiments up to 640 °C, to assess the heat transfer performance of the TFHX. Accordingly, high temperature materials were used, and the needed space to assemble thermal insulation, such as numerous TCs were installed alongside to sensors to measure the gas pressure and media flow rates. The starting point for the cold experiments was provided by the most promising packing geometries in the previously conducted numerical pre-selection. During the cold-experiments, the same assessment criteria as for the DEM study in chapter 3 were applied for the analysis of the experimental results. The dynamic particle hold-up, representing the void fraction of the trickling particles in the packed column, was measured to determine the heat transfer surface between the gas-particle interaction. In accordance with literature, the majority of the heat transfer is accounted to the particle surface of the trickling particle, why the dynamic hold-up was used as assessment criteria for the assessment of packing geometries and the determination of heat transfer area. By gradually refining and adapting the packing geometries in the vertical HX channel, a structure was identified that provided a high particle hold-up at stable flow conditions within the defined media flow rates and the used 1 mm bauxite particles. Also, for the selected packing geometry with a bar width of 10 mm, a bar height of 2 mm, 3 bars per packing layer and a particle falling height of 10 mm, no particle segregation was observed in the flow regimes of interest. During the cold experiments it was found, that a minimal bar width of the composed packing geometry can be beneficial for static particles to accumulate to a layer of small particles. The static particles in the packed column absorb the kinetic falling energy of the trickling particles, and thereby reduce actively the particle sink velocity within the packing. To small bar widths did not provide the possibility for static particle accumulation, whereas the particle flow within wider bar widths was more pronounced of a more uneven spatial particle distribution, due to larger areas below the wider bar elements.

The in the cold tests identified packing structure was investigated with air inlet temperatures up to 640 °C to assess the heat transfer capabilities of the packed column, used as a gas-particle direct contact trickle flow heat exchanger. The experimental setup was upgraded accordingly, by applying high temperature insulation at the HX channel and the media inlet and outlet tubing. Particles at ambient temperature with varying flow rates were fed into the top of the column, while air at ambient pressure was induced at the bottom of the HX. The air flow rate such as the air inlet temperature were adjustable. Four different air inlet temperatures up to 640 °C, such as five different media flow rates were defined. The particle and air flow rates were chosen to achieve roughly equal heat capacity flow rates, since a high temperature change in both media flows was defined in the requirement of this work. The smallest orifice diameter was identified in order to ensure the reliable delivery of a minimum mass flow rate for grains of 1 mm in size. The maximum particle mass flow was estimated analytically, based on the theory of the particle terminal velocity, where the resulting air flow rate was backwardly matched to the corresponding solid flow rate for equal heat capacity flow rates. In total 4 x 5 x 5 = 100 conditions were measured during the hot experiments end analyzed. Also, the corresponding uncertainties with a confidence level of 95 % was determined. For the highest air inlet temperature, the power density of the investigated TFHX was determined over 1,000 $\mathrm{kW/m^3}$ for media flow rates above 2 $\mathrm{kg/(m^2 \cdot s)}$. The volumetric heat transfer coefficient ranges in the same operating conditions at approximately 15 $\mathrm{kW/m^3}$, with NTU numbers for the particle and air flow of approximately 5 and 8 respectively. The available experimental work of TFHX is rather limited. Accessible literature used 0.37 mm particle diameter at temperature levels of 250 °C and 400 °C. The temperature level in this work, that resembles most the operational condition in the literature is for air inlet temperatures of 325 °C. In the corresponding subsections of section 4.2.2 it was illustrated and discussed, that the developed TFHX in this work is capable to increase the determined power densities, volumetric heat transfer coefficients, and NTU values by approximately 100 % compared to the available data in literature. As mentioned in the designated subsections, it can be assumed, that the increase in performance can be deduced by an increased surface of the trickling particles within the packed column, or conversely by a reduced sink velocity of the grains of approximately 0.1 m/s, compared to the determined velocities of roughly 0.2 m/s in the literature. This leads to the assumption that an optimized packing structure in a trickle flow reactor is capable to increase the gas-particle interaction and therefore can enhance the heat transfer capabilities substantially. Due to the analogy of heat- and mass-transfer, it is assumed that this finding can also be applied in chemical reactors. As mentioned in section 2.2.2, is a comprehensive comparison to other HX technologies due to the limited data availability rather limited, especially regarding the envisioned increase of volumetric heat transfer coefficient and conversely power density. Nevertheless, the determined metrices, such as the heat transfer coefficients, or the NTU-values are in the higher range for standard air-solid heat transfer problems. Also, the in section 4.2.2 conducted comparison to other work, also investigating the TFHX concept, showed a notable improvement of the heat transfer capabilities of the device in this work.

Finalizing this work, a first conceptual design of a scaled TFHX for industrial application with part-load capabilities was proposed. The concept provides in the design point a thermal heat transfer capability of 250 kW, with estimated power losses of max. 3 %. A simplified cost analysis was performed, estimating the unit to 250 k€. Although this estimation comes with a high degree of uncertainty due to limited long-term operational experience with particle systems. Ongoing advancements in engineering and operation of particle systems are expected to enhance the performance and durability of components and allow for more precise cost predictions. To address these uncertainties and unlock further potential, it is strongly recommended to validate the operability of the 250 kW TFHX system, for instance, in the Solar Tower Juelich. Such investigations would provide valuable long-term operational data, laying the foundation for scaling particle systems to MW-scale applications. This would push forward the development of concentrated receiver systems to operate at temperatures near 1,000 °C, making it more interesting for a variety of industrial processes with demand for thermal energy. By further exploring and refining the gas-particle direct-contact trickle flow heat exchanger, it is anticipated that efficiency gains in upscaling could further enhance the technology's potential for large-scale deployment, thereby contributing to a future in which sustainable high-temperature energy is made available for industrial processes.

6.2 Outlook

The present work demonstrated a method to identify for a given particle type an optimized packing geometry for a trickle flow reactor. During experimental campaigns, it was shown that an optimization of the packing geometry for a given particle type is capable to increase substantially the with the gas flow interacting total particle surface within the packed column. For the used 1 mm bauxite proppants, the identified packing geometry provided a bar width of 10 mm, that allowed the accumulation of a static particle layer upon each bar element. This results in absorption of the kinetic fall energy of the trickling particles, causing the particle sink velocity in the packing to reduce and conversely increase the total particle surface within the void volume. It is assumed, that in a certain range of particle diameter static particles can be beneficial in providing the effect to enhance the interacting particle surface with the gas flow. However, the bandwidth of particle diameters, where this assumption might apply is not known, since the particle hydrodynamics and flow behavior can be influenced by additional interparticle forces, alongside to the drag force of the gas flow, and the gravitational force of the particles. Therefore, it is recommended to investigate over a wide range of particle diameters the positive effect of static particles within a packed column, increasing the particle hold-up.

The behavior of powder like bulk material is dominated by interparticle forces, causing effects like poor flowability or particle accumulation and agglomeration. Depending on the conditions of the bulk material, different mechanisms can cause those interparticle adhesive forces. The bulk behavior of dry and powder like material is dominated by adhesion forces due to the van-der-Waals interactions and electro-static forces. The van-der-Waals forces are based on the electric dipole moment of atoms and molecules. The dominance of those forces is dependent on the particle diameter, the distances among the particles and the material properties. If the bulk material is not dry and contains a certain moisture content, additional interparticle binging forces can influence the bulk flowability. [96] Given the current state of knowledge, it is reasonable to conclude that a general prediction of particle flow behavior in a packed column is not possible. Instead, such predictions must be made on an individual basis, taking into account the specific particle types and conditions under consideration.

Alongside to the particle diameter, it is considered that further parameters like the particle sphericity, the material of the grains and the packed column such as the material properties of the gas, have an influence during the development of a packing structure. Why, although it would be preferably, it is assumed that no general rule of thumb can be provided in the selection of a packing structure for a TFHX.

The conducted hot experiments showed for the developed TFHX with the optimized packing structure, improved the heat transfer capabilities to comparable work. However, a scaled version of the experiments is recommended. Due to the unfavorable dimensions of $V_{\mathrm{HX}} = 0.875\ \mathrm{m\ x\ }(0.05\ \mathrm{m})^2 = 2.2 \cdot 10^{-3}\ \mathrm{m}^3$ with its poor surface to volume ratio for the used heat exchanger channel, where the different packing structures were assembled, additional affects have to be mentioned. Along the packing height, in the wall region of the HX duct, see Fig. 25, it must be assumed, that erroneous air leakage flow between the sheet metal elements, composing the packing geometries could falsify the measurement results. The influence of those boundary effect cannot be quantified, since this effect is expected to occur due to accidental and unforeseeable production tolerances, assembly inaccuracies and material distortion at higher temperatures. It is assumed, that the air leakage flow in the wall region of the TFHX is not dominant, since the air mass flow will distribute according to the regions with the widest void spaces within the packed column, being in the center of the packing in the laser cut sheet metal elements, composing the packing structure. By increasing the cross-sectional width of the HX channel from 50 mm by 50 mm, the influence of the boundary effect is expected to be reduced und more neglectable. Also, an increase of the width of the channel width, is expected to be beneficial in terms of heat losses. At the end of the hot experiments it was intended to operate the test setup with the design flow rate of the air heater at its maximum temperature of 700 °C. With additional heating elements, attached after the air heater, the air inlet temperature was increased close to 750 °C. However, after assessing the experimental data, no significant increase of heat transfer capabilities was observed, since the heat losses increased significantly. At these high temperatures the unfavorable dimension of the investigated, rather thin packed column showed its operational limits. Furthermore, by increasing the HX width, the bandwidth of the particle mass flow rate would widen, and by operating the unit in an environment allowing particle flow rates of a wider range, the heat exchanger characteristic as $\epsilon - NTU$ correlation could be elaborated more thoroughly and also in the range for low NTU numbers. This would permit the mapping of more comprehensive HX characteristic maps, thereby facilitating the engineering and prediction of a TFHX. However, as previously stated, it must be assumed that, due to the limited predictability of grain flow of varying particle materials and conditions, in changing packing geometries, the results of determined correlations may only be applicable to the specific particle type tested within the same packing geometry.

For future work, it is recommended to emphasize research efforts on the scaling of the TFHX. With further experiments the expected operational limit of the channel width should be clarified. As outlined in section 2.2.3, based on the documented observations in the literature, it is anticipated that if the width of the packed column exceeds a certain threshold, the induced particle flow may not distribute evenly within the column, potentially leading to particle segregation. The packing structure identified during the cold experiments, was investigated in the hot experiments. It is recommended to clarify, if the packing geometry along the height of the packed column has to be optimized, due to the changing media temperatures and material properties at different packing heights and a potentially change of particle flow behavior.

Also, and like outlined in chapter 5, the identified HX channel, with potentially increased channel width, should be installed in a TFHX, consisting of various TFHX segments, allowing to operate and investigate a correspondingly designed unit. This would allow to assess the behavior in part load operation, and the scaled-up version of a TFHX, comprising a more favorable surface to volume ratio, also would allow to assess the heat transfer capabilities in temperature ranges above 640 °C. Making such experiments a viable data basis to refine the cost estimations and conduct a techno-economic analysis of a TFHX system. Testing the TFHX in temperature ranges above 640 °C, it is anticipated that particularly in areas excessing those temperatures, the packing structure itself will exert an additional positive influence on the heat transfer capabilities of a TFHX, since the volume specific surface area of the particles and the packing structure are of a comparable number of magnitude, see Fig. 16 and Fig. 17. It is assumed that particles with high temperature, originating from a CST receiver, would enter the HX and heat the packing structure not only by convection, but additionally by thermal radiation. Consequently, the heat transfer in the high-temperature zone of the TFHX would not occur dominantly between the air and the particles, but also more pronounced between air and the packing. Resulting in an increased surface area involved in the heat transfer, increasing further the heat transfer capabilities in higher temperature ranges. It is recommendable to investigate those assumptions further, for example, using the high temperature particle testing facilities, available in the Solar Tower Julich in Germany. Thereby, further experience can be gained in the use of ceramic particles as HTF. The handling of this new HTF at the envisioned temperature range of 1,000 °C, must be investigated further, to gain long time experience, not only of the heat transfer and storage capabilities of the particles itself, but also of the durability of the plant components regarding abrasion and cycling temperature load. Currently, high temperature steel or ceramic materials are used to handle the ceramic HTF, at a corresponding cost. Inspired of the development of the packing structures, and the finding, that a static particle layer can serve as cushioning layer for the moving grains. Accordingly, if applicable, particle handling and guiding components could be engineered to allow purposely accumulate static particles in regions of moving, trickling or falling particles. Thereby, the impacts of particles with the system components could be reduced significantly, and conversely it is expected that the durability of system components and consequently the competitiveness of the technology can be increased.

The gas-particle direct-contact trickle flow heat exchanger demonstrated successfully in small scale operation its efficient working principle up to a temperature of 640 °C. As mentioned above, it is expected to increase further the potential of the technology in a scaled version. A continuation of the TFHX would further enable the high potential of ceramic particles, to provide process temperatures in CSP and CST applications. Further work in the field should be: Optimization of the packing geometry and heat exchanger design with long-term tests; the development of a scale-up unit, with part load capability and conduct a detailed cost analysis, and thereby preparing the applicability in the various fields of the TFHX in the future.

Bibliography

1. Fernández, A., et al., *Net Zero Roadmap A Global Pathway to Keep the 1.5 °C Goal in Reach*, in *Net Zero Emissions*. 2023, International Energy Agency: online. p. 226.
2. Chen, O., V.G. Tapia, and A. Rogé, *CO2 Emissions in 2022*. 2023, International Energy Agency. p. 19.
3. Quaschning, V., *Regenerative Energiesysteme: Technologie - Berechnung - Simulation*. 2015, Hanser: München.
4. Moradi-Shahrbabak, Z. and M. Jadidoleslam, *A new index for techno-economical comparison of storage technologies considering effect of self-discharge.* IET Renewable Power Generation, 2023. 17(7): p. 1699-1712, https://doi.org/10.1049/rpg2.12704.
5. Schöniger, F., et al., *Making the sun shine at night: comparing the cost of dispatchable concentrating solar power and photovoltaics with storage.* Energy Sources, Part B: Economics, Planning, and Policy, 2021. 16(1): p. 55-74, https://10.1080/15567249.2020.1843565.
6. Pitz-Paal, R., *Concentrating Solar Power*, in *Futurer Energy*, T. Letcher, Editor. 2020, Elsevier. p. 413-430.
7. Ho, C.K., *Advances in central receivers for concentrating solar applications.* Solar Energy, 2017. 152: p. 38-56, https://doi.org/10.1016/j.solener.2017.03.048.
8. Ebert, M., et al., *Upscaling, Manufacturing and Test of a Centrifugal Particle Receiver*. 2016. 7, https://doi.org/10.1115/ES2016-59252.
9. Stieglitz, R. and V. Heinzel, *Thermische Solarenergie : Grundlagen, Technologie, Anwendungen*. 2012, Berlin: Springer. 703, https://doi.org/10.1007/978-3-642-29475-4.
10. Kaltschmitt, M., W. Streicher, and A. Wiese, eds. *Erneuerbare Energien : Systemtechnik, Wirtschaftlichkeit, Umweltaspekte*. 6., vollständig neu überarbeitete Auflage ed. Springer eBook Collection. 2020, Springer: Berlin.
11. Wesselak, V., *Handbuch Regenerative Energietechnik*. 3. Aufl. 2017 ed. Bücher. 2017, Berlin, Heidelberg: Springer, https://doi.org/10.1007/978-3-662-53073-3.
12. Reich, G. and M. Reppich, *Regenerative Energietechnik : Überblick über ausgewählte Technologien zur nachhaltigen Energieversorgung*. 2013, Wiesbaden: Springer.
13. Bollin, E., D. Mangold, and K. Huber, *Solare Wärme für große Gebäude und Wohnsiedlungen*. BINE-Fachbuch. 2013, Stuttgart: Fraunhofer IRB Verlag.
14. Santamouris, M., ed. *Solar thermal technologies for buildings: the state of the art*. Buildings, energy, solar technology. 2013, Earthscan from Routledge: Abingdon, Oxon.
15. GlobalSolarAtlas. *Solar Resource Map - Direct Normal Irradiation*. 2024 [cited 2024 22.02.2024]; Available from: https://globalsolaratlas.info/.
16. Krüger, D., et al., *Solar Steam Supply: Initial Operation of a Plant*. Vol. 5. 2011, https://doi.org/10.18086/swc.2011.23.10.

17. Eck, M., et al., *Direct Steam Generation in parabolic troughs at 500°C - first results of the REAL-DISS project*, in *17th SolarPACES conference*. 2011: Granada.

18. Zarza, E., et al., *INDITEP: The first pre-commercial DSG solar power plant.* Solar Energy, 2006. 80(10): p. 1270-1276, https://doi.org/10.1016/j.solener.2005.04.019.

19. Eck, M., et al., *Applied research concerning the direct steam generation in parabolic troughs.* Solar Energy, 2003. 74(4): p. 341-351, https://doi.org/10.1016/S0038-092X(03)00111-7.

20. Krüger, D.R., et al., *Operating Parabolic Troughs with Molten Salt: Solar Field Optimisation and Ternary Salt Properties*, in *Solarpaces 2022*. 2022: Albuquerque NM, USA.

21. Riffelmann, K.-J., T. Richert, and T. Kuckelkorn, *Optimized molten salt receivers for ultimate trough solar fields*. Vol. 1734. 2016. 020021, https://doi.org/10.1063/1.4949045.

22. Ruegamer, T., et al., *Molten Salt for Parabolic Trough Applications: System Simulation and Scale Effects.* Energy Procedia, 2014. 49: p. 1523-1532, https://doi.org/10.1016/j.egypro.2014.03.161.

23. DLR. *Dish-Stirling-Anlage*. 2024 [cited 2024 21.02.2024]; Available from: https://www.dlr.de/de/bilder/2011/4/dish-stirling-anlage_3750.

24. Weinrebe, G., *Technische, ökologische und ökonomische Analyse von solarthermischen Turmkraftwerken*, in *Institute of Energy Economics and Rational Energy Use*. 2000, Stuttgart: Stuttgart. p. 205.

25. Carrizosa, E., et al., *Optimal Design of Solar Power Tower Systems*. 2016. 179-186, https://doi.org/10.1007/978-3-319-23413-7_23.

26. Leary, P.L. and J.D. Hankins, *User's guide for MIRVAL: a computer code for comparing designs of heliostat-receiver optics for central receiver solar power plants*. 1979: United States. p. Medium: ED; Size: Pages: 128, https://doi.org/10.2172/6371450.

27. Wendelin, T. *SolTRACE: A New Optical Modeling Tool for Concentrating Solar Optics*. in *ASME 2003 International Solar Energy Conference*. 2003. https://doi.org/10.1115/isec2003-44090.

28. Kistler, B.L., *A user's manual for DELSOL3: A computer code for calculating the optical performance and optimal system design for solar thermal central receiver plants*. 1986: United States. p. Medium: ED; Size: Pages: 239, https://doi.org/10.2172/7228886.

29. Schwarzbözl, P., R. Pitz-Paal, and M. Schmitz, *Visual HFLCAL - A Software Tool for Layout and Optimisation of Heliostat Fields*, in *SolarPACES 2009*, T. Mancini and R. Pitz-Paal, Editors. 2009: Berlin.

30. Schmitz, M., et al., *Assessment of the potential improvement due to multiple apertures in central receiver systems with secondary concentrators.* Solar Energy, 2006. 80: p. 111-120.

31. Lang, C. and B. Lee, *Heat Transfer Fluid Life Time Analysis of Diphenyl Oxide/Biphenyl Grades for Concentrated Solar Power Plants.* Energy Procedia, 2015. 69: p. 672-680, https://doi.org/10.1016/j.egypro.2015.03.077.

32. Jung, C., et al., *Technological Perspectives of Silicone Heat Transfer Fluids for Concentrated Solar Power.* Energy Procedia, 2015. 69: p. 663-671, https://doi.org/10.1016/j.egypro.2015.03.076.

33. Weinstein, L.A., et al., *Concentrating Solar Power.* Chemical Reviews, 2015. 115(23): p. 12797-12838, https://doi.org/10.1021/acs.chemrev.5b00397.

34. Bauer, T., *Overview of molten salt technology in the CSP sector - state of the art and current research*, in *Euchemsil 2022 - 28th Euchem conference on Molten Salts & Ionic Liquids*. 2022: Patras, Griechenland.

35. Puppe, M., et al., *Techno-economic optimization of molten salt solar tower plants.* AIP Conference Proceedings, 2018. 2033(1), https://doi.org/10.1063/1.5067069.

36. Bauer, T., et al., *High-Temperature Molten Salts for Solar Power Application*, in *Molten Salts Chemistry*, F. Lantelme and H. Groult, Editors. 2013, Elsevier: Oxford. p. 415-438, https://doi.org/10.1016/B978-0-12-398538-5.00020-2.

37. Aga, V., et al., *Adaptation of a Direct Steam Solar Tower Plant with Molten Salt Storage for Optimum Value Creation under Different Incentive Schemes.* Energy Procedia, 2014. 49: p. 1097-1106, https://doi.org/10.1016/j.egypro.2014.03.119.

38. Wetzel, T., R. Stieglitz, and W. Hering, *Application of liquid metals for solar energy systems.* EPJ Web of Conferences, Vol 33, p 03003 (2012), 2012: p. 1, https://doi.org/10.1051/epjconf/20123303003.

39. Gao, C.-h., et al., *One step sintering of homogenized bauxite raw material and kinetic study.* International Journal of Minerals, Metallurgy, and Materials, 2016. 23(10): p. 1231-1238, https://doi.org/10.1007/s12613-016-1343-8.

40. Messing, G.L., D. Kupp, and J.R. Hellmann, *Sintering of Coarse Ceramic Particles*. 1986, Sandia National Lab. (SNL-NM), Albuquerque, NM (United States).

41. Hruby, J.M., *Technical feasibility study of a solid particle solar central receiver for high temperature applications*. 1986, Sandia National Labs., Livermore, CA (USA). p. Medium: X; Size: Pages: 75.

42. Ho, C.K., *A review of high-temperature particle receivers for concentrating solar power.* Applied Thermal Engineering, 2016. 109: p. 958-969, https://doi.org/10.1016/j.applthermaleng.2016.04.103.

43. Knott, R.C., et al. *Sintering of Solid Particulates Under Elevated Temperature and Pressure in Large Storage Bins for Thermal Energy Storage*. in *ASME 2014 8th International Conference on Energy Sustainability collocated with the ASME 2014 12th International Conference on Fuel Cell Science, Engineering and Technology*. 2014. https://doi.org/10.1115/es2014-6588.

44. Siegel, N.P., M.D. Gross, and R. Coury, *The Development of Direct Absorption and Storage Media for Falling Particle Solar Central Receivers.* Journal of solar energy engineering : including wind energy and building energy conservation, 2015. 137(4), https://doi.org/10.1115/1.4030069.

45. Al-Ansary, H., et al., *Characterization and sintering potential of solid particles for use in high temperature thermal energy storage system.* SolarPACES 2013, 2013: p. 17-20.

46. Mehos, M., et al., *Concentrating Solar Power Gen3 Demonstration Roadmap*. 2017, National Renewable Energy Lab. (NREL), Golden, CO (United States). p. Medium: ED; Size: 140 p.

47. Gobereit, B., *Theoretische und experimentelle Untersuchungen zur Weiterentwicklung von solaren Partikelreceivern*. 2015. p. 114.

48. Siegel, N.P., et al., *Development and Evaluation of a Prototype Solid Particle Receiver: On-Sun Testing and Model Validation.* Journal of Solar Energy Engineering, 2010. 132(2), https://doi.org/10.1115/1.4001146.

49. Ho, C., et al., *Technology Advancements for Next Generation Falling Particle Receivers.* Energy Procedia, 2014. 49: p. 398-407, https://doi.org/10.1016/j.egypro.2014.03.043.

50. Röger, M., et al., *Face-Down Solid Particle Receiver Using Recirculation.* Journal of Solar Energy Engineering, 2011: p. 031009-1-031009-8.

51. Ebert, M., et al., *Operational experience of a centrifugal particle receiver prototype.* AIP Conference Proceedings, 2019. 2126(1): p. 8, https://doi.org/10.1063/1.5117530.

52. Amsbeck, L., et al., *First tests of a centrifugal particle receiver with a 1m2 aperture.* 2018. 2033(1): p. 040004, https://doi.org/10.1063/1.5067040.

53. Wu, W., et al., *Prototype Testing of a Centrifugal Particle Receiver for High-Temperature Concentrating Solar Applications.* Journal of Solar Energy Engineering, 2015. 137.

54. Wu, W., et al., *Numerical Simulation of a Centrifugal Particle Receiver for High-Temperature Concentrating Solar Applications.* Numerical Heat Transfer; Part A: Applications, 2015. 68(2): p. 133-149.

55. Wu, W., *A Centrifugal Particle Receiver for High-Temperature Solar Applications*. 2014. p. 195.

56. Wu, W., et al., *Proof of Concept Test of a Centrifugal Particle Receiver.* Energy Procedia, 2014. 49: p. 560-568.

57. Wu, W., et al., *On the influence of rotation on thermal convection in a rotating cavity for solar receiver applications.* Applied Thermal Engineering, 2014. 70(1): p. 694-704.

58. Yue, L., N. Schroeder, and C.K. Ho. *Particle Flow Testing of a Multistage Falling Particle Receiver Concept: Staggered Angle Iron Receiver (STAIR)*. in *14th International conference on energy sustainability, ES2020*. 2020. Online: American Society of Mechanical Engineers (ASME).

59. Shaeffer, R., et al. *Evaluation of Performance Factors for a Multistage Falling Particle Receiver*. in *14th International conference on energy sustainability, ES2020*. 2020. Online: American Society of Mechanical Engineers (ASME).

60. Sandlin, M.J., *Sandlin Matthew. Experimental verification of numerical models of granular flow through wire mesh screens*, in *School of Mechanical Engineering*. 2017, Georgia Institute of Technology.

61. Ho, C., et al., *Performance Evaluation of a High-Temperature Falling Particle Receiver*. 2016. V001T04A006, https://doi.org/10.1115/ES2016-59238.

62. Ho, C.K., et al., *On-sun testing of an advanced falling particle receiver system.* 2016. 1734(1): p. 030022, https://doi.org/10.1063/1.4949074.

63. Tregambi, C., et al., *A novel autothermal fluidized bed reactor for concentrated solar thermal applications.* Chemical Engineering Journal, 2020. 398: p. 125702, https://doi.org/10.1016/j.cej.2020.125702.

64. Ma, Z., G. Glatzmaier, and M. Mehos, *Fluidized Bed Technology for Concentrating Solar Power With Thermal Energy Storage.* Journal of Solar Energy Engineering, 2014. 136(3), https://doi.org/10.1115/1.4027262.

65. Baud, G., et al., *A theoretical and experimental study of the time-dependent radiative properties of a solar bubbling fluidized bed receiver.* Solar Energy, 2014. 105: p. 341-353, https://doi.org/10.1016/j.solener.2014.02.028.

66. Flamant, G., et al., *A New Heat Transfer Fluid for Concentrating Solar Systems: Particle Flow in Tubes.* Energy Procedia, 2014. 49: p. 617-626, https://doi.org/10.1016/j.egypro.2014.03.067.

67. Flamant, G., et al., *Dense suspension of solid particles as a new heat transfer fluid for concentrated solar thermal plants: On-sun proof of concept.* Chemical Engineering Science, 2013. 102: p. 567-576, https://doi.org/10.1016/j.ces.2013.08.051.

68. Martinek, J. and Z. Ma. *Granular Flow and Heat Transfer Study in a Near-Blackbody Enclosed Particle Receiver*. in *ASME 2014 8th International Conference on Energy Sustainability collocated with the ASME 2014 12th International Conference on Fuel Cell Science, Engineering and Technology*. 2014. https://doi.org/10.1115/es2014-6393.

69. Falter, C.P. and R. Pitz-Paal, *Modeling counter-flow particle heat exchangers for two-step solar thermochemical syngas production.* Applied Thermal Engineering, 2018. 132: p. 613-623, https://doi.org/10.1016/j.applthermaleng.2017.12.087.

70. Falcone, P.K., J.E. Noring, and J.M. Hruby, *Assessment of a solid particle receiver for a high temperature solar central receiver system.* 1985, https://doi.org/10.2172/6023191.

71. Kolb, G.J., R.B. Diver, and N. Siegel, *Central-Station Solar Hydrogen Power Plant.* Journal of Solar Energy Engineering, Transactions of the ASME 2007. 129(2): p. 179-183.

72. Tan, T. and Y. Chen, *Review of study on solid particle solar receivers.* Renewable and Sustainable Energy Reviews, 2010. 14(1): p. 265-276.

73. Khalsa, S.S.S., et al. *ES2011-54430 CFD Simulation and Performance Analysis of Alternative Designs for High-Temperature Solid Particle Receivers*. in *International conference; 5th, Energy sustainability*. 2012. New York, Washington, DC: American Society of Mechanical Engineers (ASME).

74. Ho, C.K., S.S. Khalsa, and N.P. Siegel. *Modeling On-Sun Tests of a Prototype Solid Particle Receiver for Concentrating Solar Power Processes and Storage*. in *ASME 2009 3rd International Conference on Energy Sustainability collocated with the Heat Transfer and InterPACK09 Conferences*. 2009. https://doi.org/10.1115/es2009-90035.

75. Chen, Z., et al. *FEDSM2008-55285 Numerical Analysis on the Performance of the Solid Solar Particle Receiver With the Influence of Aerowindow*. in *Summer Conference, American Society of Mechanical Engineers*. 2008. New York, Jacksonville, FL: American Society of Mechanical Engineers (ASME).

76. Tan, T., Y. Chen, and E. American Society of Mechanical. *HT2009-88059 Protection of an Aerowindow, One Scheme to Enhance the Cavity Efficiency of a Solid Particle Solar Receiver*. in *ASME Summer Heat Transfer Conference*. 2009. New York, N.Y., San Francisco, CA: American Society of Mechanical Engineers (ASME).

77. Tan, T., et al., *Wind effect on the performance of solid particle solar receivers with and without the protection of an aerowindow.* Solar Energy, 2009. 83(10): p. 1815-1827, https://doi.org/10.1016/j.solener.2009.06.014.

78. Al-Ansary, H., et al., *Solid particle receiver with porous structure for flow regulation and enhancement of heat transfer* K.S. University, Editor. 2017, King Saud University. p. 18.

79. Lee, T., et al., *Numerical simulation of particulate flow in interconnected porous media for central particle-heating receiver applications.* Solar Energy, 2015. 113: p. 14-24, https://doi.org/10.1016/j.solener.2014.12.017.

80. Flamant, G., *Theoretical and experimental study of radiant heat transfer in a solar fluidized-bed receiver.* AIChE Journal, 1982. 28(4): p. 529-535, https://doi.org/10.1002/aic.690280402.

81. Flamant, G., et al., *Experimental aspects of the thermochemical conversion of solar energy; Decarbonation of CaCO3.* Solar Energy, 1980. 24(4): p. 385-395, https://doi.org/10.1016/0038-092X(80)90301-1.

82. Steinfeld, A., A. Imhof, and D. Mischler, *Experimental Investigation of an Atmospheric-Open Cyclone Solar Reactor for Solid-Gas Thermochemical Reactions.* Journal of Solar Energy Engineering, 1992. 114(3): p. 171-174, https://doi.org/10.1115/1.2930001.

83. Bai, F., et al. *Thermal Performance of a Quartz Tube Solid Particle Air Receiver*. in *SolarPACES, International Symposium on Concentrating Solar Power and Chemical Energy Technologies, 2013*. 2014. https://doi.org/10.1016/j.egypro.2014.03.031.

84. Wang, F., et al., *Numerical Simulation of Quartz Tube Solid Particle Air Receiver.* Energy Procedia, 2015. 69: p. 573-582, https://doi.org/10.1016/j.egypro.2015.03.066.

85. Zhang, Y., et al., *Experimental Study of a Single Quartz Tube Solid Particle Air Receiver.* Energy Procedia, 2015. 69: p. 600-607, https://doi.org/10.1016/j.egypro.2015.03.069.

86. Benoit, H., et al., *On-sun demonstration of a 750°C heat transfer fluid for concentrating solar systems: Dense particle suspension in tube.* Solar Energy, 2015. 118: p. 622-633, https://doi.org/10.1016/j.solener.2015.06.007.

87. Albrecht, K., M. Carlson, and C. Ho, *Integration, control, and testing of a high-temperature particle-to-sCO2 heat exchanger*. Vol. 2126. 2019. 030001, https://doi.org/10.1063/1.5117513.

88. Repole, K.K.D. and S.M. Jeter. *Design and Analysis of a High Temperature Particulate Hoist for Proposed Particle Heating Concentrator Solar Power Systems*. in *ASME 2016 10th International Conference on Energy Sustainability collocated with the ASME 2016 Power Conference and the ASME 2016 14th International Conference on Fuel Cell Science, Engineering and Technology*. 2016. https://doi.org/10.1115/es2016-59619.

89. Ma, Z., P. Davenport, and R. Zhang, *Design analysis of a particle-based thermal energy storage system for concentrating solar power or grid energy storage.* Journal of Energy Storage, 2020. 29: p. 101382, https://doi.org/10.1016/j.est.2020.101382.

90. Ho, C.K., et al., *Evaluation of Alternative Designs for a High Temperature Particle-to-sCO2 Heat Exchanger.* Journal of Solar Energy Engineering, 2019. 141(2), https://doi.org/10.1115/1.4042225.

91. Carlson, M.D. and C.K. Ho, *A Particle/sCO2 Heat Exchanger Testbed and Reference Cycle Cost Analysis*. 2016. V001T04A017, https://doi.org/10.1115/ES2016-59607.

92. Baumann, T. and S. Zunft, *Experimental Investigation on a Moving Bed Heat Exchanger used for discharge of a particle-based TES for CSP*, in *Eurotherm Seminar #99*. 2014: Lleida, Spanien.

93. Babcock and Wilcox, *Selection and conceptual design of an advanced thermal-energy-storage subsystem for commercial-scale (100 MWe) solar central-receiver power plant*. 1981, Sandia National Labs., Livermore, CA (USA); Babcock and Wilcox Co., Lynchburg, VA (USA). Nuclear Power Generation Div. p. Medium: ED; Size: Page197 p.

94. Albrecht, K.J. and C.K. Ho, *Design and operating considerations for a shell-and-plate, moving packed-bed, particle-to-sCO2 heat exchanger*. Solar Energy, 2019. 178: p. 331-340, https://doi.org/10.1016/j.solener.2018.11.065.

95. Levenspiel, O., *Engineering Flow and Heat Exchange*. 2014: Springer.

96. Schulze, D., *Pulver und Schüttgüter : Fließeigenschaften und Handhabung*. 2014.

97. VDI-GVC, ed. *VDI Heat Atlas*. 2010, VDI-Gesellschaft Verfahrenstechnik und Chemieingenieurwesen: Berlin, Heidelberg.

98. Masuda, H., K. Higashitani, and H. Yoshida, *Powder technology handbook*. 3 ed. 2006, Boca Raton: Taylor & Francis.

99. Woodcock, C.R. and J.S. Mason, *Bulk Solids Handling : an Introduction to the Practice and Technology*. 1988. 534, https://doi.org/10.1007/978-1-4757-1358-9.

100. Kunii, D. and O. Levenspiel, *Fluidization engineering*. 2nd ed. Butterworth-Heinemann series in chemical engineering. 1991, Boston: Butterworth-Heinemann. xxvii, 491 pages.

101. Stieß, M., *Partikeltechnologie*. 3., vollst. neu bearb. Aufl. ed. Mechanische Verfahrenstechnik. 2009, Berlin; Heidelberg: Springer. XI, 498 Seiten.

102. Reichart, M., *Konzeptentwicklung und Konstruktion eines Direktkontakt-Warme¨ubertragers für Keramikpartikel und atmospharische Luft*, in *Institut fur Thermodynamik und Wärmetechnik*. 2014, Stuttgart: Stuttgart. p. 146.

103. Warerkar, S., et al., *Air-Sand Heat Exchanger for High-Temperature Storage*. Journal of Solar Energy Engineering, 2011. 133(2), https://doi.org/10.1115/1.4003583.

104. Baumann, T., et al., *AIR-SAND HEAT EXCHANGER: MATERIALS AND FLOW PROPERTIES*, in *SolarPACES 2011*. 2011: Granada, Spanien.

105. Larsen, E.S. and M.J. Pilat, *DESIGN AND TESTING OF A MOVING BED VOC ADSORPTION SYSTEM*. Environmental Progress, 1991. 10(1): p. 75-82, https://doi.org/10.1002/ep.670100119.

106. Rajan, K.S., et al., *Studies on gas–solid heat transfer during pneumatic conveying*. International Journal of Heat and Mass Transfer, 2008. 51(11): p. 2801-2813, https://doi.org/10.1016/j.ijheatmasstransfer.2007.09.042.

107. Duda, W.H., *Internationale Verfahrenstechniken der Zementindustrie : zweisprachig*. 3., neubearb. u. erw. Aufl. ed. Cement data book. 1985, Wiesbaden: Bauverlag. XIX, 636 Seiten.

108. Maarup, C., *Gas-Solid Heat Exchanger for Cement Production*, in *Department of Chemical and Biochemical Engineering*. 2013, Technical University of Denmark. p. 314.

109. Geldart, D. and A.R. Abrahamsen, *Homogeneous fluidization of fine powders using various gases and pressures.* Powder Technology, 1978. 19(1): p. 133-136, https://doi.org/10.1016/0032-5910(78)80084-9.

110. Jain, A., et al., *Studies on gas-solid heat transfer in cyclone heat exchanger.* Journal of Heat Transfer-Transactions of the Asme, 2006. 128(8): p. 761-768, https://doi.org/10.1115/1.2217748.

111. Green, H.J., C.M. Leboeuf, and M.S. Bohn, *Technical and economic evaluation of a solid-particle/air direct-contact heat exchanger.* 1986.

112. Amirante, R., E. Distaso, and P. Tamburrano, *Novel, cost-effective configurations of combined power plants for small-scale cogeneration from biomass: Design of the immersed particle heat exchanger.* Energy Conversion and Management, 2017. 148: p. 876-894, https://doi.org/10.1016/j.enconman.2017.06.047.

113. Verver, A.B. and W.P.M. Van Swaaij, *The heat-transfer performance of gas—solid trickle flow over a regularly stacked packing.* Powder Technology, 1986. 45: p. 133-144, https://doi.org/10.1016/0032-5910(66)80005-0.

114. Verver, A.B. and W.P.M. van Swaaij, *The hydrodynamic behaviour of gas—solid trickle flow over a regularly stacked packing.* Powder Technology, 1986. 45(2): p. 119-132, https://doi.org/10.1016/0032-5910(66)80004-9.

115. Limburg, D.v.d.S.i., *Procédé pour augmenter la concentration des particules solides dans un courant de milieu gazeux*, in *11.04.1951*, D.v.d.S.i. Limburg, Editor. 1948: France.

116. Gringras, M.B., *Zwischenprodukt für die Herstellung von Glas und von anderen Silikaten sowie Verfahren und Vorrichtungen zu dessen Herstellung*, in *04.03.1971*, C.d. Saint-Gobain, Editor. 1965: France. p. 46.

117. Roes, A.W.M. and W.P.M. Van Swaaij, *Gas/Feststoff-Rieselströmung in einer Füllkörperkolonne.* 1979. 51(5): p. 529-529, https://doi.org/10.1002/cite.330510531.

118. Roes, A.W.M. and W.P.M. Van Swaaij, *Mass transfer in a gas-solid packed column at trickle flow.* The Chemical Engineering Journal, 1979. 18(1): p. 29-37, https://doi.org/10.1016/0300-9467(79)80011-8.

119. Obradovic, A. and J. Levec, *High Purity Hydrogen with Sorption-Enhanced Steam Methane Reforming (SE−SMR) in a Gas–Solid Trickle Bed Reactor.* Industrial & Engineering Chemistry Research, 2017. 56, https://doi.org/10.1021/acs.iecr.7b01832.

120. Kuczynski, M., et al., *Methanol synthesis in a countercurrent gas—solid—solid trickle flow reactor. An experimental study.* Chemical Engineering Science, 1987. 42(8): p. 1887-1898, https://doi.org/10.1016/0009-2509(87)80135-5.

121. Westerterp, K.R. and M. Kuczynski, *A Model for a countercurrent gas-solid-solid trickle flow reactor for equilibrium reactions. The methanol synthesis.* Chemical Engineering Science - CHEM ENG SCI, 1987. 42(8): p. 1871-1885, https://doi.org/10.1016/0009-2509(87)80134-3.

122. Veneman, R., et al., *CO2 capture in a continuous gas–solid trickle flow reactor.* Chemical Engineering Journal, 2016. 289: p. 191-202, https://doi.org/10.1016/j.cej.2015.12.066.

123. Obradović, A. and J. Levec, *Countercurrent gas–solid trickle flow reactor with structured packing: Hydrodynamics and CaO−CO2 reaction.* AIChE Journal, 2015. 61, https://doi.org/10.1002/aic.14731.

124. Kiel, J.H.A., W. Prins, and W.P.M. van Swaaij, *Modelling of non-catalytic reactors in a gas-solid trickle flow reactor: Dry, regenerative flue gas desulphurization using a silica-supported copper oxide sorbent.* Chemical engineering science, 1992. 47(17): p. 15, https://doi.org/10.1016/0009-2509(92)85105-K.

125. Verver, A.B. and W.P.M. van Swaaij, *The gas-solid trickle-flow reactor for the catalytic oxidation of hydrogen sulphide: a trickle-phase model.* Chemical engineering science, 1987. 42(3): p. 435-445, https://doi.org/10.1016/0009-2509(87)80006-4.

126. Verver, A.B., *The catalytic oxidation of hydrogen sulphide to sulphur in a gas-solid trickle-flow reactor*. 1984, University of Twente.

127. Large, J.F., P. Guignon, and Y. Molodtsof, *The hydrodynamics of raining- particle heat exchangers and their applications.* International chemical engineering, 1987. 27: p. 607-614.

128. Westerterp, K.R. and M. Kuczynski, *Gas-solid trickle flow hydrodynamics in a packed column.* Chemical Engineering Science, 1987. 42(7): p. 1539-1551, https://doi.org/10.1016/0009-2509(87)80159-8.

129. Saatdjian, E. and J.F. Large, *Heat transfer simulation in a raining packed bed exchanger.* Chemical Engineering Science, 1985. 40: p. 693-697, https://doi.org/10.1016/0009-2509(85)85021-1.

130. Large, J.F., P. Guignon, and E. Saatdjian, *Multistaging and solids distributor effects in a raining packed bed exchanger*. 1983. 389-396.

131. Roes, A.W.M. and W.P.M. Van Swaaij, *Hydrodynamic behavior of a gas-solid counter-current packed column at trickle flow.* The Chemical Engineering Journal, 1979. 17: p. 81–89, https://doi.org/10.1016/0300-9467(79)85001-7.

132. Roes, A.W.M. and W.P.M. Van Swaaij, *Axial dispersion of gas and solid phases in a gas-solid packed column at trickle flow.* The Chemical Engineering Journal, 1979. 18(1): p. 13-28, https://doi.org/10.1016/0300-9467(79)80010-6.

133. Ergun, S., *Fluid flow through packed columns.* Chemical Engineering Progress, 1952. 48(n 2): p. 89-94.

134. James, R.M., *Introduction to particle technology*, M.J. Rhodes, Editor. 2008, Wiley: Chichester, England ; Hoboken, NJ.

135. Large, J.F., et al., *Hydrodynamics of the raining packed-bed gas-solids heat exchanger.* Chemical Engineering Journal and the Biochemical Engineering Journal, 1981. 22(2): p. 95-100, https://doi.org/10.1016/0300-9467(81)80026-3.

136. Nikacevic, N.M., A.P. Dudukovic, and Z.J. Predojevic, *Dynamic holdup in a countercurrent gas - flowing solids - packed bed contactors.* Journal of the Serbian Chemical Society, 2004. 69(1): p. 77-84, https://doi.org/10.2298/jsc0401077n.

137. Dudukovic, A.P., et al., *Solids holdup and pressure drop in gas-flowing solids-fixed bed contactors.* Industrial & Engineering Chemistry Research, 2003. 42(12): p. 2530-2535, https://doi.org/10.1021/ie020541s.

138. Dudukovic, A.P., N.M. Nikacevic, and Z.V. Kuzeljevic, *Modeling and predictions of solids dynamic holdup in gas-flowing solids-fixed bed contactors.* Industrial & Engineering Chemistry Research, 2004. 43(23): p. 7445-7448, https://doi.org/10.1021/ie0401105.

139. Claus, G., F. Vergnes, and P.L. Goff, *Hydrodynamic study of gas and solid flow through a screen - packing.* The Canadian Journal of Chemical Engineering, 1976. 54(3): p. 143-147, https://doi.org/10.1002/cjce.5450540304.

140. Roes, A.W.M., *The behavior of a gas-solid packed column at trickle flow*. 1978, University of Twente: Enschede, The Netherlands.

141. Roes, A.W.M. and W.P.M. Van Swaaij, *An evaluation of radial solid spread factors in a gas-solid packed column at trickle flow.* Chemical Engineering Science, 1979. 34(1): p. 131-133, https://doi.org/10.1016/0009-2509(79)85186-6.

142. Saatdjian, E. and J.F. Large, *Heat Transfer in a Countercurrent, Gas–Solid, Packed Column.* Journal of Heat Transfer-transactions of The ASME, 1988. 110: p. 385-389, https://doi.org/10.1115/1.3250496.

143. Kiel, J.H.A., W. Prins, and W.P.M. van Swaaij, *Mass transfer between gas and particles in a gas—solid trickle flow reactor.* Chemical Engineering Science, 1993. 48(1): p. 117-125, https://doi.org/10.1016/0009-2509(93)80288-2.

144. Kiel, J.H.A., *Removal of sulphur oxides and nitrogen oxides from flue gas in a gas-solid trickle flow reactor* 1990.

145. Westerterp, K.R. and M. Kuczynski, *Neues Verfahren zur Methanol- und Ammoniak-Synthese. Der Gas/Feststoff/Feststoff-Rieselströmungsreaktor – ein neuer Reaktortyp zur Führung chemischer Gleichgewichtsprozesse.* 1986. 58(12): p. 929-933, https://doi.org/10.1002/cite.330581202.

146. Nagata, K., et al., *The heat transfer performance of a gas-solid contactor with regularly arranged baffle plates.* Powder Technology, 1998. 99(3): p. 302-307, https://doi.org/10.1016/s0032-5910(98)00127-2.

147. Reichart, M., et al. *Numerical Assessment of Packing Structures for Gas-Particle Trickle Flow Heat Exchanger for Application in CSP Plants*. in *ASME 2021 15th International Conference on Energy Sustainability collocated with the ASME 2021 Heat Transfer Summer Conference*. 2021. https://doi.org/10.1115/es2021-62746.

148. Saint-Gobain-Proppants, *UltraProp/ Sintered Bauxite High Strength Proppants*, in *Summary of Typical Properties*. 2014, Saint-Gobain. p. 2.

149. Cundall, P.A. and O.D.L. Strack, *A discrete numerical model for granular assemblies*, in *The Essence of Geotechnical Engineering: 60 years of Géotechnique*. 1979. p. 305-329, https://doi.org/10.1680/ege.35362.0025.

150. Grobbel, J., *Modeling Solar Particle Receivers with the Discrete Element Method*, in *Fakultät für Maschinenwesen*. 2019, RWTH Aachen. p. 206.

151. Glowinski, R., et al., *A distributed Lagrange multiplier/fictitious domain method for particulate flows.* International Journal of Multiphase Flow, 1999. 25(5): p. 755-794, https://doi.org/10.1016/S0301-9322(98)00048-2.

152. van Wachem, B.G.M., et al., *Comparative analysis of CFD models of dense gas–solid systems.* 2001. 47(5): p. 1035-1051, https://doi.org/10.1002/aic.690470510.

153. Zhu, H.P., et al., *Discrete particle simulation of particulate systems: Theoretical developments.* Chemical Engineering Science, 2007. 62(13): p. 3378-3396, https://doi.org/10.1016/j.ces.2006.12.089.

154. Coetzee, C.J., *Review: Calibration of the discrete element method.* Powder Technology, 2017. 310: p. 104-142, https://doi.org/10.1016/j.powtec.2017.01.015.

155. Yeom, S.B., et al., *Application of the Discrete Element Method for Manufacturing Process Simulation in the Pharmaceutical Industry.* Pharmaceutics, 2019. 11(8): p. 414, https://doi.org/10.3390/pharmaceutics11080414.

156. van der Hoef, M.A., et al., *Numerical Simulation of Dense Gas-Solid Fluidized Beds: A Multiscale Modeling Strategy.* 2008. 40(1): p. 47-70, https://doi.org/10.1146/annurev.fluid.40.111406.102130.

157. Zhu, H.P., et al., *Discrete particle simulation of particulate systems: A review of major applications and findings.* Chemical Engineering Science, 2008. 63(23): p. 5728-5770, https://doi.org/10.1016/j.ces.2008.08.006.

158. Li, Y., Y. Xu, and C. Thornton, *A comparison of discrete element simulations and experiments for 'sandpiles' composed of spherical particles.* Powder Technology, 2005. 160(3): p. 219-228, https://doi.org/10.1016/j.powtec.2005.09.002.

159. Grima, A.P. and P.W. Wypych, *Discrete element simulations of granular pile formation: Method for calibrating discrete element models.* Engineering Computations, 2011. 28(3): p. 314-339.

160. Thornton, C., *Granular Dynamics, Contact Mechanics and Particle System Simulations : A DEM study*. 1st 2015 ed. Bücher. Vol. 24. 2015, Cham: Springer, https://doi.org/10.1007/978-3-319-18711-2.

161. Yan, Z., et al., *Discrete element modelling (DEM) input parameters: understanding their impact on model predictions using statistical analysis.* Computational Particle Mechanics, 2015. 2: p. 283-299, https://doi.org/10.1007/s40571-015-0056-5.

162. Noordergraaf, I.W., A.B. Verver, and W.P.M. Van Swaaij, *Gas/Feststoff-Rieselstromung und Austauschprozesse in einem Zickzack-Kontaktor.* Sprechsaal, 1981. 114: p. 3.

163. Noordergraaf, I.W., W.P.M. van Swaaij, and A.W.M. Roes, *Axial mixing and mass transfer in a zig-zag contactor.* 1980.

164. Nikacevic, N.M., M. Petkovska, and M.P. Dudukovic, *Solids flow pattern in gas-flowing solids-fixed bed contactors. Part I Experimental.* Chemical Engineering Science, 2009. 64(10): p. 2501-2509, https://doi.org/10.1016/j.ces.2009.02.029.

165. Hruby, J., et al., *An Experimental and Numerical Study of Flow and Convective Heat Transfer in a Freely Falling Curtain of Particles.* Journal of Fluids Engineering-transactions of The Asme - J FLUID ENG, 1988. 110, https://doi.org/10.1115/1.3243531.

166. Kim, K., et al., *A study of solid particle flow characterization in solar particle receiver.* Solar Energy, 2009. 83(10): p. 1784-1793, https://doi.org/10.1016/j.solener.2009.06.011.

167. Albrecht, K. and C.K. Ho, *Heat Transfer Models Of Moving Packed-Bed Particle-To-sCO2 Heat Exchangers*. Conference: Proposed for presentation at the ASME 2017 Power and Energy Conference held June 25-30, 2017 in Charlotte, North Carolina, United States.

2017: Sandia National Lab. (SNL-NM), Albuquerque, NM (United States). Medium: ED; Size: 10 p.

168. Stoddard, L., et al., *Falling Particles: Concept Definition and Capital Cost Estimate*, B. Veatch, Editor. 2016, https://doi.org/10.2172/1335155.

169. Lemmon, E.W. and R.T. Jacobsen, *Viscosity and Thermal Conductivity Equations for Nitrogen, Oxygen, Argon, and Air.* International Journal of Thermophysics, 2004. 25(1): p. 21-69, https://doi.org/10.1023/B:IJOT.0000022327.04529.f3.

170. Lemmon, E.W., et al., *Thermodynamic Properties of Air and Mixtures of Nitrogen, Argon, and Oxygen From 60 to 2000 K at Pressures to 2000 MPa.* Journal of Physical and Chemical Reference Data, 2000. 29(3): p. 331-385, https://doi.org/10.1063/1.1285884.

171. Olchowy, G.A. and J.V. Sengers, *A simplified representation for the thermal conductivity of fluids in the critical region.* International Journal of Thermophysics, 1989. 10(2): p. 417-426, https://doi.org/10.1007/BF01133538.

172. Shaw, W.T., *Sampling Studen" s T distribution@ use of the inverse cumulative distribution function.* Journal of Computational Finance, 2006. 9(4): p. 37-73.

173. Festo, *Schwenkantriebe DSM/DSM-B*. 2022, Festo: online. p. 56.

174. Scheller, G. and S. Krummeck, *Messunsicherheit einer Temperaturmesskette mit Beispielrechnungen*, ed. J.G.C. KG. 2018, www.jumo.net.

175. YASKAWA. *Datenblatt SM 331 - Analoge Eingabe (331-7KF01)*. 2023 [cited 2023 09]; 25]. Available from: https://www.yaskawa.de/_downloads/download_d14977.

176. Naohisa, T., et al., *Development of an optical imaging technique for particle number density.* Journal of Fluid Science and Technology, 2018. 13(1): p. 11, https://doi.org/10.1299/jfst.2018jfst0001.

177. Harth, K., et al., *Granular Gases of Rod-Shaped Grains in Microgravity.* Physical Review Letters, 2013. 110(14): p. 5, https://doi.org/10.1103/PhysRevLett.110.144102.

178. Nichol, K. and K.E. Daniels, *Equipartition of Rotational and Translational Energy in a Dense Granular Gas.* Physical Review Letters, 2012. 108(1): p. 018001, https://doi.org/10.1103/PhysRevLett.108.018001.

179. Dijksman, J.A., et al., *Invited Article: Refractive index matched scanning of dense granular materials.* Review of Scientific Instruments, 2012. 83(1): p. 12, https://doi.org/10.1063/1.3674173.

180. Weis, S. and M. Schröter, *Analyzing X-ray tomographies of granular packings.* Review of Scientific Instruments, 2017. 88(5): p. 16, https://doi.org/10.1063/1.4983051.

181. Neudecker, M., et al., *Jammed Frictional Tetrahedra are Hyperstatic.* Physical Review Letters, 2013. 111(2): p. 5, https://doi.org/10.1103/PhysRevLett.111.028001.

182. Baur, M., *X-ray radiography of granular systems - particle densities and dynamics*. 2020, Friedrich-Alexander-Universität Erlangen-Nürnberg (FAU): Erlangen. p. 135.

183. Heindel, T.J., *A Review of X-Ray Flow Visualization With Applications to Multiphase Flows.* Journal of Fluids Engineering, 2011. 133(7): p. 16, https://doi.org/10.1115/1.4004367.

184. OpenCV. *Camera Calibration*. 2023 [cited 2023 21.07.2023]; Available from: https://docs.opencv.org/3.4/dc/dbb/tutorial_py_calibration.html.

185. JCGM, J.C.f.G.i.M., *Evaluation of measurement data — Guide to the expression of uncertainty in measurement*. 2008, www.bipm.org. p. 134.

186. Brauer, H., *Grundlagen der Einphasen- und Mehrphasenströmungen*. Grundlagen der chemischen Technik. 1971, Aarau, Frankfurt (am Main): Sauerländer. 955.

187. Kiel, J. and W. Van Swaaij, *A theoretical model for the hydrodynamics of gas-solid trickle flow over regular stacked packings.* AIChE Symposium Series, 1989. 85: p. 11-21.

188. Schiller, L. and A. Naumann, *Über die grundlegende Berechnungen bei der Schwerkraftaufbereitung*, in *Zeitschrift des Vereines Deutscher Ingenieure, VDI-Z*. 1933, Vereines Deutscher Ingenieure (VDI): Leipzig. p. 318-320.

List of Symbols

This work was elaborated at the German Aerospace Center - Institute of Solar research, the syntax of this work is, despite written in English language, oriented to the German declaration of variables.

Latin Letters

a	$\mathrm{m^2/m^3}$	volumetric specific surface area
	$[var]$	half-width interval of measurement uncertainty
	$-$	coefficient for exponential curve fit
	$\mathrm{m/s^2}$	acceleration
b	$-$	variable represents one of the roots of (26) for approximation Rayleigh timestep
	$\mathrm{s^{-1}}$	exponent for exponential curve fit
b_i	$-$	parameter provided by [169] to calculate collision integral, see Tab. 15
A	$\mathrm{m^2}$	surface area
c_D	$-$	drag coefficient
c_p	$\mathrm{J/(g \cdot K)}$	isobar heat capacity
C_{AIA}	$\mathrm{m^3 \cdot kg/J}$	auxiliary factor, combining multiple variables to determine air leakage flow
d	m	diameter
d_i	$-$	exponents for determination of residual fluid viscosity, see Tab. 16
d_S	m	Sauter diameter
E	MPa	Young's modulus
f	$-$	inverse cumulative distribution function or inverse t-distribution
F	N	force
g	$\mathrm{m/s^2}$	gravitational acceleration: 9.81
G	MPa	shear modulus
h	m	height
i	$-$	number
k	$\mathrm{W/\,(m^2 \cdot K)}$	heat transfer coefficient
	$-$	uncertainty coverage factor for normal distribution
	$-$	radial distortion coefficient

	–	geometric concentration factor
l_i	–	exponents for determination of residual fluid viscosity, see Tab. 16
m	kg	mass
m'	kg	auxiliary mass
$\dot{m}$	kg/s	mass flow
M	g/mol	molar mass
n	–	number
N	–	number
N_i	–	coefficients for determination of residual fluid viscosity, see Tab. 16
	–	coefficients for the ideal gas expressions, see Tab. 17
NTU	–	Number of Transfer Units
p	Pa	pressure
	%	level of confidence
	–	tangential distortion coefficient
	–	probability
p'	Pa/m	pressure, normalized to the height of the packed column
P	–	overall mixing composition of two components
q	$[var]$	measurement value of one sample
$\dot{q}$	$\mathrm{W/m^2}$	specific heat flux
$\dot{Q}$	W	heat flux
R	J/(mol · K)	universal gas constant
R_a	J/(kg · K)	gas constant air
R^2	–	root-mean-square deviation or coefficient of determination
Re	–	Reynolds number
t	m	thickness
	s	point in time
	–	uncertainty coverage factor for student distribution
t_i	–	exponents for determination of residual fluid viscosity, see Tab. 16
Δt	s	timestep
T	K; °C	temperature
T^*	–	air temperature, normalized with the Lennard-Jones energy parameter
ΔT_m	K	logarithmic mean temperature difference
u	m/s	velocity
	$[var]$	uncertainty

$u_{\mathrm{a,0}}$	m/s	air superficial velocity without packed column
u_{rel}	$[var]$	relative, linear particle distribution
u_n^2	$[var]$	mean square deviation of the empirical variance or mixing quality of two quantities
U	$[var]$	extended uncertainty for a defined level of confidence
V	m^3	volume
$\dot{V}$	m^3/s	volume flow
w	m	width
$\dot{W}$	$J/(s \cdot K)$	heat capacity flow rate
$\dot{W}_{\mathrm{r}}$	$-$	heat capacity flow ratio
X	$-$	sample mixing composition
z	m	distance

Greek Letters

β	$\mathrm{m}_{\mathrm{p}}^3/\mathrm{m}_{\mathrm{void}}^3$	volumetric particle fraction within packing void or hold-up
β^*	$\mathrm{m}_{\mathrm{p}}^3/\mathrm{m}_{\mathrm{HX}}^3$	volumetric particle fraction within heat exchanger or extended hold-up
γ	deg	pivoting, rotating angle
γ_i	$-$	is zero for $l_i = 0$ and one for $l_i \neq 0$, used for determination of air propperties
Γ	$-$	gamma function
δ	$-$	dimensionless critical density
π	$-$	circle number
ρ	kg/m^3	density
σ	$[var]$	standard deviation or uncertainty of the population
	$-$	Lennard-Jones size parameter
σ_0^2	$-$	fully segregated mixture
σ_{id}^2	$-$	ideal uniform mixture
σ_{z}^2	$-$	stochastic uniform mixture
ϵ	$-$	coefficient of restitution
	$-$	heat exchanger effectiveness
	$-$	porosity
ϵ_0	$\mathrm{m}_{\mathrm{void}}^3/\mathrm{m}_{\mathrm{pac}}^3$	void fraction within packing volume
ϵ_{eff}	$\mathrm{m}_{\mathrm{void}}^2/\mathrm{m}_{\mathrm{pac}}^2$	void fraction within packing surface ($A_{\mathrm{void}} \perp \vec{g}$)
ϵ/k	K	Lennard-Jones energy parameter
η	$Pa \cdot s$	dynamic viscosity

η^0	$Pa \cdot s$	dilute gas viscosity
η^r	$\mu Pa \cdot s$	residual fluid velocity
λ	$W/(m \cdot K)$	thermal conductivity
λ^0	$W/(m \cdot K)$	dilute thermal gas conductivity
λ^{c}	$W/(m \cdot K)$	thermal conductivity critical enhancement
λ^{r}	$W/(m \cdot K)$	residual fluid thermal conductivity
ζ	$-$	coefficient of pressure loss
μ	$-$	friction coefficient
	$-$	population mean
ν	$-$	Poisson's ratio
	m^2/s	kinematic viscosity
	$-$	degree of freedom
τ	$-$	dimensionless critical temperature
ψ	$-$	sphericity
ω	s/deg	angle velocity
Ω	$-$	collision integral

Subscripts and Superscripts

#	normalized to A_{HX}; $[var]/\mathrm{m}^2$	D	drag
a	air	DC	discrete cell
abs	absolute	DSM	Festo pneumatic motor
amb	ambient	eff	effective
A	component A	eq	equipment
AI	analog input	err	erroneous
AIA	air inlet area	f	free
b	buoyancy	ff	free-fall
bar	bar	g	gravitational
bottom	bottom area	h	hydraulic
c	critical	HX	heat exchanger
cell	cell	i	index number
ci	channel inside	in	inlet
cl	closing process	in2out	inlet to outlet
dr	drainage	leak	leakage
dyn	dynamic	loss	loss

lnz	linearized
n	number, sample number
npias	no pixel in a slide
npiof	no particle in a frame
Nag98	referring to [146]
min	minimum
off-gas	off-gas section
op	opening process
out	outlet
p	particle
	level of confidence
pac	packing
pi	particle inlet
piaf	particle in a frame
pios	particle at last in one slide
pp	particle-particle
pw	particle-wall
r	relative
raw	raw
rd	reading
rel	relative
R	rolling friction
Rei24	referring to the results of this work
sa	sample, containing component A and B
sc	scale
sec	section
sm	sheet metal
stat	static
S	sliding friction
	Sauter
sec	section
SPS	Speicherprogrammierbare Steuerung
t	terminal conditions
ts	tray support
top	top area, upper area
tot	total
TC	Thermo Couple
TL	thermal line
Ver86	referring to [113]
void	void
vol	normalized to V_{HX}; $[var]/\mathrm{m}^3$
w	wall

Abbreviations

AIA	air inlet area
CO_2	carbon dioxide
COF	coefficient of friction
COP 21	21st UN Climate Change Conference of the Parties
COR	coefficient of restitution
CSP	concentrating solar power
CST	concentrating solar thermal
DC	discrete cells
DEM	Discrete Element Method
DNI	direct normal irradiance
EPSD2	elastic-plastic spring dashpot
FB	fluidized bed
FCC	fluid cracking catalyst
GSTF	gas-solid trickle flow
HTF	heat transfer medium
IEA	International Energy Agency
IGL	Ideal Gas Law

LMTD	logarithmic mean temperature difference
NTU	Number of Transfer Units
PIV	particle image velocimetry
PL	packing layer
PU	packing unit
RMSE	root mean squared error
RPBE	raining packed bed exchanger
sCO_2	super critical carbon-dioxide
SF	solar field
SHIP	solar heat for industrial processes
SM	sheet metal
SotA	state-of-the-art
SR	solar receiver
SSTFR	gas-solid-solid trickle flow reactor
TC	thermocouple
TES	Thermal energy storage
TFHX	trickle flow heat exchanger
TS	tray support
UNFCCC	United Nations Framework Convention on Climate Change

List of Figures

List of Tables

Appendix

A.1 Complimentary measurement results

A.1.1 Provided heat from the air flow

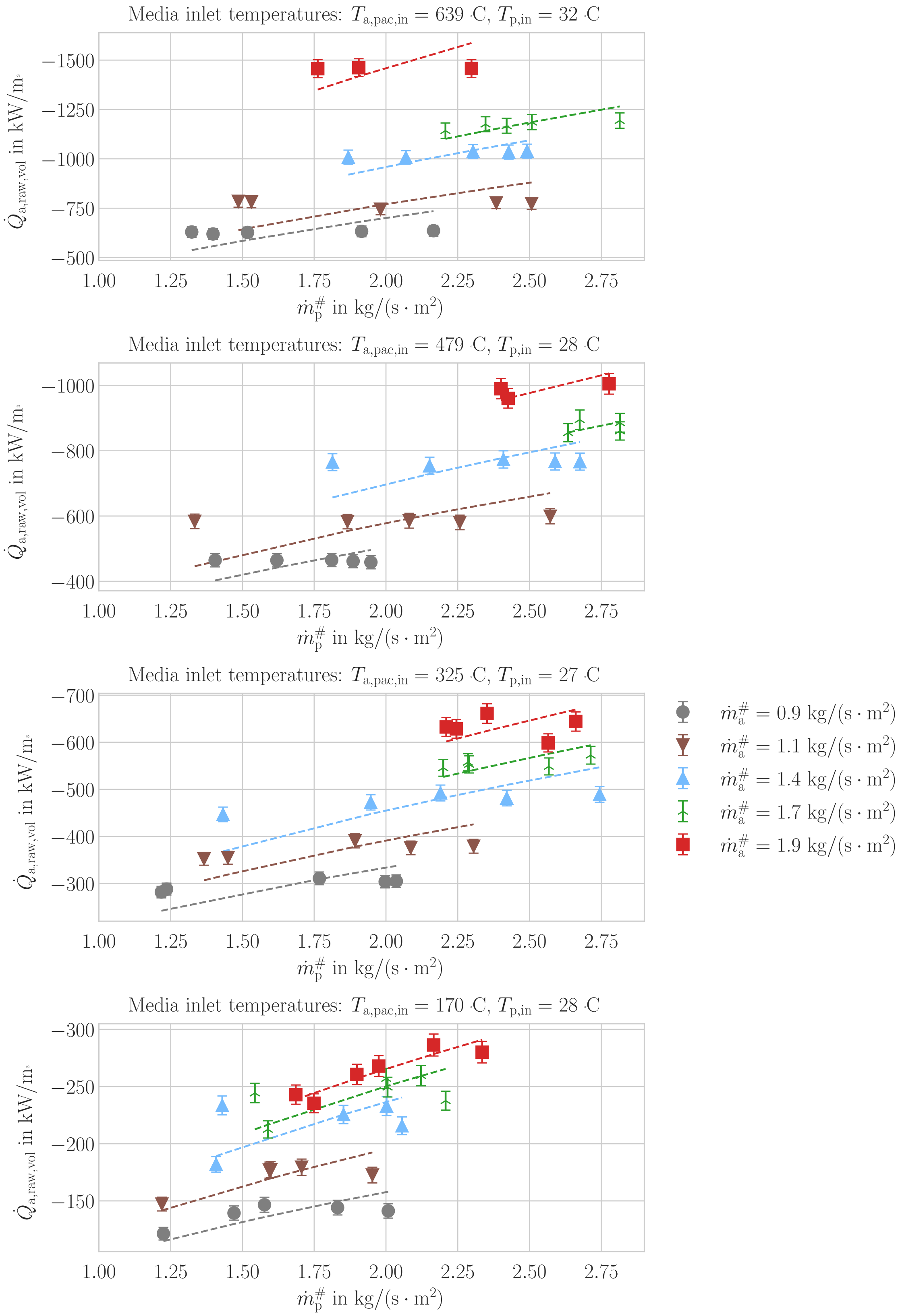

Fig. 58 Normalized transferred raw-heat at four temperature levels with varying media flow rates.

Section 4.2.2.3 illustrates and discusses the transfer of heat into the particle flow, shown in Fig. 40. In addition, the raw heat flow provided by the air stream, $\dot{Q}_{\mathrm{a,raw,vol}}$, is depicted in Fig. 58. According to equation (54), $\dot{Q}_{\mathrm{a,raw}}$ is constituted by the heat flow required to heat the particles and by the thermal losses to the surrounding environment. Whereas the latter is assumed to be accounted solely to the air flow. By applying equation (55), the raw heat flow can be depicted nominalized to the packing volume of the TFHX, see Fig. 58. Fig. 58 shows a similar behavior to that observed in the transferred heat into the particles, $\dot{Q}_{\mathrm{vol}}$, depicted in Fig. 40 in section 4.2.2.3. However, the values and trendlines of $\dot{Q}_{\mathrm{vol}}$ are lower than those of $\dot{Q}_{\mathrm{a,raw,vol}}$, since the thermal losses are accounted to $\dot{Q}_{\mathrm{a,raw,vol}}$.

A.1.2 Effectiveness

The effectiveness, ϵ, of a heat exchanger is defined as the ratio of the transferred heat to the theoretical maximum transferrable heat in the heat exchanger:

$$\epsilon = \frac{\dot{Q}}{\dot{Q}_{\mathrm{max}}} = \frac{\dot{Q}}{\min(\dot{W}_{\mathrm{p}}, \dot{W}_{\mathrm{a}})\ (T_{\mathrm{a,in}} - T_{\mathrm{p,in}})} = \frac{\min(T_{\mathrm{a,in}} - T_{\mathrm{a,out}}, T_{\mathrm{p,out}} - T_{\mathrm{a,in}})}{T_{\mathrm{p,in}} - T_{\mathrm{a,in}}} \text{ in} - \qquad (82)$$

Whereas the uncertainty can be expressed as follows

$$u_{\epsilon} = \sqrt{\left(\frac{\partial\epsilon}{\partial\dot{Q}}u_{\dot{Q}}\right)^2 + \left(\frac{\partial\epsilon}{\partial\dot{W}_{\mathrm{min}}}u_{\dot{W}_{\mathrm{min}}}\right)^2 + \left(\frac{\partial\epsilon}{\partial T_{\mathrm{p,in}}}u_{T_{\mathrm{p,in}}}\right)^2 + \left(\frac{\partial\epsilon}{\partial T_{\mathrm{a,in}}}u_{T_{\mathrm{a,in}}}\right)^2} \qquad (83)$$

with the corresponding sensitivity coefficients.

$$\frac{\partial\epsilon}{\partial\dot{Q}} = \frac{1}{\dot{W}_{\mathrm{min}}\ (T_{\mathrm{a,in}} - T_{\mathrm{p,in}})} \text{ in } \frac{1}{\mathrm{W}} \qquad (84)$$

$$\frac{\partial\epsilon}{\partial\dot{W}_{\mathrm{min}}} = -\frac{\dot{Q}}{\dot{W}_{\mathrm{min}}^2\ (T_{\mathrm{a,in}} - T_{\mathrm{p,in}})} \text{ in } \frac{\mathrm{g}\cdot\mathrm{K}}{\mathrm{J}} \qquad (85)$$

$$\frac{\partial\epsilon}{\partial T_{\mathrm{p,in}}} = -\frac{\dot{Q}}{\dot{W}_{\mathrm{min}}\ (T_{\mathrm{a,in}} - T_{\mathrm{p,in}})^2} \text{ in } \frac{1}{\mathrm{K}} \qquad (86)$$

$$\frac{\partial\epsilon}{\partial T_{\mathrm{a,in}}} = \frac{\dot{Q}}{\dot{W}_{\mathrm{min}}\ (T_{\mathrm{a,in}} - T_{\mathrm{p,in}})^2} \text{ in } \frac{1}{\mathrm{K}} \qquad (87)$$

As with the $\epsilon - NTU$ method, the NTU values for both media flow rates are condensed into one NTU value by selecting the smaller value of heat capacity flow rate of the both media flow rates in the denominator: $\dot{W}_{\mathrm{min}} = \min(\dot{W}_{\mathrm{p}}, \dot{W}_{\mathrm{a}})$.

$$NTU = \frac{k\ A_{\mathrm{p,pac}}}{\dot{W}_{\mathrm{min}}} \qquad (88)$$

The uncertainty of NTU can be determined according to (65). ϵ and the Number of Transfer Units according to (88) can provide the heat transfer performance of a heat exchanger type. In order to classify the experimental data in terms of the effectiveness, the $\epsilon - NTU$ diagram for the conducted experiments at the various temperature stages and flow rates is depicted, with different groups of heat capacity flow ratios, $\dot{W}_{\mathrm{r}}$, see Fig. 59. The heat capacity flow ratio can be calculated by:

$$\dot{W}_{\mathrm{r}} = \frac{\min(\dot{W}_{\mathrm{p}}, \dot{W}_{\mathrm{a}})}{\max(\dot{W}_{\mathrm{p}}, \dot{W}_{\mathrm{a}})} \tag{89}$$

In order to contextualize the plotted experimental data, the theoretical values for a heat capacity flow ratio $\dot{W}_{\mathrm{r}}$ of 0 and 1 for idealized countercurrent and parallel flow heat exchangers is also plotted. No discernible trend emerges when the data are examined at different temperature levels. As already demonstrated for the values of NTU_{a} and NTU_{p}, the range of available data is insufficient to reproduce a functional relation over a wide range of operational conditions. The experimental results are within the physical boundaries and demonstrate a relatively high effectiveness. This can be attributed to the selected operational mode, in the range of approximately equal heat capacity flow ratios and the limited technical capabilities to vary the particle and air mass flow rate across a wide range of operational modes, which in turn constrains the range of available data points. As previously stated, in order to reproduce the map of operation, a scaled version of the TFHX with fewer technical limitations in terms of operational freedom should be developed. This would enable further investigation of the initial promising results obtained from the particle-air direct-contact trickle flow heat exchanger.

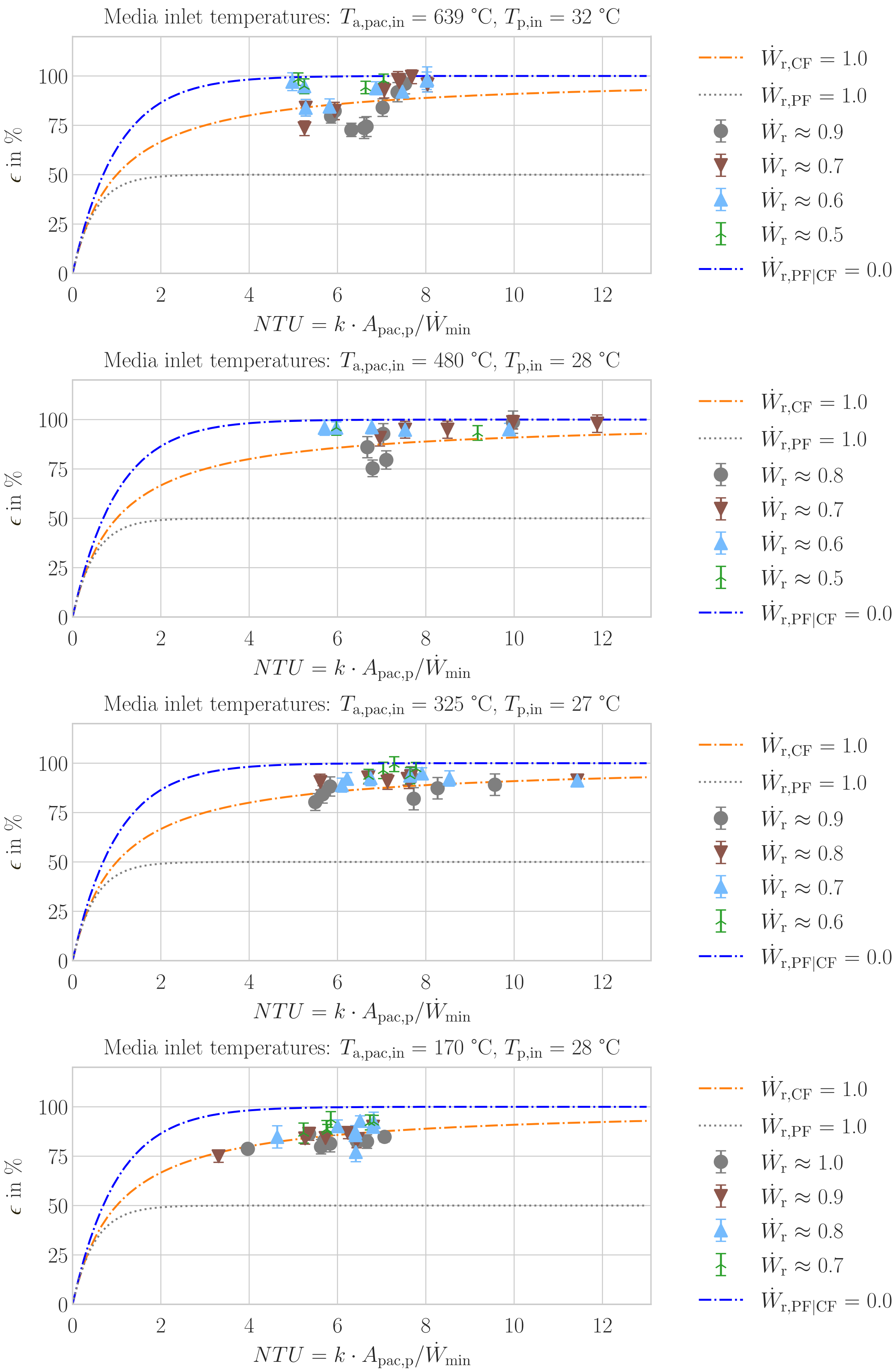

Fig. 59 *ϵ-NTU* diagram at four temperature levels with varying media flow rates.

A.1.3 Particle Reynolds number

The particle Reynolds numbers, Re_p, are calculated for each of the four temperature levels.

$$Re_\mathrm{p} = u \frac{d_\mathrm{p}\, \rho_\mathrm{a}}{\eta_\mathrm{a}} = u \frac{d_\mathrm{p}}{\nu_\mathrm{a}} = \frac{u_{\mathrm{a},0}}{\epsilon_\mathrm{eff}} \frac{d_\mathrm{p}}{\nu_\mathrm{a}} \qquad (90)$$

In order to determine Re_p, the averaged values of air at the packing inlet and outlet were employed. Similarly, in order to determine the reference velocity, the averaged air velocity in the free sectional area, with the packing structure blocked, ϵ_eff, was considered. Fig. 60 illustrates the variation in density, kinematic viscosity, and dynamic viscosity of atmospheric air with temperature. It can be observed that as temperature increases, the density of the air decreases, while the dynamic viscosity increases. The ratio of these material properties, represented by the kinematic viscosity, ν, increases for air at the pressure of interest, with increasing air temperatures.

$$\nu = \frac{\eta}{\rho} \qquad (91)$$

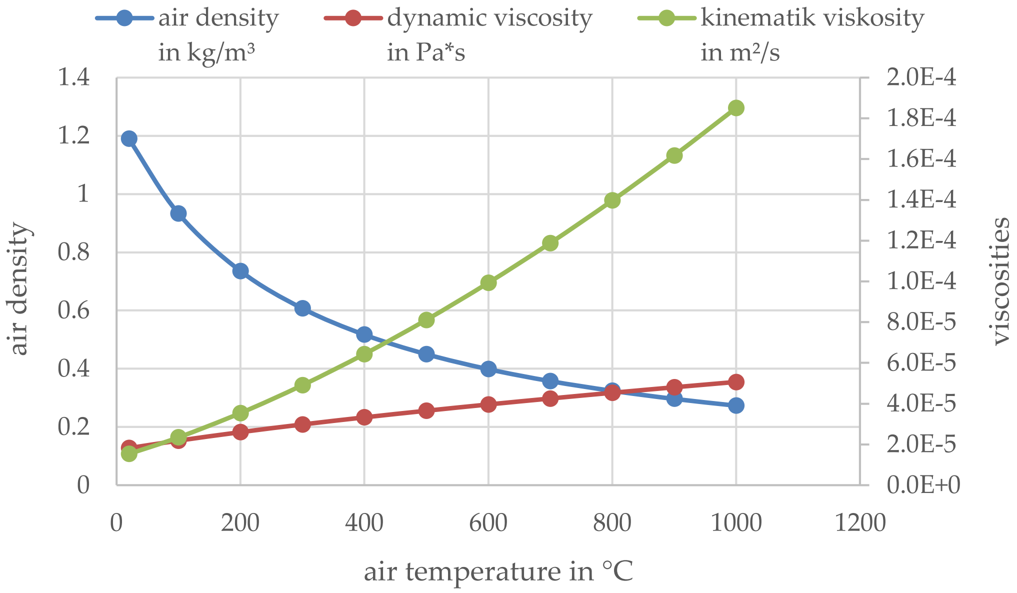

Fig. 60 Temperature dependence of density, kinematic and dynamic viscosity for atmospheric air.

Fig. 60 presents the averaged air media temperatures, $\overline{T}_\mathrm{a}$, for all measurements at each temperature level. The material data were calculated using the approach described in section A.2.2. described calculation approach. The slight tendency of reduced Reynolds numbers for increasing air temperatures can be explained by the increasing kinematic viscosity, as illustrated in Fig. 60 and detailed in (90). Fig. 61 demonstrates the particle Reynolds numbers for the four distinct temperature levels. The Reynolds numbers demonstrate a notable proportionality with the air flow rate. As the temperature level increases, the Reynolds numbers exhibit a slight decline.

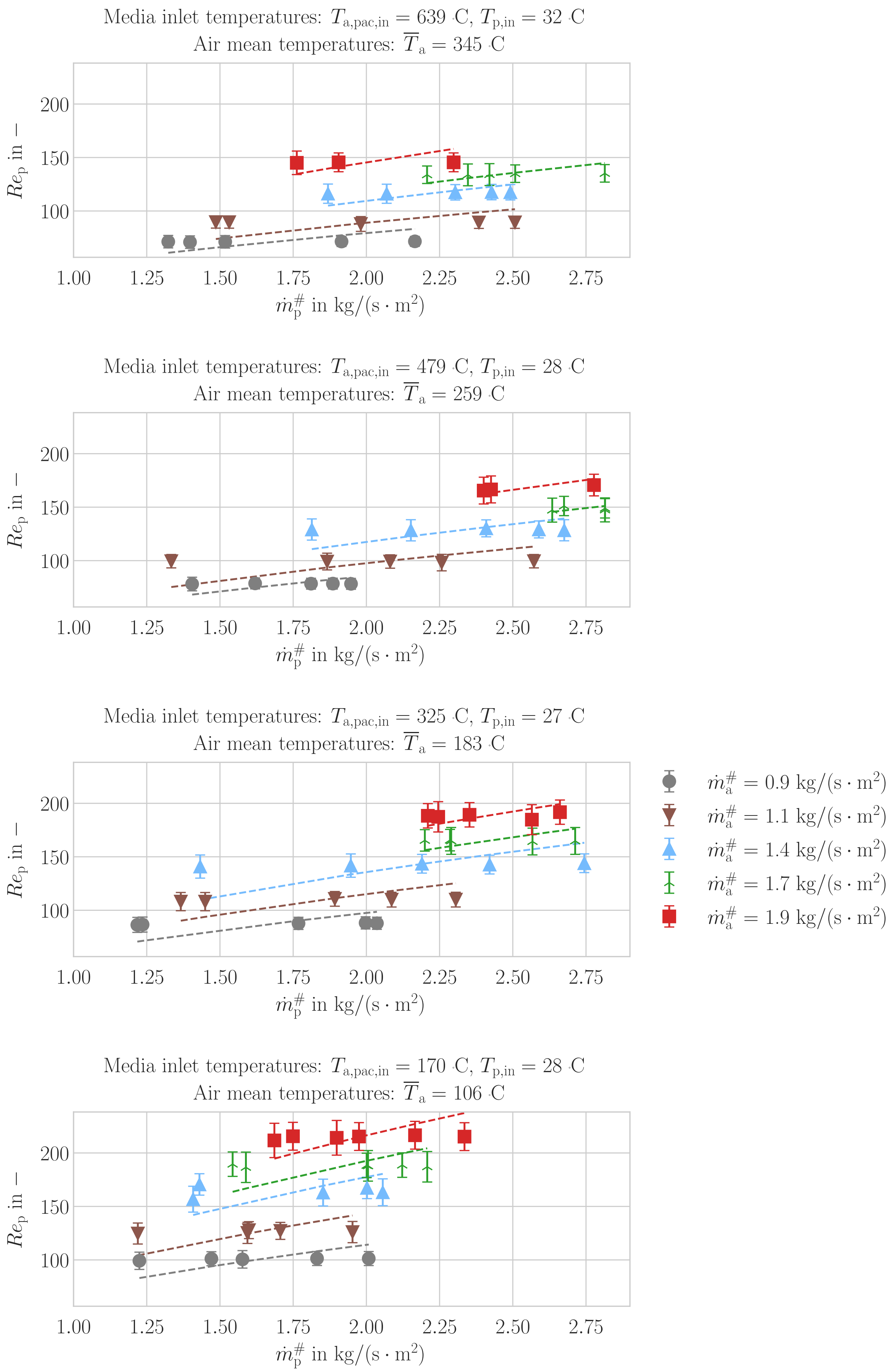

Fig. 61 Particle Reynolds numbers at four temperature levels with varying media flow rates.

A.2 Material properties and uncertainties

A.2.1 Particles

The particles utilized in this study were selected based on the successful large-scale technical demonstration of a solar direct-absorbing particle centrifugal receiver, which heated the particles to an average outlet temperature of 965 °C [51]. In this work, Saint-Gobain Proppants 16/30 sintered bauxite was used [8]. The properties of the bauxite particles with an approximate diameter of 1 mm are listed in Tab. 5.

A.2.1.1 Diameter

With the provided cumulative weight distribution of the particle size fractions the main particle- or sieve diameter, d_p, can be calculated, see (22). For spherical or near spherical particles the volume diameter is equal to the sieve diameter. A sieve analysis allows the calculation of d_p by using the retained particle mass at each sieve screen, $m_{\mathrm{p},i}$, with the corresponding sieve class mean value, $\bar{d}_{\mathrm{p},i}$, [134].

According to (22),(21) the particle diameter can be determined to be 0.98 mm, see Tab. 5, while the uncertainty of the particle diameter is derived from the particle size distribution. Fig. 62 shows the sieve analysis of the used particles, provided by the manufacturer [148]. It can be observed, that 84 % of the particles were retained by the sieve No. 20 during the sieve analysis, with a lower and upper limit for the particle diameter of 0.841 mm and 1.190 mm, respectively, giving a half-width interval uncertainty of $a_{\mathrm{p}=84\,\%} = \pm 1/2\ (1.190 - 0.851) = \pm 0.1745$ mm. The percentage of retained particle is assumed to be equal to the level of confidence p = 84 %. Using Tab. 18, the corresponding coverage factor $k_{\mathrm{p}=84\,\%}$ can be estimated to 1.467. Assuming a rectangular distribution of the particles, the uncertainty of the particle diameter, u_{d_p}, can be estimated for a standard confidence level of p = 68.27 %.

$$u_{d_\mathrm{p}} = \frac{\pm 0.1745\ \mathrm{mm}}{1.467 \cdot \sqrt{6}} = 0.0687\ \mathrm{mm} \qquad (92)$$

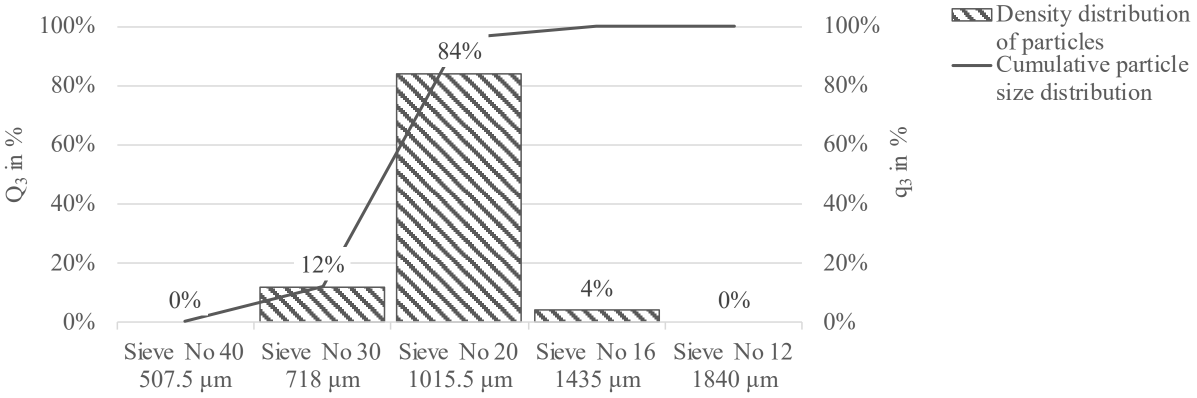

Fig. 62 Sieve analysis, Saint-Gobain 16/30 proppants bauxite particles, provided by the manufacturer, [148].

A.2.1.2 Density

Grobbel [150] investigated different particles as well as the bauxite 16/30 UltraProp/Sintered Bauxite proppant from Sant Gobain used in this work. The particles differ in size and shape, but the composition among different particles and manufacturers is quite similar, so the densities do not deviate more than 2 % from the mean value of $\rho_\mathrm{p} = 3{,}560\ \mathrm{kg/m^3}$ [150]. Assuming a rectangular distribution of the density deviation, the resulting uncertainty of the particle density is

$$u_{\rho_\mathrm{p}} = \frac{a_{\rho_\mathrm{p}} = 2\ \%\ \rho_\mathrm{p}}{\sqrt{3}} = 71.2\ \frac{\mathrm{kg}}{\mathrm{m^3}} / \sqrt{3} = 41.1\ \frac{\mathrm{kg}}{\mathrm{m^3}} \tag{93}$$

A.2.1.3 Heat capacity

The isobar heat capacity of the Saint Gobain bauxite proppant used was fitted by Wu [55], based on the measurements by Nathan P. Siegel.

$$\begin{aligned} c_{p,\mathrm{p}} = [&-2.853 \cdot 10^{-9}\, T^4 + 7.059 \cdot 10^{-6}\, T^3 - 5.795 \cdot 10^{-3}\, T^2 + 2.439\, T \\ &+ 677.0]\ \frac{\mathrm{J}}{\mathrm{kg\ °C}} \text{ for } 25\ °\mathrm{C} \le T \le 1{,}000\ °\mathrm{C} \end{aligned} \tag{94}$$

Note that the fitted correlation for $c_{p,\mathrm{p}}$ was derived for T in °C and must be taken into account, when using particle temperatures in Kelvin. An uncertainty of $a_{c_{p,\mathrm{p}}} = 2\ \%$ RD is given, according to the manual of the used Netzsch DSC 404 F1 measurement device [55]. A rectangular distribution of the uncertainty is assumed.

$$u_{c_{p,\mathrm{p}}} = \frac{2\ \%\ c_{p,\mathrm{p}}}{\sqrt{3}} \tag{95}$$

A.2.2 Air

Ambient air was used to study the performance of the TFHX. Dry air is used to determine the thermophysical properties. The properties are calculated as a function of gas absolute pressure and gas temperature. The dependence of dry air has been extensively investigated by Lemmon and Jacobsen [169], and Lemmon, Jacobsen [170] and is used, for example, to calculate the material properties for dry air in the VDI-Heat-Atlas [97], a standard reference work in German language for heat transfer applications. All parameters and coefficients not explicitly mentioned in the following are listed at the end of this section A.2.2. The calculation of thermophysical properties for dry air, which is a composition of three pure gases, is based on the thermophysical behavior of each mixing fraction. As proposed in the work of Lemmon, Jacobsen [170], the mixed composition of dry air is summed with the following mole fractions 78.12 % nitrogen, 20.96 % oxygen, and 0.92 % argon.

A.2.2.1 Density

To calculate the density of dry air (hereafter referred to as "gas" or "air"), the ideal gas law (IGL) can be applied, since the pressure range takes place at ambient conditions and the gas temperatures do not exceed 800 °C.

$$\rho_\mathrm{a} = \frac{p_\mathrm{a}}{R_\mathrm{a}\, T_\mathrm{a}} \tag{96}$$

Accordingly, the uncertainty of air density can be expressed as follows:

$$u_{\rho_\mathrm{a}} = \sqrt{\left(\frac{\partial \rho_\mathrm{a}}{\partial p_\mathrm{a}} u_{p_\mathrm{a}}\right)^2 + \left(\frac{\partial \rho_\mathrm{a}}{\partial R_\mathrm{a}} u_{R_\mathrm{a}}\right)^2 + \left(\frac{\partial \rho_\mathrm{a}}{\partial T_\mathrm{a}} u_{T_\mathrm{a}}\right)^2} \tag{97}$$

With the corresponding sensitivity coefficients:

$$\frac{\partial \rho_\mathrm{a}}{\partial p_\mathrm{a}} = \frac{1}{R_\mathrm{a}\, T_\mathrm{a}};\ \mathrm{in}\, \frac{\mathrm{g}}{\mathrm{N\ m}} \tag{98}$$

$$\frac{\partial \rho_\mathrm{a}}{\partial R_\mathrm{a}} = -\frac{p_\mathrm{a}}{R_\mathrm{a}^2\, T_\mathrm{a}};\ \mathrm{in}\, \frac{\mathrm{g}^2\ \mathrm{K}}{\mathrm{N\ m}^4} \tag{99}$$

$$\frac{\partial \rho_\mathrm{a}}{\partial T_\mathrm{a}} = -\frac{p_\mathrm{a}}{R_\mathrm{a}\, T_\mathrm{a}^2};\ \mathrm{in}\, \frac{\mathrm{g}}{\mathrm{N\ m}^3} \tag{100}$$

A.2.2.1.1 Uncertainty of specific gas constant of dry air

The specific gas constant of dry air, R_a, is calculated from the universal gas constant, R, and the molar mass of the aforementioned mixing composition of dry air, M_a.

$$R_\mathrm{a} = \frac{R}{M_\mathrm{a}} = 287.117126 \cdot 10^{-3}\ \frac{\mathrm{J}}{\mathrm{g\,K}} \tag{101}$$

Accordingly, the uncertainty can be expressed as follows:

$$u_{R_\mathrm{a}} = \sqrt{\left(\frac{\partial R_\mathrm{a}}{\partial R} u_R\right)^2 + \left(\frac{\partial R_\mathrm{a}}{\partial M_\mathrm{a}} u_{M_\mathrm{a}}\right)^2} = 3.1265 \cdot 10^{-6}\ \frac{\mathrm{J}}{\mathrm{g\,K}} \tag{102}$$

With the corresponding sensitivity coefficients:

$$\frac{\partial R_\mathrm{a}}{\partial R} = \frac{1}{M_\mathrm{a}} \tag{103}$$

$$\frac{\partial R_\mathrm{a}}{\partial M_\mathrm{a}} = -\frac{\mathrm{R}}{M_\mathrm{a}^2} \tag{104}$$

Where Lemmon, Jacobsen [170] provides

- R = 8.314 510 J/(mol · K) with u_R=0.000 070 J/(mol · K) and
- M_a = 28.9586 g/mol with u_{M_a} = 0.0002 g/mol.

A.2.2.1.2 Uncertainty of air pressure measurement

Depending on the measurement range, different instrument uncertainties must be applied. Sections A.3.3 and 0 describe the relative and absolute pressure measurement procedures. Accordingly, the air pressure at the inlet or bottom of the THFX, see Fig. 19, can be calculated by evaluating the logged data provided by the WIKA absolute pressure sensor. The gas pressure at the top of the column can be estimated by reducing the pressure at the bottom of the THFX by the pressure drop measured by the relative pressure sensor:

$$p_{\mathrm{HX,top}} = p_{\mathrm{HX,bottom}} - p_{\mathrm{rel,HX}} = p_{\mathrm{abs}} - p_{\mathrm{rel,HX}} \tag{105}$$

The uncertainties for the air pressure at the top and at the bottom of the TFHX can be calculated as follows:

$$u_{p_{\mathrm{HX,top}}} = \sqrt{u^2_{p_{\mathrm{abs}}} + u^2_{p_{\mathrm{rel,HX}}}} \tag{106}$$

$$u_{p_{\mathrm{HX,bottom}}} = u_{p_{\mathrm{abs}}} \tag{107}$$

However, regarding the uncertainty of the pressure measurement for gas flow measurement a different absolute pressure transducer is used, see A.3.6.1.1.

A.2.2.1.3 Uncertainty of air temperature

The combined uncertainty for gas temperature measurement as a combination of the equipment uncertainty for the temperature measurement $u_{T_{\mathrm{eq}}}$ is described in section A.3.9.1 and the reading uncertainty can be calculated as shown in section A.3.2.

$$u_{T_{\mathrm{a}}} = \sqrt{u^2_{T_{\mathrm{a,eq}}} + u^2_{T_{\mathrm{a,rd}}}} \tag{108}$$

A.2.2.1.4 Air dynamic viscosity

To calculate the dynamic viscosity of air, η_{a}, Lemmon and Jacobsen [169] propose the following approach

$$\eta_{\mathrm{a}} = \eta^0(T_a) + \eta^{\mathrm{r}}(\tau, \delta) \tag{109}$$

To calculate the dynamic air viscosity in $\mu\mathrm{Pa} \cdot \mathrm{s}$, the dilute gas viscosity η^0, the residual fluid viscosity η^{r}, $\tau = T_{\mathrm{c}}/T$ and $\delta = \rho/\rho_{\mathrm{c}}$ must be known, where ρ_{c} and T_{c} are critical parameters and are also given in Lemmon and Jacobsen [169]. The behavior and effects of viscosity in the critical region are negligible for most practical applications, so no extension to calculate viscosity in the critical region was made for this work. The dilute gas contribution can be calculated as follows:

$$\eta^0(T) = \frac{0.0266958 \cdot \sqrt{M_a\, T_a}}{\sigma^2\, \Omega(T^*)} \tag{110}$$

With σ as the dimensionless Lennard-Jones energy parameter and Ω is the collision integral.

$$\Omega(T^*) = \exp\left(\sum_{i=0}^{4} b_i \cdot\ [\ln(T^*)]^i\right) \tag{111}$$

In (111), $T^* = T_a/(\epsilon/k)$, where ϵ/k is the Lennard-Jones energy parameter and b_i is given in Lemmon and Jacobsen [169].

$\eta^{\mathrm{r}}$is described in (112), where γ_i is zero for $l_i = 0$ and one for $l_i \neq 0$.

$$\eta^{\mathrm{r}}(\tau\,,\delta) = \sum_{i=1}^{n} N_i\, \tau^{t_i}\, \delta^{d_i} \cdot \exp\left(-\gamma_i\, \delta^{l_i}\right) \qquad (\ 112\ )$$

The uncertainty of the dynamic air viscosity $u_{\eta_{\mathrm{a}}}$ is estimated to be 1 % for temperatures above 200 K [169]. It is assumed that the uncertainty given by the authors is applied to the reading (RD) value, thus: $u_{\eta_{\mathrm{a}}}$ = 1 % RD.

A.2.2.2 Thermal conductivity

Lemmon and Jacobsen [169] provide the thermal conductivity of dry air, λ, in mW/(m · K) as follows:

$$\lambda = \lambda^0(T) + \lambda^{\mathrm{r}}(\tau\,,\delta) + \lambda^{\mathrm{c}}(\tau, \delta) \qquad (\ 113\ )$$

With λ^0 as the dilute gas thermal conductivity. The residual fluid thermal conductivity is represented by λ^{r} and λ^c is the thermal conductivity critical enhancement where ρ_{c} and T_{c} are critical parameters and are also given in Lemmon and Jacobsen [169].

$$\lambda^0(T) = N_1 \cdot \left[\frac{\eta^0(T)}{1\ \mu\mathrm{Pa}\cdot\mathrm{s}}\right] + N_2\, \tau^{t_2} + N_3\, \tau^{t_3} \qquad (\ 114\ )$$

$$\lambda^{\mathrm{r}}(\tau, \delta) = \sum_{i=4}^{n} N_i\, \tau^{t_i}\, \delta^{d_i} \cdot \exp\left(-\gamma_i \delta^{l_i}\right) \qquad (\ 115\ )$$

To calculate the properties of the gas in the critical region, Lemmon and Jacobsen [169] propose to use the thermal conductivity critical enhancement model of Olchowy and Sengers [171]. However, this part is neglected since the gas properties of interest in this work are considered sufficiently far from the critical condition of air $\left(T_{\mathrm{c}} = 132.631\ \mathrm{K}; p_{\mathrm{c}} = 3.785\ \mathrm{MPa}\right)$. An uncertainty of 2 % for the thermal conductivity was estimated by the authors, that increases in vicinity to the critical region [169]. It is assumed that the uncertainty given by the authors is applied to the current value, hence: $u_{\lambda_{\mathrm{a}}} = 2$ % RD.

A.2.2.3 Heat capacity

Lemmon, Jacobsen [170] describes a general approach to calculate the ideal gas heat capacity as a function of the mole fraction average c_p by:

$$c_p = R \sum_{i=1}^{4} N_i\, T^{i-1} + \frac{N_5}{T^{1.5}} + \frac{N_6\, u^2\, e^u}{(e^u - 1)^2} + \frac{N_7\, v^2\, e^v}{(e^v - 1)^2} + \frac{\left(\frac{2}{3}\right) N_8\, w^2\, e^{-w}}{\left(\left(\frac{2}{3}\right) e^{-w} + 1\right)^2} \qquad (\ 116\ )$$

with $u = N_9/T$, $\mathrm{v} = N_{10}/t$ and $w = \mathrm{N}_{11}/T$

For dry air, the mole fractions for nitrogen, oxygen and argon can be substituted as previously described. The uncertainty of the heat capacity of air $u_{c_{p,\mathrm{a}}}$ is estimated to 1 % [170]. It is assumed that the uncertainty given by the authors is applied to the current value, therefore: $u_{c_{p,\mathrm{a}}}$ = 1 % RD.

Tab. 14 Parameter for calculation of viscosity and thermal conductivity for air, [169].

T_c in K	132.6312
ρ_c in mol/dm^3	10.4477
p_c in MPa	3.78502
M_a in g/mol	28.9586
ϵ/k in K	103.3
σ in nm	0.360
ξ_0 in nm	0.11
Γ in $-$	0.055
q_D in nm	0.31
T_{ref} in K	265.262

Tab. 15 Coefficients of the collision integral equation, [169].

i	b$_i$
0	0.431
1	-0.4623
2	0.08406
3	0.005341
4	-0.00331

Tab. 16 Coefficients and exponents of the residual fluid viscosity equations, [169].

i	N_i	t_i	d_i	l_i
0	10.72	0.2	1	0
1	1.122	0.05	4	0
2	0.002019	2.4	9	0
3	-8.876	0.6	1	1
4	-0.02916	3.6	8	1

Tab. 17 Coefficients for the ideal gas expressions, [170].

i	N_i
1	$0.6057194\cdot 10^{-7}$
2	$-0.210274769\cdot 10^{-4}$
3	$-0.158860716\cdot 10^{-3}$
4	-13.841928076
5	17.275266575
6	$-0.195363420\cdot 10^{-3}$
7	2.490888032
8	0.791309509
9	0.212236768
10	-0.197938904
11	25.36365
12	16.90741
13	87.31279

A.3 Measurement methods and uncertainties

A.3.1 t-distribution and expanded measurement uncertainty

In the current test setup, all measurements taken were performed by a series of repeated measurements taken manually or recorded by the data logger. When only a limited number of observations can be made during a measurement campaign, the resulting uncertainties must be corrected if the degrees of freedom, ν, are relatively small. ν is the number of observations reduced by one.

$$\nu = n - 1 \tag{117}$$

For a large number of observations, $n > 1{,}000$, it can be assumed that the uncertainty of the taken repeated measurements corresponds to a normal distribution, also for $\nu > 30$ it can be said that the taken observations still approximate a normal distribution with sufficient accuracy. However, for a smaller number of observations, the calculated uncertainties must be corrected by the coverage factor derived by the Student or t-distribution, $t_\mathrm{p}(\nu)$, with $\lim_{\nu\to\infty} t_\mathrm{p}(\nu) \to k_\mathrm{p}$. The required correction $t_\mathrm{p}(\nu)$ can be calculated with the inverse cumulative distribution function, also called the inverse t-distribution, $f(t,\nu)$, see e.g. [172].

$$f(t,\nu) = \frac{1}{\sqrt{\pi\nu}} \frac{\Gamma\left(\frac{\nu+1}{2}\right)}{\Gamma\left(\frac{\nu}{2}\right)} \left(1 + \frac{t^2}{\nu}\right)^{-\frac{(\nu+1)}{2}}, -\infty < t < +\infty \tag{118}$$

The values for $t_\mathrm{p}(\nu)$ is determined numerically and can be found in publicly available tables, in Excel by using the T.INV-function or e.g. also in Python using the NumPy-package and is shown in Tab. 18. By selecting $t_\mathrm{p}(\nu)$ or k_p, the desired level of confidence, p, must be chosen.

Tab. 18 Values of accumulated inverse t-distribution as function of degrees of freedom and level of confidence.

	level of confidence p					
degree of freedom ν	68.27 %	90.00 %	95.00 %	95.45 %	99.00 %	99.73 %
1	1.8374	6.3138	12.7062	13.9678	63.6567	235.7837
2	1.3213	2.9200	4.3027	4.5266	9.9248	19.2060
3	1.1969	2.3534	3.1824	3.3068	5.8409	9.2187
4	1.1417	2.1318	2.7764	2.8693	4.6041	6.6201
5	1.1105	2.0150	2.5706	2.6487	4.0321	5.5070
10	1.0526	1.8125	2.2281	2.2837	3.1693	3.9569
15	1.0345	1.7531	2.1314	2.1812	2.9467	3.5864
20	1.0257	1.7247	2.0860	2.1330	2.8453	3.4221
50	1.0101	1.6759	2.0086	2.0513	2.6778	3.1571
100	1.0050	1.6602	1.9840	2.0253	2.6259	3.0767
1000	1	1.645	1.96	2	2.576	3

A.3.2 Calculation of the experimental measurement uncertainty

Taking into account the above mentioned considerations of a limited number of observations, the measurement uncertainty can be corrected as follows, where for this work and unless otherwise stated, the confidence level is defined as $p = 95.00$ %, represented by the use of a coverage factor of $k_\mathrm{p} = 1{,}96$, applied to calculate the corresponding extended uncertainties, U. Furthermore, for the calculation of uncertainties within this work it was assumed that the Central Limit Theorem is applicable.

$$U = k_\mathrm{p}\, u(\bar{q}) = t_\mathrm{p}(\nu)\, u(\bar{q}) \tag{119}$$

The arithmetic mean of the n measurements is calculated by:

$$\bar{q} = \frac{1}{n}\sum_{i=1}^{n} q_i \tag{120}$$

The experimental standard deviation of the mean, $u(\bar{q})$, and the experimental standard deviation, $u(q_i)$, are calculated as follows:

$$u(\bar{q}) = \frac{u(q_i)}{\sqrt{n}} = \frac{1}{\sqrt{n}}\sqrt{\frac{1}{(n-1)}\sum_{i=1}^{n}(q_i - \bar{q})^2} \tag{121}$$

In this work, the mean of a sample is taken as the result of a finite number of repeated measurements and is denoted by $\bar{q}$, while in other sources $\bar{x}$ is used. This value differs from the population mean, which is the result of an infinite number of measurements and is denoted by μ. Similarly, the sample standard deviation is denoted by u, while other sources also use s. This value differs from the standard deviation of the population, σ.

Thus, the mean of the sample, $\bar{q}$, is an estimate of the population mean, μ, and the standard deviation of the sample, u, is an estimate of the standard deviation of the population, σ. Thus, the symbol σ is reserved for uncertainties with an ideal normal distribution obtained with an infinite number of repeated measurements, representing the entire population.

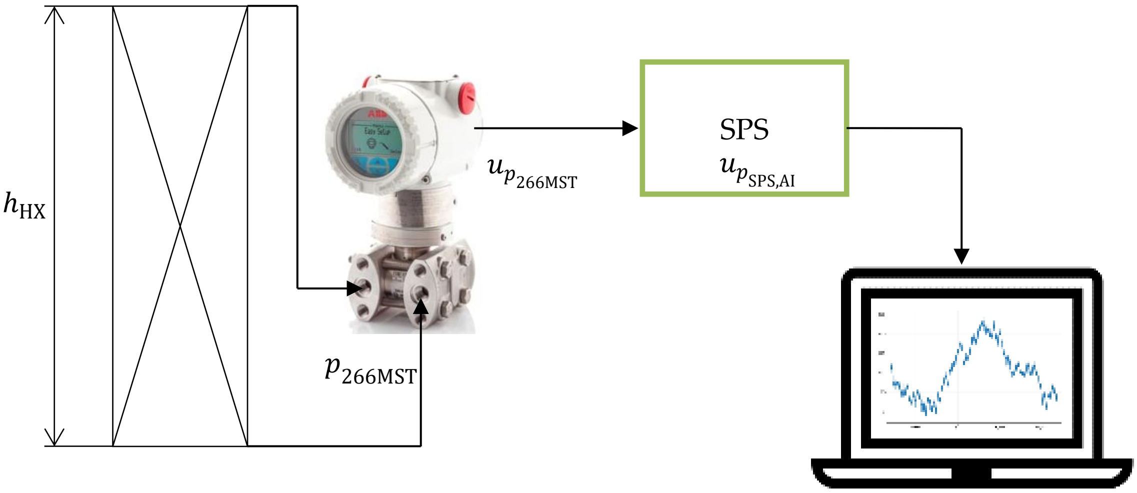

Fig. 63 Measuring section relative pressure measurement within the TFHX height.

A.3.3 Presure loss in packed column

The air pressure drop along the TFHX is measured with an ABB 266MST relative pressure transducer. The device has two inlets, see Fig. 63. One inlet connected to the bottom of the TFHX where the last packing element is mounted. The other inlet is connected to the top the packed column at a height of $h_{\mathrm{HX}} = 0.875$ m. The relative gas pressure, $p_{266\mathrm{MST}}$, is measured directly in the 266MST sensor and converted into a 4..20 mA signal. A VIPA-SPS analog input module (331-1KF01) constantly reads the signal from the pressure transducer and digitizes the sensors signal into a databank. According to the supplier of the pressure transducer and the VIPA-SPS analogue input module, the measurement uncertainty half-width intervals are ± 0.04 % FS and ± 0.5 %. For the VIPA-module, however, no information is provided s to whether the measurement uncertainty for the analogue input module is to be applied to FS or RD. Therefore, FS is chosen conservatively. Furthermore, a rectangular distribution from the uncertainties provided by the manufacturer is assumed: $u = a/\sqrt{3}$. Calibration of both the analog module and the pressure transducer confirms that the measurement uncertainties of both devices are within the limits specified by the manufacturer. The full range of the relative pressure transducer is provided with $p_{266\mathrm{MST,FS}} = 12000$ Pa. Accordingly, the equipment uncertainty of measurement for relative pressure within the TFHX can be determined as:

$$\begin{aligned} u_{p_{\mathrm{rel,HX,eq}}} &= \sqrt{u_{p_{266\mathrm{MST}}}^2 + u_{p_{\mathrm{SPS,AI}}}^2} \\ &= \sqrt{\left(\frac{0.04\ \%\ p_{266\mathrm{MST,FS}}}{\sqrt{3}}\right)^2 + \left(\frac{0.5\ \%\ p_{266\mathrm{MST,FS}}}{\sqrt{3}}\right)^2} = 34.8\ \mathrm{Pa} \end{aligned} \quad (122)$$

Accordingly, the total measurement uncertainty is a combination of the equipment uncertainty and the reading uncertainty, where the latter is the result of the experimental standard deviation of the mean from a number of n repeated measurements, as shown in section A.3.2.

$$u_{p_{\mathrm{rel,HX}}} = \sqrt{u_{p_{\mathrm{rel,HX,eq}}}^2 + u_{p_{\mathrm{rel,HX,rd}}}^2} \quad (123)$$

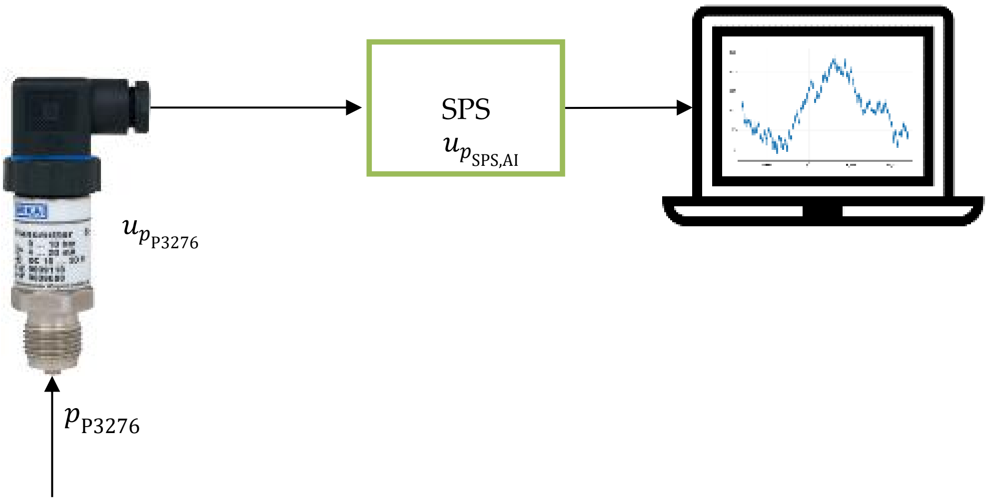

Fig. 64 Measuring section absolute pressure measurement.

A.3.4 Absolute pressure

The total ambient pressure and the absolute pressure at the bottom of the TFHX are measured. Therefore, two equal measuring sections are installed, see Fig. 64. The gas pressure applied to the absolute pressure sensor, p_{P3276}, is transduced into a 4..20 mA signal by a Tecsis (former WIKA) sensor of the type P3276 S070493. A VIPA-SPS analog input module (331-1KF01) continuously reads the signal from the pressure transducer and digitizes the sensor signal in a database. According to the suppliers of both the pressure transducer and the VIPA-SPS analog input module, both have a half-width interval of their upper and lower limits of $a_{\mathrm{P327}} = a_{\mathrm{SPS,AI}} = \pm 0.5\ \%\ \mathrm{FS}$. For the VIPA-module, however, no information is provided as to whether the half-width interval for the analog input module is to be applied to FS or RD. Therefore, FS is chosen conservatively. Furthermore, a rectangular distribution is applied to the uncertainties specified by the manufacturer: $u = a/\sqrt{3}$. Calibration of the analog module and the pressure transducer confirms that the measurement uncertainties of both devices are within limits specified by the manufacturer. The full range of the absolute pressure transducer is provided with $p_{\mathrm{P3276,FS}} = 1.6$ bar

$$u_{p_{\mathrm{abs,eq}}} = \sqrt{u_{p_{\mathrm{P3276}}}^2 + u_{p_{\mathrm{SPS,AI}}}^2} = \sqrt{2\left(\frac{0.5\ \%\ p_{\mathrm{P3276,FS}}}{\sqrt{3}}\right)^2} = 653.2\ \mathrm{Pa} \qquad (124)$$

Accordingly, the total measurement uncertainty is a combination of the equipment uncertainty and reading uncertainty, where the latter is the result of the experimental standard deviation of the mean from a number of repeated measurements, see section A.3.2.

$$u_{p_{\mathrm{abs}}} = \sqrt{u_{p_{\mathrm{abs,eq}}}^2 + u_{p_{\mathrm{abs,rd}}}^2} \qquad (125)$$

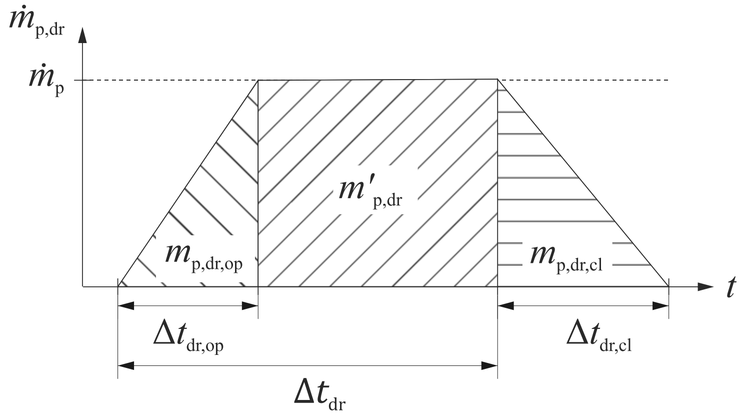

Fig. 65 Development of drained particle mass during drainage process.

A.3.5 Particle mass flow

A.3.5.1 Measurement equipment uncertainty

The mass flow in the test setup is determined by draining the particles below the packed column through a particle two-way valve or the drainage valve see, see Fig. 19 ⑧, while measuring the drainage time. The drained particles are set on a scale to determine its weight. However, since the opening and closing process of the particle drainage valve cannot be assumed to be instantaneous, the closing and opening time of the drainage valve must be taken into account, which could potentially falsify the measurement result.

The drained particle mass, $m_{\mathrm{p,dr}}$, is the sum of the drained particle mass during the opening and closing process of the drainage valve and the drained mass when the drainage valve is completely open, see Fig. 65.

$$m_{\mathrm{p,dr}} = m_{\mathrm{p,dr,op}} + m'_{\mathrm{p,dr}} + m_{\mathrm{p,dr,cl}} \tag{126}$$

During the opening and closing time of the drainage valve, the drained particle mass flow must be described as a function of time. Assuming a linear behavior for the opening and closing of the drainage valve, the extracted particle mass flow is assumed as a time-dependent fraction of the particle mass flow in the packed column, $\dot{m}_{\mathrm{p}}$. The opening and closing times need not be equal.

$$\dot{m}_{\mathrm{p,dr,op}}(t) = \frac{\dot{m}_{\mathrm{p}}}{\Delta t_{\mathrm{dr,op}}}\left(t - t_{\mathrm{dr,1}}\right) \tag{127}$$

$$\dot{m}_{\mathrm{p,dr,cl}}(t) = \frac{\dot{m}_{\mathrm{p}}}{\Delta t_{\mathrm{dr,cl}}}\left(t_{\mathrm{dr,cl}} - t\right) = \frac{\dot{m}_{\mathrm{p}}}{\Delta t_{\mathrm{dr,cl}}}\left(t_{\mathrm{dr,1}} + \Delta t_{\mathrm{dr}} + \Delta t_{\mathrm{dr,cl}} - t\right) \tag{128}$$

$$\text{with: } t_{\mathrm{dr,cl}} = t_{\mathrm{dr,2}} + \Delta t_{\mathrm{dr,cl}} \text{ and } t_{\mathrm{dr,2}} = t_{\mathrm{dr,1}} + \Delta t_{\mathrm{dr}}$$

During the time, when the drainage valve is fully open and particles are drained, the drainage mass flow is equal to the particle mass flow in the heat exchanger, $\dot{m}_{\mathrm{p}}$. The different particle masses during the drainage process, see (126), can be calculated as follows.

$$m_{\mathrm{p,dr,op}} = \int_{t_{\mathrm{dr,1}}}^{t_{\mathrm{dr,op}}} \dot{m}_{\mathrm{p,dr,cl}}(t)\mathrm{d}t = \int_{t_{\mathrm{dr,1}}}^{t_{\mathrm{dr,op}}} \frac{\dot{m}_{\mathrm{p}}}{\Delta t_{\mathrm{dr,op}}}\left(t - t_{\mathrm{dr,1}}\right)\mathrm{d}t = \frac{\Delta t_{\mathrm{dr,op}}}{2}\dot{m}_{\mathrm{p}} \tag{129}$$

$$\text{with: } t_{\mathrm{dr,op}} = t_{\mathrm{dr,1}} + \Delta t_{\mathrm{dr,op}}$$

$$m'_{\mathrm{p,dr}} = \int_{t_{\mathrm{dr,op}}}^{t_{\mathrm{dr,2}}} \dot{m}_{\mathrm{p}}\mathrm{d}t = \dot{m}_{\mathrm{p}}\left(t_{\mathrm{dr,2}} - t_{\mathrm{dr,op}}\right) = \dot{m}_{\mathrm{p}}\left(\Delta t_{\mathrm{dr}} - \Delta t_{\mathrm{dr,op}}\right) \tag{130}$$

$$\text{with: } t_{\mathrm{dr,2}} = t_{\mathrm{dr,1}} + \Delta t_{\mathrm{dr}} \text{ and } t_{\mathrm{dr,op}} = t_{\mathrm{dr,1}} + \Delta t_{\mathrm{dr,op}}$$

$$m_{\mathrm{p,dr,cl}} = \int_{t_{\mathrm{dr,2}}}^{t_{\mathrm{dr,cl}}} \dot{m}_{\mathrm{p,dr,cl}}(t)\mathrm{d}t = \int_{t_{\mathrm{dr,2}}}^{t_{\mathrm{dr,cl}}} \frac{\dot{m}_{\mathrm{p}}}{\Delta t_{\mathrm{dr,cl}}}\left(t_{\mathrm{dr,1}} + \Delta t_{\mathrm{dr}} + \Delta t_{\mathrm{dr,cl}} - t\right)\mathrm{d}t = \frac{\Delta t_{\mathrm{dr,cl}}}{2}\dot{m}_{\mathrm{p}} \tag{131}$$

$$\text{with: } t_{\mathrm{dr,cl}} = t_{\mathrm{dr,2}} + \Delta t_{\mathrm{dr,cl}} \text{ and } t_{\mathrm{dr,2}} = t_{\mathrm{dr,1}} + \Delta t_{\mathrm{dr}}$$

By inserting (129), (130), and (131) into (126), the particle mass flow in the heat exchanger can be calculated by measuring the total drained particle mass, $m_{\mathrm{p,dr}}$:

$$\dot{m}_{\mathrm{p}} = \frac{m_{\mathrm{p,dr}}}{\Delta t_{\mathrm{dr}} + \frac{1}{2}\left(\Delta t_{\mathrm{dr,cl}} - \Delta t_{\mathrm{dr,op}}\right)} \tag{132}$$

Where the equipment uncertainty of the particle mass flow can be calculated as follows:

$$u_{\dot{m}_{\mathrm{p,eq}}} = \sqrt{\left(\frac{\partial \dot{m}_{\mathrm{p}}}{\partial m_{\mathrm{p,dr}}}u_{m_{\mathrm{p,dr}}}\right)^2 + \left(\frac{\partial \dot{m}_{\mathrm{p}}}{\partial \Delta t_{\mathrm{dr,cl}}}u_{t_{\mathrm{dr,cl}}}\right)^2 + \left(\frac{\partial \dot{m}_{\mathrm{p}}}{\partial \Delta t_{\mathrm{dr,op}}}u_{t_{\mathrm{dr,op}}}\right)^2 + \left(\frac{\partial \dot{m}_{\mathrm{p}}}{\partial \Delta t_{\mathrm{dr}}}u_{t_{\mathrm{dr}}}\right)^2} \tag{133}$$

With the corresponding sensitivity coefficients:

$$\frac{\partial \dot{m}_{\mathrm{p}}}{\partial m_{\mathrm{p,dr}}} = \frac{1}{\Delta t_{\mathrm{dr}} + \frac{1}{2}\left(\Delta t_{\mathrm{dr,cl}} - \Delta t_{\mathrm{dr,op}}\right)};\ \text{in}\,\frac{1}{\mathrm{s}} \tag{134}$$

$$\frac{\partial \dot{m}_{\mathrm{p}}}{\partial \Delta t_{\mathrm{dr,cl}}} = -\frac{1}{2}\frac{m_{\mathrm{p,dr}}}{\left[\Delta t_{\mathrm{dr}} + \frac{1}{2}\left(\Delta t_{\mathrm{dr,cl}} - \Delta t_{\mathrm{dr,op}}\right)\right]^2};\ \text{in}\,\frac{\mathrm{g}}{\mathrm{s}} \tag{135}$$

$$\frac{\partial \dot{m}_{\mathrm{p}}}{\partial \Delta t_{\mathrm{dr,op}}} = \frac{1}{2}\frac{m_{\mathrm{p,dr}}}{\left[\Delta t_{\mathrm{dr}} + \frac{1}{2}\left(\Delta t_{\mathrm{dr,cl}} - \Delta t_{\mathrm{dr,op}}\right)\right]^2};\ \text{in}\,\frac{\mathrm{g}}{\mathrm{s}} \tag{136}$$

$$\frac{\partial \dot{m}_{\mathrm{p}}}{\partial \Delta t_{\mathrm{dr}}} = -\frac{m_{\mathrm{p,dr}}}{\left[\Delta t_{\mathrm{dr}} + \frac{1}{2}\left(\Delta t_{\mathrm{dr,cl}} - \Delta t_{\mathrm{dr,op}}\right)\right]^2};\ \text{in}\,\frac{\mathrm{g}}{\mathrm{s}} \tag{137}$$

A.3.5.1.1 Uncertainty of drained particle mass

The drained particles are measured, using a 440-49A scale from Kern & Sohn GmbH. The calibration certificate states an expanded uncertainty of $U_{\mathrm{sc,eq}} = 0.26$ g with a stated coverage factor of $k_{\mathrm{p}} = 2$, corresponding to a confidence interval of 95.45 %, see Tab. 18. According to (119), the normal standard uncertainty of the scale can be calculated to: $u_{\mathrm{sc,eq}} = 0.26\,\mathrm{g}/2 = 0.13\,\mathrm{g}$. In addition, the drainage process itself carries the risk of particle loss or measuring additional particles, emerging from dead volume within the drainage section. separate testing was performed, to avoid particle loss during the drainage process, so the uncertainty of lost particles during the drainage process will be neglected, $u_{\mathrm{p,err,dr}} = 0$ g. From the equipment and reading uncertainties, the uncertainty of the drained particle mass can be calculated as follows

$$u_{m_{\mathrm{p,dr}}} = \sqrt{u_{\mathrm{sc,eq}}^2 + u_{\mathrm{sc,rd}}^2 + u_{\mathrm{p,err,dr}}^2} \tag{138}$$

A.3.5.1.2 Drainage valve actuation time

The opening and closing times of the drainage valve are set to the same value. A Festo DSM-25-270-P pneumatic swivel motor [173] is used to actuate the drainage valve. The actuation speed for the application is provided by the manufacturer with an angular velocity of $\omega_{\mathrm{DSM}} = 0.2\,\mathrm{s}/90\,° = 0.0022\,\mathrm{s/deg}$. No further information on the uncertainty is provided, so the half-width interval of the provided angular velocity was conservatively assumed to be $a_{\omega_{\mathrm{DSM,rel}}} = 20\,\%$. Therefore, the uncertainty of the angular velocity can be determined to $u_{\omega_{\mathrm{DSM}}} = \omega_{\mathrm{DSM}} \cdot a_{\omega_{\mathrm{DSM,rel}}}/\sqrt{3} = 0.00026\,\mathrm{s/deg}$, assuming a rectangular distribution.

The DSM actuator type was used for both the automatically triggered particle inlet valve directly above the heat exchanger and the drainage valve directly below the HX. Fig. 20 illustrates the drainage valve in the discharge position such as the pivoting angle to rotate the funnel towards the silo of $\gamma_{\mathrm{DSM,dr}} = 22\,°$. The inaccuracy to position the funnel is estimated to be within a half-width interval of $a_{\gamma_{\mathrm{DSM,dr}}} = 5\,°$. Correspondingly, the standard uncertainty was determined by assuming a rectangular distribution, to be $u_{\gamma_{\mathrm{DSM,dr}}} = a_{\gamma_{\mathrm{DSM,dr}}}/\sqrt{3} = 2.89\,°$. The actuation time, opening and closing, of the DSM actuators can be calculated as follows:

$$\Delta t_{\mathrm{DSM}} = \omega_{\mathrm{DSM}} \cdot \gamma_{\mathrm{DSM}} \tag{139}$$

Correspondingly, the uncertainties of the actuation time can be calculated as follows:

$$\begin{aligned} u_{\Delta t_{\mathrm{DSM}}} &= \sqrt{\left(\frac{\partial \Delta t_{\mathrm{DSM}}}{\partial \omega_{\mathrm{DSM}}} u_{\omega_{\mathrm{DSM}}}\right)^2 + \left(\frac{\partial \Delta t_{\mathrm{DSM}}}{\partial \gamma_{\mathrm{DSM}}} u_{\gamma_{\mathrm{DSM}}}\right)^2} \\ &= \sqrt{\left(\gamma_{\mathrm{DSM}} \cdot u_{\omega_{\mathrm{DSM}}}\right)^2 + \left(\omega_{\mathrm{DSM}} \cdot u_{\gamma_{\mathrm{DSM}}}\right)^2} \end{aligned} \tag{140}$$

Applying (139) and (140), the actuation time of the drainage valve can be calculated to 0.049 s with an uncertainty of $u_{\Delta t_{\mathrm{DSM}}} = 0.007$ s. The drainage valve opening and closing time is assumed to be the same value $\Delta t_{\mathrm{DSM}} = \Delta t_{\mathrm{dr,op}} = \Delta t_{\mathrm{dr,cl}}$, correspondingly the uncertainties is set to the same value $u_{\Delta t_{\mathrm{DSM}}} = u_{\Delta t_{\mathrm{dr,op}}} = u_{\Delta t_{\mathrm{dr,cl}}}$.

A.3.5.1.3 Uncertainty in synchronizing drainage time

The drainage time is measured, simultaneously with the trigger to open and close the drainage, which is done in the LabView control system. Since the time measurement and trigger to actuate the drainage valve are performed in the same LabView control system, it is assumed that the uncertainties of the drainage time can be neglected, $u_{\Delta t_{\mathrm{dr}}} \approx 0$ s.

A.3.5.2 Combined particle mass flow uncertainty

The combined particle mass flow uncertainty is calculated from the root mean square of the measurement equipment uncertainty and the reading uncertainty (see section A.3.2).

$$u_{\dot{m}_{\mathrm{p}}} = \sqrt{u_{\dot{m}_{\mathrm{p,eq}}}^2 + u_{\dot{m}_{\mathrm{p,rd}}}^2} \qquad (141)$$

A.3.6 Air mass flow

In order to determine the air mass flow, an ABB SwirlMaster FSS450 was employed in conjunction with an ABB 261AS absolute pressure transducer. The air mass flow, $\dot{m}_{\mathrm{a,FFS450}}$, determined in the measurement section illustrated in Fig. 66, had to be corrected for the air leakage flow occurring in the air inlet area (AIA). During the design and assembly of the test rig, great emphasis was placed on ensuring an airtight system. Nevertheless, a minor air leakage flow could not be avoided, which must be accounted for and compensated for in the measured air flow as a function of the relative overpressure to the ambient. Accordingly, the gas flow rate entering the TFHX can be expressed as the measured gas flow rate from the measuring sensors and the air leakage flow rate.

$$\dot{m}_{\mathrm{a}} = \dot{m}_{\mathrm{a,FSS450}} + \dot{m}_{\mathrm{a,leak}} \qquad (142)$$

$\dot{m}_{\mathrm{a,leak}}$ is defined in a negative manner, indicating the flow of air out of the AIA. IN accordance with (142), the uncertainty of the air mass flow can be expressed as follows:

$$u_{\dot{m}_{\mathrm{a}}} = \sqrt{\left(\frac{\partial \dot{m}_{\mathrm{a}}}{\partial \dot{m}_{\mathrm{a,FSS450}}} u_{\dot{m}_{\mathrm{a,FSS450}}}\right)^2 + \left(\frac{\partial \dot{m}_{\mathrm{a}}}{\partial \dot{m}_{\mathrm{a,leak}}} u_{\dot{m}_{\mathrm{a,leak}}}\right)^2} = \sqrt{u_{\dot{m}_{\mathrm{a,FSS450}}}^2 + u_{\dot{m}_{\mathrm{a,leak}}}^2} \qquad (143)$$

$\dot{m}_{\mathrm{a,FSS540}}$ and $\dot{m}_{\mathrm{a,leak}}$ with its associated uncertainties are described in the following sections.

A.3.6.1 Measuring air flow

In the test setup, an adjustable airflow is provided by a HERZ HD140 side channel blower, which aspirates the ambient air. Subsequently, the air flow passes through an ABB SwirlMaster FSS450 swirl flowmeter, wherein the gas volume flow is measured. The integrated PT100 sensor, which measures the temperature of the gas in the FSS450, in conjunction with an ABB 261AS absolute pressure transducer that was directly wired to the SwirlMaster, enabled the FSS450 to calculate the internally the air mass flow and output it as a 4.. analog signal. A VIPA-SPS analog input module (331-1KF01) is responsible for the continuous reading of the signal from the FSS450, subsequently digitizing the sensor signal within a database.

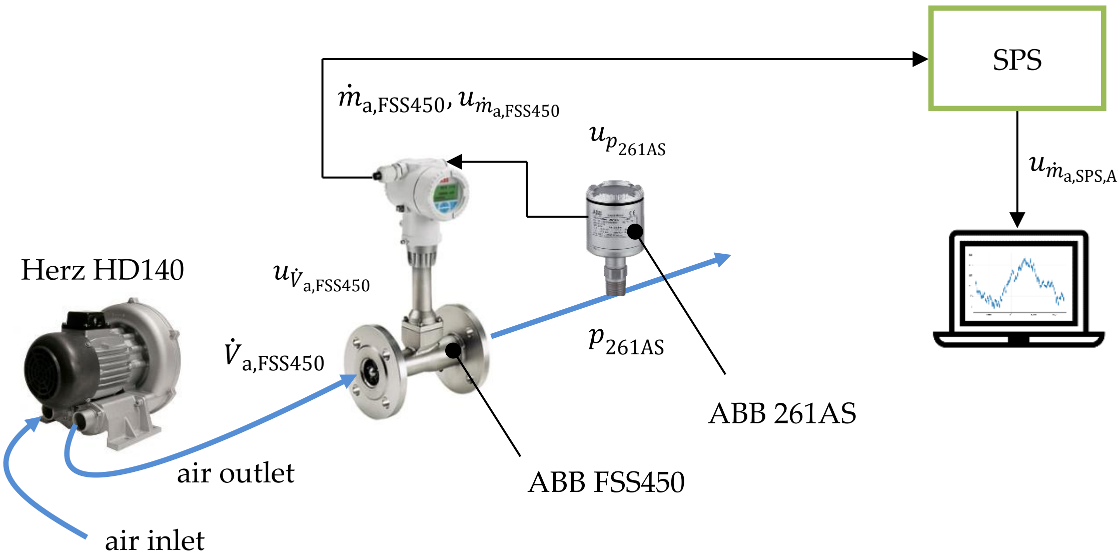

Fig. 66 Measuring section air mass flow rate provided by sensors.

The VIPA-SPS analog input module is reported to exhibit a half-width interval of $a_{\mathrm{SPS,AI}} = \pm\, 0.5\ \%$ FS for its upper and lower limits, as indicated by the supplier. However, no information is provided regarding whether the width of the half-width interval for the analog input module should be applied to FS or RD. Accordingly, conservatively the value of FS was used. Also, a rectangular distribution will be applied to the provided uncertainty: $u_{\dot{m}_{\mathrm{a,SPS,AI}}} = 0.039$ g/s. Fig. 66 provides a simplified illustration of the air mass flow measuring section. The blue arrow depicts the air path that occurs in DN20 tubes, while the black path illustrates the electrical wiring.

As previously stated, the FFS450 is utilized to quantify the air volume flow. The corresponding air mass flow at the sensor is calculated by multiplying $\dot{V}_{\mathrm{a,FSS450}}$ with the air density $\rho_{\mathrm{a,261AS}}$ in the vicinity of the SwirlMaster.

$$\dot{m}_{\mathrm{a,FSS450}} = \dot{V}_{\mathrm{a,FSS450}}\ \rho_{\mathrm{a,261AS}} \tag{144}$$

The equipment uncertainty of the air mass flow can be calculated as follows, by already considering the uncertainty of the SPS-AI:

$$\begin{aligned} u_{\dot{m}_{\mathrm{a,FSS450,eq}}} &= \sqrt{\left(\frac{\partial \dot{m}_{\mathrm{a,FSS450}}}{\partial \dot{V}_{\mathrm{a,FSS450,}}} u_{\dot{V}_{\mathrm{a,FSS450}}}\right)^2 + \left(\frac{\partial \dot{m}_{\mathrm{a,FSS450}}}{\partial \rho_{\mathrm{a,261AS}}} u_{\rho_{\mathrm{a,261AS}}}\right)^2 + u^2_{\dot{m}_{\mathrm{a,SPS,AI}}}} \\ &= \sqrt{\left(\rho_{\mathrm{a,261AS}}\ u_{\dot{V}_{\mathrm{a,FSS450}}}\right)^2 + \left(\dot{V}_{\mathrm{a,FSS450}}\ u_{\rho_{\mathrm{a,261AS}}}\right)^2 + \left(0.039\ \frac{\mathrm{g}}{\mathrm{s}}\right)^2} \end{aligned} \tag{145}$$

The value of $\rho_{\mathrm{a,261AS}}$ is dependent on both $p_{\mathrm{a,261AS}}$ and $T_{\mathrm{a,FSS450}}$, and can be calculated in accordance with the methodology outlined in section A.2.2.1. It should be noted that $p_{\mathrm{a,261AS}}$ and $T_{\mathrm{a,FSS450}}$ have not been logged directly, as they were processed internally by the FFSS450 to calculate the air mass flow. However, to calculate the uncertainty of the measurement equipment, corresponding values are assumed. From the experiments, it was known, that the air temperature after the HERZ blower never exceeded 55 °C correspondingly this was assumed for $T_{\mathrm{a,FSS450}}$. Additionally, the overpressure within the system never exceeded 5,000 Pa (see

Fig. 68) and the averaged ambient temperature within the workshop was 0.97 bar, and thus the pressure utilized for calculating the uncertainty of the gas flow rate will be calculated with the assumed maximum value of the absolute pressure within the air flow measurement section, resulting in $p_{261\mathrm{AS}}$ = 1.02 bar.

A.3.6.1.1 Uncertainty of air density for air mass flow measurement

The calculation of the air density uncertainty is provided in (97).

$$u_{\rho_{\mathrm{a,FSS450}}} = \sqrt{\left(\frac{\partial \rho_{\mathrm{a,FSS450}}}{\partial p_{261\mathrm{AS}}} u_{p_{\mathrm{a,261AS}}}\right)^2 + \left(\frac{\partial \rho_{\mathrm{a}}}{\partial R_{\mathrm{a}}} u_{R_{\mathrm{a}}}\right)^2 + \left(\frac{\partial \rho_{\mathrm{a,FSS450}}}{\partial T_{\mathrm{a,FSS450}}} u_{T_{\mathrm{a,FSS450}}}\right)^2} \qquad (146)$$

The uncertainty of R_{a} is outlined in section A.2.2.1. The supplier of the device provides the measurement half-width interval of the ABB absolute pressure sensor as $a_{\mathrm{a,261AS}} = \pm 0.05$ % RD. Throughout the course of all testing procedures, the maximum absolute pressure within the system did not exceed 1.03 bar. Therefore, for the sake of simplicity and conservatism, the max. pressure within the system is assumed to derive a constant uncertainty for $u_{p_{261\mathrm{AS}}}$. Assuming a rectangular distribution, the uncertainty can be calculated as follows:

$$u_{p_{261\mathrm{AS}}} = \frac{0.05\ \%\ p_{261\mathrm{AS}}}{\sqrt{3}} \approx \frac{0.05\ \%\ \max(p_{261\mathrm{AS}})}{\sqrt{3}} = \frac{0.05\ \%\ 1.03\ \mathrm{bar}}{\sqrt{3}} = 29.73\ \mathrm{Pa} \qquad (147)$$

The manufacturer provides the uncertainty of the internal temperature measurement in the FSS450 according to the installed PT100 thermo element, class A, in accordance with the standard IEC 751. For temperatures up to 100 °C, the half-width interval is stated to be $a_{\mathrm{a,PT100}} = \pm 0.35$ K. The uncertainty can be calculated assuming a rectangular distribution as follows:

$$u_{T_{\mathrm{a,FSS450}}} = \frac{0.35\ \mathrm{K}}{\sqrt{3}} = 0.20\ \mathrm{K} \qquad (148)$$

A.3.6.1.2 Uncertainty of air volume flow

The maximum uncertainty half-width interval of the utilized ABB SwirlMaster sensor is provided by the manufacturer as $a_{\mathrm{a,FSS450}} = \pm 0.5\%$ RD. Under the assumption of a rectangular distribution, the overall uncertainty of the volume measurement can be calculated by:

$$u_{\dot{V}_{\mathrm{a,FSS450}}} = \sqrt{u^2_{\dot{V}_{\mathrm{a,FSS450,eq}}} + u^2_{\dot{V}_{\mathrm{a,FSS450,rd}}}} = \sqrt{\left(\frac{0.005\ \dot{V}_{\mathrm{a,FSS450}}}{\sqrt{3}}\right)^2 + u^2_{\dot{V}_{\mathrm{a,FSS450,rd}}}} \qquad (149)$$

A.3.6.1.3 Measurement uncertainty gas flow rate at sensor

The total measurement uncertainty is derived from the combination of the equipment uncertainty and the reading uncertainty. The latter is represented by the experimental standard deviation of the mean derived from a series of repeated measurements, see section A.3.2.

$$u_{\dot{m}_{\mathrm{a,FSS450}}} = \sqrt{u^2_{\dot{m}_{\mathrm{a,FSS450,eq}}} + u^2_{\dot{m}_{\mathrm{a,FSS450,rd}}}} \qquad (150)$$

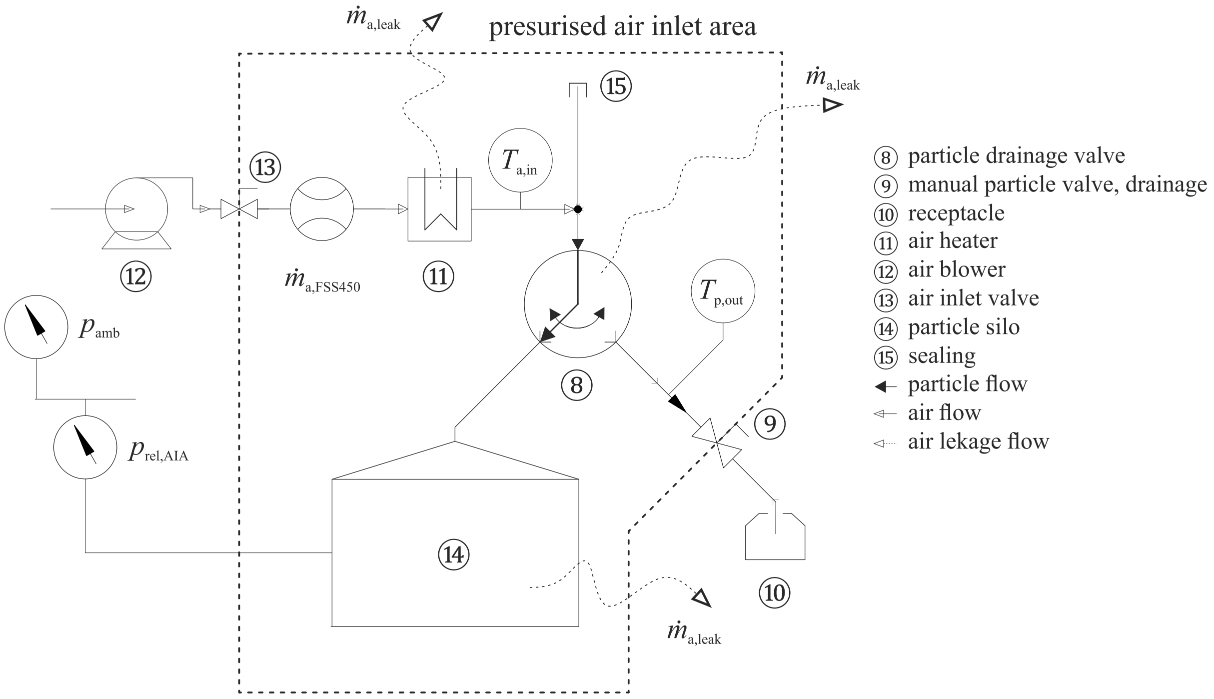

Fig. 67 Temporarily changed setup to measure the air leakage flow within the air inlet area.

A.3.6.2 Air leakage mass flow in the air inlet section

The air inlet area is defined as all components in the gas flow path after the air blower toward the packing inlet. Components such as the particle silo must also be airtight to allow the air flow to pass completely through the packed column. Fig. 67 illustrates the boundary of the air inlet area. In addition, $\dot{m}_{\mathrm{a,leak}}$ is shown exemplarily and must be compensated when measuring the air mass flow $\dot{m}_{\mathrm{a,FSS450}}$.

In Fig. 67 illustrates the provisional alterations to the TFHX configuration, which are necessary to ascertain the volume of airflow through the inlet area. Consequently, the interconnecting pipe that directs the airflow from the particle drainage valve to the packing structure has been temporarily disconnected and sealed airtight, see Fig. 67 ⑮. To measure the relative overpressure within the AIA in relation to the surrounding environment, the relative pressure sensor described in section A.3.3 has been temporarily installed at the particle silo. The aforementioned modifications to the setup permit the pressurization of the AIA with air, whereby only the leakage mass flow will escape the system over a specified period of time. The measurement procedure entails pressurizing the air inlet section to a pressure exceeding 4,800 Pa until the overpressure reaches a steady state condition of less than < 5 Pa/min. Subsequently, the air inlet valve is closed and the air inlet area is sealed hermetically. The air inlet valve is closed using the LabView control system, see Fig. 67 ⑬. The closing time of the air inlet pneumatic solenoid valve is considered negligible in the analysis. Only air leakage flow is able to leave the system and can be indirectly measured with the relative pressure transducer. The corresponding pressure relaxation curves were logged 10 times. The first three relative pressure relaxation curves of the AIA are shown exemplarily in Fig. 68.

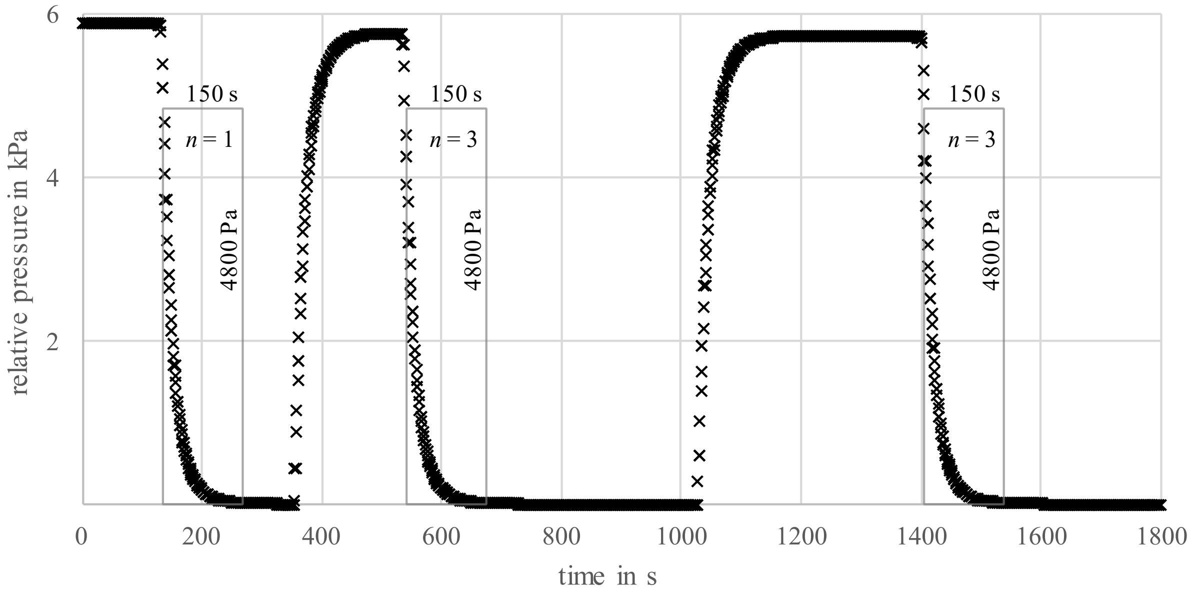

Fig. 68 Relative pressure relaxation curves for air leakage measurement in air inlet area.

In order to calculate the air leakage mass flow, it is necessary to determine the air mass in the AIA at discrete points in time, using the absolute pressure in the AIA as a reference point. The general correlation used to determine the gas leakage mass flow by measuring the change in the absolute pressure in the AIA is based on the ideal gas law.

$$p_{\mathrm{abs,AIA}} = \frac{m_{\mathrm{a,AIA}}\, R_{\mathrm{a}}\, T_{\mathrm{a,AIA}}}{V_{\mathrm{a,AIA}}} \qquad (151)$$

This enables the calculation of the pressure at each discrete time step of the recorded pressure relaxation curve in the AIA. By differentiating (151) with respect to time, the change in air mass within the air inlet area can be expressed as follows and simultaneously represents the air leakage mass flow.

$$\frac{\mathrm{d}p_{\mathrm{abs,AIA}}}{\mathrm{d}t} = \frac{\mathrm{d}\left(\frac{m_{\mathrm{a,AIA}}\, R_{\mathrm{a}}\, T_{\mathrm{a,AIA}}}{V_{\mathrm{a,AIA}}}\right)}{\mathrm{d}t}$$

$$\frac{\mathrm{d}p_{\mathrm{abs,AIA}}}{\mathrm{d}t} = \frac{\mathrm{d}m_{\mathrm{a,AIA}}}{\mathrm{d}t}\frac{R_{\mathrm{a}}\, T_{\mathrm{a,AIA}}}{V_{\mathrm{a,AIA}}}$$

$$\dot{m}_{\mathrm{a,leak}} = \frac{\mathrm{d}m_{\mathrm{a,AIA}}}{\mathrm{d}t} = \frac{\mathrm{d}p_{\mathrm{abs,AIA}}}{\mathrm{d}t}\frac{V_{\mathrm{a,AIA}}}{R_{\mathrm{a}}\, T_{\mathrm{a,AIA}}} = \frac{\mathrm{d}p_{\mathrm{abs,AIA}}}{\mathrm{d}t} C_{\mathrm{AIA}} \qquad (152)$$

with:

$$C_{\mathrm{AIA}} = \frac{V_{\mathrm{a,AIA}}}{R_{\mathrm{a}}\, T_{\mathrm{a,AIA}}}$$

The total air volume enclosed within the air inlet area, represented by $V_{\mathrm{a,AIA}} = 0.0867\ \mathrm{m}^3 \approx$ 90 liter, is subject to temperature changes due to the relatively low pressure changes < 4,800 Pa within a relatively large air volume. These changes are assumed to be negligible and $T_{\mathrm{a,AIA}}$ is therefore considered to be constant.

The change in air pressure between two discrete time points, t_i and t_{i+1}, directly corresponds to a change in the relative pressure within the AIA of the corresponding timestep $\Delta t_\mathrm{i} = t_{i+1} - t_i$. This results in a discrete approximation for $\mathrm{d}p_\mathrm{rel,AIA}/\mathrm{d}t$, which can be expressed as follows:

$$\frac{\mathrm{d}p_{\mathrm{abs,AIA},i}}{\mathrm{d}t_i} = \frac{\mathrm{d}p_{\mathrm{rel,AIA},i}}{\mathrm{d}t_i} \approx \frac{\Delta p_\mathrm{rel,AIA,i}}{\Delta t_i} = \frac{p_\mathrm{rel,AIA,i+1} - p_\mathrm{rel,AIA,i}}{t_{i+1} - t_i} \tag{153}$$

By applying this simplification, the air leakage mass flow can be approximated for each of the $N = 10$ timesteps for all n relaxation curves by the following equation:

$$\begin{aligned} \dot{m}_\mathrm{a,leak,n}(t_i) &= \frac{\mathrm{d}m_{\mathrm{a,AIA},i}}{\mathrm{d}t_i} = \frac{\mathrm{d}p_\mathrm{rel,AIA}}{\mathrm{d}t} C_\mathrm{AIA} \approx \frac{\Delta p_{\mathrm{rel,AIA},i}}{\Delta t_i} C_\mathrm{AIA} \\ &= \frac{p_{\mathrm{rel,AIA},i+1} - p_{\mathrm{rel,AIA},i}}{t_{i+1} - t_i} \frac{V_\mathrm{a,AIA}}{R_\mathrm{a}\, T_\mathrm{a,AIA}} \end{aligned} \tag{154}$$

A.3.6.2.1 Reading uncertainty of air leakage flow

To ascertain the statistical significance of the determination of the leakage mass flow, the air inlet area was pressurized $N = 10$ times, with the relaxation curves of the relative pressure recorded at each instance. To superimpose the various relaxation curves, curve fits were made for each relaxation curve in the area of 4,800 Pa and 150 s, see Fig. 68. The pressure data points utilized for the assessment, which also serve to indicate the commencement of the 150-second interval, were selected as soon as a pressure value fell below or reached 4,800 Pa. By fitting a curve to the discrete data points for each logged relative pressure, the discrete data could be transferred and approximated by a continuous correlation of the time-dependent pressure development in the AIA. This enabled the N measurements to be superimposed, and the corresponding reading uncertainty to be determined consecutively. The following section describes this process in further detail. In order to fit each relative pressure relaxation curve within the AIA, an exponential approach was employed to describe the development of the overpressure, $p_\mathrm{rel,AIA}$.

$$p_{\mathrm{rel,AIA},n}(t) = a_{\mathrm{AIA},n} \mathrm{e}^{-(b_{\mathrm{AIA},n}\, t)} \tag{155}$$

With n representing the curve fit and its parameters of the exponential approach for each of the $N = 10$ logged relaxation curves. According to (155), the time development as a function of relative pressure can be expressed as follows:

$$t\left(p_{\mathrm{rel,AIA},n}\right) = \frac{\ln\left(\dfrac{p_{\mathrm{rel,AIA},n}}{a_{\mathrm{AIA},n}}\right)}{-b_{\mathrm{AIA},n}} \tag{156}$$

In order to describe the change of the relative pressure over time, it is necessary to form the derivative of (155):

$$\frac{\mathrm{d}p_{\mathrm{rel,AIA},n}}{\mathrm{d}t} = -b_{\mathrm{AIA},n}\, a_{\mathrm{AIA},n} \mathrm{e}^{-(b_{\mathrm{AIA},n}\, t)}$$

with (156)

$$\frac{\mathrm{d}p_{\mathrm{rel,AIA},n}}{\mathrm{d}t} = -b_{\mathrm{AIA},n}\, a_{\mathrm{AIA},n} \mathrm{e}^{-\left(b_{\mathrm{AIA},n} \frac{\ln\left(\frac{p_{\mathrm{rel,AIA},n}}{a_{\mathrm{AIA},n}}\right)}{-b_{\mathrm{AIA},n}}\right)} = -b_{\mathrm{AIA},n}\, p_{\mathrm{rel,AIA},n}(t) \\ = -b_{\mathrm{AIA},n}\, a_{\mathrm{AIA},n} \mathrm{e}^{-(b_{\mathrm{AIA},n}\, t)} \qquad (157)$$

The description of the change in relative pressure in the AIA can be incorporated into (154), thereby enabling the continuous correlation of the resulting air leakage flow for each measurement n of N measurements to be expressed as follows:

$$\dot{m}_{\mathrm{a,leak,n}} = \frac{\mathrm{d}p_{\mathrm{rel,AIA,n}}}{\mathrm{d}t} C_{\mathrm{AIA}} = -b_{\mathrm{AIA},n}\, p_{\mathrm{rel,AIA},n}(t)\, C_{\mathrm{AIA}} \\ = -b_{\mathrm{AIA},n}\, a_{\mathrm{AIA},n} \mathrm{e}^{-(b_{\mathrm{AIA},n}\, t)} \frac{V_{\mathrm{a,AIA}}}{R_{\mathrm{a}}\, T_{\mathrm{a,AIA}}} = \frac{\mathrm{d}\dot{m}_{\mathrm{a,leak,n}}}{\mathrm{d}p_{\mathrm{rel,AIA}}} p_{\mathrm{rel,AIA},n} \\ \text{with} \\ \frac{\mathrm{d}\dot{m}_{\mathrm{a,leak,n}}}{\mathrm{d}p_{\mathrm{rel,AIA}}} = -b_{\mathrm{AIA},n} \frac{V_{\mathrm{a,AIA}}}{R_{\mathrm{a}}\, T_{\mathrm{a,AIA}}} \qquad (158)$$

The coefficients $a_{\mathrm{AIA},n}$ and $b_{\mathrm{AIA},n}$ for the N curve fits were determined, see Tab. 19. The curve fits exhibited a high degree of accuracy in correlation with the measured data, with a coefficient of determination, R_n^2, exceeding 0.998 for each fit. Continuous exponential curve fits for $\dot{m}_{\mathrm{a,leak,n}}$ were determined for each of the N measurements using (158). The corresponding curve fits for the developments of the air overpressure versus pressure relaxation time, see (155), the air leakage flow versus the relaxation time, see (158), and the air leakage mass flow versus the air overpressure, see (158), are plotted in Fig. 69, using the coefficients $a_{\mathrm{AIA},n}$ and $b_{\mathrm{AIA},n}$. The air leakage flow leaves the air inlet area, which necessitates the formulation of a negative correlation for the air leakage.

Tab. 19 Determined coefficients to fit for each air leakage measurement.

n	$a_{\mathrm{AIA},n}$ in $10^3\ N/m^2$	$b_{\mathrm{AIA},n}$ in $10^{-2}\ 1/s$
1	4.55651	5.53465
2	4.51666	5.48930
3	4.55838	5.55332
4	4.55374	5.67700
5	4.44028	5.54731
6	4.36737	5.60916
7	4.55428	5.54440
8	4.66736	5.56864
9	4.56248	5.56836
10	4.38951	5.60219

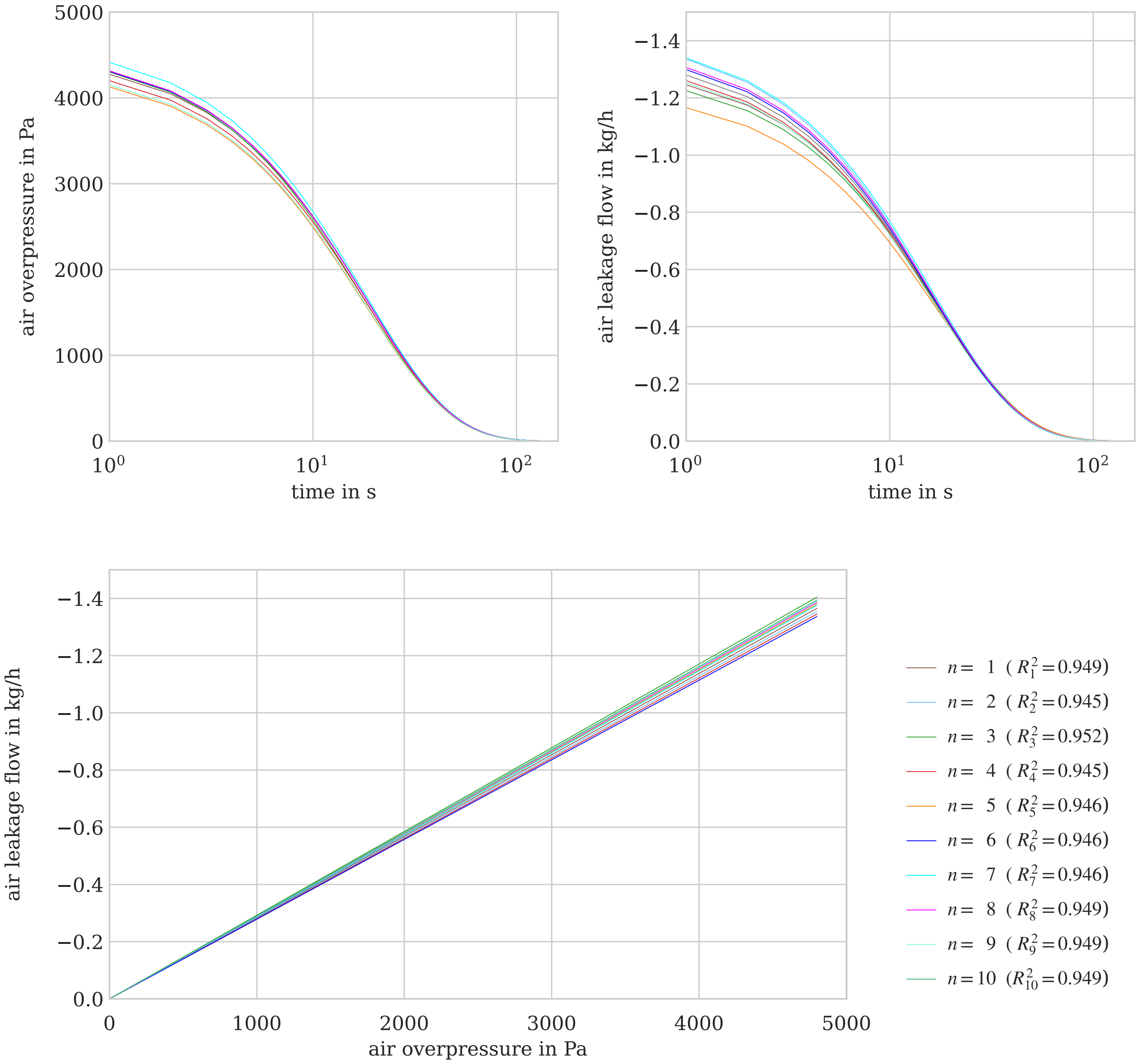

Fig. 69 Fitted air overpressure vs. relaxation time (upper left), air leakage flow vs. relaxation time (upper right) and air leakage flow vs. overpressure (bottom).

For relaxation times of $t_n < 20$ s, the relaxation curves exhibit a deviation in the measured air overpressure, which decreases over time with the reduction of overpressure in the AIA. Due to the large number of plots in Fig. 69, the usage of symbols was omitted. For each of the 10 fitted curves at predefined x-values, the corresponding y-values were calculated. This resulted in the calculation of the arithmetic mean and experimental standard deviation of the mean for each x-value, as detailed in section A.3.2. The influence of the t-distribution on the experimental standard deviation of the mean was also considered, see (119) and Tab. 18. The coefficients for the fitted curve of the mean for air overpressure versus relaxation time (see Fig. 70, upper left) were determined according to (155) to be $\bar{a}_{\mathrm{AIA}} = 4.51658 \cdot 10^3\ \mathrm{N/m^2}$ and $\bar{b}_{\mathrm{AIA}} = 5.56886 \cdot 10^{-2}\ \mathrm{s^{-1}}$. The linear correlation and steepness of the graph plotted in Fig. 70 (bottom) can be determined according to (158) to be $\mathrm{d}\dot{m}_{\mathrm{a,leak}}/\mathrm{d}p_{\mathrm{rel,AIA}} = -5.77361 \cdot 10^{-5}$ kg/h/Pa, with a relative uncertainty of $u_{\dot{m}_{\mathrm{a,leak,rd}}} = 0.966$ % RD. Any additional uncertainties that may arise due to the superimposition of the ten relaxation curves, such as those resulting from minor deviations in R_n^2 values greater than 0.998, are considered to be negligible and thus will not be addressed further in the subsequent deduction of the air leakage mass flow reading uncertainty. The derived air leakage flow correlation was also applied during the hot test campaign.

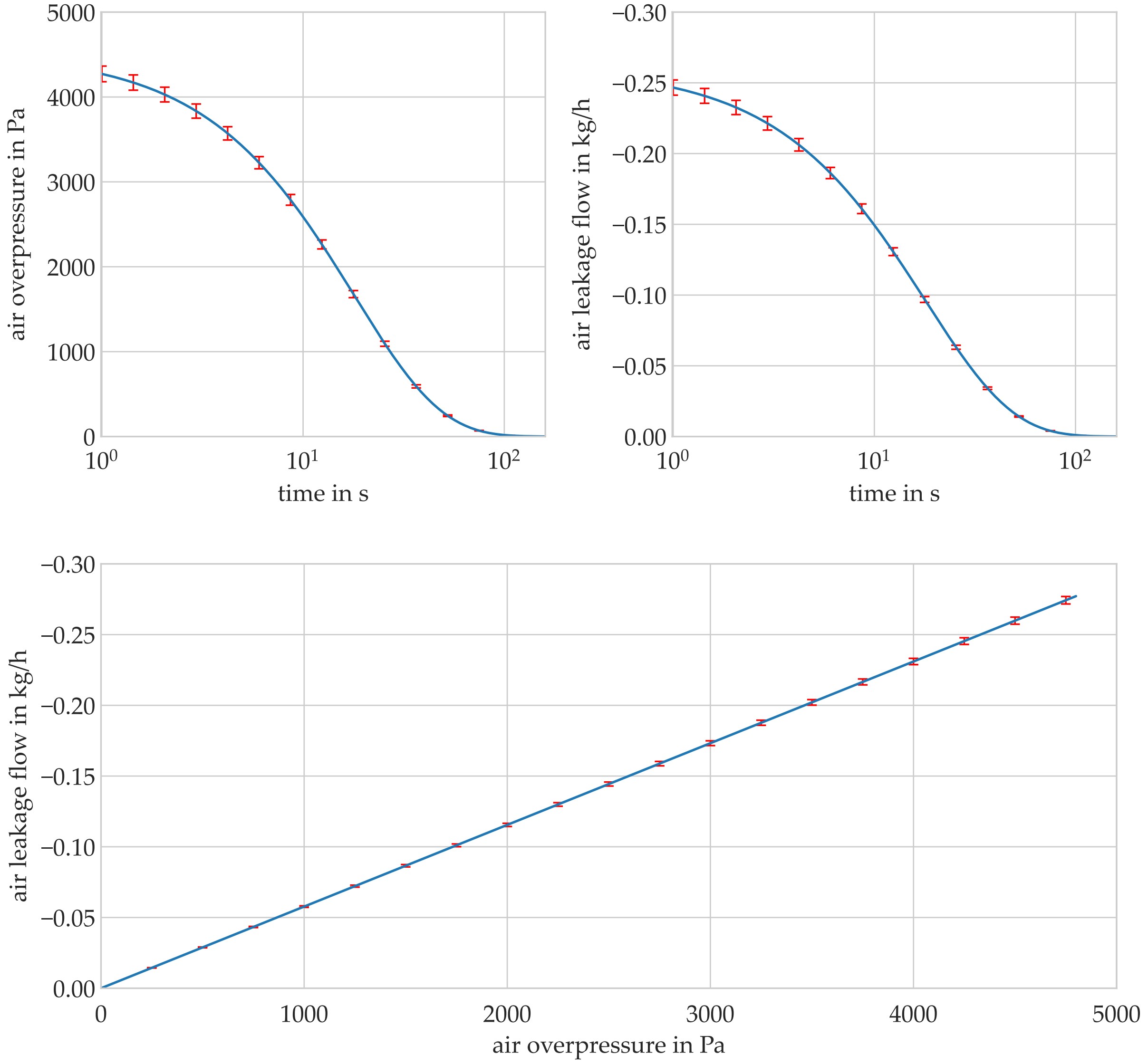

Fig. 70 Mean and uncertainty measurement of air overpressure vs. relaxation time (upper left), air leakage flow vs. relaxation time (upper right) and air leakage flow vs. overpressure (bottom).

A.3.6.2.2 Equipment uncertainty of air leakage flow

(158) correlates the behavior of the air leakage mass flow with the overpressure in the air inlet area. The uncertainty for b_{AIA}, is assumed to be negligible. Accordingly, the equipment uncertainty of the air leakage mass flow can be expressed as follows:

$$u_{\dot{m}_{\mathrm{a,leak,eq}}} = \sqrt{\begin{array}{l}\left(\dfrac{\partial \dot{m}_{\mathrm{a,leak,eq}}}{\partial p_{\mathrm{rel,AIA}}} u_{p_{\mathrm{rel,AIA}}}\right)^2 + \left(\dfrac{\partial \dot{m}_{\mathrm{a,leak,eq}}}{\partial V_{\mathrm{a,AIA}}} u_{V_{\mathrm{a,AIA}}}\right)^2 + \\ \quad + \left(\dfrac{\partial \dot{m}_{\mathrm{a,leak,eq}}}{\partial R_{\mathrm{a}}} u_{R_{\mathrm{a}}}\right)^2 + \left(\dfrac{\partial \dot{m}_{\mathrm{a,leak,eq}}}{\partial T_{\mathrm{a,AIA}}} u_{T_{\mathrm{a,AIA}}}\right)^2\end{array}} \qquad (159)$$

With the corresponding sensitivity coefficients:

$$\frac{\partial \dot{m}_{\text{a,leak,eq}}}{\partial p_{\text{rel,AIA}}} = -b_{\text{AIA}} \frac{V_{\text{a,AIA}}}{R_{\text{a}}\, T_{\text{a,AIA}}}; \text{in} \frac{\text{g}}{\text{s}} \cdot \frac{\text{m}^2}{\text{N}} \tag{160}$$

$$\frac{\partial \dot{m}_{\text{a,leak,eq}}}{\partial V_{\text{a,AIA}}} = -b_{\text{AIA}}\, p_{\text{rel,AIA}} \frac{1}{R_{\text{a}}\, T_{\text{a,AIA}}}; \text{in} \frac{\text{g}}{\text{s}} \cdot \frac{\text{N}}{\text{m}^3} \tag{161}$$

$$\frac{\partial \dot{m}_{\text{a,leak,eq}}}{\partial R_{\text{a}}} = b_{\text{AIA}}\, p_{\text{rel,AIA}} \frac{V_{\text{a,AIA}}}{R_{\text{a}}^2\, T_{\text{a,AIA}}}; \text{in} \frac{\text{g}}{\text{s}} \cdot \frac{\text{g N}}{\text{N m}} \tag{162}$$

$$\frac{\partial \dot{m}_{\text{a,leak,eq}}}{\partial T_{\text{a,AIA}}} = b_{\text{AIA}}\, p_{\text{rel,AIA}} \frac{V_{\text{a,AIA}}}{R_{\text{a}}\, T_{\text{a,AIA}}^2}; \text{in} \frac{\text{g}}{\text{s}} \cdot \text{K} \tag{163}$$

The uncertainty for the specific gas constant for air is given in section A.2.2.1.1

By using this method of quantifying the air leak mass flow rate for the TFHX, one can correlate the relative overpressure in the air inlet area of the test rig from the measured pressure drop in the HX. This assumption seems to be valid since the dimensions of the cross sectional areas in the piping of the exhaust section after the TFHX are relatively large, therefore it was assumed that the pressure drop in the off-gas section $\Delta p_{\text{off-gas}}$ is negligible and therefore the measured relative overpressure is equal to the overpressure in the air inlet system respectively to the ambient.

$$p_{\text{rel,HX}} + \overbrace{\Delta p_{\text{off-gas}}}^{\approx 0} = p_{\text{rel,AIA}} \tag{164}$$

A.3.6.2.2.1 Uncertainty of air temperature for AIA

The air temperature was measured with the installed TCs in the air inlet area with $T_{\text{a,AIA}} = 24.975\ °\text{C}$, see Fig. 67. Due to the low change in pressure within the AIA, during the leakage experiments, the theoretical change in temperature is neglected and assumed to be constand. During the pressure relaxation measurements, more than 300,000 data points were measured for the gas temperature, while the experimental standard deviation was determined to be 0.0927 °K. According to (121) the experimental standard deviation of the mean is neglected due to the large number of data points: $u_{T_{\text{a,AIA}}} = 0.0927\ °\text{K} \backslash \sqrt{300\ 000}\ \approx 0\ °\text{K}$. It follows that for this part of the analysis, the uncertainty of the temperature is mainly provided by the equipment uncertainty of the temperature measurement, and according to (198) can be calculated to $u_{T_{\text{a,AIA}}} = 0.30\ \text{K}$.

A.3.6.2.2.2 Uncertainty of relative pressure in the AIA

As shown in Fig. 61, in order to determine the pressure relaxation curve for the means of determining the air leakage mass flow, the ABB 266MST relative pressure sensor was temporarily connected to one of the two pressure inlets to the AIA and the second inlet to the atmosphere to measure the evolution of the relative overpressure in the pressurized AIA. In section A.3.1 describes the uncertainty of the relative pressure measurement section. While for the current modification of the test setup it can be set: $u_{p_{\text{rel,AIA}}} = u_{p_{\text{rel,HX}}}$, see (123).

A.3.6.2.2.3 Uncertainty of air volume of the AIA

The air volume was measured according to the existing CAD model of the test setup with $V_{\mathrm{a,AIA}} = 88{,}743{,}894.5\ \mathrm{mm}^3 = 88.74$ liters. Despite the care taken in assembling the heat exchanger test setup and keeping the CAD model up to date. Differences between the CAD model and the real setup must be expected. This is estimated to be 10 %, resulting to $u_{V_{\mathrm{a,AIA}}} = 8.874\ \text{liters}/\sqrt{3} = 51.236\ \text{liters}$.

A.3.6.2.3 Overall Measurement uncertainty for air leakage mass flow

In the previous two sections, the equipment and reading uncertainties for the air leakage mass flow were derived. Accordingly, the corresponding total measurement uncertainty is calculated by:

$$u_{\dot{m}_{\mathrm{a,leak}}} = \sqrt{u^2_{\dot{m}_{\mathrm{a,leak,eq}}} + u^2_{\dot{m}_{\mathrm{a,leak,rd}}}} \tag{165}$$

A.3.7 Values normalized to cross-sectional area of TFHX

In the literature on trickling reactors, it is typical to normalize the flow rates to the free cross sectional area of the reactor, A_{HX}. By normalizing, a better comparability between other works can be achieved. The normalization process can be performed for different variables, such as particle or air mass flow, and the corresponding uncertainty is also determined. Here the approach to normalize a variable is shown for the general variable var. A normalized variable to the cross-sectional area is marked with # in the superscript.

$$var^{\#} = \frac{var}{A_{\mathrm{HX}}} = \frac{var}{w^2_{\mathrm{HX}}};\ \mathrm{in}\ \frac{[var]}{\mathrm{m}^2} \tag{166}$$

The uncertainty can be calculated as follows:

$$u_{var^{\#}} = \sqrt{\left(\frac{\partial var^{\#}}{\partial var} u_{var}\right)^2 + \left(\frac{\partial var^{\#}}{\partial w_{\mathrm{HX}}} u_{w_{\mathrm{HX}}}\right)^2};\ \mathrm{in}\ \frac{[var]}{\mathrm{m}^2} \tag{167}$$

The corresponding sensitivity coefficients are:

$$\frac{\partial var^{\#}}{\partial var} = \frac{1}{w^2_{\mathrm{HX}}};\ \mathrm{in}\ \frac{1}{\mathrm{m}^2} \tag{168}$$

$$\frac{\partial var^{\#}}{\partial w_{\mathrm{HX}}} = -2\frac{var}{w^3_{\mathrm{HX}}};\ \mathrm{in}\ \frac{[var]}{\mathrm{m}^3} \tag{169}$$

A.3.8 Particle hold-up

As outlined in section 4.1.1.4, the dynamic particle hold-up is measured by closing the particle inlet valve, see Fig. 19 ④, and simultaneously opening the particle drainage valve, see Fig. 19 ⑧. This procedure allows for the extraction of a "snapshot" of the freely trickling particle cloud within the packed column. As outlined in section 4.1.1.4, it is assumed that the drained particles represent the total amount of solids accountable for the dynamic particle hold-up. The theoretical basis and experimental procedure to determine β are described in sections 3.3 and 4.1.1.4, respectively.

The equipment uncertainty of β can be derived based on (21) and is expressed as follows:

$$u_{\beta,\mathrm{eq}} = \sqrt{\left(\frac{\partial \beta}{\partial m_{\mathrm{p,pac}}} u_{m_{\mathrm{p,pac}}}\right)^2 + \left(\frac{\partial \beta}{\partial \rho_{\mathrm{p}}} u_{\rho_{\mathrm{p}}}\right)^2 + \left(\frac{\partial \beta}{\partial V_{\mathrm{HX}}} u_{V_{\mathrm{HX}}}\right)^2 + \left(\frac{\partial \beta}{\partial \epsilon_0} u_{\epsilon_0}\right)^2} \tag{170}$$

The corresponding sensitivity coefficients are:

$$\frac{\partial \beta}{\partial m_{\mathrm{p,pac}}} = \frac{1}{V_{\mathrm{HX}}\, \epsilon_0\, \rho_{\mathrm{p}}};\ \mathrm{in}\,\frac{1}{\mathrm{g}} \tag{171}$$

$$\frac{\partial \beta}{\partial \rho_{\mathrm{p}}} = -\frac{m_{\mathrm{p,pac}}}{V_{\mathrm{HX}}\, \epsilon_0\, \rho_{\mathrm{p}}^2};\ \mathrm{in}\,\frac{\mathrm{m}^3}{\mathrm{g}} \tag{172}$$

$$\frac{\partial \beta}{\partial V_{\mathrm{HX}}} = -\frac{m_{\mathrm{p,pac}}}{V_{\mathrm{HX}}^2\, \epsilon_0\, \rho_{\mathrm{p}}};\ \mathrm{in}\,\frac{1}{\mathrm{m}^3} \tag{173}$$

$$\frac{\partial \beta}{\partial \epsilon_0} = -\frac{m_{\mathrm{p,pac}}}{V_{\mathrm{HX}}\, \epsilon_0^2\, \rho_{\mathrm{p}}};\ \mathrm{in}\ - \tag{174}$$

As derived in section 3.3, the extended particle hold-up, β^* (21), was applied when comparing different packing geometries. In the following, only the uncertainty for β is derived, and not explicitly for β^*, since the extended particle hold-up can be determined for setting ϵ_0 to unity, see (21). The same applies for the uncertainties: $u_{\beta^*} = u_\beta(\epsilon_0 = 1)$.

The geometrical uncertainties $u_{V_{\mathrm{HX}}}$ and u_{ϵ_0} in (170) can be directly determined as a function of the geometric parameters of each packing structure and the HX with its corresponding individual uncertainties, including manufacturing and assembling tolerances, see section A.3.8.2 and A.3.8.3. The manufacturer provides the uncertainty of the particle density, see section A.2.1.2. The uncertainty of the particle mass within the packing void, $u_{m_{\mathrm{p,pac}}}$, is determined by considering the reading uncertainty of the drained particle mass for a number of repeated measurements and by considering the corresponding measurement equipment uncertainty. The following subsections address additional measurement errors in the determination of $m_{\mathrm{p,pac}}$ and describe the compensation measures that were taken.

A.3.8.1 Uncertainty of particle mass within packing void

In section 3.3, the definition of the particle hold-up is described in (21). The same high-speed pneumatic motors were employed to actuate the armatures of both the particle inlet valve, see Fig. 19 ④, and the particle drainage valve, see Fig. 19 ⑧. As stated by the manufacturer, the used Festo DSM-25-270-P high-speed pneumatic motors offer closing times within the range of 0.2 s/90° [173]. To determine the particle hold-up, the solenoid valves of both pneumatic motors are triggered simultaneously via the SPS. Thus, it can be confidently asserted that both DSM actuators for the particle inlet and drainage are actuated simultaneously.

For the determination of the particle hold-up (21), it is necessary to determine the particle mass within the packed column, $m_{\mathrm{p,pac}}$. However, the designed measurement procedure entails the drainage of an additional particle mass. The drainage of erroneous particles is attributable to the height between the particle inlet valve and the top of the packing, $m_{\mathrm{p,err,in}}$, see Fig. 35, and between the bottom of the packing and the pivoting funnel of the drainage valve, $m_{\mathrm{p,err,dr}}$ see Fig. 20. In order to obtain exclusively the particle cloud within the packed column and calculate the particle hold-up, it is necessary to estimate and compensate for the two additional free-falling particle clouds. Moreover, although the same pneumatic motors were used to actuate both valves, the inlet valve and the drainage valve possess different actuation angles, resulting in different actuation times $\Delta t_{\mathrm{DSM,pi}}$ $\Delta t_{\mathrm{DSM,dr}}$. Those different actuation times also have to be considered when determining the erroneous drained particle mass. Therefore, the drained particle mass must be corrected by a number of fractions in order to calculate the particle mass exclusively within the void of the packed column.

$$m_{\mathrm{p,pac}} = m_{\mathrm{p,dr}} - m_{\mathrm{p,err,in}} - m_{\mathrm{p,err,out}} - m_{\mathrm{p,err,DSM}} - m_{\mathrm{p,err,dr}} \tag{175}$$

Preliminary measurements were conducted to ensure that no particles are lost during the drainage process: $m_{\mathrm{p,err,dr}} = 0$.

In order to estimate the amount of the falling particle clouds above and below the packed column, the results provided by Kim, Siegel [166] are applied. The authors conducted an experimental investigation into the velocity development of particles with varying diameters and mass flows. The sintered bauxite proppants, CarboCeramics, CARBOSHP, were selected as they provide the same density as the bauxite particles used in this work. The mass flows depicted in Fig. 71 are provided in kg/m/s. In their work, the authors employed a slide valve to regulate the particle flow and normalized the flow rate to the constant slot width of the valve, which was set at 30 cm. This allowed for adjustments in the flow rate by modifying the slot thickness.

As illustrated in Fig. 71 (left), he velocity development of falling particles appears to be approximately independent of different particle mass flows, particularly for low falling heights below 1.3 m. Additionally, within the particle diameters of 0.697 mm up to 1.291 mm, the particles exhibit a nearly equal velocity development within a falling cloud. The plots in Fig. 71 (right) was interpolated for particles of 1 mm in diameter and is presented in Fig. 72.

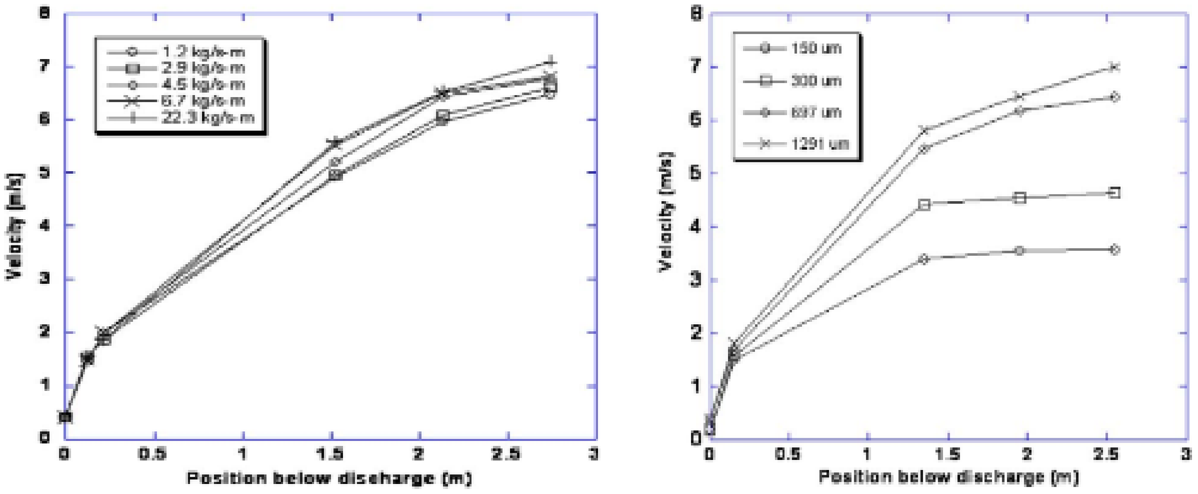

Fig. 71 Left: particle velocity distribution along the drop length (particle size: 0.697 mm); right: velocity profile for different size particles (mass flow: 4.5 kg/s/m), [166].

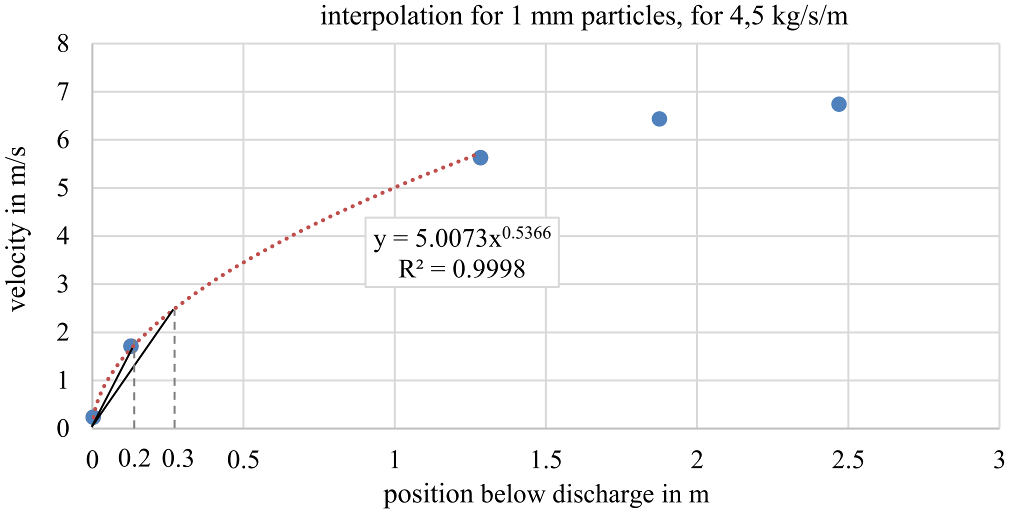

Fig. 72 Experimentally investigated velocity development of free-falling particles with 1 mm, [166].

For falling heights < 1.3 m, the velocity development can be approximated as follows:

$$u_{\mathrm{p,ff}}(h_{\mathrm{ff}}) = 5.0073\, h_{\mathrm{ff}}{}^{0.5366} \text{ with } 0 < h_{\mathrm{ff}} < 1.3 \text{ m} \qquad (176)$$

The free-falling distances at the particle inlet of $h_{\mathrm{ff,pi}} = 219$ mm and at the drainage section of $h_{\mathrm{ff,dr}} = 321$ mm, see Fig. 35 and Fig. 20, are in a region of the velocity development where a simplified linear behavior of the velocity development can be assumed with initial particle velocity of 0 m/s, see Fig. 72. Correspondingly, the erroneous particle mass in the free-fall zones can be calculated as follows:

$$m_{\mathrm{p,err,ff}}(h_{\mathrm{ff}}) = \dot{m}_{\mathrm{p}}\, t_{\mathrm{p,ff}} \approx \dot{m}_{\mathrm{p}} \frac{h_{\mathrm{ff}}}{\overline{u_{\mathrm{p,ff}}}(h_{\mathrm{ff}})} = \dot{m}_{\mathrm{p}} \frac{h_{\mathrm{ff}}}{u_{\mathrm{p,ff}}(h_{\mathrm{ff}})/2} \qquad (177)$$

The uncertainty of the velocity measurement is given with $u_{u_{\mathrm{p,ff}}} = 0.1297$ m/s [166]. No information on the confidence level was stated, so a confidence level of 68.27 % was assumed, which results in a corresponding coverage factor of $k_{p_{u_{\mathrm{p,ff}}}} = 1$.

Due to $\Delta t_{\mathrm{DSM,pi}} > \Delta t_{\mathrm{DSM,dr}}$, see section A.3.5.1.2, the particle inlet valve is still in the process of closing when the drainage valve finishes its pivoting movement. As a result, additional particles can pass through the particle inlet valve for a short period of time while particles are already being discharged at the drainage valve. This additional particle quantity $m_{\mathrm{p,err,DSM}}$ must be taken into account.

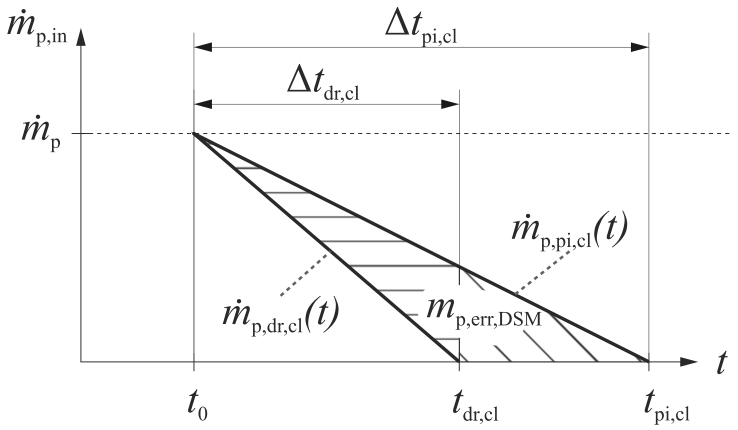

Fig. 73 Erroneous measured particle mass, due to unequal closing times of the particle inlet- and drainage-valve.

Fig. 73 illustrates the aforementioned difference in the unequal closing times of the two DSM actuators for the particle inlet and outlet valves. Starting from a steady state where the current particle mass flow, $\dot{m}_{\mathrm{p}}$, enters and leaves the system equally, the actuators are triggered simultaneously and close with their characteristic closing time. A linear behavior was assumed for both, the reduction of the particle mass flow entering the heat exchanger at the particle inlet valve, $\dot{m}_{\mathrm{p,pi,cl}}(t)$, and the particle mass flow entering particle silo at the drainage valve, $\dot{m}_{\mathrm{p,dr,cl}}(t)$. Note: $\dot{m}_{\mathrm{p,dr,cl}} \neq \dot{m}_{\mathrm{p,dr}} \rightarrow \dot{m}_{\mathrm{p,dr,cl}} = \dot{m}_{\mathrm{p,dr}} - \dot{m}_{\mathrm{p}}$

According to Fig. 73, the erroneous particle mass due to the unequal actuator times can be calculated as follows:

$$\begin{gathered}
m_{\mathrm{p,err,DSM}} = \int_{t_0}^{t_{\mathrm{dr,cl}}} \left(\dot{m}_{\mathrm{p,dr,cl}}(t) - \dot{m}_{\mathrm{p,pi,cl}}(t)\right) dt + \int_{t_{\mathrm{dr,cl}}}^{t_{\mathrm{pi,cl}}} \dot{m}_{\mathrm{p,pi,cl}}(t) dt = \\
= \dot{m}_{\mathrm{p}} \frac{1}{2} \left(\Delta t_{\mathrm{pi,cl}} - \Delta t_{\mathrm{dr,cl}}\right) \\
\text{with:} \\
\dot{m}_{\mathrm{p,pi,cl}}(t) = \frac{\dot{m}_{\mathrm{p}}}{\Delta t_{\mathrm{pi,cl}}} \left(t_{\mathrm{pi,cl}} - t\right); t_0 \leq t \leq t_{\mathrm{pi,cl}} \\
\dot{m}_{\mathrm{p,dr,cl}}(t) = \frac{\dot{m}_{\mathrm{p}}}{\Delta t_{\mathrm{dr,cl}}} \left(t_{\mathrm{dr,cl}} - t\right);\ t_0 \leq t \leq t_{\mathrm{dr,cl}} \text{ and} \\
t_{\mathrm{dr,cl}} = t_0 + \Delta t_{\mathrm{dr,cl}};\ t_{\mathrm{dr,pi}} = t_0 + \Delta t_{\mathrm{pi,cl}}
\end{gathered} \tag{178}$$

With (177) and (178), equation (175) can be rewritten as the drained particle mass for hold-up measurement as function of the governing input parameters:

$$m_{\mathrm{p,pac}} = m_{\mathrm{p,dr}} - 2\,\dot{m}_{\mathrm{p}} \left[\frac{h_{\mathrm{ff,pi}}}{u_{\mathrm{p,ff}}\left(h_{\mathrm{ff,pi}}\right)} + \frac{h_{\mathrm{ff,dr}}}{u_{\mathrm{p,ff}}\left(h_{\mathrm{ff,dr}}\right)} + \frac{1}{4}\left(\Delta t_{\mathrm{pi,cl}} - \Delta t_{\mathrm{dr,cl}}\right)\right] \tag{179}$$

The uncertainty of the particle mass, $u_{m_{\mathrm{p,pac}}}$, can be calculated as follows:

$$u_{m_{\mathrm{p,pac}}} = \sqrt{\begin{gathered} \left(\frac{\partial m_{\mathrm{p,pac}}}{\partial m_{\mathrm{p,dr}}} u_{m_{\mathrm{p,dr}}}\right)^2 + \left(\frac{\partial m_{\mathrm{p,pac}}}{\partial \dot{m}_{\mathrm{p}}} u_{\dot{m}_{\mathrm{p}}}\right)^2 + \left(\frac{\partial m_{\mathrm{p,pac}}}{\partial h_{\mathrm{ff,pi}}} u_{h_{\mathrm{in}}}\right)^2 + \\ + \left(\frac{\partial m_{\mathrm{p,pac}}}{\partial u_{\mathrm{p,ff}}\left(h_{\mathrm{ff,pi}}\right)} u_{u_{\mathrm{p,ff}}\left(h_{\mathrm{ff,pi}}\right)}\right)^2 + \left(\frac{\partial m_{\mathrm{p,pac}}}{\partial h_{\mathrm{dr}}} u_{h_{\mathrm{ff,dr}}}\right)^2 + \\ + \left(\frac{\partial m_{\mathrm{p,pac}}}{\partial u_{\mathrm{p,ff}}\left(h_{\mathrm{ff,dr}}\right)} u_{u_{\mathrm{p,ff}}\left(h_{\mathrm{ff,dr}}\right)}\right)^2 + \left(\frac{\partial m_{\mathrm{p,pac}}}{\partial \Delta t_{\mathrm{pi,cl}}} u_{\Delta t_{\mathrm{pi,cl}}}\right)^2 + \left(\frac{\partial m_{\mathrm{p,pac}}}{\partial \Delta t_{\mathrm{dr,cl}}} u_{\Delta t_{\mathrm{act,dr}}}\right)^2 \end{gathered}} \tag{180}$$

$$\text{with: } t_{\mathrm{act,pi}} = \Delta t_{\mathrm{pi,cl}};\ t_{\mathrm{act,dr}} = \Delta t_{\mathrm{dr,cl}}$$

The corresponding sensitivity coefficients are:

$$\frac{\partial m_{\mathrm{p,pac}}}{\partial m_{\mathrm{p,dr}}} = 1;\ \text{in } - \tag{181}$$

$$\frac{\partial m_{\mathrm{p,pac}}}{\partial \dot{m}_{\mathrm{p}}} = -2\left[\frac{h_{\mathrm{ff,pi}}}{u_{\mathrm{p,ff}}\left(h_{\mathrm{ff,pi}}\right)} + \frac{h_{\mathrm{ff,dr}}}{u_{\mathrm{p,ff}}\left(h_{\mathrm{ff,dr}}\right)} + \frac{1}{4}\left(\Delta t_{\mathrm{pi,cl}} - \Delta t_{\mathrm{dr,cl}}\right)\right];\ \text{in s} \tag{182}$$

$$\frac{\partial m_{\mathrm{p,pac}}}{\partial h_{\mathrm{pi}}} = -\frac{2\,\dot{m}_{\mathrm{p}}}{u_{\mathrm{p,ff}}\left(h_{\mathrm{ff,pi}}\right)};\ \text{in g} \cdot \frac{1}{\mathrm{m}} \tag{183}$$

$$\frac{\partial m_{\mathrm{p,pac}}}{\partial u_{\mathrm{p,ff}}\left(h_{\mathrm{ff,pi}}\right)} = \frac{2\,\dot{m}_{\mathrm{p}}\,h_{\mathrm{ff,pi}}}{u_{\mathrm{p,ff}}^2\left(h_{\mathrm{ff,pi}}\right)};\ \text{in g} \cdot \frac{\mathrm{s}}{\mathrm{m}} \tag{184}$$

$$\frac{\partial m_{\mathrm{p,pac}}}{\partial h_{\mathrm{ff,dr}}} = -\frac{2\,\dot{m}_{\mathrm{p}}}{u_{\mathrm{p,ff}}\left(h_{\mathrm{ff,dr}}\right)};\ \text{in g} \cdot \frac{1}{\mathrm{m}} \tag{185}$$

$$\frac{\partial m_{\mathrm{p,pac}}}{\partial u_{\mathrm{p,ff}}\left(h_{\mathrm{ff,dr}}\right)} = \frac{2\,\dot{m}_{\mathrm{p}}\,h_{\mathrm{ff,dr}}}{u_{\mathrm{p,ff}}^2\left(h_{\mathrm{ff,dr}}\right)};\ \text{in g} \cdot \frac{\mathrm{s}}{\mathrm{m}} \tag{186}$$

$$\frac{\partial m_{\mathrm{p,pac}}}{\partial \Delta t_{\mathrm{pi,cl}}} = -\frac{1}{2}\,\dot{m}_{\mathrm{p}};\ \text{in g} \cdot \frac{1}{s} \tag{187}$$

$$\frac{\partial m_{\mathrm{p,pac}}}{\partial \Delta t_{\mathrm{dr,cl}}} = \frac{1}{2}\,\dot{m}_{\mathrm{p}};\ \text{in g} \cdot \frac{1}{s} \tag{188}$$

A.3.8.1.1 Uncertainty of drained particle mass

The uncertainty of the drained particle mass is composed of two components: the equipment uncertainty, $u_{m_{\mathrm{p,eq,dr}}}$, which is described in section A.3.5.1.1, and the reading uncertainty, $u_{m_{\mathrm{p,rd,dr}}}$. The latter can be determined by extracting and measuring n times the drained particle mass, as described in section A.3.2.

$$u_{m_{\mathrm{p,dr}}} = \sqrt{u_{m_{\mathrm{p,eq,dr}}}^2 + u_{m_{\mathrm{p,rd,dr}}}^2} \tag{189}$$

A.3.8.1.2 Uncertainty of particle mass flow

The uncertainty of the particle mass flow, $u_{\dot{m}_{\mathrm{p}}}$, can be applied as described in section A.3.5.2. It changes with changing particle mass flow rates, such as by changing the orifice plate and varying gas flow rates, see 4.1.1.3.

A.3.8.1.3 Uncertainty of the free-falling heights

Due to inherent inaccuracies in the manufacturing and assembly process, the free-falling heights h_{pi} and h_{dr} must be assumed with a certain degree of uncertainty. The maximum variation for both free-falling heights is estimated to $a_{h_{\mathrm{pi}}} = \pm 5$ mm. Under the assumption of a rectangular distribution of the length uncertainties, the standard uncertainty is: $u_{h_{\mathrm{pi}}} = u_{h_{\mathrm{dr}}} = 5\ \mathrm{mm}/\sqrt{3} = 2.9$ mm.

A.3.8.1.4 Uncertainty of the particle final free-fall velocity in a particle cloud

The uncertainties of the final free-fall velocities are assumed as approximately equally $u_{u_{\mathrm{p,ff}}(h_{\mathrm{ff,pi}})} = u_{u_{\mathrm{p,ff}}(h_{\mathrm{ff,dr}})} = u_{u_{\mathrm{p,ff}}}$ and used with the provided uncertainty by [166], described in the beginning of section A.3.8.1.

A.3.8.1.5 Uncertainty of the closing time of the particle inlet and drainage valves

As previously stated in section A.3.5.1.2, the pivoting angle required to close the drainage valve $\gamma_{\mathrm{DSM,dr}} = 22\ °$ with an assumed uncertainty of $u_{\gamma_{\mathrm{dr,DSM}}} = 2.89\ °$, see Fig. 20. The resulting drainage closing time was identified as $\Delta t_{\mathrm{DSM,dr}} = 0.049$ s with a corresponding uncertainty of $u_{\Delta t_{\mathrm{DSM,dr}}} = 0.007$ s. However, the pivoting angle of the particle inlet valve is $\gamma_{\mathrm{DSM,pi}} = 90\ °$, whereas the uncertainty of the angle position is assumed to be $u_{\gamma_{\mathrm{DSM,pi}}} = 2.89\ °$. By employing (139) and (140) from section A.3.5.1.2, the actuation time of the particle inlet valve can be determined to be $\Delta t_{\mathrm{DSM,pi}} = 0.2$ s, with a corresponding uncertainty of $u_{\Delta t_{\mathrm{DSM,pi}}} = 0.023$ s.

A.3.8.2 Uncertainty of heat exchanger volume

According to (10), $u_{V_{\mathrm{HX}}}$ can be calculated by:

$$u_{V_{\mathrm{HX}}} = \sqrt{\left(\frac{\partial u_{V_{\mathrm{HX}}}}{\partial w_{\mathrm{HX}}} u_{w_{\mathrm{HX}}}\right)^2 + \left(\frac{\partial u_{V_{\mathrm{HX}}}}{\partial h_{\mathrm{HX}}} u_{h_{\mathrm{HX}}}\right)^2} \qquad (190)$$

The corresponding sensitivity coefficients are:

$$\frac{\partial u_{V_{\mathrm{HX}}}}{\partial w_{\mathrm{HX}}} = 2\, w_{\mathrm{HX}}\, h_{\mathrm{HX}};\ \mathrm{in\ m^2} \qquad (191)$$

$$\frac{\partial u_{V_{\mathrm{HX}}}}{\partial h_{\mathrm{HX}}} = w_{\mathrm{HX}}^2;\ \mathrm{in\ m^2} \qquad (192)$$

For the test setup a channel width of $w_{\mathrm{HX}} = 50$ mm was chosen, the height of the packed column resulted to be $h_{\mathrm{HX}} = 875$ mm. Due to inaccuracies during the manufacturing and the assembling process uncertainties were assumed. Assuming a rectangular distribution, the uncertainty of $u_{w_{\mathrm{HX}}}$ and $u_{h_{\mathrm{HX}}}$ is estimated to $u_{w_{\mathrm{HX}}} = 0.5\ \mathrm{mm}/\sqrt{3} = 0.3\ \mathrm{mm}$ and $u_{h_{\mathrm{HX}}} = 5\ \mathrm{mm}/\sqrt{3} = 2.9\ \mathrm{mm}$.

A.3.8.3 Uncertainty of the packing void fraction

According to (33) u_{ϵ_0} can be calculated as follows:

$$u_{\epsilon_0} = \sqrt{\left(\frac{\partial u_{\epsilon_0}}{\partial t_{\mathrm{sm}}} u_{t_{\mathrm{sm}}}\right)^2 + \left(\frac{\partial u_{\epsilon_0}}{\partial w_{\mathrm{bar}}} u_{w_{\mathrm{bar}}}\right)^2 + \left(\frac{\partial u_{\epsilon_0}}{\partial w_{\mathrm{HX}}} u_{w_{\mathrm{HX}}}\right)^2 + \left(\frac{\partial u_{\epsilon_0}}{\partial h_{\mathrm{HX}}} u_{h_{\mathrm{HX}}}\right)^2} \qquad (193)$$

The corresponding sensitivity coefficients are:

$$\frac{\partial u_{\epsilon_0}}{\partial t_{\mathrm{sm}}} = -\frac{n_{\mathrm{sm}}\, n_{\mathrm{ts}}\, w_{\mathrm{bar}}\, n_{\mathrm{bar}}}{w_{\mathrm{HX}}\, h_{\mathrm{HX}} \left(1 + n_{\mathrm{ts,f}}\right)};\ \mathrm{in}\ \frac{1}{\mathrm{m}} \qquad (194)$$

$$\frac{\partial u_{\epsilon_0}}{\partial w_{\mathrm{bar}}} = -\frac{n_{\mathrm{sm}}\, t_{\mathrm{sm}}\, n_{\mathrm{ts}}\, n_{\mathrm{bar}}}{w_{\mathrm{HX}}\, h_{\mathrm{HX}} \left(1 + n_{\mathrm{ts,f}}\right)};\ \mathrm{in}\ \frac{1}{\mathrm{m}} \qquad (195)$$

$$\frac{\partial u_{\epsilon_0}}{\partial w_{\mathrm{HX}}} = \frac{n_{\mathrm{sm}}\, t_{\mathrm{sm}}\, n_{\mathrm{ts}}\, w_{\mathrm{bar}}\, n_{\mathrm{bar}}}{w_{\mathrm{HX}}^2\, h_{\mathrm{HX}} \left(1 + n_{\mathrm{ts,f}}\right)};\ \mathrm{in}\ \frac{1}{\mathrm{m}} \qquad (196)$$

$$\frac{\partial u_{\epsilon_0}}{\partial h_{\mathrm{HX}}} = \frac{n_{\mathrm{sm}}\, t_{\mathrm{sm}}\, n_{\mathrm{ts}}\, w_{\mathrm{bar}}\, n_{\mathrm{bar}}}{w_{\mathrm{HX}}\, h_{\mathrm{HX}}^2 \left(1 + n_{\mathrm{ts,f}}\right)};\ \mathrm{in}\ \frac{1}{\mathrm{m}} \qquad (197)$$

The uncertainties $u_{w_{\mathrm{HX}}}$, and $u_{h_{\mathrm{HX}}}$ are described in the preceding section A.3.8.2. The sheet metals, which constitute the packing structure, are laser cut and assembled, as illustrated in Fig. 24. Due to the manufacturing process, the allowed maximum manufacturing tolerance was defined to be ± 0.1 mm. Therefore, assuming a rectangular distribution $u_{t_{\mathrm{sm}}}$ and $u_{w_{\mathrm{bar}}}$ can be calculated to $u_{t_{\mathrm{sm}}} = u_{w_{\mathrm{bar}}} = 0.1\ \mathrm{mm}/\sqrt{3} = 0.06\ \mathrm{mm}$.

A.3.9 Temperature

Fig. 74 depicts the aforementioned test setup, which is described in greater detail in chapter 4, see Fig. 19. Fig. 34 depicts the test setup, which was equipped with insulation for the hot test campaign. Fig. 74 provides a schematic illustration of the components with attached insulation, including the most crucial temperature measurement points. For the sake of simplicity, additional components, such as the pressure sensors, and redundant temperature measurement points, such as the labeling of the insulation TC, were not included in the illustration.

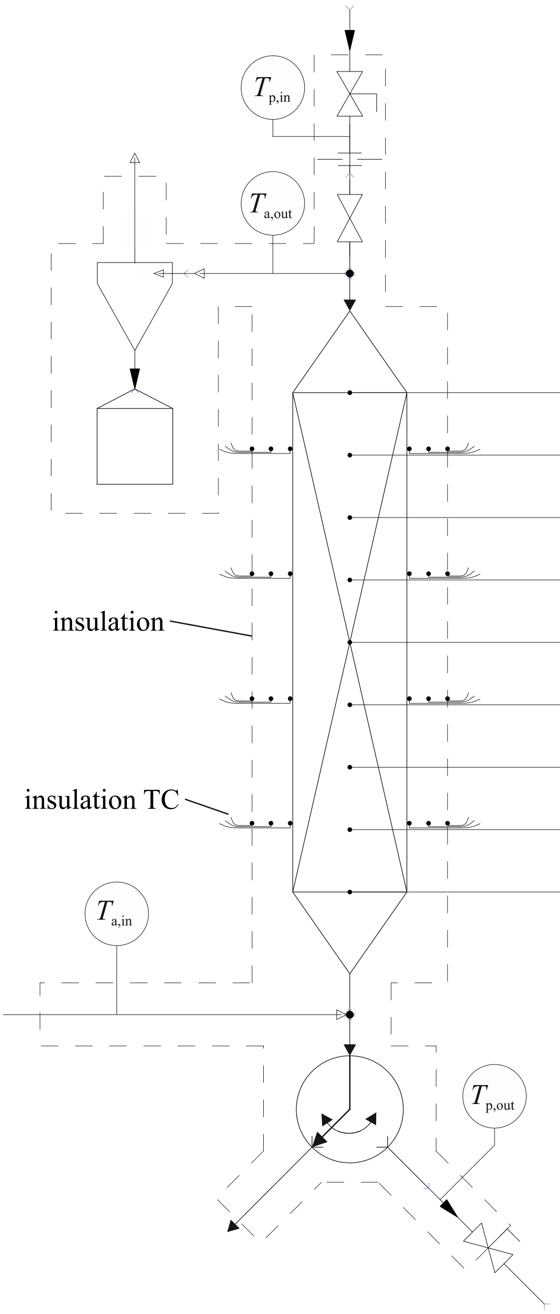

Fig. 74 Schematic insulation of TFHX test setup and location of temperature sensors for measuring media inlet and outlet temperatures, such as the temperatures inside the HX.

A.3.9.1 Equipment uncertainty of temperature sensor equipment

All temperatures in the test setup are measured by thermocouples of type N class 1, which, in accordance with the standard IEC 584-3 and DIN EN 60584, exhibit a half-width interval of maximum ± 0.4 % for the temperature range from -40 °C to 1,000 °C. It is necessary to adapt the reading values (RD) in °C [174] to Kelvin when implementing the correlation in the analysis of the raw data. The thermocouples are connected to the VIPA-SPS data logger via a thermal line class 1, which, in accordance with the standard to IEC 584-3 and DIN EN 60584, exhibits the same tolerated half-width interval as the temperature sensor itself. The VIPA-SPS analog data logger of the type "331-7KF01," as specified by the supplier, is reported to exhibit a half-width interval of up to ± 0.2 % RD [175].

Consequently, the combined uncertainty of the temperature measurement equipment can be expressed as follows:

$$u_{T_{\mathrm{eq}}} = \sqrt{u_{\mathrm{TC}}^2 + u_{\mathrm{TL}}^2 + u_{\mathrm{SPS,TC}}^2} \tag{198}$$

The uncertainties provided by the supplier are assumed to follow a rectangular distribution.

$$u_{\mathrm{TC}} = \frac{0.4\,\% \cdot T}{\sqrt{3}} \tag{199}$$

$$u_{\mathrm{TL}} = \frac{0.4\,\% \cdot T}{\sqrt{3}} \tag{200}$$

$$u_{\mathrm{SPS,TC}} = \frac{2\,\% \cdot T}{\sqrt{3}} \tag{201}$$

A.3.9.2 Reading uncertainty of temperature measurement

The reading uncertainty of a set of logged data can be calculated in accordance with the general approach for determining the reading uncertainty, $u_{T_{\mathrm{rd}}}$, of a sensor value, as outlined in section A.3.2.

A.3.9.3 Combined temperature measurement uncertainty

In order to determine the combined temperature measurement uncertainty, it is standard practice to employ the root mean square of the equipment uncertainty and the reading uncertainty of a temperature sensor.

$$u_T = \sqrt{u_{T_{\mathrm{eq}}}^2 + u_{T_{\mathrm{rd}}}^2} \tag{202}$$

Some of the temperature measurements are implemented with a number of n redundant sensors, to detect possible measurement errors of one sensor, but also to measure over a wider range of data points. The uncertainty, u_{T_i}, of each redundant TC, T_i, can be calculated as described in section A.3.2. The mean value of a redundant group of TCs can be determined as follows:

$$\bar{T} = \frac{\sum_{i=1}^{n} T_i}{n} \tag{203}$$

The corresponding uncertainty can be expressed as follows:

$$u_{\bar{T}} = \sqrt{\left(\frac{\partial T}{\partial T_1}\right)^2 u_{T_1}^2 + \left(\frac{\partial T}{\partial T_2}\right)^2 u_{T_2}^2 + \cdots + \left(\frac{\partial T}{\partial T_n}\right)^2 u_{T_n}^2} = \frac{1}{n}\sqrt{u_{T_1}^2 + u_{T_2}^2 + \cdots + u_{T_n}^2} \tag{204}$$

The corresponding sensitivity coefficient is:

$$\frac{\partial T}{\partial T_i} = \frac{1}{n};\ \text{in} - \tag{205}$$

A.3.9.4 Estimation of the air temperature, entering and leaving the packing structure

In section 4 it was described, that the TCs for the determination of the air temperature at the inlet, see Fig. 20, and outlet, see Fig. 35, were not positioned directly below and above the packed column, see Fig. 19 and Fig. 74. This was done to ensure the measurement of the temperature of the air exclusively, without the presence of particles. Furthermore, Fig. 74 demonstrates that supplementary TCs were mounted on the interior of the HX channel, $T_{\mathrm{ci},i}$. In total, the temperature in the TFHX is determined at nine distinct heights, which subdivide the internal temperature measurement into eight sections. The measurements were conducted by a pair of TCs at each level. At the levels of $T_{\mathrm{ci},1}$ and $T_{\mathrm{ci},9}$, TCs were installed to determine the temperature at the corresponding levels, as the second opening in the channel wall was utilized to connect the tubing for the relative pressure measurement of the gas flow along the packed column, see A.3.1. The measurement positions for the inlet and outlet temperatures of the media flow are equipped with three redundant TC units each. This approach enhances the precision of the measurement by calculating the mean value and its corresponding uncertainty. Moreover, the use of a redundant group of three TC at one measurement point increases the likelihood of detecting a potential malfunction of one TC. The mean value of the temperature was determined for each TC group according to (203), and the corresponding uncertainty was calculated according to (204).

During the operation of the TFHX with air and particle flow in the test rig, the TCs inside the channel cannot be used to exclusively measure one media temperature unless technical shielding measures are installed to insulate one media at the specific points of $T_{\mathrm{ci},i}$. Due to spatial limitations, this was not performed, as outlined in the sections 4.2.1.1 and 4.1.2.2. In section 4.2.1.1, the methodology for estimating the particle temperature was outlined. The following section will describe the method used to determine the air inlet and outlet temperature at the packing inlet and outlet. For a given air flow rate of $\dot{m}_{\mathrm{a}} = 6.8\ \mathrm{g/s} = 24.5\ \mathrm{kg/h}$, representing the upper limit operating area of gas flow, different air inlet temperatures, $T_{\mathrm{a,in}}$, were applied to the system in absence of particle flow. Fig. 75 shows the measured temperatures for the $T_{\mathrm{ci},i}$ points within the HX, including the temperature values at the air inlet and outlet measurement positions, see Fig. 19 and Fig. 74. The objective was to derive linearized correlations and uncertainties for the temperature losses along different sections of the heat exchanger assembly, with the purpose of estimating the air temperatures directly at the packing inlet and outlet, based on known reference temperatures. As the air mass flow rate decreases, the heat transfer from the air to the wall also declines, leading to a reduction in the heat loss from the hot gas to the surrounding environment. Consequently, the temperature gradient becomes less pronounced. However, for the sake of simplicity and to ensure a conservative approach, the highest air flow in the system will be used to derive correlations of the temperature change in various sections of the HX system. As a result, the temperature change from the TC at the air inlet, $T_{\mathrm{a,in}}$, and air outlet measurement, $T_{\mathrm{a,out}}$, to the packing structure, represented by $T_{\mathrm{ci},1}$ and $T_{\mathrm{ci},9}$ were estimated.

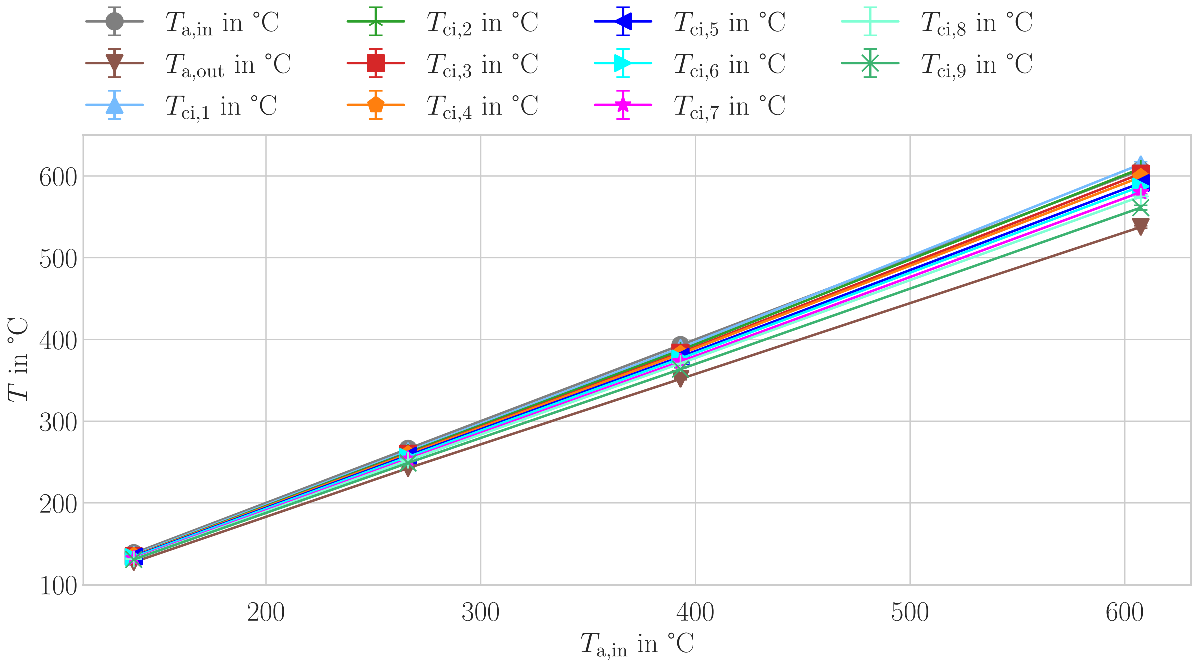

Fig. 75 Temperatures in the HX for varying air inlet temperatures; air flow 2.76 kg/(s · m^2); particle flow 0 kg/(s · m^2).

In Tab. 20 a total of four sections were defined for the purpose of determining the extent of temperature change resulting from thermal losses along the corresponding sections. The "inlet to outlet" section (sec,in2out) is defined as the air path from the measurement point at $T_{a,in}$ to $T_{a,out}$, see Fig. 74. The "outlet" section (sec,out) is the air path from the measurement point at $T_{ci,9}$ to $T_{a,out}$, see Fig. 74. The "HX" section (sec,HX) describes the air path between measurement point from $T_{ci,1}$ to $T_{ci,9}$, see Fig. 74. The "inlet" section (sec,in) describes the air path from $T_{a,in}$ to $T_{ci,1}$, see Fig. 74. For the determination of material properties, also a suitable reference pressure and temperature was defined for each section, see Tab. 20.

Tab. 20 Definition of different temperature sections in the TFHX test rig.

Section	name	start	end	ref temperature	ref. pressure
inlet to outlet	sec,in2out	$T_{a,in}$	$T_{a,out}$	$T_{a,in}$	$p_{in} - \frac{p_{rel,HX}}{2}$
outlet	sec,out	$T_{ci,9}$	$T_{a,out}$	$T_{a,out}$	$p_{in} - p_{rel,HX}$
HX	sec,HX	$T_{ci,1}$	$T_{ci,9}$	$T_{a,pac,in}$	$p_{in} - \frac{p_{rel,HX}}{2}$
inlet	sec,in	$T_{a,in}$	$T_{ci,1}$	$T_{a,in}$	p_{in}

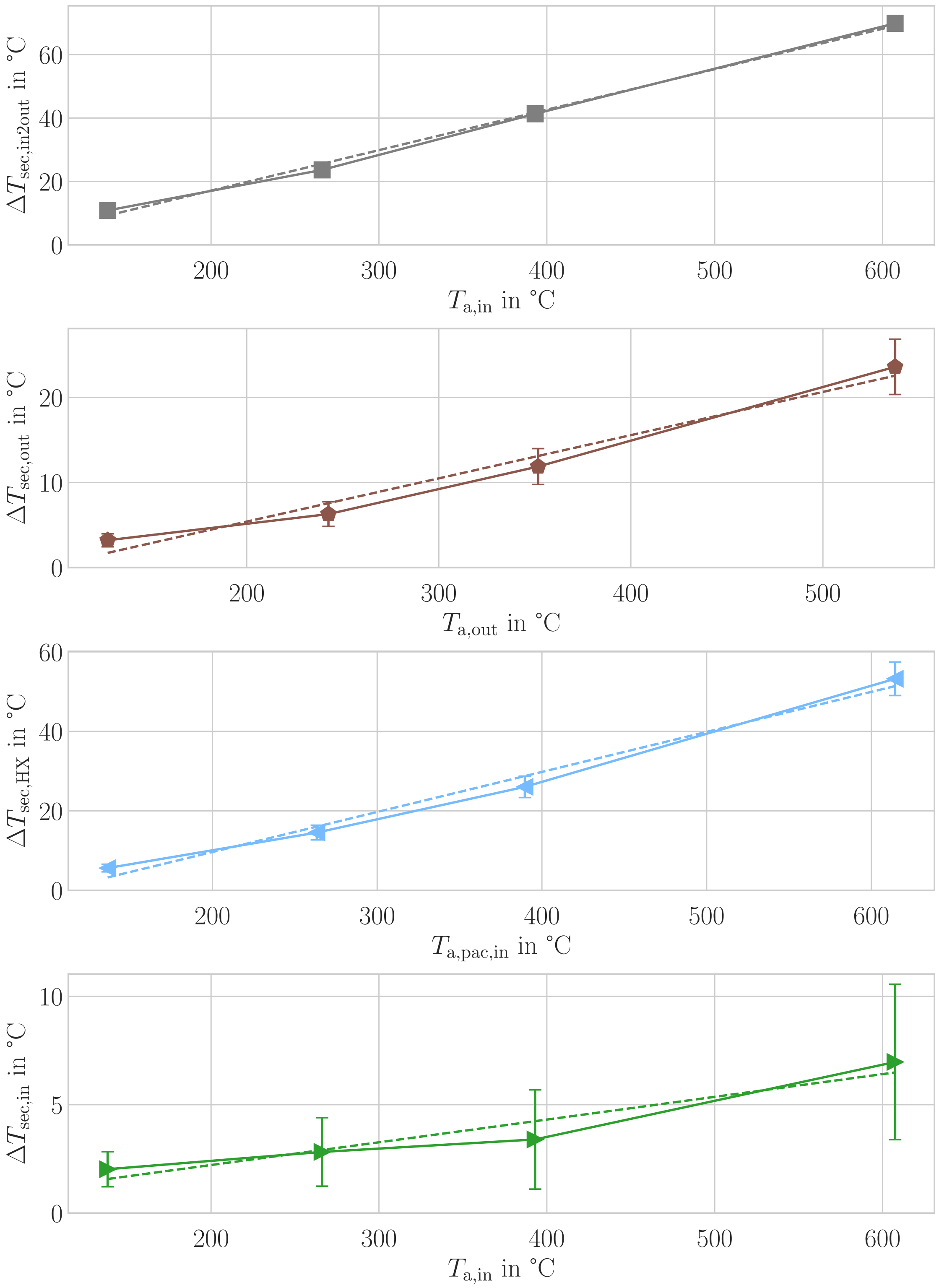

Fig. 76 Temperature drop along different sections in the test setup versus a suitable reference temperature; air flow 2.76 kg/(s · m^2); particle flow 0 kg/(s · m^2).

Fig. 76 shows the change of gas temperature along the in Tab. 20 defined sections, plotted versus each reference temperature. For the calculation of the temperatures and its uncertainties, the methods described in section A.3.9.3 and A.3.2 were applied. The measurement data was used to conduct linear fits, see Fig. 76, where the dotted lines represent the corresponding linear fits: $\Delta T_{\mathrm{sec,out,lnz}}(T_{\mathrm{a,out}})$, $\Delta T_{\mathrm{sec,in2out,lnz}}(T_{\mathrm{a,in}})$, $\Delta T_{\mathrm{sec,HX,lnz}}(T_{\mathrm{a,pac,in}})$, $\Delta T_{\mathrm{sec,in,lnz}}(T_{\mathrm{a,in}})$. When no particle flow is applied to the system, the air temperatures just above, $T_{\mathrm{a,pac,out}}$, and below the packing, $T_{\mathrm{a,pac,in}}$, can be determined with the temperature measurements at $T_{\mathrm{ci,9}}$ and $T_{\mathrm{ci,1}}$ respectively. When grain flow was introduced into the setup, this assumption was no longer valid: $T_{\mathrm{a,pac,in}} \neq T_{\mathrm{ci,1}}$ and $T_{\mathrm{a,pac,out}} \neq T_{\mathrm{ci,9}}$ for $\dot{m}_{\mathrm{p}} > 0\ \mathrm{kg/(s \cdot m^2)}$. When particle flow was feed into the setup, the linearized temperature offset from the air measurements points at $T_{\mathrm{a,in}}$ and $T_{\mathrm{a,out}}$ were applied, using $\Delta T_{\mathrm{sec,in,lnz}}(T_{\mathrm{a,in}})$ and $\Delta T_{\mathrm{sec,out,lnz}}(T_{\mathrm{a,out}})$ to estimate the air temperature at the packing inlet, $T_{\mathrm{a,pac,in}}$, and outlet, $T_{\mathrm{a,pac,out}}$.

Tab. 21 Parameter for linearized temperature differences as function of a reference temperature.

Section	Reference temperature	steepness in $\mathrm{K}_{\Delta T}/\mathrm{K}_{T_{\mathrm{ref}}}$	offset in $\mathrm{K}_{\Delta T}$	$u_{\Delta T}$ in %	RMSE in %
$\Delta T_{\mathrm{sec,in2out,lnz}}$	$T_{\mathrm{a,in}}$	0.127599	-43.277504	0.209626	0.996497
$\Delta T_{\mathrm{sec,out,lnz}}$	$T_{\mathrm{a,out}}$	0.050806	-18.637284	0.302066	0.973421
$\Delta T_{\mathrm{sec,HX,lnz}}$	$T_{\mathrm{a,pac,in}}$	0.100733	-38.015963	0.364901	0.985507
$\Delta T_{\mathrm{sec,in,lnz}}$	$T_{\mathrm{a,in}}$	0.010533	-2.780435	0.309650	0.919523

In order to calculate the air inlet temperature at the packing, $T_{\mathrm{a,pac,in}}$, at $T_{\mathrm{ci,1}}$, the linearized offset temperature $\Delta T_{\mathrm{sec,in,lnz}}$ must be subtracted from the reference temperature, $T_{\mathrm{a,in}}$. Similarly, for the calculation of the estimated air outlet temperature at the packing top, $T_{\mathrm{a,pac,out}}$, at $T_{\mathrm{ci,9}}$, the offset temperature $\Delta T_{\mathrm{sec,out,lnz}}$ must be added to the corresponding reference temperature, $T_{\mathrm{a,out}}$. The linearized functions, their parameters, and the root mean squared error (RMSE) of the linearized curve fit are presented in Tab. 21. The assumption to only use a linear fit is strengthened for RMSE values relatively close to 1. The corresponding equation for the air inlet and outlet temperatures at the packing inlet and outlet can be used to estimate $T_{\mathrm{a,pac,in}}$ and $T_{\mathrm{a,pac,out}}$ during HX operation with particle flow. The measurement uncertainties for the linearized functions in the inlet and outlet sections do not exceed 0.31 %, with the reference temperature in Kelvin. This was finding was applied in determining the uncertainty of the offset temperatures.

$$T_{\mathrm{a,pac,in}} = T_{\mathrm{a,in}} - \Delta T_{\mathrm{sec,in,lnz}} = T_{\mathrm{a,in}} - 0.010533\, T_{\mathrm{a,in}} + 2.780435 \qquad (206)$$

$$T_{\mathrm{a,pac,out}} = T_{\mathrm{a,out}} + \mathit{\Delta} T_{\mathrm{sec,out,lnz}} = T_{\mathrm{a,out}} + 0.050806\, T_{\mathrm{a,out}} - 18.637284 \qquad (207)$$

With the corresponding uncertainties:

$$U_{T_{\mathrm{a,pac,in}}} = 0.31\ \%\ T_{\mathrm{a,in}} \qquad (208)$$

$$U_{T_{\mathrm{a,pac,out}}} = 0.31\ \%\ T_{\mathrm{a,out}} \qquad (209)$$

A.4 Measurement to assess the spatial distribution in dilute particle flow

---

The findings of this section has already been published by the author of this thesis.

Reichart, M, Hirt, A, Technau, J, Raab, A, Lackovic, L, Uhlig, R, Neises-von Puttkamer, R, & Pitz-Paal, R. " Experimental Development of Packing Structures in a Gas-Particle Trickle Flow Heat Exchanger for Application in Concentrating Solar Tower Systems." Advanced Powder Technology; ISSN: 0921-8831, Elsevir; London; ISSN 0921-8831; published on 27. May 2024; https://doi.org/10.1016/j.apt.2024.104481

Furthermore, contributed Anja Raab in the development of the optical measurement method.

As outlined in section 2.2, in addition to high particle hold-up, a uniform spatial particle density distribution within the packing void is preferred for optimized gas-particle interaction in a packed column. Complimentary to measuring the particle hold-up, as described in section 4.1.1.4, also a method is needed to assess the particle density distribution of the particles in various packing configurations. The literature describes a variety of methods for visualizing grain systems, depending on the specific measurement task and the characteristics of the particle flow in question. Optical approaches such as camera systems or lasers are limited in measuring dense granular flow systems to analyze only the boundary of the particle flow, due to its optically opaque nature [176-178]. If the particles are immersed in a fluid that matches the refractive index of the grains, the full three-dimensional particle distribution of the particle cloud can be determined [179]. In contrast to optical methods, X-rays technology can penetrate even an optically opaque, dense particle cloud, providing information on particle density, structure and spatial position. Full three-dimensional spatial information of the particle cloud can be obtained using X-ray tomography [180, 181]. Typically, the processing of standard X-ray setups takes several minutes to acquire a single image, which limits these methods to the analysis of static systems. However, development is underway to visualize and capture the dynamics of moving grain flow at higher frame rates [182, 183].

In the following sections a method to assess the spatial particle density distribution within different packing structures for diluted particle flow is described, that was applied within this work. Unlike the before-mentioned methods, a rather simplistic setup was aimed to be used, using a consumer digital camera with video functionality to record various particle flow conditions in two exemplary packing structures. Thereby, the three-dimensional diluted particle flow within the TFHX, comprising a volume fraction in the range of 1 %, is reduced to a two-dimensional series of images, that is analyzed and assessed. Therefore, image processing methods were applied to prepare the videos for the analysis process to qualify the distribution of the trickling particles in space.

A.4.1 Experimental setup

The same assembly method and labeling system for the packing structure is used, as described in section 4.1.1.1. For the scope of the optical measurement, the in section 4.1.1. described test setup was temporarily modified to characterize different packing structures by using an optical measurement technique during the cold test procedure, see Fig. 77. For clarity, some of the in Fig. 19 shown components are not displayed in Fig. 77, if not needed for the measurement.

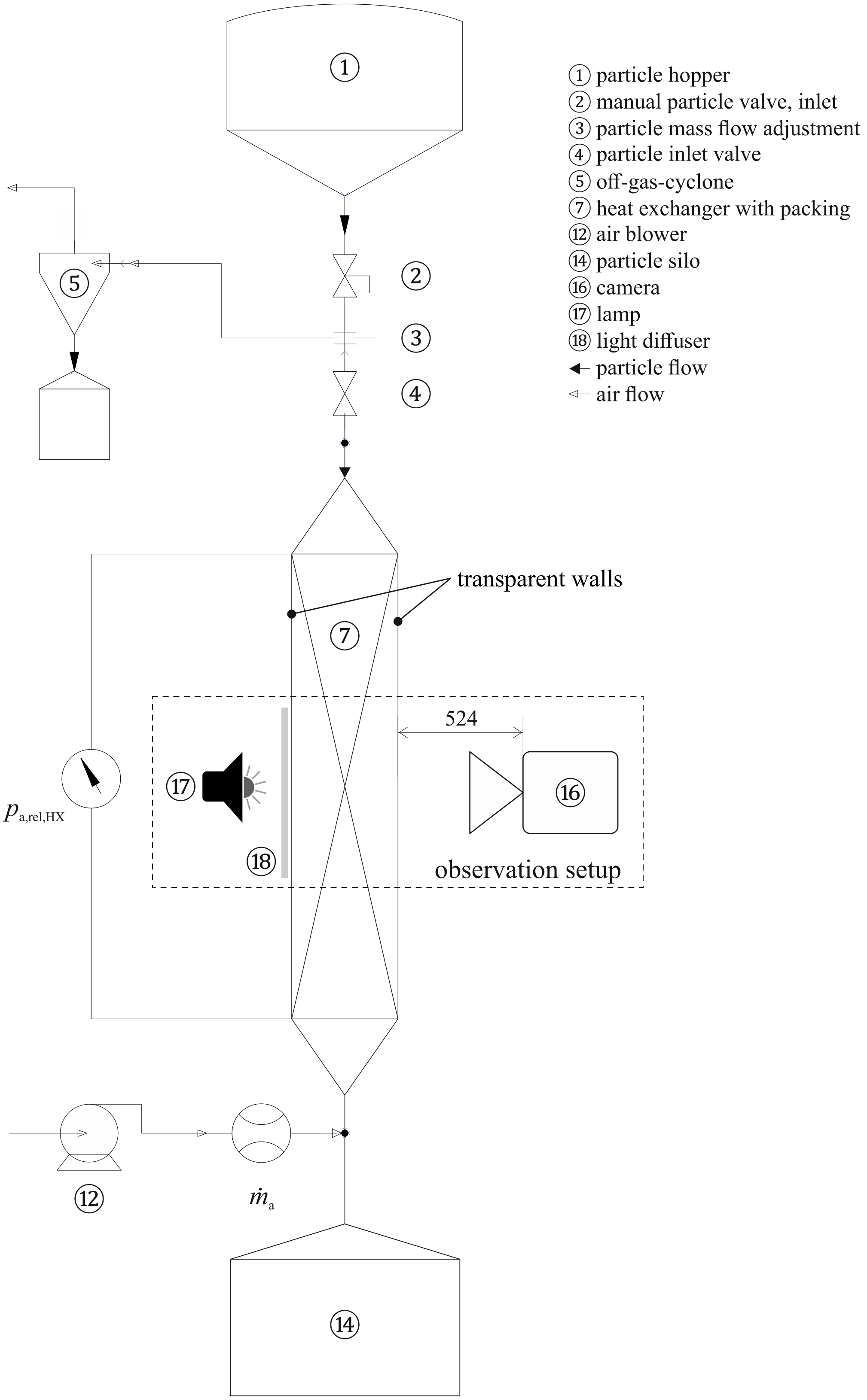

Fig. 77 Experimental set-up for cold testing of packing structures and video analysis.

The particle mass flow is adjusted by interchangeable plates with different orifice diameters ③, causing the particles above to dam up and form a moving particle bed, fed by the particle hopper above ①. Gravity driven, the particles fall through the orifice plate into the heat exchanger and the assembled packing structure ⑤. The solids trickle through the packed column and are collected in the airtight particle silo ⑦. For countercurrent gas flow, atmospheric air is injected into the setup by an air blower ⑥, which can also be used to manipulate the air flow, that is measured before entering the heat exchanger. Special care has been taken in the design to obtain gas-tightness of the test setup, so that the incoming air flow is exclusively directed through the heat exchanger. A small air leakage flow was determined, and considered in the determination of the air gas flow and its uncertainty, see section A.3.6.2. The exhaust gas exits the system through an off-gas cyclone, where potentially entrained particles are separated. Due to the relatively narrow shape of the 50 mm squared heat exchanger channel, no additional engineering measures have been taken to evenly distribute the incoming particles and gas flow. Qualitative observations and preliminary simulations show an even distribution of both media flows after entering the TFHX at each media inlet. For the cold tests, transparent front and back walls, made of methacrylate, are installed to observe the particle flow at different media flow conditions. The same 1 mm bauxite particle type was used, as described in section 3.4. Depending on the chosen packing structures, the vertical interstitial spacing between wo packing layers can result rather narrow, making it difficult to clearly observe the free-falling particles between two PL. Therefore, only for the optical evaluation of the particle distribution, several packing layers were removed to obtain a clear view in this observation area, see Fig. 78. It is to be expected that the particle hydrodynamics and thus the particle density distribution in the observation area will differ from areas within the packing void, but since rather a relative comparison between different packing structures is of interest in this study, by determining the influence of the particle shaded areas, see Fig. 78 (left), this approach was considered as valid. From the back, a lamp in combination with a diffuser provides uniform illumination, see Fig. 19, allowing measurements with sufficiently low shutter speeds for sharp recordings.

Fig. 78 (left) shows an illustration of the trickling particles within the packing structure. Depending on the orientation of the packing elements, only areas with a rather opaque curtain of particles can observed. It is assumed that the grain distribution within the packing elements rotated by 90 ° will be similar to the particle hydrodynamics, caused by packing layers with a co-linear alignment of the bar elements and the camera optics, such applied in the observation area, shown in Fig. 78 (left). Accordingly, the region where the packing bar elements are aligned with the camera view is of interest in this study.

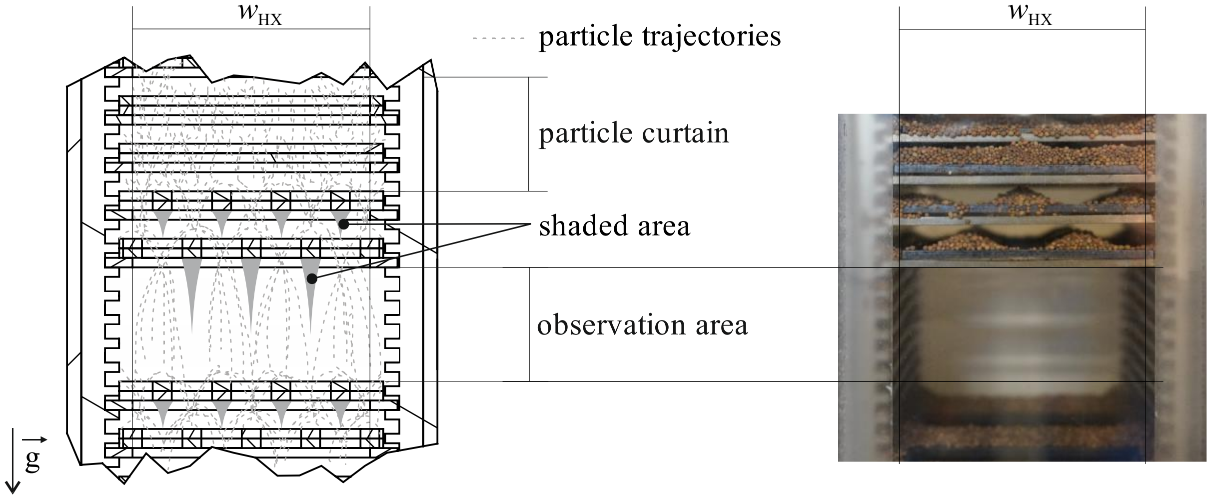

Fig. 78 Trickling particles in observation area (left) and observation area of the test setup after experiment (right).

Tab. 22 Configuration of camera setup.

optical camera specifications		video recording specifications	
aperture	16	resolution	HD (1.920 x 1.080)
shutter speed	1/125 s	frame rate	120 fps
ISO	3200	digital video format	NTSC
white balance	4300 K	recording duration	1 min

Given the impact of bar width, the formation of shaded areas below is anticipated, resulting in an uneven distribution of particle density in space. The theory for the calculation of the particle density distribution is applied, as described in section 3.2.

For the camera setup shown in Fig. 77, a Sony Alpha ILCE-6400 was used in combination with a Tokina FIRIN macro lens, providing a fixed focal length of 100 mm and a minimum aperture of 2.8. A distance of 524 mm between the camera sensor and the transparent wall provided a clear view of the observation area, see Fig. 78 (right). The illumination was employed by an industrial LED floodlight with a color temperature of 6,500 K and a brightness of 5,000 lm. A diffuser was installed between the lamp and the backside observation area to even out the lighting. The camera setup was controlled using the proprietary program “Imaging Edge Desktop”. During pre-testing, the camera setup was fine-tuned with emphasis on obtaining images with high contrast, high sharpness and low image noise, see Tab. 22.

The focal area was set to half the depth of the observation area. To obtain sharp images throughout the whole depth of the heat exchanger width, an aperture of 16 was chosen. The bright lighting provided clear and sharp at a shutter speed of 1/125 s, which allowed to set the frame rate to 120 fps. Despite the high frame rate, no effort was made in this study to track individual particles to determine further characteristics such as the individual particle velocities and trajectories as performed in particle image velocimetry (PIV) approaches.

A.4.2 Measurement method

In order to measure a variety of packing geometries, the packing structures were assembled as described in section A.4.1. The different orifice plates were installed and the air blower was set to the desired air mass flow rate. After opening the particle inlet valve, the solids distribute throughout the packed column of TFHX. Depending on the packing structure installed, different transient times were required to reach steady state condition. For all geometries and media flow rates studied, a 5-minute waiting period guaranteed a steady state of particle flow. Additionally, the relative pressure sensor provided for the shown setup a reliable indicator for reaching steady-state conditions within the TFHX for gradients below 8 $\mathrm{Pa/(m^2 \cdot min)}$. When steady state was reached, a 1 minute video of the observation area was recorded. This process was repeated for all packing geometries and media flow rates of interest.

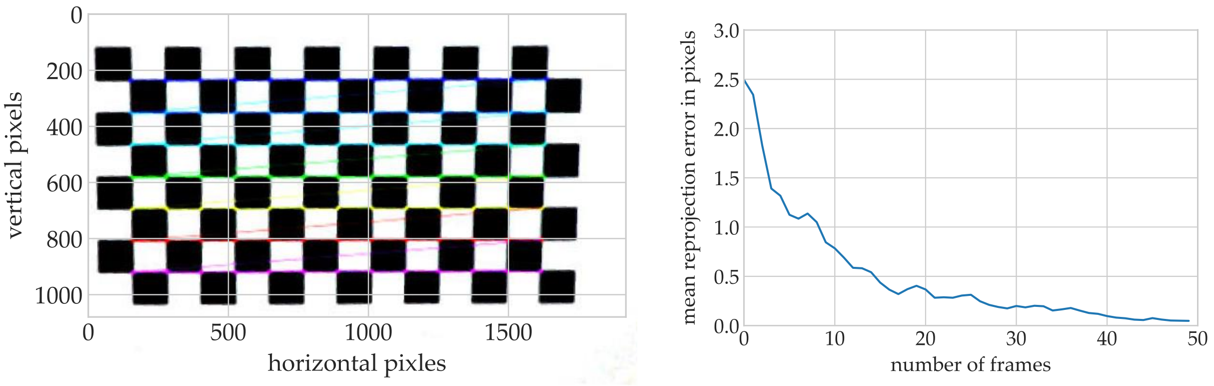

Fig. 79 Frame of calibration video with detected corners highlighted (left), mean error of detection algorithm for a number of frames (right).

A.4.2.1 Calibration of camera setup

The Python programming language was used to calibrate and analyze the particle density distribution. In addition, the “Open Computer Vision”-Library, (OpenCV, www.opencv.org), was used to prepare each frame of the videos for the detection of the trickling particles. However, before analyzing the videos, a one-time calibration of the camera setup was performed to compensate for the non-avoidable barrel distortion of a camera lens. Therefore, a chessboard pattern was placed in front of the camera. The OpenCV library provides functions to detect the edges of the chessboard, along with methods to calculate the distortion or potential misalignment of the camera, and also the scale in the image can be determined if the information of the chessboard is provided, see OpenCV [184]. For the current setup, an 8 by 14 chessboard with a field with and height of 5 mm was used. For the calibration procedure a video was recorded and the distortion coefficients, consisting of the radial distortion coefficients k_1, k_2, and k_3 as well as the tangential distortion coefficients p_1, and p_2 were determined. For the definition and further use of these parameters, see OpenCV [184]. The distortion coefficients are determined for each frame of the calibration video.

Fig. 79 (left) shows an example frame from the calibration video. The detected corners of the chessboard pattern are highlighted. It shows that the camera is mounted slightly higher than the center of the image, but no adjustment was needed there, as the calibration parameters are also able to compensate slight misalignment. The pixel count is set to the upper right corner of a frame. Since there is an uncertainty in detecting the exact position of the chessboard corners, it is recommended to use frames from different perspectives, this helps the calibration process to generate a reprojection of the calibration image and to determine the distortion coefficients, see OpenCV [184]. To make sure, that enough images are being used, the mean reprojection error is calculated and depictured in Fig. 79 (right). It can be seen that the evolution of the mean reprojection error decreases as the number of used frames of the calibration video increase. For a number of 50 frames, the error can be considered negligible. Accordingly, the averaged distortion coefficients for the presented setup are: $\bar{k}_1 = 5.655$, $\bar{k}_2 = -3479$, $\bar{p}_1 = -1.23 \cdot 10^{-3}$, $\bar{p}_2 = 4.32 \cdot 10^{-3}$ and $\bar{k}_3 = -5.654$. Furthermore, the scale for all evaluated images in the current setup was determined to $1\ \text{px} \mathrel{\hat{=}} 0.03655\ \text{mm}$. Applying the found parameters, all images are evaluated in the aligned position and without distortion for the used setup.

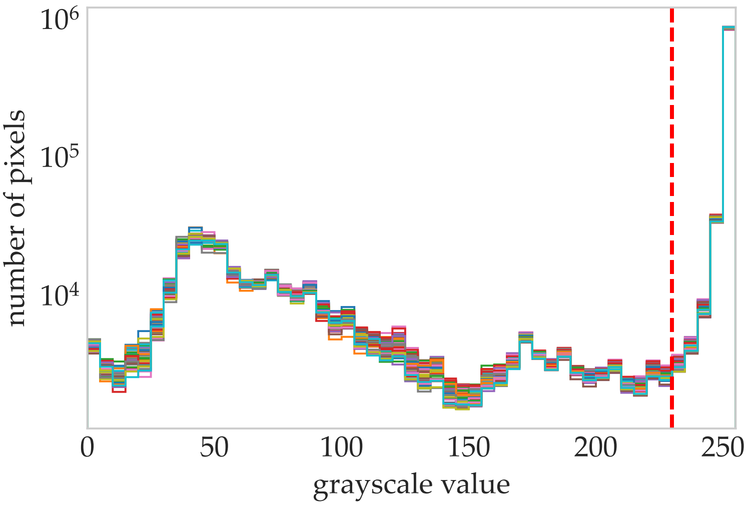

Fig. 80 Histogram of gray values distribution for 50 frames of the representative video.

A.4.2.2 Image cleaning

In order to distinguish between the background and all other material components that are recorded, a sensitivity study was performed to identify a threshold within the captured images between bright background areas and dark areas. Whereby the latter would be represented by particles, dirt or dust and parts of the test setup structure shown in Fig. 78. Therefore, the distribution of gray values for all pixels of all frames per video was analyzed. The gray scale ranges from values of 0, representing a totally black pixel of an image, up to a gray value of 255 representing a perfect white image information. It was found that the distribution of gray values shows the same type of distribution for all evaluated videos, why in the following, a representative video, with a particle mass flow rate of 2.6 $\mathrm{kg/(s \cdot m^2)}$ and no air flow in the "w14 h02 n2 z10" packing is used to describe the cleaning and evaluation procedure.

Fig. 80 shows the superimposed histograms of the first 50 frames of the representative video. A clear threshold can be identified for gray values greater than 230, representing bright pixels in the background. Pixels with gray values above this threshold are whitened out and ignored for further evaluation. Before evaluating the recorded videos, the raw images were further processed by cropping them to the observation area. The upper limit is set slightly below the last support frame holding the packing elements before the free fall area within the observation area begins, see Fig. 78 (left). A free fall height of about 26 mm is observed, corresponding to a height of 700 px. This granted that the resting, static particles on the packing structure on the lower end of the observation area were excluded, see Fig. 81. The left and right limits are set to correspond to an observation width equal to the $w_{\mathrm{HX}} = 50$ mm, represented by a width of 1368 px. Despite the selected objective focal length of 100 mm and calibrating the camera setup, the perspective depth cannot be avoided, so the lateral limits are set to correspond to about half the width of the ribbed structure of the tray support, see Fig. 78 (left). Fig. 81 shows an example raw image with all four boundaries, defining the observation area.

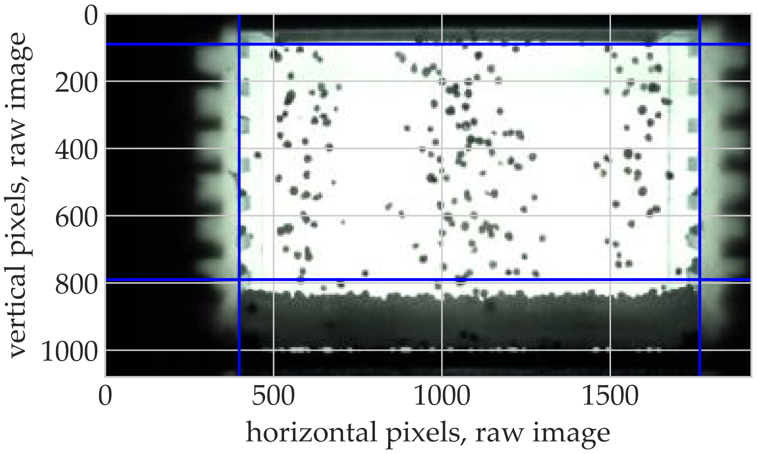

Fig. 81 Example of raw image, with cropping boundaries.

After cropping the images, static areas in the images were removed, since the interest of this work was to evaluate only the moving particles. Therefore, the pixels of static areas such as dirt and dust on the transparent walls, non-moving particles resting in the tray support structure, and the support structure itself had to be identified and whitened.

To distinguish static areas from moving particles for all frames in each video, the current frame was compared to a number of previous frames. To eliminate all elements in the videos that are not moving, a number of consecutive frames must be defined in which the color of the pixel must change at least once. By doing so, the case of different particles passing the same pixel in a series of consecutive frames can be identified, assuming that after n frames a white background must appear if no static elements are recorded at a pixel. To distinguish the relevant number of frames, n, a statistical approach is used. Knowing the particle volume fraction and assuming a uniform mixing, the binomial distribution (210) is used to estimate probabilities of particles appearing at a pixel during n consecutive frames.

$$p = \binom{n}{k} p^k \, (1 - p)^{n-k} \tag{210}$$

Each pixel in the image frames represents the projection of information from a three-dimensional volume to a flat screen. The probability estimation if a pixel shows a particle or a static element is done two-fold. Therefore, the observed volume is virtually sliced along the projected direction. The slice width of the virtual layers is set equal to the particle diameter, resulting in $n = 50$ slices. The single probability, p, that there is a particle at the pixel in one slice is represented by the particle hold-up, assuming simplified an equal particle distribution for all slices. Typical particle volume fractions within the TFHX were investigated in numerical and experimental studies, including this work, where β was found to be in the range of 1 % [124, 127, 131, 147]. Using (210) the probability, that no particle is present at one pixel within the virtual slices can be estimated by setting $k = 0$, resulting to $p_{\mathrm{npias}} = (1 - 0{,}01)^{50} = 0.605$. Hence, the probability that at the same pixel a particle is present at least once in one of the slices, can be determined by subtracting one by p_{npias}, resulting in $p_{\mathrm{pios}} = 1 - p_{\mathrm{npias}} = 0.395$. Inserting p_{pios} into (210) and setting n to a number of frames and setting $k = n$, the probability that there is always in every frame a particle at the pixel, p_{piaf}, can be estimated. Conversely, the probability that in n frames there is at least one frame without a particle at the pixel can be calculated by subtracting one by p_{piaf}, resulting in $p_{\mathrm{npiof}} = 1 - {p_{\mathrm{pios}}}^5 = 1 - p_{\mathrm{piaf}} = 0.99$ for a number of 5 frames.

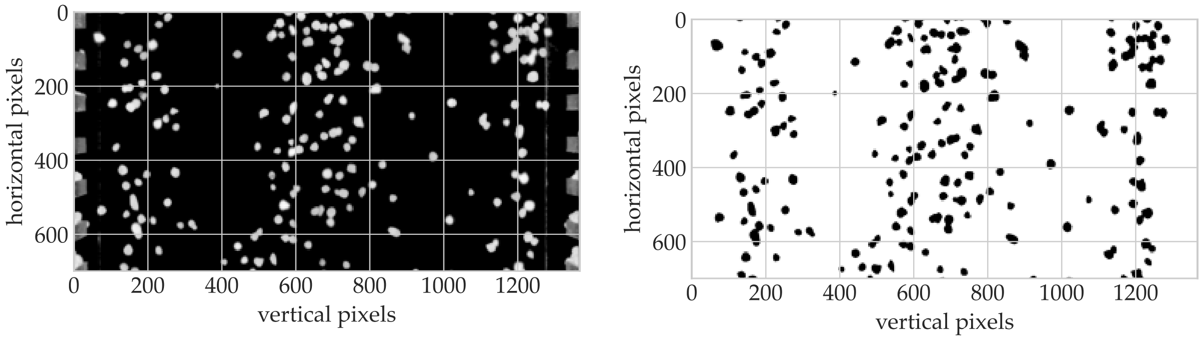

Fig. 82 Frame with inverse gray scale, before cleaning static pixels (left) and cleaned frame with b/w color (right).

Thus, it can be determined with 99 % probability, that if a pixel remains black for a consecutive series of five video frames, the pixel with a probability of 99 % represents a non-moving element. In other words, the probability of a particle passing at the same pixel in five consecutive frames is 1 %, and thus, it will not be assessed. The number of frames can be increased if a higher accuracy is desired, however at the cost of an increased computational burden.

Fig. 82 (left) shows a cropped image, with the gray threshold applied before cleaning. For better illustration, the color scheme is inverted. Fig. 82 (right) shows the same, cleaned frame after the static pixels were identified, using the method as described before. In the cleaned image, the tray support structure with static particles resting on the sides and small defects in the image, representing dirt on the transparent walls, are successfully removed. Only moving particles in the cleaned image are represented by black pixels, which is why the cleaned frame is shown in binary color. Depending on the individual camera and test setup, the particles used, and the lighting conditions, the identified thresholds may vary, or additional image processing might necessary, like the application of image filters. This will not be discussed further in this work, since the quality of the cleaned images was considered sufficient for further processing of the videos.

A.4.3 Evaluation procedure

Each images of the calibrated and cleaned videos were divided into a number of equally spaced sample cells. A cell width and height of 136 px, corresponding to a square of 5 x 5 mm, proved to be suitable for the current setup. Subdividing the cropped image into an integer number of cells in the horizontal and vertical directions typically leaves a residue of pixels. The evaluation area with all subdivided cells is centered on the cropped frame, resulting in the omission of view pixels at the border, that were not considered further during the analysis. According to the mixing theory of two components, described in section 3.2, each cell represents one sample with an individual mixing ratio, X_i. By counting the number of black and white pixels the quantity of the mixing components A and B were determined. For all individual cells per frame all local mixing compositions and the overall mixing composition were calculated.

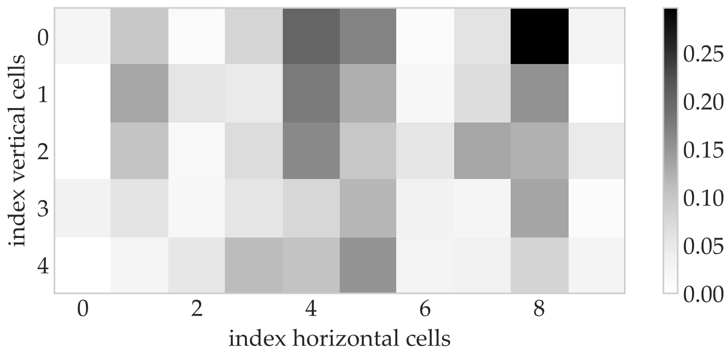

Fig. 83 Mixing composition per cell.

Fig. 83 shows the same frame that was cleaned in Fig. 82 (right), after subdividing the frame and calculating the mixing composition for each cell. The high concentration of particles shown in Fig. 82 (right) in the upper right corner is represented by a high mixing composition of about $X_{\mathrm{cell}(0,8)} = 0.3$, while in the lower left corner rather view particles are present. The two shaded, bright areas without particles, caused by the two bar elements of the “w14 h02 n2 z10” packing, are noticeable rendered in the cell columns 2 and 6. As the particle falling height increases, an equalization of the particle distribution can be observed.

For each frame the mixing quality u_n^2 , see (11), and the total mixing composition P , see (12), were calculated. Since the number of particles for each frame, P fluctuates constantly, the theoretical maxima and minima of the mixing quality σ_0^2 , see (13), and σ_z^2, see (15), were determined for each individual frame. For the exemplary frame shown in Fig. 82 and Fig. 83, the described parameters were determined to be: $u_\mathrm{n}^2 = 5.206 \cdot 10^{-3}$, $\sigma_\mathrm{z}^2 = 2.094 \cdot 10^{-3}$, $\sigma_0^2 = 76.749 \cdot 10^{-3}$. This shows that the mixing quality is rather in the range of good mixing. The relative linear particle distribution, u_{rel} see (16), for the current frame represents a deviation of 11.4 % from the best achievable mixing quality, σ_z.

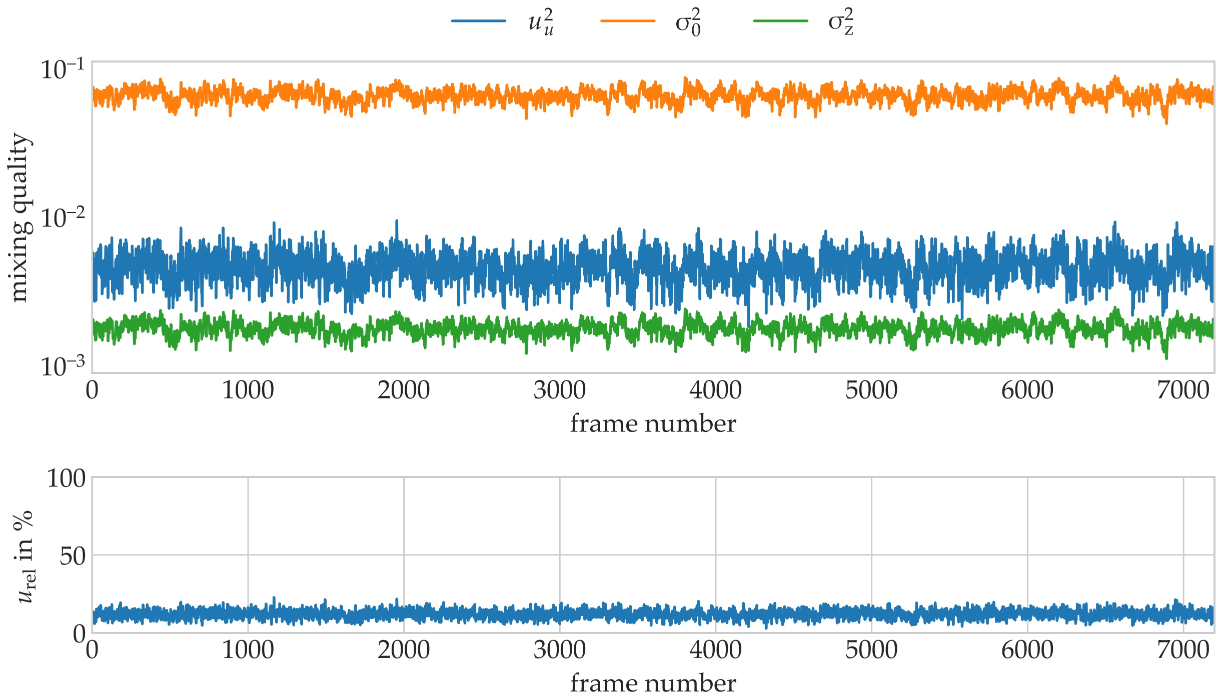

Fig. 84 Mixing quality for all frames and the corresponding minima and maxima (top) and linear, relative mixing quality (bottom).

For the evaluation of the particle distribution for each recorded video, representing each a specific combination of packing geometry and media flow rate, the values of u_n^2 and its individual extrema are determined for each frame. This is shown exemplarily in Fig. 84 (top) for the representative video. Fig. 84 (bottom) shows the relative mixing quality u_{rel} for all frames of the reference video. The arithmetic mean of all measurements can be calculated with standard statistical methods with (120), see [185], to be $\bar{u}_{\mathrm{rel}} = 11.9\ \%$. Using (121), the corresponding experimental standard deviation was determined to be $u_{u_{\mathrm{rel}}} = 1.0449 \cdot 10^{-3}$ and the experimental standard deviation of the mean was determined to be $u_{\bar{u}_{\mathrm{rel}}} = 12.314 \cdot 10^{-6}$. Both values were calculated according to standard statistical approaches such as described in section A.3.2, see [185]. $u_{\bar{u}_{\mathrm{rel}}}$ is considerably low due to the large number of samples, represented by 7,200 frames for the videos of 1 min length and a frame rate of 120 fps, see Tab. 22. Therefore, in the following, the presentation of the individual uncertainties is omitted, since for all evaluated videos the determined values for $u_{\bar{u}_{\mathrm{rel}}}$ don't exceed values of 10^{-5}.

A.4.4 Results and discussion

For two different packing structures "w10 h02 n3 z10" and "w14 h02 n2 z10" videos were recorded and analyzed. Fig. 33 in section 4.1.2.3 shows the corresponding values of $\bar{u}_{\mathrm{rel}}$ for each varying flow and packing condition. Air mass flow rates ranging from $0\ \mathrm{kg/(s \cdot m^2)}$ to $9\ \mathrm{kg/(s \cdot m^2)}$ were investigated. Additionally, three orifice plates with different diameters were installed to obtain different particle mass flow rates for the measurements. It was observed that for one orifice plate the resulting particle mass flows were not necessarily constant, but decrease with increasing air mass flow rates, see Tab. 9 in section 4.1.1.3. Accordingly, only ranges of particle mass flows can be provided for the results in Fig. 33. The origins of this observation are not yet fully understood and should be investigated in more detail. What can be observed is that a narrower orifice, with a diameter closer to a critical diameter where particle blockage is more likely to occur, has a greater sensitivity to a reduced particle mass flow for an increased airflow. In terms of the particle mixing quality, Fig. 33 illustrates that the packing structure with a higher bar width of 14 mm results in a measurable deterioration of particle mixing quality. The effect of increased particle shaded areas can be measured. Independent of the measured particle mass flows, Fig. 33 shows that the quality of particle distribution increases proportionally with air flow for air mass flow rates greater than $2\ \mathrm{kg/(s \cdot m^2)}$. This effect is amplified by approaching air velocities of $8\ \mathrm{kg/(s \cdot m^2)}$ and thus entering the range of the particle terminal velocity of about 8 m/s, which can be determined with the correlations for the particle drag coefficient, e.g. provided by or Kaskas [186]. With further increase of the gas flow rate, the hydrodynamics of the particles started to change from a trickling state to a fluidized state, resulting in mixing qualities close to ideal stochastic uniform mixing, but no data for air mass flow rates higher than $9\ \mathrm{kg/(s \cdot m^2)}$ can be provided, since the blower used in the presented setup was not able to provide higher air flow rates.

A.4.5 Conclusion

A method was developed and tested to determine and evaluate the particle density distribution of a diluted grain stream. A rather simple measurement setup was intentionally designed, using consumer optics and a camera with video functionality. The method describes the cleaning of the video frames and discusses the validity of reducing the three-dimensional problem to a two-dimensional one. The presented method should only be applied if it can be assumed that the spatial grain distribution along the projection depth in the observation area is statistically equal. Another limitation of the method could be the grain size. The camera setup was able to produce videos with sharp images for the particles used. When using much smaller or powder-like particles, the optics needed for sharp images could limit the observable depth of the observation area, where other approaches such as laser or X-ray might be more advantageous. For the particle type presented in this work, in combination with the installed packing structures, the provided results allow to measure the particle density distribution in different packing geometries.

A.5 Particle terminal velocity in air

A.5.1 Theory

Assuming single particle behavior for freely falling particles, where the development and terminal velocity can be considered as independent of interacting particles, or shielding or agglomeration, causing to increase the particle falling velocity, the velocity of the grain can be derived of the conservation of momentum (215), with the following exerting forces:

- Acceleration force, F_a

$$F_\mathrm{a} = m_\mathrm{p}\, a_\mathrm{p} = \rho_\mathrm{p}\, V_\mathrm{p} \frac{du_\mathrm{p}}{dt} \qquad (211)$$

- Gravitational force, F_g

$$F_\mathrm{g} = m_\mathrm{p}\, \mathrm{g} \qquad (212)$$

- Buoyancy force in air, F_b

$$F_\mathrm{b} = \rho_\mathrm{a}\, \mathrm{g}\, V_\mathrm{p} \qquad (213)$$

- Drag or frictional force, F_D, exerted by the relative velocity between the air and the particle as a function of the cross-sectional area of the projected particle, A_p

$$F_\mathrm{D} = c_\mathrm{D}(Re_{d_\mathrm{p}})\, A_\mathrm{p} \frac{\rho_\mathrm{a}}{2} u_\mathrm{r}(t)^2 \qquad (214)$$

$$\vec{F}_\mathrm{a} + \vec{F}_\mathrm{g} + \vec{F}_\mathrm{b} + \vec{F}_\mathrm{D} = 0 \qquad (215)$$

As depicted in Fig. 85, all forces are assumed to act at the center of the particle. Additionally, the figure depicts the relative velocity, $u_\mathrm{r}(t)$, of a freely falling particle in a constant airflow.

$$u_\mathrm{r}(t) = u_\mathrm{p}(t) - u_\mathrm{a} \qquad (216)$$

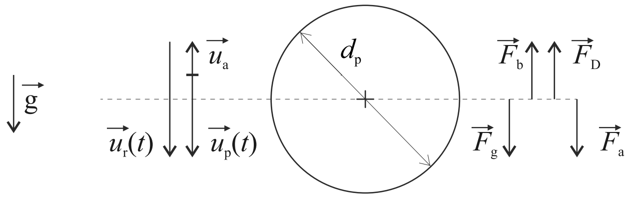

Fig. 85 Simplified force and velocity model, exerting on a freely falling single sphere.

In accordance with the orientation of the exerting forces illustrated in Fig. 85, (215) can be rewritten as follows:

$$F_\mathrm{a} = F_\mathrm{g} - F_\mathrm{b} - F_\mathrm{D} \qquad (217)$$

Inserting the equations from (211) to (214) in (217) the momentum equation can be rewritten as follows:

$$\begin{aligned} \rho_\mathrm{p}\,\frac{du_\mathrm{p}}{dt} &= \left(\rho_\mathrm{p}-\rho_\mathrm{a}\right)\mathrm{g} - c_\mathrm{D}(Re_{d_\mathrm{p}})\frac{A_\mathrm{p}}{V_\mathrm{p}}\frac{\rho_\mathrm{a}}{2}u_\mathrm{r}(t)^2 \\ \rho_\mathrm{p}\,\frac{du_\mathrm{p}}{dt} &= (\rho_\mathrm{p}-\rho_\mathrm{a})\,\mathrm{g} - c_\mathrm{D}(Re_{d_\mathrm{p}})\frac{3}{4}\frac{\rho_\mathrm{a}}{p_\mathrm{p}}u_\mathrm{r}(t)^2 \end{aligned} \tag{218}$$

In stationary conditions, the acceleration of a particle is zero, $\dot{u}_\mathrm{p} = 0$. For a free falling particle in a non-moving atmosphere, $u_\mathrm{a} = 0$, the relative velocity is equal to the particle velocity, $u_\mathrm{r} = u_\mathrm{p}$. Hence, the free-fall, or terminal velocity of a particle, u_t, can be deduced: [101]

$$u_\mathrm{t} = \sqrt{\frac{4}{3}\cdot\frac{\rho_\mathrm{p}-\rho_\mathrm{a}}{\rho_\mathrm{a}}\cdot\frac{g\,d_\mathrm{p}}{c_\mathrm{D}(Re_\mathrm{t})}} \tag{219}$$

The Reynolds number at terminal conditions is a function of the particle diameter and fluid velocity and conditions regarding pressure and temperature. [101]

$$Re_\mathrm{t} = \frac{u_\mathrm{t}\,d_\mathrm{p}\,\rho_\mathrm{a}}{\eta_\mathrm{a}} = \frac{u_\mathrm{t}\,d_\mathrm{p}}{\nu_\mathrm{a}} \tag{220}$$

In section 2.2.3, the referenced literature, for example, [114, 187], typically employs the drag force model proposed by Schiller-Naumann [188], which is applicable up to Reynolds numbers of 800.

$$c_\mathrm{D}(Re_\mathrm{t}) = \frac{24}{Re_\mathrm{t}}\left(1+0.150\cdot {Re_\mathrm{t}}^{687}\right), \text{for } Re_\mathrm{t} < 800 \tag{221}$$

The particles, used in the mentioned literature, typically do not exceed particle diameters of more than 0.5 mm. However, the 1 mm particles employed within the temperature ranges outlined in section 2.2.1 exceed the maximum Reynolds number of the Schiller-Naumann model. Consequently, in this work, an alternative the correlation provide by Kaskas [186] was applied.

$$c_\mathrm{D}(Re_\mathrm{t}) = \frac{24}{Re_\mathrm{t}} + \frac{4}{\sqrt{Re_\mathrm{t}}} + 0.28\,;\text{for } Re_\mathrm{t} < 2\cdot 10^5 \tag{222}$$

The particle terminal velocity must be determined through an iterative process, assuming, for example, an initial drag coefficient. Tab. 23 shows u_t for varying gas temperatures and particle diameters.

A.5.2 Tables

Tab. 23 Terminal velocity in m/s for a single bauxite sphere, for varying air temperature at ambient pressure and varying particle diameter.

	d_p in mm												
				[113]									
				[146]	[148]	[148]		[148]					
T in °C	0.05	0.1	0.30	0.37	0.59	0.84	1.00	1.19	1.5	2.0	3.0	10.0	30.0
1000	0.093	0.36	2.46	3.39	6.38	9.58	11.5	13.5	16.6	21.0	28.3	59.7	109
900	0.098	0.37	2.53	3.46	6.41	9.52	11.3	13.3	16.3	20.5	27.5	57.5	105
800	0.104	0.39	2.59	3.52	6.42	9.43	11.2	13.1	16.0	20.0	26.6	55.3	100
700	0.110	0.41	2.66	3.58	6.42	9.33	11.0	12.8	15.5	19.3	25.6	52.9	95.6
600	0.118	0.44	2.73	3.64	6.40	9.18	10.8	12.5	15.1	18.7	24.6	50.3	90.8
500	0.127	0.47	2.80	3.70	6.36	9.00	10.5	12.1	14.5	17.9	23.5	47.6	85.6
400	0.138	0.50	2.86	3.74	6.29	8.77	10.2	11.7	13.9	17.1	22.2	44.7	80.1
300	0.152	0.54	2.92	3.77	6.17	8.47	9.76	11.2	13.2	16.1	20.8	41.4	74.0
200	0.171	0.60	2.97	3.77	5.99	8.08	9.25	10.5	12.4	15.0	19.2	37.9	67.5
100	0.199	0.67	2.99	3.72	5.72	7.57	8.60	9.7	11.3	13.6	17.4	33.9	60.1
20	0.230	0.74	2.96	3.62	5.39	7.02	7.93	8.9	10.3	12.3	15.6	30.2	53.3

Tab. 24 Air flow in kg/(s · m^2) required to reach terminal conditions by Kaskas, for varying air temperature at ambient pressure and varying bauxite particle diameter.

	d_p in mm												
				[113]									
				[146]	[148]	[148]		[148]					
T in °C	0.05	0.1	0.30	0.37	0.59	0.84	1.00	1.19	1.5	2.0	3.0	10.0	30.0
1000	0.026	0.097	0.67	0.93	1.74	2.62	3.13	3.70	4.55	5.75	7.73	16.3	29.8
900	0.029	0.111	0.75	1.03	1.90	2.82	3.37	3.96	4.84	6.09	8.15	17.1	31.1
800	0.034	0.127	0.84	1.14	2.08	3.06	3.63	4.25	5.18	6.48	8.62	17.9	32.5
700	0.039	0.148	0.95	1.28	2.30	3.34	3.94	4.59	5.56	6.92	9.17	18.9	34.2
600	0.047	0.175	1.09	1.45	2.55	3.66	4.30	4.99	6.01	7.44	9.81	20.1	36.2
500	0.057	0.210	1.26	1.67	2.87	4.05	4.73	5.47	6.55	8.06	10.6	21.4	38.5
400	0.071	0.260	1.48	1.94	3.25	4.53	5.26	6.05	7.20	8.82	11.5	23.1	41.4
300	0.093	0.331	1.78	2.29	3.75	5.14	5.93	6.78	8.03	9.77	12.6	25.2	45.0
200	0.126	0.440	2.19	2.78	4.41	5.95	6.81	7.74	9.10	11.0	14.1	27.9	49.6
100	0.185	0.622	2.79	3.48	5.34	7.06	8.03	9.07	10.6	12.7	16.2	31.6	56.1
20	0.273	0.875	3.52	4.31	6.42	8.36	9.43	10.6	12.3	14.7	18.6	35.9	63.5

Tab. 25 Drag coefficient for a single sphere, for varying air temperature at ambient pressure and varying bauxite particle diameter.

	d_p in mm												
				[113]									
				[146]	[148]	[148]		[148]					
T in °C	0.05	0.1	0.30	0.37	0.59	0.84	1.00	1.19	1.5	2.0	3.0	10.0	30.0
1000	1E+03	1E+02	8.4	5.48	2.467	1.559	1.296	1.104	0.923	0.771	0.639	0.478	0.431
900	8E+02	1E+02	7.4	4.86	2.255	1.455	1.220	1.048	0.884	0.746	0.624	0.474	0.430
800	7E+02	9E+01	6.4	4.28	2.053	1.354	1.147	0.993	0.846	0.721	0.609	0.470	0.428
700	537	76	5.5	3.75	1.861	1.257	1.075	0.939	0.808	0.695	0.594	0.465	0.427
600	422	61	4.7	3.25	1.679	1.163	1.005	0.887	0.770	0.670	0.579	0.461	0.425
500	322	47	4.0	2.80	1.507	1.072	0.937	0.834	0.733	0.645	0.563	0.456	0.423
400	237	36	3.3	2.38	1.343	0.984	0.870	0.783	0.696	0.619	0.547	0.451	0.421
300	165	26	2.7	1.99	1.188	0.898	0.804	0.732	0.658	0.593	0.531	0.446	0.419
200	108	18	2.2	1.65	1.041	0.814	0.739	0.681	0.621	0.566	0.514	0.441	0.417
100	63	11	1.7	1.33	0.901	0.732	0.674	0.629	0.582	0.538	0.496	0.435	0.415
20	37	7	1.3	1.10	0.793	0.666	0.622	0.587	0.550	0.515	0.480	0.430	0.413

Tab. 26 Reynolds numbers for a single sphere, for varying air temperature at ambient pressure and varying bauxite particle diameter.

	d_p in mm												
				[113]									
				[146]	[148]	[148]		[148]					
T in °C	0.05	0.1	0.30	0.37	0.59	0.84	1.00	1.19	1.5	2.0	3.0	10.0	30.0
1000	0.025	0.192	3.992	6.777	20.33	43.45	61.90	87.05	134.8	227.0	458.0	3224	17629
900	0.030	0.231	4.686	7.905	23.37	49.42	70.09	98.16	151.3	253.6	509.1	3557	19401
800	0.037	0.280	5.568	9.327	27.13	56.74	80.10	111.7	171.3	285.8	570.8	3957	21531
700	0.046	0.348	6.715	11.16	31.89	65.91	92.59	128.6	196.2	325.6	647.0	4450	24147
600	0.059	0.441	8.243	13.58	38.06	77.69	108.5	150.0	227.7	376.0	743.0	5068	27425
500	0.078	0.576	10.35	16.87	46.28	93.21	129.5	178.1	268.9	441.5	867.7	5868	31660
400	0.107	0.780	13.35	21.52	57.65	114.5	158.1	216.3	324.7	530.0	1035	6939	37322
300	0.155	1.111	17.88	28.43	74.17	144.9	198.9	270.7	403.9	655.3	1272	8443	45266
200	0.242	1.690	25.18	39.42	99.8	191.8	261.4	353.6	524.1	844.8	1629	10702	57172
100	0.423	2.843	38.22	58.73	143.7	270.9	366.5	492.8	725.1	1161	2222	14434	76805
20	0.750	4.798	57.91	87.46	207.6	384.8	517.1	691	1011	1609	3060	19683	104374

Tab. 27 Air flow in kg/(s · m^2) required to reach terminal conditions by Kaskas, for varying air temperature at ambient pressure and varying silica particle diameter.

	d_p in mm												
				[113] [146]	[148]	[148]		[148]					
T in °C	0.05	0.1	0.30	0.37	0.59	0.84	1.00	1.19	1.5	2.0	3.0	10.0	30.0
1000	0.019	0.073	0.522	0.725	1.40	2.13	2.57	3.06	3.79	4.82	6.54	13.98	25.60
900	0.022	0.083	0.583	0.805	1.53	2.31	2.77	3.28	4.04	5.11	6.90	14.63	26.71
800	0.025	0.096	0.656	0.899	1.68	2.51	2.99	3.53	4.32	5.45	7.31	15.37	27.99
700	0.029	0.112	0.744	1.01	1.86	2.74	3.25	3.82	4.66	5.83	7.78	16.23	29.45
600	0.035	0.132	0.854	1.15	2.07	3.02	3.56	4.16	5.04	6.28	8.33	17.22	31.16
500	0.043	0.159	0.994	1.33	2.34	3.35	3.93	4.57	5.51	6.82	8.99	18.40	33.19
400	0.053	0.197	1.17	1.55	2.66	3.76	4.39	5.07	6.07	7.47	9.78	19.83	35.65
300	0.069	0.252	1.42	1.85	3.09	4.29	4.96	5.70	6.78	8.29	10.78	21.62	38.74
200	0.095	0.337	1.76	2.25	3.65	4.98	5.72	6.53	7.71	9.36	12.08	23.96	42.75
100	0.140	0.480	2.26	2.85	4.44	5.94	6.77	7.67	8.99	10.83	13.87	27.18	48.30
20	0.207	0.680	2.88	3.56	5.38	7.05	7.99	9.00	10.47	12.53	15.93	30.89	54.68